STAR BUR Runs 24 - 25

STAR Collaboration

2023

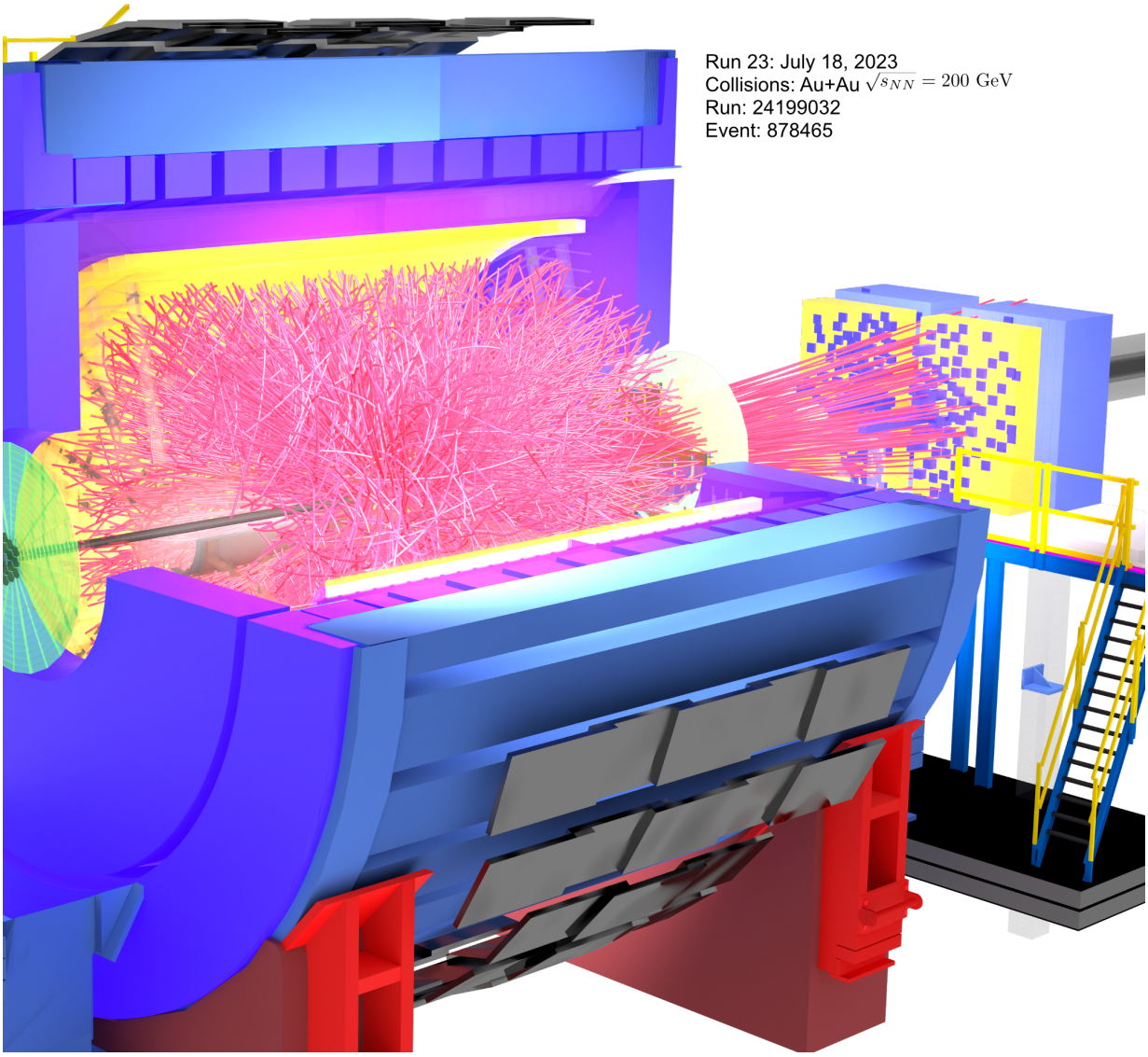

Executive Summary

This Beam Use Request outlines the compelling physics programs proposed by STAR collaboration for data taking in 2024-25.

STAR's **highest scientific priority** is to complete the "must-do" Cold QCD forward physics program enabled by the recently completed suite of forward detectors via the collection of transversely polarized p+p and p+Au data at 200 GeV in Run-24. A combination of soft and hard probes collected during 2024-25, as outlined in Table 1, will be used to probe the QGP's microstructure and continue our unique forward physics program via the collection of high statistics Au+Au, p+Au, and p+p data at $\sqrt{s_{\rm NN}}$ = 200 GeV.

Table 1: Proposed Run-24 - Run-25 assuming 28 cryo-weeks of running every year, and 5.5 weeks set-up time to switch species in 2024. For p+p and p+Au sampled luminosities assume a "take all" trigger. For Au+Au we provide the requested event count for our minimum bias trigger, and the requested sampled luminosity from our a high-$p_{\rm T}$ trigger that covers all v_z. Due to the recent Blue Ring valve box event, we ended Run-23 in August. Six Au+Au weeks from Run-23 will be carried forward into Run-24 and are taken into account for our combined Au+Au program.

$\sqrt{s_{\rm NN}}$ (GeV)	Species	Number Events/ Sampled Luminosity	Year
200	p+p	142 pb^{-1}/12w	2024
200	p+Au	0.69 pb^{-1}/10.5w	2024
200	Au+Au	18B / 32.7 nb^{-1}/40w	2023+2025

STAR's scientific program is enabled by the combination of the detector upgrades for Beam Energy Scan phase II (BES-II) and the Forward Upgrades. In combination they generate STAR's unique capabilities in particle identification (PID) over an extended rapidity acceptance and down to very low transverse momentum ($p_{\rm T}$), while maintaining a low material budget. All these new detectors are now fully commissioned and operated exceptionally well during Run-22 and Run-23.

STAR considers it critical that we collect approximately equal nucleon-nucleon luminosities for p+p and p+Au at 200 GeV during Run-24. This optimizes the statistical precision of several critical observables that require comparisons between results in both p+p and p+Au. We request radially polarized protons for both datasets. Assuming 28 cryo-weeks in Run-24 we expect to record samples that represent a factor 2.7 times the luminosity that STAR sampled during the last transversely polarized p+p collisions in Run-15, and 1.5 times the luminosity sampled during Run-15's transversely polarized p+Au collision period.

Significantly increased luminosities, the extended acceptance at mid-rapidity due to the iTPC, improved event plane and triggering capabilities via the EPD, and the ability to probe the previously inaccessible forward region are all exploited in our Hot QCD program, that informs on the microstructure of the QGP, and our Cold QCD program that will utilize transverse polarization setting the stage for related future measurements at the Electron-Ion Collider (EIC).

Combined Au+Au datasets collected in Run-23 and Run-25 will allow STAR to address important questions about the inner workings of the QGP, including the temperature dependence of the shear and bulk viscosities, the 3-D nature of the initial state, how global vorticity is transferred to the spin angular momentum of particles on such short time scales and the chiral properties of the medium.

As requested, we also considered the scenario that each run is reduced to 24 cryo-weeks. Under this scenario the STAR collaboration continues to request Au+Au, p+Au, and p+p running as outlined in Table 2. In this way we will take the best possible advantage of our recent upgrades. However, this scenario would result in a significant increase in both the statistical and systematic uncertainties of all the data, impacting the excellent precision we aim for with the measurements described in this BUR.

We estimate that 24 as opposed to 28 cryo-weeks will decrease STAR's Au+Au data sample by at least 9%. Measurements of hard probes (jets and quarkonia), thermal di-lepton and photon-induced processes (di-lepton and J/ψ) will be most impacted since they are the most statistically demanding Hot QCD measurements proposed.

There is a much more significant effect on p+p and p+Au running due to both the 5.5 weeks needed to change beam species, the ramp-up times, and the fact that no low-luminosity running is requested. We estimate at least a 24-16% loss in sampled p+p and p+Au luminosity. There will be an even larger impact on the nuclear PDFs, fragmentation functions, and gluon saturation measurements since these require comparisons of the same observables measured in both p+p and p+Au collisions.

With further reduction to 20 cryo-weeks for Run-24, STAR collaboration requests p+Au, and p+p running as outlined in Table 3, and the significant reduction will impact the excellent precision as described in our BUR.

Table 2: Proposed Run-24 - Run-25 assuming 24 cryo-weeks of running every year, and 5.5 weeks set-up time to switch species in 2024. For p+p and p+Au sampled luminosities assume a "take all" trigger. For Au+Au we provide the requested event count for our minimum bias trigger, and the requested sampled luminosity from our a high-p_{T}trigger that covers all v_z.

$\sqrt{s_{\mathrm{NN}}}$ (GeV)	Species	Number Events/ Sampled Luminosity
200	p+p	108 pb^{-1}/9.5w
200	p+Au	0.58 pb^{-1}/9w
200	Au+Au	16B / 29.4 nb^{-1}/36w

Finally in Section 5 we propose the collection of two datasets if the opportunity arises after collection of our higher priority datasets outlined above. One proposal enables the imaging of the shape and radial profile of atomic nuclei via collective flow measurements. Such studies are important to improve our understanding of the complex initial conditions and subsequent hydrodynamical response of the medium. Information on these deformation and nuclear skin parameters are also of significant interest to the nuclear structure physics community.

Table 3: Proposed Run-24 assuming 20 cryo-weeks of running every year, and 5.5 weeks set-up time to switch species in 2024.

$\sqrt{s_{\rm NN}}$ (GeV)	Species	Number Events/ Sampled Luminosity
200	p+p	81 pb^{-1}/7.5w
200	p+Au	0.42 pb^{-1}/7w

Heavy ion collision data have different sensitivities to nuclear structure experiments and are therefore promising complementary tools to probe different aspects of the nucleus' shape and substructure. The other proposal expands our fixed-target program to include other light beam and target combinations. These data will help clarify the role and mechanisms of nucleon stopping. In addition, light nucleus cross sections in the target/projectile regions using beams of 3-50 GeV/n are of great interest to the NASA Space Radiation Protection community.

Contents

1 Highlights from the STAR Program **2**
- 1.1 Highlights from the Spin and Cold QCD Program . . . 2
- 1.2 Highlights from the Heavy Ion Program . . . 8
  - 1.2.1 BES-II Status and Overview . . . 8
  - 1.2.2 Spectra Highlights . . . 10
  - 1.2.3 Flow, Chirality and Vorticity Highlights . . . 16
  - 1.2.4 Correlations and Fluctuations Highlights . . . 26
  - 1.2.5 Hard Probes Highlights . . . 30
- 1.3 Run 23 Performance . . . 36
  - 1.3.1 DAQ Upgrade and Performance . . . 36
  - 1.3.2 Forward Detector Upgrade . . . 37

2 Run-24 Request for Polarized p+p and p+Au Collisions at 200 GeV **40**
- 2.1 Spin Physics with Polarized p+p and p+Au Collisions at 200 GeV . . . 41
  - 2.1.1 Forward Transverse-Spin Asymmetries . . . 41
  - 2.1.2 Sivers and Efremov-Teryaev-Qiu-Sterman Functions . . . 44
  - 2.1.3 Transversity, Collins Function and Interference Fragmentation Function 48
  - 2.1.4 Ultra-peripheral Collisions . . . 55
- 2.2 Physics Opportunities with Unpolarized p+Au Collisions . . . 57
  - 2.2.1 The Initial State of Nuclear Collisions . . . 58
  - 2.2.2 The Final State-Fragmentation Functions . . . 69
  - 2.2.3 QGP Droplet Substructure . . . 71

3 Run-25 Requests for Au+Au Collisions at 200 GeV **76**
- 3.1 Explore the Microstructure of the QGP . . . 76
  - 3.1.1 What is the Nature of the 3D Initial State? . . . 80
  - 3.1.2 What is the Precise Temperature Dependence of Viscosity? . . . 83
  - 3.1.3 What can Charmonium Tell Us About Deconfinement? . . . 85
  - 3.1.4 What is the Temperature of the Medium? . . . 86
  - 3.1.5 What are the Electrical, Magnetic, and Chiral Properties of the Medium? 88
  - 3.1.6 What are the Underlying Mechanisms of Jet Quenching? . . . 97
  - 3.1.7 What is the Nature of the Phase Transition Near $\mu_B = 0$? . . . 100
  - 3.1.8 What Can We Learn About the Strong Interaction? . . . 101
- 3.2 Ultra-Peripheral Collisions . . . 104

4 Computing Resources **120**

5 Future Opportunities **121**
- 5.1 Imaging Shape and Radial Profile of Atomic Nuclei . . . 121
- 5.2 Nuclear Data for Space Radiation Protection . . . 128

1 Highlights from the STAR Program

1.1 Highlights from the Spin and Cold QCD Program

The goal of the STAR Cold QCD program is to probe the spin and flavor structure of the proton and to understand the role of spin in Quantum Chromodynamics, exploiting the unique capability of RHIC to provide longitudinally and transversely polarized p+p collisions at multiple energies. Measurements with longitudinal beam polarizations have given new insights into the helicity structure of the proton, while measurements with transverse polarizations have provided new ways to probe polarized parton distribution functions in the collinear and transverse momentum dependent frameworks. This program is complemented by studies of polarized p+p elastic scattering and central exclusive production, in which a far-forward proton is detected intact.

Since 2009, RHIC STAR has completed several highly successful polarized p+p runs both at $\sqrt{s} = 200$ GeV and $\sqrt{s} = 500/510$ GeV. Moreover, p+Au and p+Al data sets with a transversely polarized proton beam have been recorded in 2015 at $\sqrt{s_{NN}} = 200$ GeV to address important physics problems, including the underlying non-perturbative mechanism responsible for large forward transverse single spin asymmetries and the possible onset of gluon saturation effects. Table 4 summarizes the STAR sampled luminosity and the mean beam polarizations as measured by the hydrogen jet (H-jet) polarimeter.

Table 4: Summary of polarized p+p and p+A running periods at RHIC since 2009, including center-of-mass energy, STAR's integrated luminosity and the average beam polarization for blue (B) and yellow (Y) beams from the H-jet polarimeter.

Year	System	$\sqrt{s}$ (GeV)	Reco. Lumi. (pb^{-1})	Polarization Orientation	B/Y $\langle P \rangle$ (%)
2009	p+p	200	25	Longitudinal	55/55
2009	p+p	500	10	Longitudinal	39/39
2011	p+p	500	12	Longitudinal	48/48
2011	p+p	500	25	Transverse	48/48
2012	p+p	200	22	Transverse	61/56
2012	p+p	510	82	Longitudinal	50/53
2013	p+p	510	300	Longitudinal	51/52
2015	p+p	200	52	Transverse	53/57
2015	p+p	200	52	Longitudinal	53/57
2015	p+Au	200	0.45	Transverse	60/–
2015	p+Al	200	1	Transverse	54/–
2017	p+p	510	320	Transverse	55/55
2022	p+p	510	400	Transverse	52

Since the last PAC meeting, three very mature analyses have been submitted or are about to be submitted for publication. The Sivers dijet analysis, which provides sensitivity

to the quark Sivers functions, has been submitted to Phys. Rev. Lett. [1]. The analysis of the Z^0 cross section and transverse single spin asymmetry, which probe the unpolarized transverse momentum dependent parton distribution (TMDs) and the Sivers function, is near submission to Phys. Lett. B. And lastly, the analysis of longitudinal and transverse spin transfer to Λ hyperons is also about to be submitted to Phys. Rev. D. In addition, the RHIC Spin Collaboration finished the RHIC Cold QCD program white paper [2], serving as an important input to the 2023 NSAC long range plan.

The measurement of the gluon polarization inside protons has been a major emphasis of the longitudinally polarized RHIC program, which concluded data taking in 2015. At RHIC, gluon polarization can be accessed by measurements of the spin-dependent rates of production of jets [3–9], dijets [7–11], neutral and charged pions [12–20], and direct photons [21]. An overall impact of the recent jet and dijet [7–9, 11, 22], pion [18, 20] and W [23, 24] data on the x-dependence of the gluon helicity distribution at $Q^2 = 10$ GeV^2 based on the global fit by the DSSV group is presented in the left panel of Fig. 1. The truncated moment of the gluon helicity from the new DSSV evaluations [25] at $Q^2 = 10$ GeV^2 integrated over a range of $x \in (0.001, 0.05)$ is 0.173(156) and a range of $x \in (0.05, 1)$ is 0.218(27) (at 68% C.L.), which can be seen in the right panel of Fig. 1.

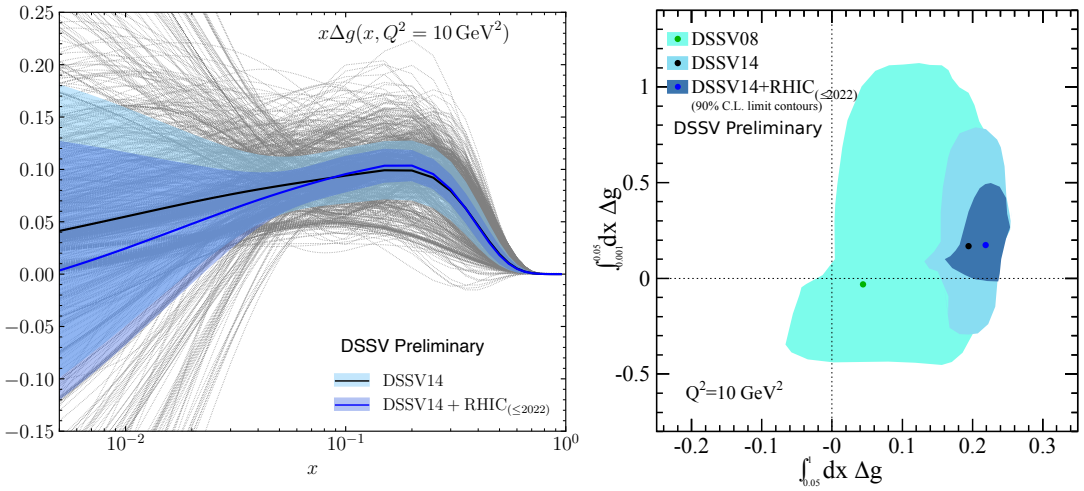

Figure 1: The impact of the recent jet and dijet, pion and W data on the gluon helicity distribution at $Q^2 = 10\,\mathrm{GeV}^2$ based on the global fit by the DSSV group. Left: the x-dependence of the gluon helicity distribution. The black curve with the 1σ uncertainty light blue band illustrates the DSSV14 results [26], while the blue curve with 1σ uncertainty band in dark blue [25] shows the preliminary results after the inclusion of the new data. Right: the gluon spin contributions in two different x ranges. Source: [2].

The truncated moment of the gluon helicity integrated from $x = 0.0071$ to 1 at $Q^2 = 10\,\mathrm{GeV}^2$ from the recent JAM global QCD analysis [27] including a subset of RHIC data,

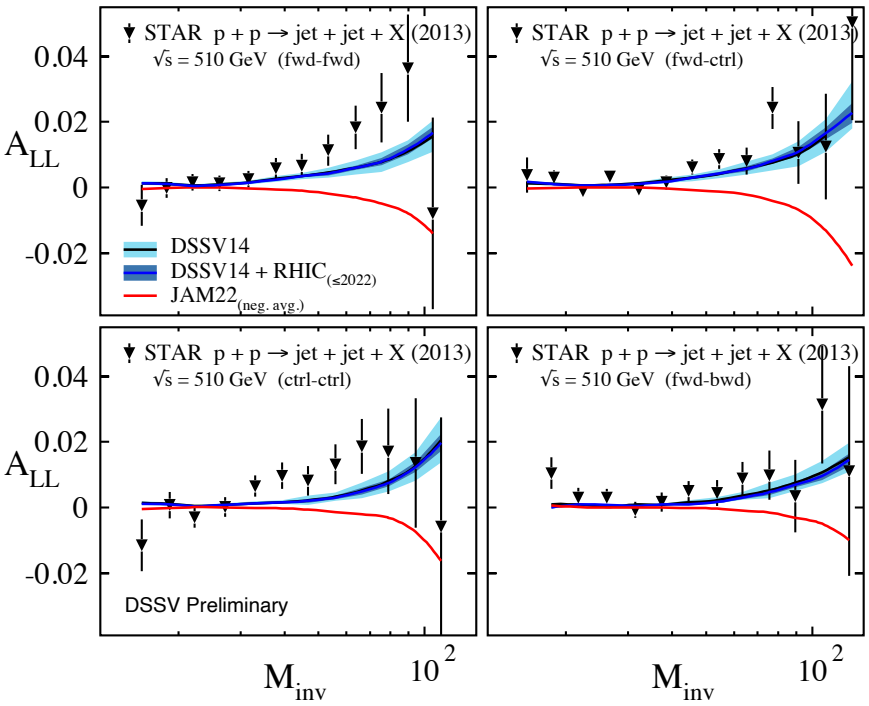

Figure 2: STAR double-helicity asymmetries A_{LL} for dijet production vs dijet invariant mass M_{inv} in polarized pp collisions at $\sqrt{s}$=510 GeV at midrapidity from the 2013 data set [9]. The DSSV14 evaluation [26] is plotted as the black curve with the 1σ uncertainty band marked in light blue. The blue curve with 1σ uncertainty band in dark blue shows the impact of all the data sets included in the new preliminary DSSV fit [25] as in Fig. 1. The red curves show the JAM $\Delta g < 0$ solution [27] calculated by the DSSV group. Source: [2].

i.e. STAR inclusive jet results, and assuming the SU(3) flavor symmetry and PDF positivity is 0.39(9). The authors of [27] also discuss the possibility of a solution with negative gluon contribution if the PDF positivity constraint is removed from the global fit. They argue that there is no fundamental theoretical requirement for PDFs to be positive at all values of x, and therefore it would be highly desirable to have an observable which is linearly sensitive to gluon helicity distribution. Direct photons coming mainly from the quark-gluon Compton process and dijets narrowing down the parton kinematics are ideal probes to distinguish between positive and negative gluon helicity solutions. Figure 2 shows that the STAR dijet data [9] strongly disfavors distributions with large and negative gluon helicities. In the plot the asymmetries A_{LL} are presented for four dijet event topologies, namely, with forward-forward jets (top left), forward-central jets (top right), central-central jets (bottom left), and forward-backward jets (bottom right), where forward jet rapidity is $0.3 < \eta < 0.9$, central jet rapidity is $|\eta| < 0.3$, and backward jet rapidity is $-0.9 < \eta < -0.3$. The forward-forward and forward-central configurations probe the most asymmetric collisions down to $x \simeq 0.015$. The forward-forward and central-central events probe collisions with $|\cos\theta^*|$ near zero, whereas forward-central and forward-backward events are more sensitive to larger $|\cos\theta^*|$, where θ^* is the scattering angle in the center-of-mass frame of scattered partons. The DSSV14 calculations are plotted as the black curves with the 1σ uncertainty bands marked in light blue. The blue curves with 1σ uncertainty bands in dark blue show the impact of all the data sets included in the new preliminary DSSV fit [25] as in Fig. 1. The curves for the JAM $\Delta g < 0$ solution [27] are presented in red.

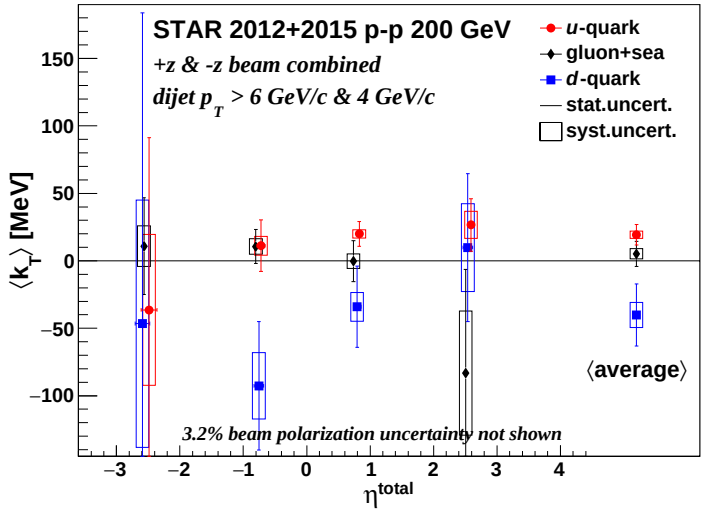

Figure 3: Results of the average transverse momentum $\langle k_T \rangle$ for individual partons, inverted using parton fractions from simulation and tagged $\langle k_T \rangle$ in data, plotted as a function of summed pseudorapidities of the outgoing jets $\eta_{\text{total}} \sim \log(x_1/x_2)$. (Positive η_{total} represents dijets emitted in the direction of the polarized beam.) The rightmost points represent the average of all the η_{total} bins. The systematic uncertainty in η_{total} is set to be non-zero to improve the visibility of the error bars [1].

In the transverse spin program, the spin-dependent Sivers function, which characterizes a scalar triple-vector correlation for an unpolarized parton and its transversely polarized parent proton, has been probed at STAR through two distinct measurements.

The first non-zero Sivers asymmetry for dijet production in collisions of polarized protons at $\sqrt{s} = 200$ GeV is presented in Fig. 3. This measurement is based on the 200 GeV transversely polarized p+p data collected in 2012 and 2015 at STAR, corresponding to an integrated luminosities of 22 pb^1 and 52 pb^1, respectively. Results are binned by the summed pseudo-rapidities of the outgoing jets, $\eta^{\text{total}} \equiv \eta_1 + \eta_2$, which is proportional to the momentum fraction ratio of two interacting partons $\eta_{total} \sim log(x_1/x_2)$. The associated Sivers observable $\langle k_T \rangle$, the average spin-dependent transverse momentum for individual partons, is extracted using simple kinematics conversion and pseudo-inversion. The u quark $\langle k_T \rangle$ and d quark $\langle k_T \rangle$ are found to have opposite signs and different magnitudes, while $\langle k_T \rangle$ for the combination of gluon and sea quarks is consistent with zero. Inclusion of these data in future global analyses will enhance a consistent extraction of Sivers observables and may also impact our understanding of evolution effects, process dependence and other important issues relating to the Sivers TMD function, e.g., factorization of the Sivers function in dijet hadroproduction [28–31].

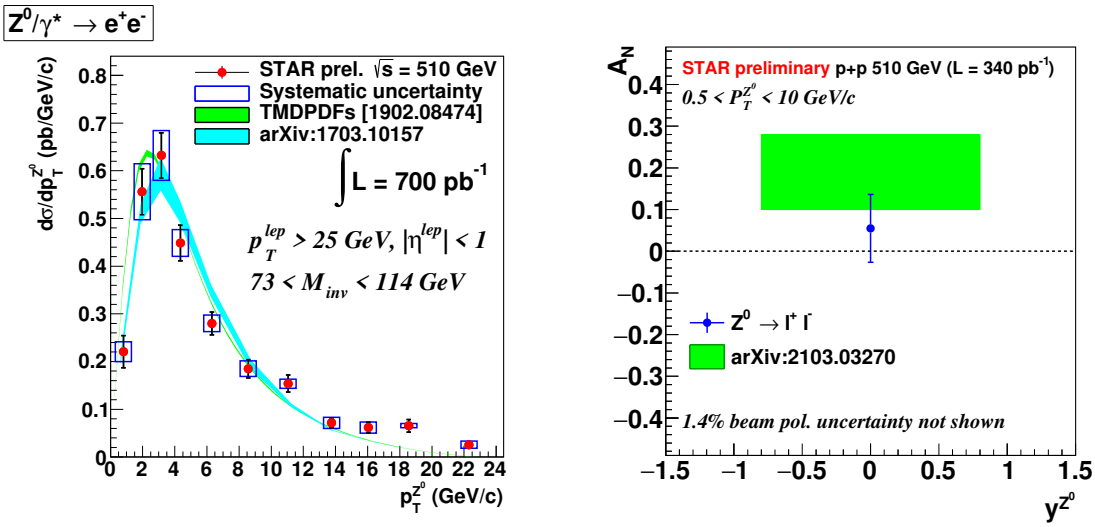

Figure 4: Left: the measured Z^0 cross section as a function of its p_{T}. The result is compared with perturbative predictions at the N^{2}LL [32] and NLL [33] accuracy. Right: the measured Z^0 transverse single spin asymmetry in transversely polarized p+p collisions. The result is compared with the theoretical predictions assuming the sign change hypothesis in green band based on the framework of TMD factorization at N^{3}LL.

Another study of the internal TMD structure of the proton is performed through Z^0 production. The left panel of Fig. 4 presents the first measurement of the Z^0 p_{T} spectrum from 510 GeV p+p collisions at STAR. The results combine all the data STAR has collected in 2011, 2012, 2013, and 2017, corresponding to a total luminosity of 690 pb^{-1}. The p_{T}

spectrum of the Z^0, together with results from other experiments on DY, SIDIS, and Z^0, provide important constraints on the x and Q^2 evolution as well as the process dependence of the unpolarized TMDs. The data are consistent with calculations by two different groups: the light green one performed the calculation of TMD evolution to next-to-next-to-leading order logarithmic (N^2LL) accuracy in perturbative QCD [32]; the light blue curve performed the calculation of TMD evolution to next-to-leading order logarithmic (NLL) accuracy [33]. RHIC provides access to a higher x region compared to the results from Tevatron and LHC [34–36], which probe the small x region. We also present the measurement of the Z^0 A_N using transversely polarized p+p collision data collected in 2017, corresponding to an integrated luminosity of 350 pb^{-1}. The result can accommodate the sign change hypothesis based on the non-universality property of the Sivers function between DY/Z/W production and SIDIS, while current data compared with the prediction based on the next-to-next-to-next-to-leading order logarithmic (N^3LL) accuracy, cannot conclusively verify the prediction.

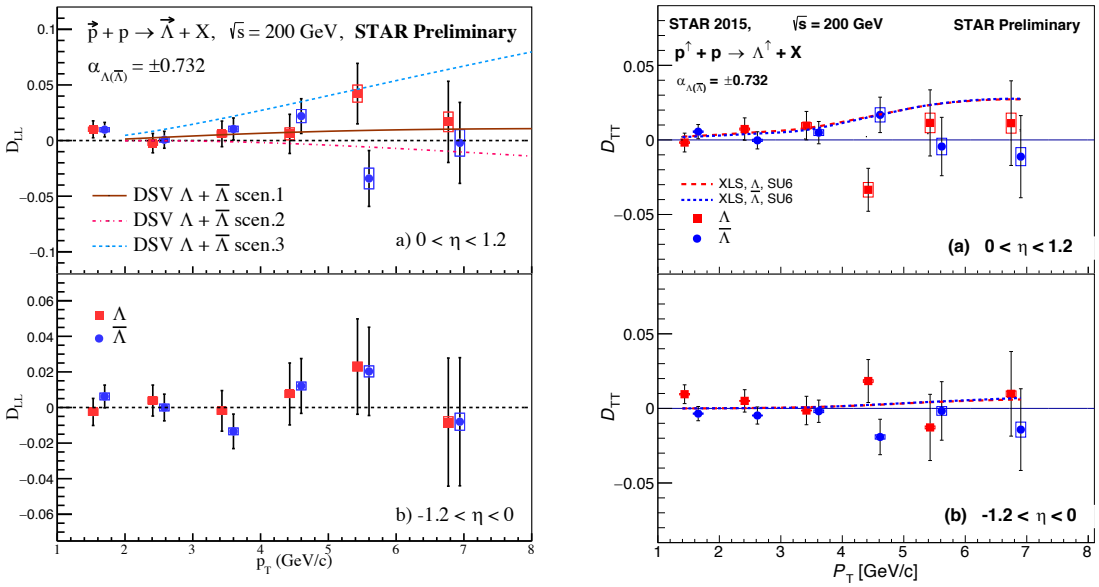

Figure 5: Left: longitudinal spin transfer, D_{LL}, of Λ hyperons as a function of their p_{T}. The top and bottom panels show the results for positive and negative hyperon η regions, respectively. The results are compared with predictions from [37–39]. Right: the results of D_{TT} as a function of p_{T}, compared with prediction from [40].

Improved measurements of the longitudinal spin transfer to Λ and $\bar{\Lambda}$, D_{LL}, and transverse spin transfer, D_{TT}, are shown in Fig. 5. The data set includes longitudinally polarized p+p collisions with an integrated luminosity of 52 pb[1], and transversely polarized p+p collisions with similar integrated luminosity. Both data sets have about twice the figure-of-merit of prior results and cover a kinematic range of $|\eta| < 1.2$ and transverse momentum p_{T} up to 8 GeV/c.

These results are expected to be sensitive to the helicity and transversity distributions of

strange and anti-strange quarks in the proton, and to the corresponding polarized fragmentation functions. The results at positive rapidity are compared with theoretical predictions for D_{LL} [37–39] and D_{TT} [40], based on different assumptions for the polarized fragmentation functions. The D_{LL} results are consistent with these predictions within uncertainties except "DSV $\Lambda + \bar{\Lambda}$ scen.3" with an extreme assumption that the polarized fragmentation functions are independent of quark flavor. The first measurements of the hyperon spin transfer D_{LL} and D_{TT}, versus fractional momentum z of the hyperon within a jet are also presented in this analysis, which can provide more direct constraints on the polarized fragmentation functions.

In addition to the above, two highlighted results from last year's Beam Use Request that were under review at the time of the 2022 PAC meeting have since been published: a study of non-linear gluon dynamics in forward rapidity back-to-back di-π^0 production [41] and a measurement of the Collins effect and other related asymmetries at mid-rapidity in p+p collisions at $\sqrt{s} = 200$ GeV [42].

1.2 Highlights from the Heavy Ion Program

1.2.1 BES-II Status and Overview

Data taking for the BES-II/FXT program was completed over runs 18-21, with all data acquisition targets being achieved or exceeded. Figure 6 shows a bar chart of the BES-II/FXT data sets recorded and compares the new datasets to the older BES-I data. Also shown in the figure are the energies for which we have overlapping coverage from both the collider and fixed-target programs. The bars are plotted as a function of μ_B, which illustrates the range of μ_B and the step size. For clarity, the collision energies ($\sqrt{s_{\rm NN}}$) are indexed along the top edge of the plot.

Data acquisition is only the first step in the process of data analysis. The calibrations team must carefully perform run-by-run calibrations for all the detector systems prior to 'production', which turns all of the raw information into tracks, time-of-flight, or energy signals (depending on the detector sub-system) which can be used by the analyzers. Following production, run-by-run QA is carried out to exclude runs for which the detector was not performing optimally. It was expected that roughly 5% of the acquired data volume would be rejected in run-by-run QA. For the collider data sets, for which run-by-run QA has been completed, we are indeed finding roughly 5% of the runs to be rejected. The fixed-target data sets from 2019 and 2020 have passed run-by-run QA at a much higher rate, most likely because they were all very short runs, and therefore the chance that a key detector component fails during the run is much smaller. Following run-by-run QA, the centrality team defines the basic event-by-event selection cuts (mostly to eliminate pile-up events) and defines the centrality selections correcting for vertex position and luminosity. Figure 7 shows a table of the energies acquired and status of each data set. This status is indicated with entries in four columns showing where each data set stands in the sequence of pre-analysis steps and whether preliminary analysis have been shown at general collaboration meetings. For the 27 GeV collider and the 3 GeV FXT datasets, which have been available to the analysis teams

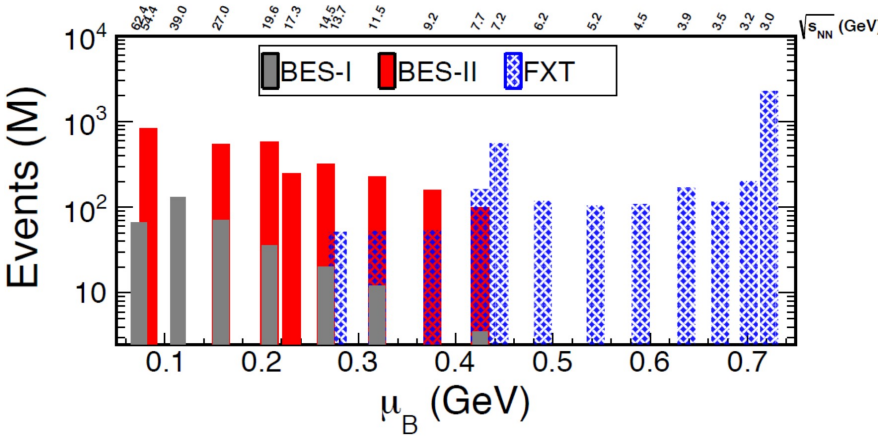

Figure 6: A summary of the good events acquired for the various collision energies (translated to μ_B). The BES-II collider data sets are shown in red bars. The FXT data sets are shown in hashed blue bars. For comparison the BES-I data sets are shown in grey bars. Note that the top FXT energy ($\sqrt{s_{\rm NN}}$= 13.7 GeV) does not quite overlap with the 14.6 GeV collider system; that FXT energy is a single beam energy of 100 GeV, which is the top energy to which RHIC can accelerate Au ions. Also note that the 54.4 GeV "BES-II" does not quite overlap with the 62.4 GeV BES-I system; the 54.4 GeV data were taken in 2017 parasitically with the first year of operation of the CeC program. This system is informally considered to be a part of the BES-II program. Likewise the data for the 7.2 GeV FXT system were parasitically acquired during single beam operations of CeC in 2018-2021.

for a few years, the Analysis column indicates the number of papers published.

The BES-II collider and FXT proposals identified a series of key physics analyses which would have sensitivity to: formation of the QGP, the first order phase transition, the critical point, and chirality. For all of these analyses, the collaboration determined the required event count needed to make a definitive measurement and those events counts were used to set the required number of events at each energy (see the "Target" numbers in Fig. 7). Analysis teams have been identified to address all of these topics. Figure 8 shows the status of all of these various analysis efforts. Significant progress has been made on all topics. To date, ten publications have come from the 3 GeV FXT [43–52] and eight have come from the 27 GeV Collider [53–60] data sets. Strategically, the collaboration plans to publish results from these two energies as separate papers from the rest of the energy scan results. These data have been available for the analysis teams significantly longer than the others energies for which production timelines were impacted due the the need to modify the software and calibration to account for the iTPC upgrade. In general, it is expected that publications addressing the other collider and fixed-target energies will wait until all (or most) of the energies are available for physics analysis, (see Fig. 8. The new results which will be shown at QM2023 will highlight FXT energies from 3.2-4.5 GeV and collider energies from 7.7-19.6 GeV The 17.3 GeV collider data set, the three high energy FXT runs (9.2, 11.5, and 13.7 GeV), and the high statistics 3.0 GeV FXT data set from 2021 will be the last produced. Those data sets are for specialized analyses which will likely result in another set of papers.

1.2.2 Spectra Highlights

The Light-flavor Spectra and Ultra-peripheral Collisions (LFSUPC) Physics Working Group (PWG) divides its efforts along six different lines of analysis: Light-charged particle (π, K, p) spectra identified through TPC dE/dx and time-of-flight (TOF) information, strange-hadron spectra identified through the secondary vertex decay topology, light-nuclei spectra identified through dE/dx and TOF, hypernuclei identified through decay topology, di-lepton production, and ultra-peripheral collisions. Analysis efforts on the first five topics have focused on newly reconstructed/processed BES-II and FXT datasets.

Five articles representing work of the LFSUPC PWG have been published since the last review [52, 61–64].

The first paper [61], presents work very similar to material that was presented as a highlight in the last review. Last year, we showed the latest dilepton excesses in the low mass and intermediate mass region which had been presented at the preceding Quark Matter conference 2022 as a preliminary result. This paper publishes the final low mass region excesses for $\sqrt{s_{NN}}$ of 27, 39, and 62.4 GeV.

New results for hypernuclei are presented in publication [52]. The masses and the Λ binding energies of the mirror hypernuclei, ${}^{4}_{\Lambda}H$ and ${}^{4}_{\Lambda}He$, are measured in Au+Au collisions at $\sqrt{s_{NN}} = 3$ GeV as shown in Fig. 9. By using the gamma-ray transition energies of the excited states from previous measurements, the Λ binding energies of them in excited states are also extracted. The Charge Symmetry Breaking (CSB) effect in A = 4 hypernuclei are then studied by measurements of the Λ binding-energy differences between the ground states

2018	Start	Stop	Good	Target	Calib/Prod	RbyR QA	Centrality	Analysis
27 GeV	May 10th	June 17th	555 M	700 M	Produced	Completed	Completed	Published 7
3.0 FXT	May 30th	June 4th	258 M	100 M	Produced	Completed	Completed	Published 9
7.2 FXT	June 11th	June 12th	155 M	none	Produced	Completed	Completed	Preliminary
2019	**Start**	**Stop**	**Good**	**Target**	**Calib/Prod**	**RbyR QA**	**Centrality**	**Analysis**
19.6 GeV	Feb 25th	April 3rd	582 M	400 M	Produced	Completed	Completed	Preliminary
14.6 GeV	April 4th	June 3rd	324 M	310 M	Produced	Completed	Completed	Preliminary
3.9 FXT	June 18th	June 18th	52.7 M	50 M	Produced	Completed	Completed	Preliminary
3.2 FXT	June 28th	July 2nd	200.6 M	200 M	Produced	Completed	Completed	Preliminary
7.7 FXT	July 8th	July 9th	50.6 M	50 M	Produced	Completed		Preliminary
200 GeV	July 11th	July 12th	138 M	140 M	Produced	Completed	Completed	
2020	**Start**	**Stop**	**Good**	**Target**	**Calib/Prod**	**RbyR QA**	**Centrality**	**Analysis**
11.5 GeV	Dec 10th	Feb 24th	235 M	230 M	Produced			Preliminary
7.7 FXT	Jan 28th	Jan 29th	112.5 M	100 M	Produced	Completed		Preliminary
4.5 FXT	Jan29th	Feb 1st	108 M	100 M	Produced	Completed		Preliminary
6.2 FXT	Feb 1st	Feb 2nd	118 M	100 M	Produced	Completed		
5.2 FXT	Feb 2nd	Feb 3rd	103 M	100 M	Produced	Completed		
3.9 FXT	Feb 4th	Feb 5th	117 M	100 M	Produced	Completed	In progress	Preliminary
3.5 FXT	Feb 13th	Feb 14th	115.6 M	100 M	Produced	Completed	In progress	Preliminary
9.2 GeV	Feb 24th	Sep 1st	161.8 M	160 M	Produced	Ready		Preliminary
7.2 FXT	Sep 12th	Sep 14th	317 M	None				
2021	**Start**	**Stop**	**Good**	**Target**	**Calib/Prod**	**RbyR QA**	**Centrality**	**Analysis**
7.7 GeV	Jan 31st	May 1st	100.9 M	100 M	Produced	Completed	In progress	Preliminary
3.0 FXT	May 1st	June 28th	2103 M	2.0 B				
9.2 FXT	May 6th	May 6th	53.9 M	50 M				
11.5 FXT	May 7th	May 7th	51.7 M	50 M				
13.7 FXT	May 8th	May 8th	50.7 M	50 M				
17.3 GeV	May 25th	June 7th	256.1 M	250 M				
7.2 FXT	June 3rd	July 3rd	88.6 M	None				

Figure 7: A summary of the BES-II collider and FXT data sets taken from 2018-2021. The Start and Stop columns indicate the periods during which each data set was acquired. The Good and Target columns indicate the number of good events taken and requested. The Calib/Prod column indicates for which data sets the initial detector calibration and production have been completed. The RbyR QA column indicates where each given data set is in the run-by-run quality assurance step. The centrality column indicates where each data set fall in the centrality determination step. And the Analysis column indicates whether there are published or preliminary results for each data set.

Physics Analysis	Status of Analyses
R_{CP} up to p_T = 5 GeV/c	Physics Working Group
Elliptic Flow	Published 3 and 27 GeV, QM2023 3.0-3.9, 7.7-19.6 GeV
Chiral magnetic Effect	Published 27 GeV, QM2023 7.7, 14.6, 19.6
Directed Flow	Published 3 GeV, QM2023 3.0-7.7, 7.7-27 GeV
Femtoscopy	QM2023 3.0-4.5 GeV
Net-proton Kurtosis	Published 3 GeV, QM2023 7.7, 14.6, 19.6
Di-leptons	Published 27 GeV, QM2023 14.6, 19.6 GeV
Lambda Polarization	Published 3, 19.6 and 27 GeV,
Multi-strange Baryons	Published 3 GeV, QM2023 3.2 GeV
Hyper-nuclei	Published 3 GeV, QM2023 3.2-4.5 and 7.7-19.6 GeV
Rapidity dependent Spectra	In-prep 3.0 GeV, QM2023 3.2, 7.7-54.4 GeV
J/psi production	QM2023 14.6, 19.6, 27 GeV

Figure 8: A summary of the key physics analyses which were listed in the BES-II collider and FXT proposals and the status of the efforts on each line of analysis. The table indicates the energies for which results have been published for each analysis topic and energies for which new results will be shown at QM2023.

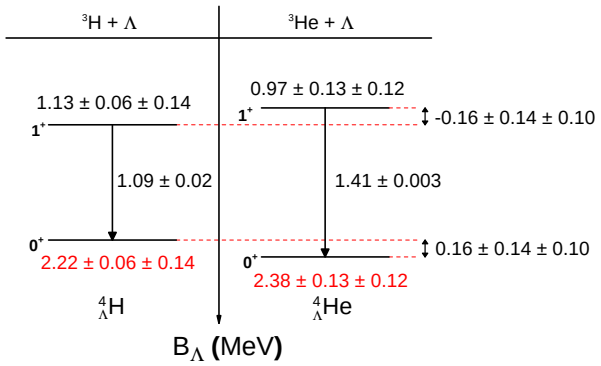

Figure 9: Energy level schemes of ${}^4_\Lambda H$ and ${}^4_\Lambda He$ in terms of Λ binding energies. The ground-state binding energies are from this analysis. The values for excited states are obtained from the gamma-ray transition energies

of ${}^4_\Lambda H$ and ${}^4_\Lambda He$ or their excited states. In comparison with other experimental measurements and theoretical studies, our results with a positive $\Delta B^4_\Lambda(0^+ - g.s.$ and a negative $\Delta B^4_\Lambda(1^+ - exc$ of comparable magnitudes within uncertainties, are consistent with the calculation using chiral effective field theory Hyperon-Nucleon (YN) potentials plus a CSB effect. Although the statistical uncertainties are large, this approach provides a new avenue to study the CSB in heavy-ion collision experiments.

In publication [62], we present the p_T spectra, dN/dy, and $< p_T >$ of K^{*0} at mid-rapidity in Au+Au collisions at $\sqrt{s_{NN}}$ = 7.7 - 39 GeV using the BES-I data. The K^{*0} $< p_T >$ is larger than that of pions and kaons and comparable to that of protons, indicating a mass dependence of $< p_T >$. The K^{*0}/K ratio in the most-central Au+Au collisions is smaller than the same in small system collision data (see Fig.'10. The K^{*0}/K ratio shows a weak centrality dependence and follows the same trend observed by previous RHIC and LHC measurements. On the contrary, the ϕ/K ratio is mostly independent of centrality. These observations support the scenario of the dominance of hadronic rescattering over regeneration for K^{*0} at BES energies. Based on the K^{*0}/K ratio, the lower limit of the time between chemical and kinetic freeze-out at BES energies is estimated. The high statistics data from the 2nd phase of BES (BES-II) will allow more precise measurements of hadronic resonances at these energies.

In publication [63] and in Fig. 11, we present the yield ratio $N_t N_p/N_d^2$ in mid-rapidity Au+Au collisions at $\sqrt{s_{NN}}$ = 7.7 – 200 GeV. The yield ratio $N_t N_p/N_d^2$ shows a monotonic decrease with increasing charged-particle multiplicity ($dN_{ch}/d\eta$) and exhibits a scaling behavior, which can be attributed to the formation of deuteron and triton via nucleon coalescence. The thermal model overestimates the triton over proton yield ratio N_t/N_p and the $N_t N_p/N_d^2$ ratio, possibly due to the effect of hadronic re-scatterings during the hadronic expansion stage. In the 0%-10% most central Au+Au collisions at $\sqrt{s_{NN}}$ = 19.6 and 27 GeV, $N_t N_p/N_d^2$ shows enhancements relative to the coalescence baseline(see Fig. 11. The significance of the

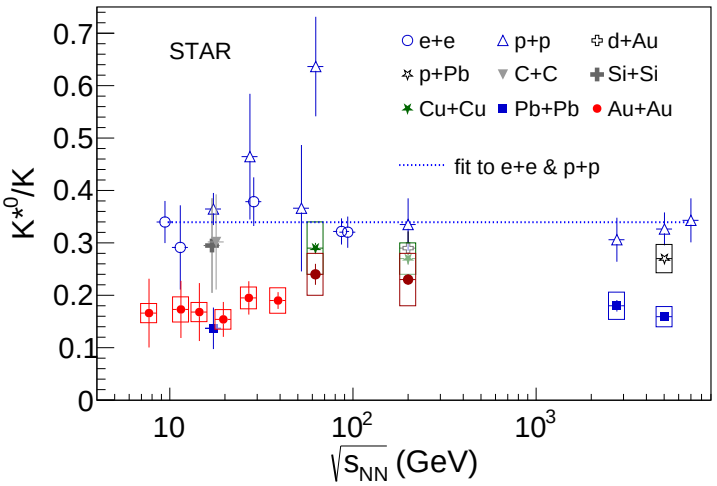

Figure 10: The beam energy dependence of K^{*0}/K ratio in e+e, p+p, d+Au, p+Au and most-central C+C, Si+Si, Au+Au and Pb+Pb collisions [62].

measurement decreases with reduced p_T range, indicating that the possible enhancement may have a strong dependence on the p_T acceptance. In peripheral collisions, similar to data, model calculations have a smooth decreasing trend as a function of energy. Further studies from dynamical modeling of heavy-ion collisions with a realistic equation of state are required to confirm if the enhancements are due to large baryon density fluctuations near the critical point. These systematic measurements of triton yields and yield ratios over a broad energy range provide important insights into the production dynamics of light nuclei and our understanding of the QCD phase diagram.

In the publication [64] we compare the light hadron production results from U+U collisions to those from Au+Au collisions at similar center-of-mass energies. The colliding nuclei have different geometrical shapes for these two systems, and hence different initial collision conditions. It is demonstrated that several physical observables: particles yields ($< dN/dy >$), average transverse momentum ($< p_T >$), particle ratios, kinetic temperature (T_k), and radial flow velocity ($< \beta >$) are consistent between U+U and Au+Au for a similar range of $< N_{part} >$ values. This might suggest that, when all the different initial state orientations of the colliding uranium nuclei are combined in the analysis, the resulting final state values approximate what is observed from colliding spherically symmetric nuclei. In other words, these observables are governed by the $< N_{part}$ for this analysis. In future experiments involving colliding uranium nuclei, it would be interesting to measure the different final state observables for identified orientations of the colliding ellipsoidal uranium nuclei. This might be done for the most central collisions where the different collision configurations can be selected by a data driven method using selections based on the probability distribution of the charged particle multiplicity and the event anisotropy for U+U collisions or by using spectator neutron measurements.

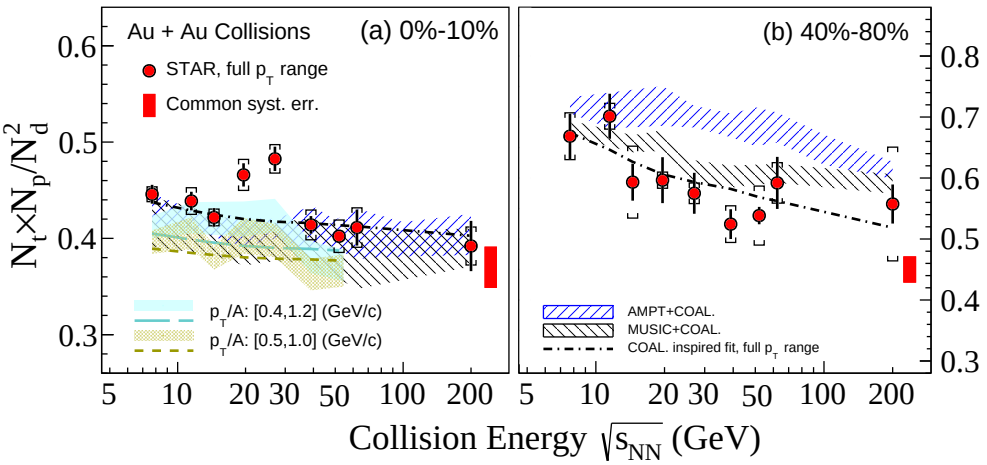

Figure 11: Collision energy, centrality, and p_T dependence of the yield ratio $N_t N_p/N_d^2$ in Au+Au collisions at RHIC. Solid circles are the results from 0%-10% central (left panel) and 40%-80% peripheral (right panel) collisions. Colored-bands in panel (a) denote p_T acceptance dependence, for which the statistical and systematic uncertainties are added in quadrature. Red solid circles are the final results with extrapolation to the full p_T range. Statistical and systematic uncertainties are shown as bars and brackets, respectively. Red vertical bands on the right side of panels represent the common systematic uncertainties. Dashed lines are the coalescence baselines obtained from the coalescence-inspired fit. Shaded areas denote the calculations from hadronic transport AMPT and MUSIC+UrQMD hybrid models.

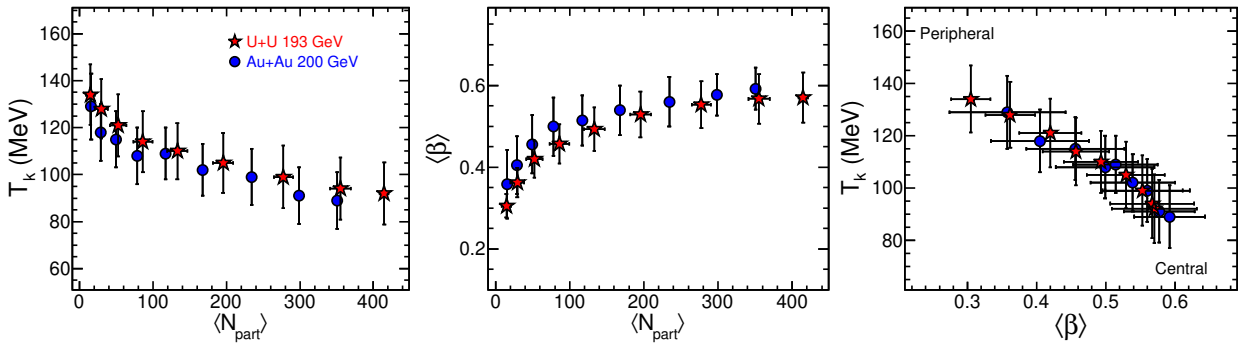

Figure 12: Left panel: T_k as a function of $< N_{part} >$. Middle panel: $< \beta >$ as a function of $< N_{part} >$. Right panel: the variation of T_k with $< \beta >$. The midrapidity ($|y| < 0.1$) results from U+U collisions at $\sqrt{s_{NN}} = 193$ GeV are compared with Au+Au collisions at $\sqrt{s_{NN}} = 200$ GeV. The uncertainties represent the total systematic and statistical uncertainties added in quadrature, dominated by systematic uncertainties.

1.2.3 Flow, Chirality and Vorticity Highlights

- Estimate of a nonflow baseline for the chiral magnetic effect in isobar collisions

  A decisive experimental test of the Chiral Magnetic Effect (CME) has become one of the primary scientific goals of the heavy-ion physics program at RHIC. Isobars have collided to utilize the fact that the collisions of ruthenium produce larger magnetic fields than those of zirconium by 5–9%, hence a 10–18% larger CME correlation signal because of its B^2 dependence. Therefore, the CME would cause the ratio of CME-sensitive observables in Ru+Ru over Zr+Zr to be greater than one, assuming that backgrounds are the same in the two systems. The isobar run was specially designed to reduce the systematics in this ratio. To minimize unconscious and pre-determined biases, a blind analysis was performed with pre-defined criteria on what would constitute observation of a CME signal. For example, the double ratio of the primary CME-sensitive correlator $\Delta\gamma$ scaled by ellipticity v_2 in ruthenium over zirconium is expected to be greater than one if there is a non-zero CME fraction. However, the isobar blind analysis results show that such a double ratio is smaller than unity, indicating that the pre-defined CME signal is not observed [65]. Recently, it was suggested that nonflow correlations are expected to cause the baseline to deviate from unity. [66] To further understand the isobar measurements, we decompose the nonflow contributions to $N\Delta\gamma/v_2$ (isobar ratio) into three terms and quantify each term by using the nonflow in v_2 measurement, published STAR data, and HIJING simulation. From these studies, we estimate a nonflow baseline of the isobar ratio of $N\Delta\gamma/v_2$ for the CME and discuss its implications.

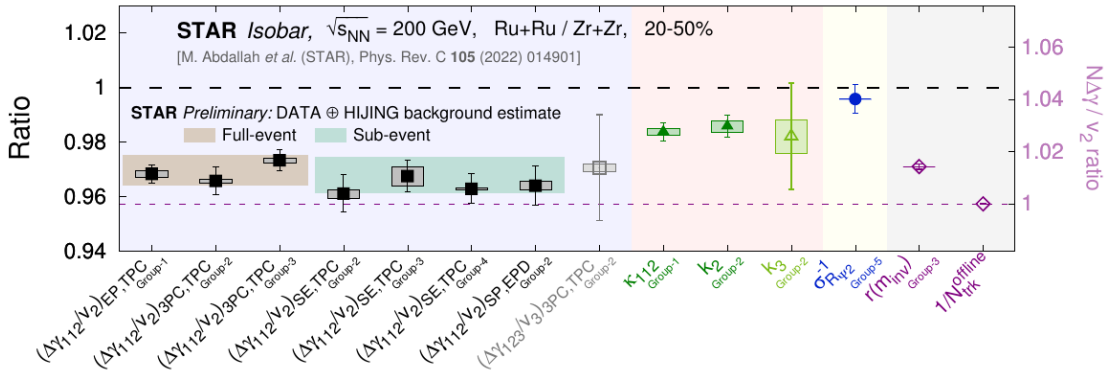

Figure 13: Background estimates with total uncertainties (bands) on the isobar ratio of $N\Delta\gamma/v_2$.

Following the procedure documented in [66], we estimate the new baseline of the isobar ratio to be $1.013 \pm 0.003 \pm 0.005$ for full-event and $1.011 \pm 0.005 \pm 0.005$ for sub-event. We plot those non-flow background estimates with the STAR isobar data in Fig. 13.

- Search for the chiral magnetic wave

  The chiral magnetic wave (CMW) has been theorized to propagate in the deconfined nuclear medium formed in high-energy heavy-ion collisions and to cause a difference

in elliptic flow (v_2) between negatively and positively charged hadrons. Experimental measurements consistent with the CMW have been reported by the STAR Collaboration at the Relativistic Heavy Ion Collider (RHIC), based on the charge asymmetry dependence of the pion v_2 from Au+Au collisions at $\sqrt{s_{\rm NN}} = 27$ to 200 GeV. Recently, the STAR experiment reported comprehensive measurements [67] of elliptic flow and triangular flow of charged pions, along with the elliptic flow of charged kaons and protons, as a function of the charge asymmetry in Au+Au collisions at $\sqrt{s_{\rm NN}} = 27$, 39, 62.4 and 200 GeV. In addition, the p+Au and d+Au at $\sqrt{s_{\rm NN}} = 200$ GeV, and U+U at 193 GeV are also measured and presented.

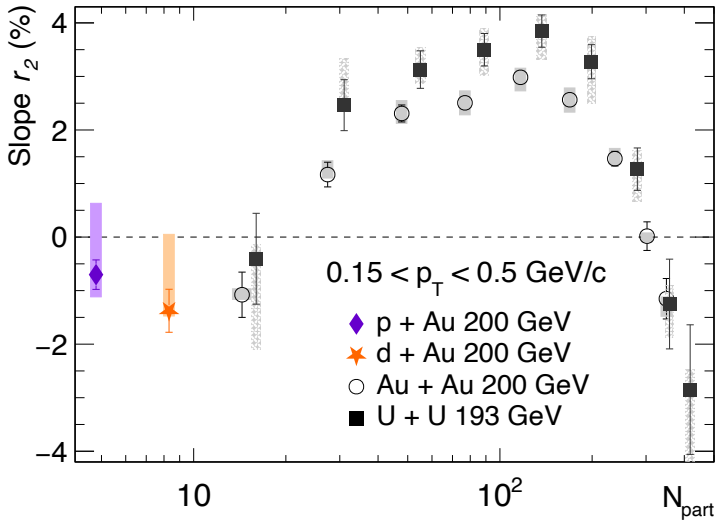

Figure 14: The $r_2 = d\Delta v_2/dA_{ch}$ slope for pions vs. $N_{\rm part}$ in p+Au, d+Au, U+U and Au+Au collisions.

Figure.14 presents the $N_{\rm part}$ dependans of th pion r_2 for p+Au, d+Au, and Au+Au collisions at 200 GeV and U+U collisions at 193 GeV. The r_2 measurements in both p+Au and d+Au are compatible with zero within uncertainties. The absence of any CMW signal in such small systems supports the picture of decoupling between the magnetic field and the second-order event plane. [68]

- Event-by-event correlations between Lambda spin measurements and CME observables in Au+Au collisions at 27 GeV from STAR

  The global polarizations (P) of Λ ($\bar{\Lambda}$) hyperons have been observed and studied in non-central heavy-ion collisions. In such collisions, a strong magnetic field is created, which causes the split of the Λ and $\bar{\Lambda}$ global polarizations ($\Delta P = P_\Lambda - P_{\bar{\Lambda}} < 0$). Quantum chromodynamics (QCD) also predicts topological charge fluctuations in a vacuum, resulting in a chirality imbalance or parity violation in a local domain. Such an effect is expected to cause a charge separation along the magnetic field, referred to as the chiral magnetic effect (CME). In addition, his charge separation can be described by the

parity-even azimuthal correlator ($\Delta\gamma$) and parity-odd azimuthal harmonic observable (Δa_1).

Recently, the STAR experiment reported the first measurements of the correlation between ΔP and $\Delta\gamma$, which is sensitive to the magnetic field in Au+Au collisions at 27 GeV. [69]

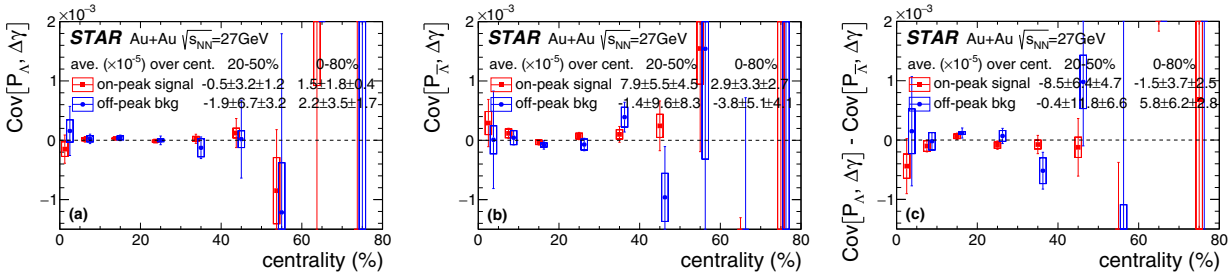

Figure 15: Covariances between the parity-even observables P_Λ and $\Delta\gamma$ (left), between $P_{\bar{\Lambda}}$ and $\Delta\gamma$ (middle), and their difference (right) as functions of centrality in Au+Au collisions at 27 GeV.

Figure 15 presents the correlation between $\Delta\gamma$ and polarizations ($\mathrm{Cov}[P_\Lambda, \Delta\gamma]$, $\mathrm{Cov}[P_{\bar{\Lambda}}, \Delta\gamma]$, and their difference) as functions of centrality. Our measurements show that the signal and background are consistent with zero within the current statistics. In addition, our measurements indicate these correlations are likely smaller than 10^{-4}. Since the correlation strengths will depend on the physics underlying the correlations, the significance of our measurements in terms of the chiral magnetic effect needs theoretical input.

Bulk Correlations

Over the past years, the STAR collaboration has conducted a series of measurements to understand the QCD phase diagram and the transport properties of the QGP phase. Here, we highlight the recent STAR bulk correlations measurements expected to shed light on QGP transport properties.

- Measurements of global and local polarization

Non-central heavy ion collisions can cause a significant orbital angular momentum (OAM) in the QGP. Part of OAM is transferred to the system in the form of preferential alignment of the intrinsic angular momentum (spin) of particles along the OAM direction through spin-orbit couplings, a phenomenon called global polarization. [70,71] Due to the nature of the weak decay, Λ hyperon's polarization can be determined through the angular distribution of the decay daughter proton in the parent's rest frame [70].

The STAR experiment has observed global polarization for Λ and $\overline{\Lambda}$ hyperons in Au+Au collisions from 7.7 to 200 GeV [72]. Large global polarization of Λ and $\overline{\Lambda}$

measured from low to high energy is compatible with the spin-orbit coupling picture, which can be described via hydrodynamic models. Theoretical calculations indicated a system size dependence of the global polarization. [73,74] Such a study can be achieved experimentally by the STAR experiment by comparing measurements from the Au+Au collisions to the isobar collisions. Furthermore, the magnetic field difference between Ru+Ru and Zr+Zr may cause a splitting between Λ and $\overline{\Lambda}$ global polarization, and this initial magnetic field difference between Ru+Ru and Zr+Zr collision may lead to different Λ global polarization in the two systems.

In our recent measurements [75], we report the Λ global and local polarization as a function of centrality in Ru+Ru and Zr+Zr collisions at $\sqrt{s_{NN}}$ = 200 GeV using the data collected by the STAR experiment.

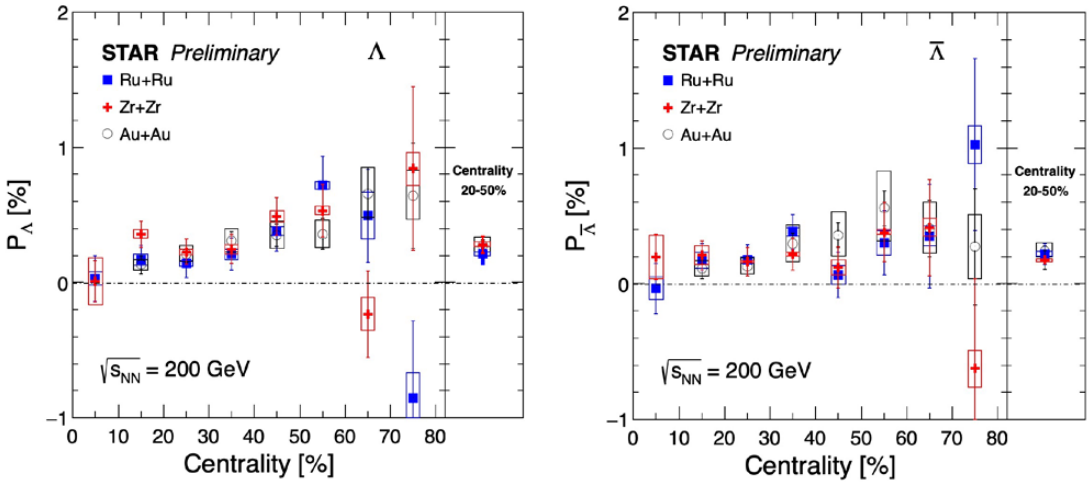

Figure 16: The centrality dependence of the global polarization of the Λ and $\overline{\Lambda}$ in Ru+Ru, Zr+Zr, and Au+Au at 200 GeV.

Figure 16 shows the centrality dependence of the global polarization of the Λ and $\overline{\Lambda}$ for Ru+Ru, Zr+Zr, and Au+Au collisions at 200 GeV. Our results are consistent between Ru+Ru, Zr+Zr, and Au+Au collisions for the whole centrality range, suggesting little if any, system size dependence.

In addition, to Ru+Ru, Zr+Zr collisions measurements STAR experiment recently published new high-statistics measurements of the global polarization of Λ and $\bar{\Lambda}$ hyperons in Au+Au collisions at $\sqrt{s_{\rm NN}}$ = 19.6 and 27 GeV. [76]

Our new measurements of the mid-central $P_{\rm H}$ at $\sqrt{s_{\rm NN}}$=19.6 and 27 GeV are presented alongside previous measurements in the upper panel of Fig. 17. The $P_{\rm H}$ measurements at $\sqrt{s_{\rm NN}}$=19.6 and 27 GeV are consistent with previous measurements at the energies studied in this work. The lower panel in Fig. 17 illustrates the difference between $P_{\bar{\Lambda}}$ and P_{Λ} integrated over 20-50% centrality as a function of $\sqrt{s_{\rm NN}}$. Our measurements with high-statistics used in this analysis indicate no statistically significant $P_{\bar{\Lambda}} - P_{\Lambda}$.

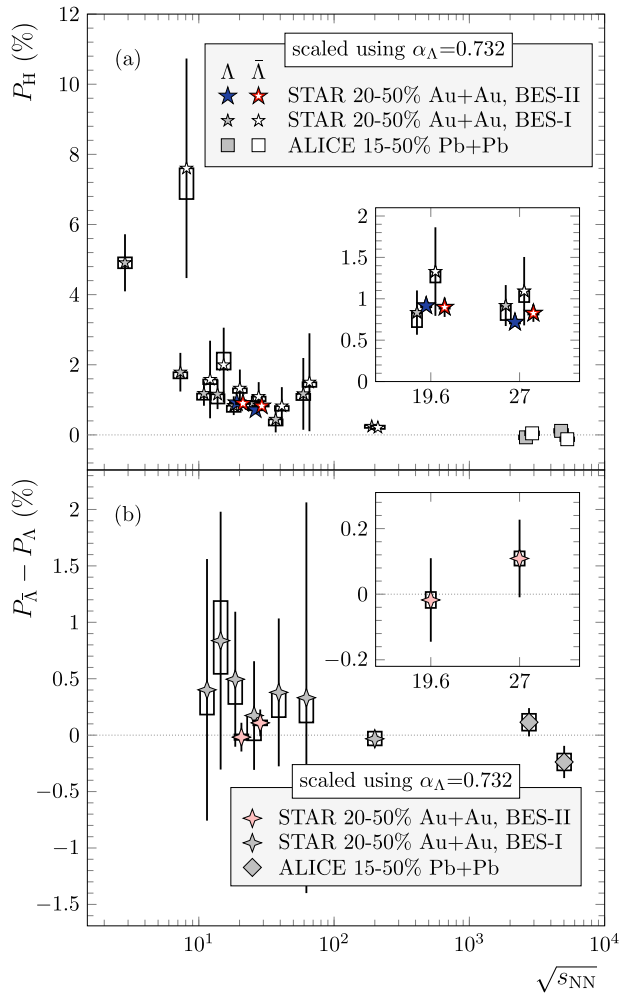

Figure 17: The new STAR measurements of the mid-central P_H at $\sqrt{s_{NN}}$=19.6 and 27 GeV are presented alongside previous measurements in the upper panel. In the lower panel, the new data of the difference between integrated $P_{\bar{\Lambda}}$ and P_Λ is shown at $\sqrt{s_{NN}}$=19.6 and 27 GeV alongside previous measurements.

At $\sqrt{s_{NN}} = 19.6$ GeV, we report $P_{\bar{\Lambda}} - P_\Lambda = -0.018 \pm 0.127(\text{stat.}) \pm 0.024(\text{syst.})\%$, and at $\sqrt{s_{NN}} = 27$ GeV, we report $P_{\bar{\Lambda}} - P_\Lambda = 0.109 \pm 0.118(\text{stat.}) \pm 0.022(\text{syst.})\%$.

- Nuclear deformation and neutron skin thickness measurements

Nuclear deformation and neutron skin thickness are fundamental properties of atomic nuclei that reflect the correlated nature of the dynamics of nucleons within a quantum many-body system. Most atomic nuclei possess an intrinsic deformation, most of which is an axial quadrupole, or ellipsoidal, deformation. Prior relativistic heavy-ion collision measurements from STAR reported signatures of nuclear deformation in U+U collisions. [77] These measurements suggest that U+U collisions are much more

deformed in their ground state. Consequently, we can say that detailed comparisons of flow measurements between different nuclei enabled us to examine the geometry of the colliding ions. [78–80]

Recently, it was suggested that one way to gain insight into the initial condition is to compare systems with similar size but different structure properties, such as the Au+Au and U+U considered in our measurements. The U has a strong-deformed prolate shape, while the Au has a mildly-deformed oblate shape. In Au+Au and U+U the formed QGP are of similar size and properties. Therefore, one can create ratios of bulk observables between the two systems to cancel most final state effects and capture mainly the variations in the initial condition. One could probe the energy deposition mechanism more directly by understanding how these ratios respond to nuclear shape.

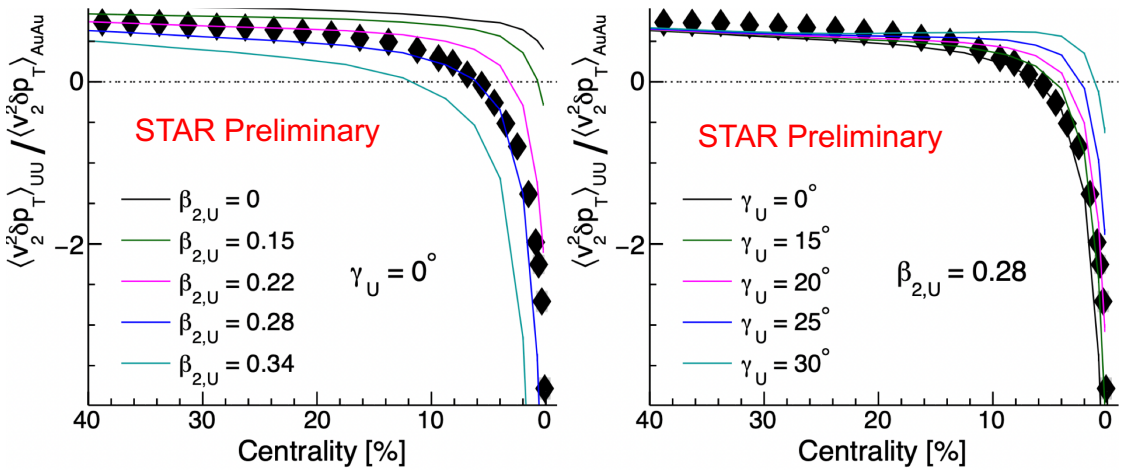

Figure 18: The ratio of the $\langle v_2^2 \delta p_T \rangle$ between Au+Au and U+U at the same centrality selections. Left: Compare the ratio with the Glauber model calculations for different $\beta_{2,U}$. Right: Compare the ratio with the Glauber model calculations for different γ_U at the same $\beta_{2,U}$.

Figure 18 presents the $\langle v_2^2 \delta p_T \rangle$ ratio between the Au+Au and U+U at the same centrality selections. Our measurement is compared with a Glauber model, which accounts for the impact of the nuclear deformation on the initial condition of the collisions. The model implements the nuclear deformation in a simple parameterization of the Woods-Saxon form. These models describe quantitatively the centrality dependence of $\langle v_2^2 \delta p_T \rangle$ when quadrupole deformation parameter $\beta_{2,U} = 0.28$ and the triaxiality parameter $\gamma_U = 0$ is used. The Glauber model calculation with varying triaxiality supports a triaxiality value of $\gamma_U < 15^o$. Although model-dependent, these precision constraints on nuclear shape parameters are the first of their kind in high-energy collisions.

In recent work, we found that Ru+Ru and Zr+Zr collision data and found that the nuclear deformation [81, 82] as well as the neutron skin thickness. [83–85] Figure 19 shows the centrality dependence of the Ru+Ru/Zr+Zr ratio of $\langle p_T \rangle$ compared to the theoretical expectations. [85] It is shown that this ratio increases with the symmetry

energy slope parameter $L(\rho_c)$ because the neutron skin effect, more significant in Zr than in Ru, increases with $L(\rho_c)$. Such an effect is non-trivial and can reach as much as 0.5%. The data model comparison helps constrain the symmetry energy slope parameter and the β_2 and β_3 deformation parameters.

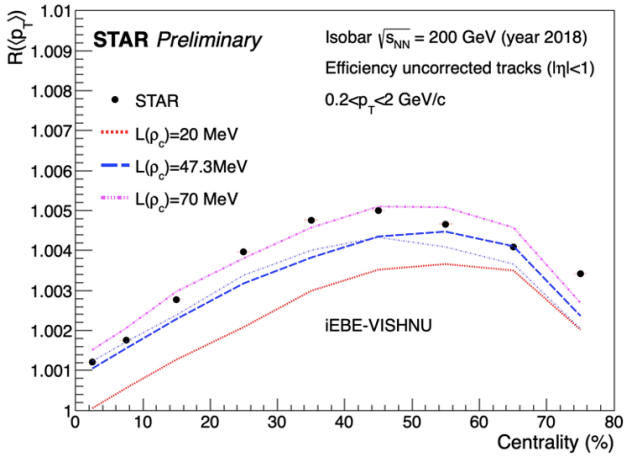

Figure 19: The centrality dependence of the Ru+Ru/Zr+Zr ratio of $\langle p_T \rangle$. The lines represent the theoretical predictions [85].

- Beam-energy dependence of anisotropic flow correlations

  The multi-particle flow harmonics $v_n\{k\}$, for k=2, 4, and 6, obtained via multi-particle correlation methods [86, 87] can give direct access to the event-by-event flow fluctuations and correlations. [88,89] Therefore, ongoing efforts aim to leverage comprehensive measurements of the Normalized Symmetric Cumulants NSC(n, m) (flow correlations) to develop unique supplemental constraints that can (i) distinguish between different initial-state models and (ii) pin down the temperature (T) and baryon chemical potential (μ_B) dependence of the specific shear viscosity $\frac{\eta}{s}(T, \mu_B)$; note that T and μ_B vary with beam energy.

  Our normalized symmetric cumulants measurements [91], shown in Fig. 20, are approximately beam-energy independent, consistent with a significant role from initial-state effects. These measurements could provide unique supplemental constraints to (i) distinguish between different initial-state models and (ii) delineate the temperature (T) and baryon chemical potential (μ_B) dependence of the specific shear viscosity $\frac{\eta}{s}(T, \mu_B)$.

- Azimuthal anisotropy measurements of identified hadrons

  Substantial constraints on transport and hydrodynamic model simulations can be achieved by investigating the azimuthal anisotropy of identified particles as a function of transverse momentum and collision centrality. Also, one can understand the initial conditions in heavy-ion collisions by varying the collision system size.

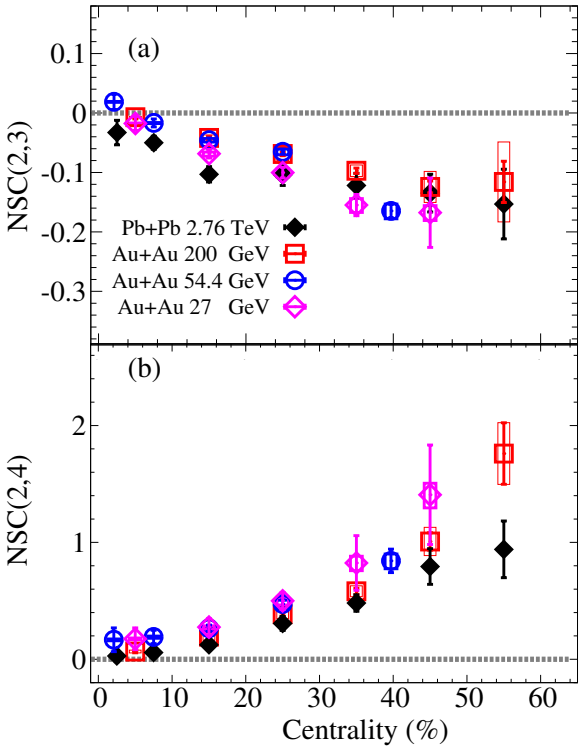

Figure 20: Comparison of the Normalized Symmetric Cumulants NSC(2, 3) (a) and NSC(2, 4) (b) using the standard cumulant method as a function of centrality for Au+Au collisions at $\sqrt{s_{\rm NN}}$ = 200, 54.4, 39 and 27 GeV. The solid diamonds indicate LHC measurements for Pb+Pb collisions at $\sqrt{s_{\rm NN}}$ = 2.76 TeV [90].

Recently we reported the results on flow coefficients of v_2 of identified particles for Au+Au at 19.6 and 14.6 GeV (BES-II) Figs. 21 22. The measurements indicate similar increasing then flattening trends as a function of $p_{\rm T}$ in (p_T) for all particles shown. In Figs. 21 22 the n_q-scaled v_2 for identified hadrons, including multi-strange hadrons, are seen to scale with the scaled kinetic energy of the particles. In order to quantify the reality of scaling, we have fitted the scaled v_2 of K^0_S with a polynomial fit, and ratios to the fit for different particles have shown in lower panels. It is found that the scaling is violated for p, Λ, and the Σ particles.

Charge dependent directed flow

In non-central heavy-ion collisions, the charged particles in the approaching nuclei can generate a substantial magnetic field. Theoretical calculations predicted that the magnetic field is large ($B \sim 10^{18}$ Gauss) but short-lived. As noted above, such a strong magnetic field can lead to novel QCD phenomena such as CME and CMW. Understanding the initial magnetic field that could drive the charge separation is of utmost

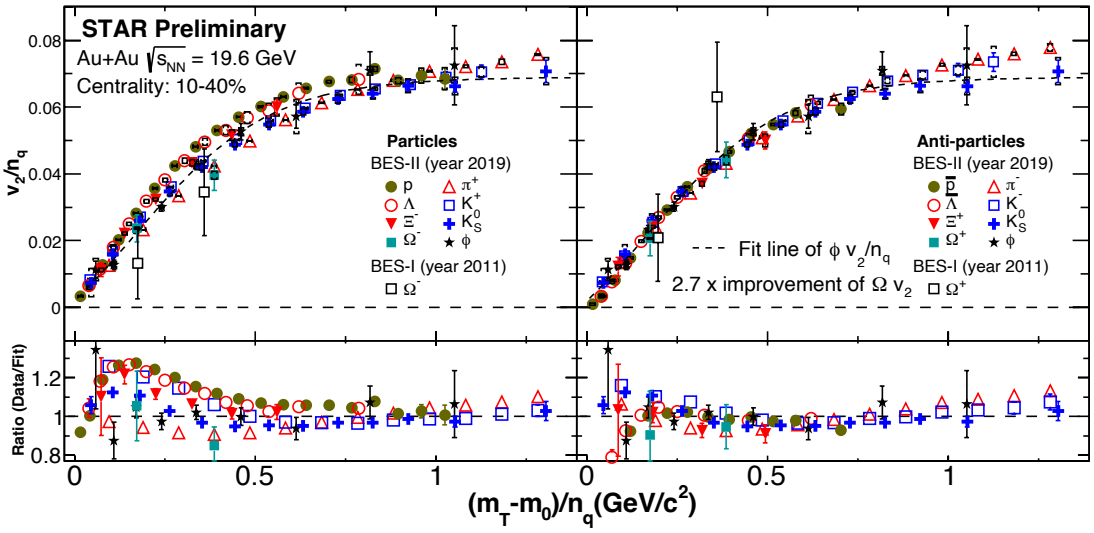

Figure 21: The v_2/n_q vs. KE_T/n_q of identified particles for Au+Au at 19.6 GeV.

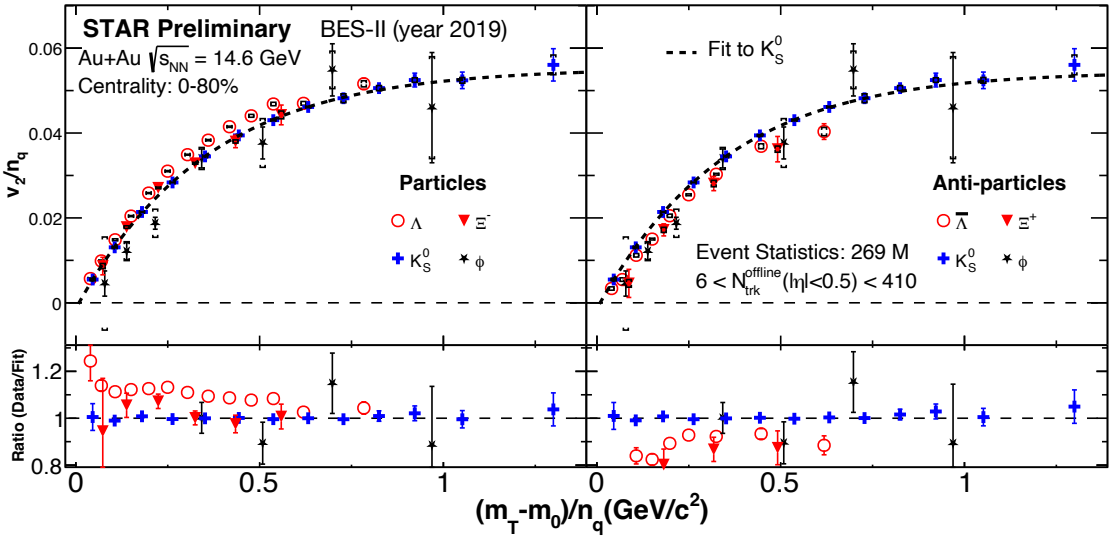

Figure 22: The v_2/n_q vs. KE_T/n_q of identified particles for Au+Au at 14.6 GeV.

importance. It was first proposed in [92] that the initial B-field can induce a measurable effect in the form of a charge-odd contribution to the directed flow coefficient (v_1). STAR and ALICE have made experimental attempts by measuring charge dependent Δv_1 for D^0, $\overline{D^0}$ and inclusive charged hadron species, but the statistical significance of those measurements are marginal.

Recently, STAR published a striking centrality dependence of the v_1 slope difference ($\Delta dv_1/dy$) of protons and anti-protons. [57] Fig. 23 presents centrality dependence of $\Delta dv_1/dy$ between positively and negatively charged pions, kaons, and protons in 200 and 27 GeV Au+Au and 200 GeV isobar collisions. It is observed that the $\Delta dv_1/dy$

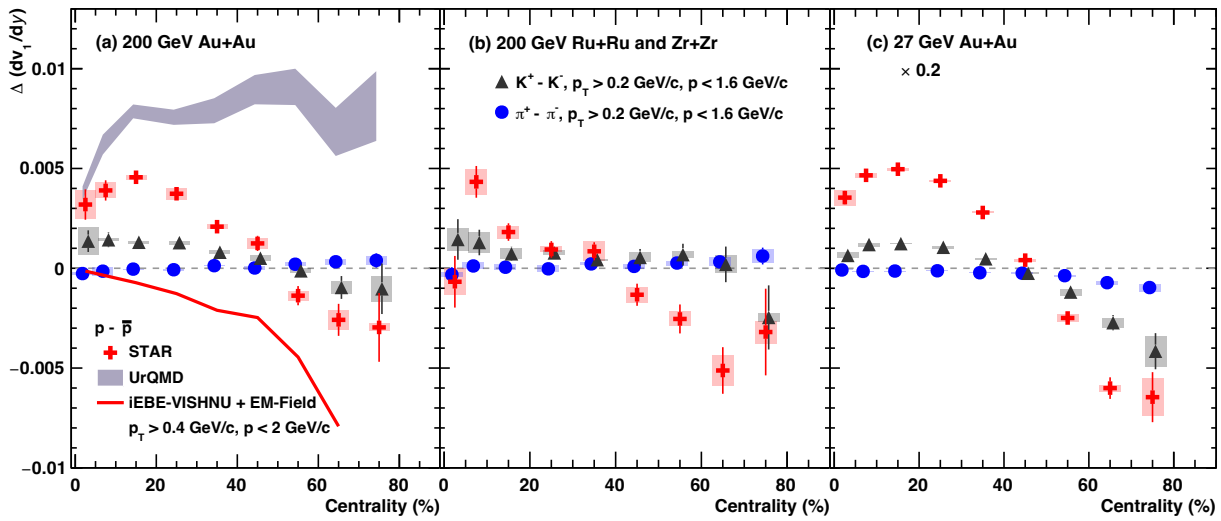

Figure 23: $\Delta(dv_1/dy)$ between positively and negatively charged pions, kaons, and protons as a function of centrality in (a) Au+Au collisions at $\sqrt{s_{NN}} = 200$ GeV, (b) isobar collisions at $\sqrt{s_{NN}} = 200$ GeV and (c) Au+Au collisions at $\sqrt{s_{NN}} = 27$ GeV. The lavender band indicates UrQMD simulations of the proton $\Delta dv_1/dy$ in Au+Au collisions at 200 GeV. In comparison, a solid curve is added correspondingly for the electromagnetic field calculation [93].

changes sign from positive to negative from central to peripheral collisions. While the positive $\Delta dv_1/dy$ is compatible with the contribution from transported quarks, the negative sign (with a significance of $\sim 5\sigma$) qualitatively agrees with the expectation from electromagnetic field-induced effects. Our measurements can be explained by the dominance of the Faraday/Coulomb effect. [92]

STAR also followed another novel approach to probe the electromagnetic fields by utilizing the hadrons with constituent quarks ($K^-, \bar{p}, \bar{\Lambda}, \phi, \Xi$ and Ω) that are produced in collisions [58], which avoids contributions from transported quarks. Under the assumptions of quark coalescence, $\Delta dv_1/dy$ is studied for various pairs of particle combinations corresponding to varying electric charge difference (Δq) and strangeness difference (ΔS). It is observed that the $\Delta dv_1/dy$ increases with Δq and ΔS, and the increase is stronger for 27 GeV than for 200 GeV Au+Au collisions. The right panel of Fig. 24 presents $\Delta dv_1/dy$ as function of ΔS for 10–40% Au+Au collisions at 27 and 200 GeV. It is found that the calculations, including electromagnetic fields, can describe the charge-dependent splitting within uncertainties.

The rapidity-odd triangular flow

The triangular flow at high collision energy is known to be caused by the initial-state fluctuations, acting in concert with the hydrodynamic-like expansion. However, such an understanding needs more investigations at low collision energy.

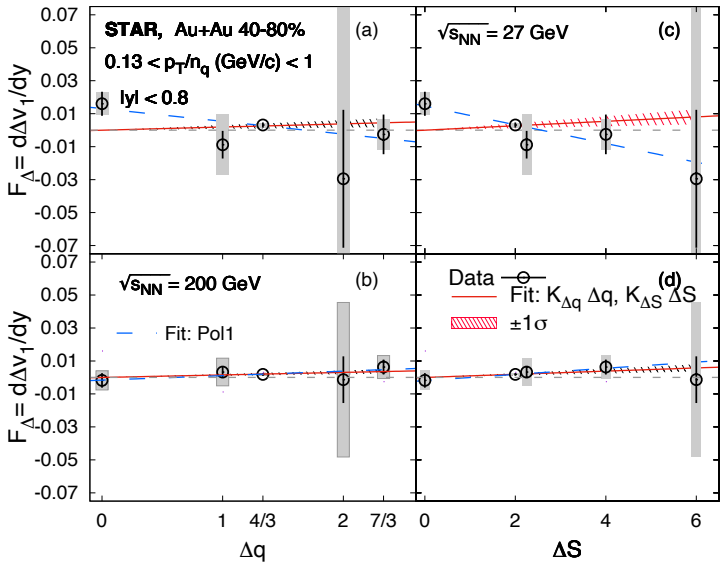

Figure 24: Midrapidity Δv_1 slope versus Δq (a, b), ΔS (c, d) in 10-40% Au+Au at 27 (a, c) and 200 (b, d) GeV, respectively. The dashed curves show AMPT calculations. The vertical bars and shaded bands denote statistical and systematic uncertainties, respectively. There are two degenerate points at $\Delta S = 2$; one is displaced horizontally for better visualization.

Recently, the STAR experiment reported the measurement of the rapidity-odd triangular flow ($V_3(\psi_1)$) at the FXT energy of 3.0 GeV. Our results show that the $V_3(\psi_1)$ depend on centrality and increase as the collision becomes more peripheral. The data model comparison suggests that the theoretical model needs more constraints to reproduce our measurement's magnitude. Such measurements are expected to constrain the Equation of State below the phase transition.

1.2.4 Correlations and Fluctuations Highlights

With the discovery of the QGP at the RHIC, physicists are investigating the QCD matter's phase structure, especially in the high baryon density region. The stark differences between the properties of QGP and lower energy nuclear matter draw interest to thermodynamics, specifically to processes related to the nature of phase transitions. Theoretical approaches work well at regions of equal baryon and anti-baryon density, with lattice QCD calculations predicting a smooth cross-over transition from hadronic to quark matter. Where the baryon density is larger than the anti-baryon density, the existence and nature of the phase transition are not well understood. The event-by-event fluctuations of conserved quantities such as net charge, net-baryon number, and net strangeness are predicted to depend on the non-equilibrium correlation length and thus serve as indicators of critical behavior.

Beam energy dependence of fifth and sixth-order net-proton number fluctuations

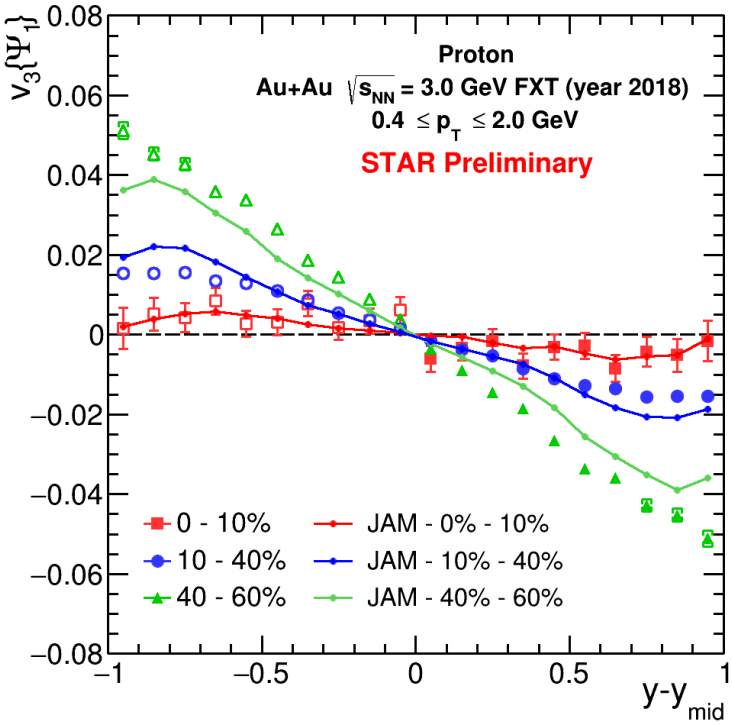

Figure 25: The rapidity dependence of the rapidity-odd triangular flow at several centrality selections for Au+Au at 3.0 GeV FXT.

Up to the fourth-order net-proton cumulant ratios, the experimental fluctuation measurements are positive and reproduced by several model calculations. These include calculations with a crossover quark-hadron transition and those without phase transition effects. Only after extending the order of fluctuations to five and six do the theoretical calculations with and without QCD phase transitions show a difference in their sign. LQCD predicts the negative sign of baryon number susceptibility ratios near the quark-hadron transition temperature. The FRG calculations also yield negative C_5/C_1 and C_6/C_2 over a wide range of the baryon chemical potential corresponding to central Au+Au collisions at $\sqrt{s_{NN}} = 7.7$ 200 GeV. A particular ordering of susceptibility ratios: $C_3/C_1 > C_4/C_2 > C_5/C_1 > C_6/C_2$ is predicted by LQCD. As proxies for net-baryon cumulant ratios, C_5/C_1 and C_6/C_2 of net-proton distributions in Au+Au collisions from 3 GeV to 200 GeV for $0-40\%$ and $50-60\%$ centralities [94] are presented in Fig. 26. C_4/C_2 for $0-40\%$ centrality is positive at all energies. Various model calculations presented for C_4/C_2 are also positive. C_5/C_1 for $0-40\%$ centrality exhibits weak collision energy dependence and fluctuates about zero except at 3 GeV, which has a significant positive value. C_6/C_2 for the same centrality is increasingly negative from higher to lower energies down to 7.7 GeV and becomes positive at 3 GeV. When interpreting the 3 GeV data, one should remember that the initial volume fluctuation effects become significant due to lower charged-particle multiplicity. The increasingly negative sign of C_6/C_2 with decreasing energy in the range of 7.7 GeV to 200 GeV is qualitatively consistent with models that include a crossover quark-hadron transition. The UrQMD expectations for these

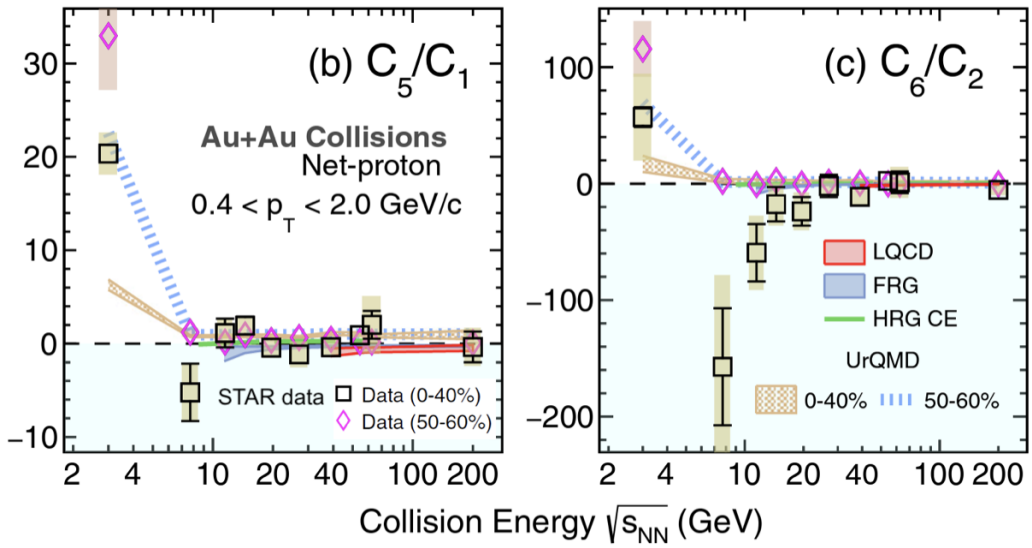

Figure 26: C_5/C_1 and C_6/C_2 of the net-proton distribution in Au+Au collisions from 3 GeV to 200 GeV. The results are shown for $0-40\%$ (squares) and $50-60\%$ (diamonds) centralities. The bars and bands on the data points represent the statistical and systematic uncertainties, respectively. LQCD (39 200 GeV), FRG (11.5 200 GeV), UrQMD, and HRG model calculations (7.7 200 GeV) with the canonical ensemble (HRG CE) are shown as red, gray, brown bands, blue and green dashed lines, respectively.

two ratios are either positive or consistent with zero within uncertainties. Expectations from HRG CE are positive for energies greater than 19.6 GeV and become negative only for lower energies. Recent hydrodynamic calculations show a similar energy-dependence trend. All three ratios are non-negative for peripheral $50-60\%$ centrality and qualitatively consistent with UrQMD. expectations.

Charged-particle multiplicity dependence of the net-proton distributions in Ru+Ru and Zr+Zr collisions

Cumulants of event-by-event net-proton number distributions and their ratios have been measured at $\sqrt{s_{NN}}$ = 200GeV for p+p and Au+Au collisions at STAR. The high-order cumulant ratios show a decreasing trend from the lowest multiplicity in p+p collisions to the highest multiplicity in Au+Au collisions. While the most central collision centrality of the Au+Au collisions shows results consistent with the Lattice Gauge Theory (LGT) calculations, the averaged value of these measurements from the p+p collisions across the whole multiplicity range shows higher values. However, the measurements at the highest multiplicity of p+p collisions show consistency with the first principle QCD calculations. This observation hints that while there is a systematic decreasing trend of the cumulant ratios for multiplicity, it varies for different colliding systems. We report the multiplicity dependence of cumulants of event-by-event net-proton number distributions and their ratios

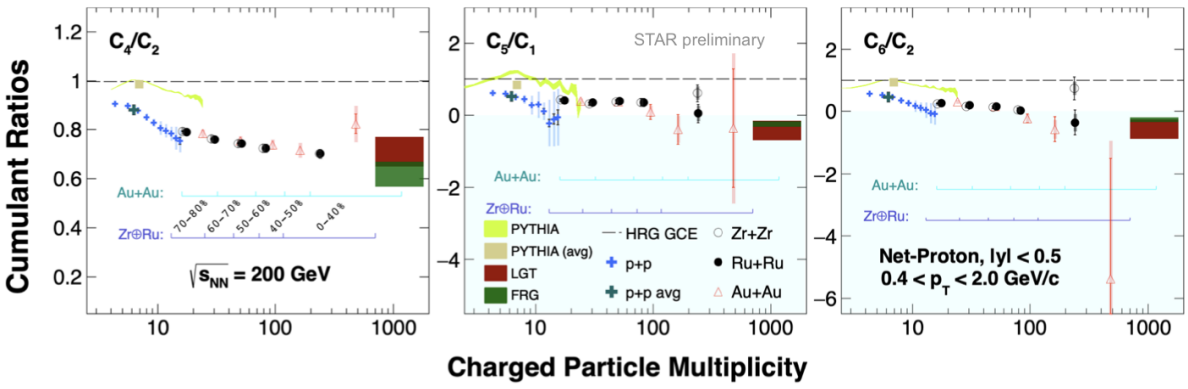

Figure 27: Net-proton cumulant ratios from p+p (blue), Zr+Zr and Ru+Ru (black), and Au+Au shown as a function of the charged-particle multiplicity. For better statistical precision, a wider $0-40\%$ centrality is shown as the top centrality for the isobar and Au+Au collisions. Model calculations from HRG GCE, PYTHIA, FRG, and Lattice Gauge Theory (LGT) are shown, in dashed lines, green bands in multiplicity and gold bands in average, and red bands, respectively.

up to the sixth order in Zr+Zr and Ru+Ru, i.e., isobars, collisions. In Fig. 27, we compare the high-order cumulant ratios of the event-by-event net-proton distributions of different colliding systems: p+p, isobars, and $Au-Au$. The LGT calculations are compatible with the highest multiplicity result of the p+p collisions and the most central collision of the Ru+Ru and Au+Au collisions. The overall decreasing trend in high-order cumulant ratios for the p+p collisions concerning multiplicity is replicated in the PYTHIA 8 calculations. However, these calculated values are consistently higher than the corresponding data. Moreover, when averaged over multiplicity, these calculations produce positive values. We reported the new STAR measurements of the cumulants of event-by-event net-proton distributions and their ratios up to the sixth order. The agreement of the results with LGT indicates a cross-over transition. Another feature to point out is that the isobar results overlap with the trends in p+p and Au+Au.

Femtoscopy of light nuclei in $\sqrt{s_{NN}} = 3$ GeV

Unveiling the interactions between baryons plays a fundamental role in understanding the structure of atomic nuclei and determining the equation of the state of neutron stars. In heavy-ion collisions, the measurements of two-particle femtoscopic correlations have proven to be a powerful tool for gaining insights into the space-time geometry of particle emitting sources and the interactions between pairs of particles. Light nuclei, such as the deuteron, consist of loosely bound nucleons with binding energies on the order of several MeV. Conducting femtoscopic measurements between pairs of particles involving light nuclei, such as proton-deuteron and deuteron-deuteron, has significant relevance for the investigation of few-nucleon systems. These systems serve as crucial testing grounds for the three-body or four-body nuclear forces, which are essential for understanding the properties of the hot and dense medium formed in heavy-ion collisions and the intrinsic structures of neutron stars.

Thermal and nucleon coalescence are the two most popular models that are proposed to explain light nuclei production in heavy-ion collisions. However, their production mechanisms remain inconclusive. Light nuclei produced through different mechanisms may exhibit distinct emitting sources size. The femtoscopic correlations, which provide information about the spatial distribution of particle emissions, are particularly sensitive to the emitting source radius. Therefore, by analyzing the femtoscopic correlations of light nuclei, we can also gain further insight into the nature of their production mechanisms. The centrality dependence of the mid-rapidity correlation functions for p-d (top panel) and d-d (bottom panel) is shown as a function of the relative momenta in Fig.28. Significant suppression of the p-d and d-d behavior is observed. The measured correlation functions are compared to those calculated using the SMASH model, considering two different production mechanisms for deuterons. The first mechanism involves deuterons formed through freeze-out protons and neutrons coalescence. This calculation is depicted by the orange band. The second mechanism accounts for directly produced deuterons through hadron scattering processes, and the corresponding calculation is represented by the gray bands. The calculations with the coalescence mechanism provide a better description of the data, accurately capturing the observed correlations. On the other hand, the latter mechanism tends to underestimate the strength of the correlations, especially for the d-d pairs. These correlation functions provide further evidence supporting the notion that deuterons are primarily created through the coalescence mechanism, as indicated by the previous measurements of collectivity and yields of light nuclei in high-energy nuclear collisions. The transport model SMASH nicely describes the measured correlation functions, which indicates that deuteron formation in such collisions is consistent with the coalescence mechanism.

1.2.5 Hard Probes Highlights

Hard probes, particles with large mass or high p_{T}, are mostly created at the early stage of heavy-ion collisions before the QGP formation, due to the large energy needed for their production. Once produced, they propagate through the medium and encode information on medium properties through interactions with medium constituents, which in turn modify their production characteristics, such as the yield or azimuthal anisotropy. At STAR, the following hard probes, including jets originated from highly-energetic partons, electrons from heavy flavor hadron decays and quarkonia, are measured to study the QCD properties in vacuum and the QGP properties in heavy-ion collisions.

Recently published results

The first measurement of the yield suppression for the three Υ states separately in heavy-ion collisions at RHIC is shown in Fig. 29. A hint of decreasing R_{AA} from peripheral to central collisions is seen, consistent with the increasing hot medium effects. When integrated over 0-60% centrality class, an upper limit of 0.17 for Υ(3S) R_{AA} with 95% confidence level is shown as the green arrow in the right panel of Fig. 29. The Υ(3S) R_{AA} is lower than Υ(1S) R_{AA} by more than 3σ, and Υ(2S) R_{AA} lies in between. This sequential suppression behavior is consistent with the theoretical expectation that it is easier for more loosely bound Υ state

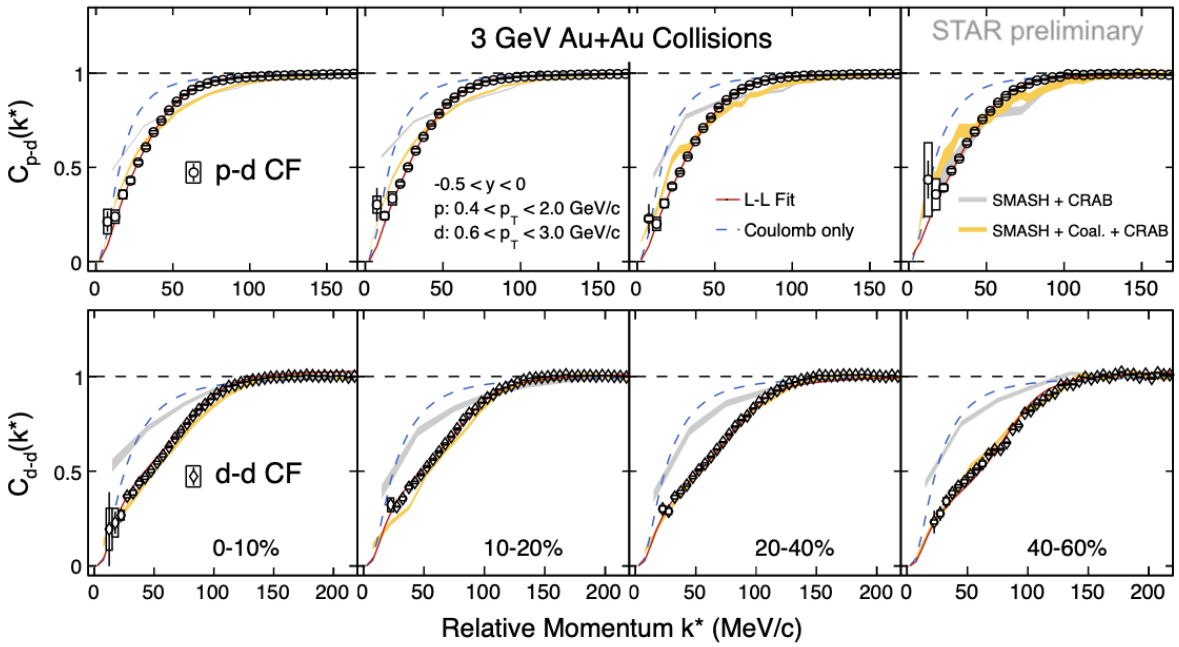

Figure 28: Centrality dependence of the mid-rapidity correlation functions, for p-d (top panel) and d-d (bottom panel), displayed as a function of the relative momenta.

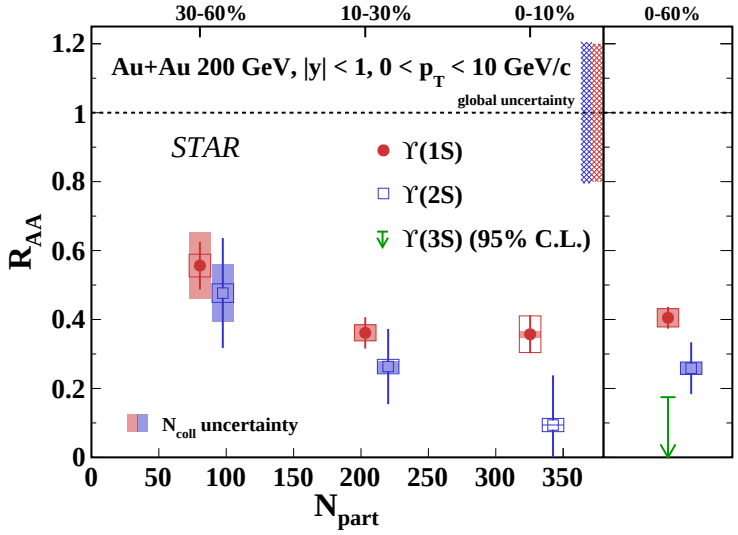

Figure 29: $R_{\rm AA}$ as a function of centrality for Υ(1S) and Υ(2S) in Au+Au collisions at $\sqrt{s_{\rm NN}}$ = 200 GeV. The Υ $R_{\rm AA}$ integrated over 0-60% centrality class is shown in the right panel, and the arrow indicates the upper limit for Υ(3S) $R_{\rm AA}$ with 95% confidence level [95].

to be dissociated in the QGP. These results are complementary to those measured at the LHC, and together they will provide stringent tests for model calculations.

Another recently published paper reports measurement of $R_{\rm AA}$ for electrons from heavy-flavor hadron decays (HFE) as a function of $p_{\rm T}$ in 0-10% central Au+Au collisions at $\sqrt{s_{\rm NN}}$ = 200 GeV, as shown in Fig. 30 [96]. A suppression by about a factor of 2 is observed

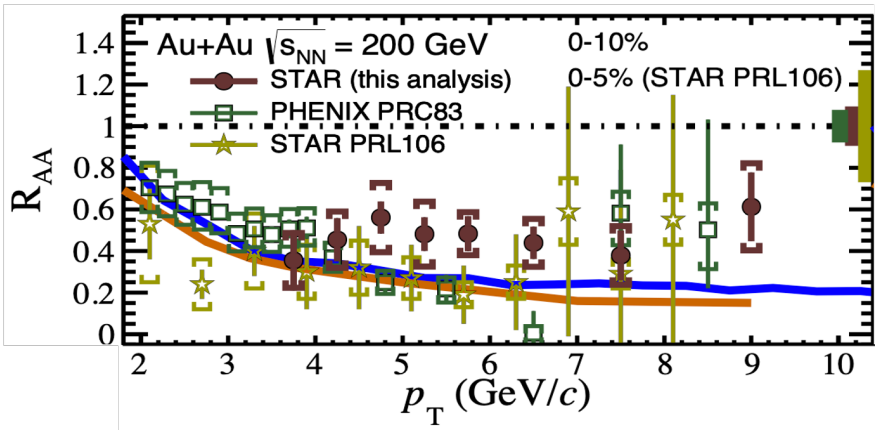

Figure 30: $R_{\rm AA}$ of HFE as a function of $p_{\rm T}$ in 0-10% central Au+Au collisions at $\sqrt{s_{\rm NN}}$ = 200 GeV (filled circles) [96], compared to previous measurements. The blue solid curve represents Duke model calculation [97], while the orange solid curve is for the PHSD calculation [98, 99].

above 3.5 GeV/c, indicating substantial energy loss of heavy quarks in the QGP due to strong interactions. Within uncertainties, no significant $p_{\rm T}$ dependence is observed in the measured range. Compared to the PHENIX results (open squares), precision of the newly published results is significantly improved for $p_{\rm T} > 6$ GeV/c. The new results also greatly reduce uncertainties across the entire $p_{\rm T}$ range and extend the measurements beyond central collisions compared to previous STAR results (open stars). Theoretical model calculations, shown as solid curves, are consistent with data within uncertainties even though they lie systematically below the data central values.

The $R_{\rm AA}$ of electrons is further measured for those from charm hadron and bottom hadron decays separately [100] in Au+Au collisions at $\sqrt{s_{\rm NN}}$ = 200 GeV. It is observed that bottom decayed electrons have a $R_{\rm AA}$ that is larger than that of charm decayed electrons, which is consistent with the expected mass ordering of parton energy loss, *i.e.*, heavier quarks are expected to lose less energy in the QGP partially due to the "dead cone" effect.

The elliptic flow (v_2) of HFE is measured in Au+Au collisions at $\sqrt{s_{\rm NN}}$ = 54.4 and 27 GeV [59] to study QGP properties at lower energies. The v_2 magnitude at $\sqrt{s_{\rm NN}}$ = 54.4 GeV is compatible to that measured at $\sqrt{s_{\rm NN}}$ = 200 GeV, suggesting intense interactions between charm quarks and medium constituents leading to possible local thermalization of charm quarks at 54.4 GeV. On the other hand, the HFE v_2 at $\sqrt{s_{\rm NN}}$ = 27 GeV is consistent with zero within uncertainties.

Hot medium effects on jets are explored by measuring non-identified charged-particle correlations projected onto two-dimensional, transverse rapidity coordinates ($y_{\rm T1}$, $y_{\rm T2}$) in

minimum-bias (0-93%) Au+Au collisions at $\sqrt{s_{\rm NN}}$ = 200 GeV [101]. The transverse rapidity is defined as $y_{\rm T} = \ln[(p_{\rm T} + \sqrt{p_{\rm T}^2 + m_0^2})/m_0]$, where m_0 is the pion rest mass. The main feature of the two-dimensional correlation is a saddle shape plus a broad peak with the maximum near $y_{\rm T} \approx 3$, corresponding to $p_{\rm T} \approx 1.5$ GeV/c. Comparisons to model calculations indicate that the correlations for peripheral to mid-central collisions can be approximated as a superposition of nucleon-nucleon collisions, while strong medium effects are needed in mid- to most-central collisions.

To study the path-length dependence of the jet quenching effect, angular distributions of charged particles associated with jets are measured as a function of the jet orientation with respect to the event plane in 20–50% Au+Au collisions at $\sqrt{s_{\rm NN}}$ = 200 GeV [102]. Yields and widths of the associated particles are extracted, and no strong dependence on the relative angel between jet axis and the event plane is seen.

Recent preliminary results

A similar measurement of sequential Υ suppression is carried out using Ru+Ru and Zr+Zr collisions at $\sqrt{s_{\rm NN}}$ = 200 GeV as a function of centrality, as shown in the left panel of Fig. 31. Similar to the Au+Au result (Fig. 29), a hint of decreasing Υ(1S) and Υ(2S) $R_{\rm AA}$ with centrality is seen, and Υ(2S) $R_{\rm AA}$ seems to be slightly smaller than that of Υ(1S). Within

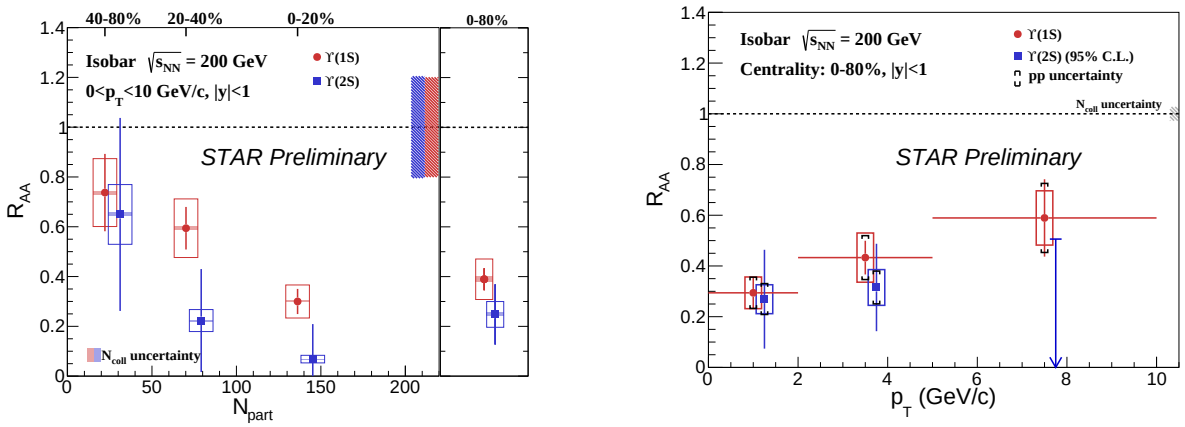

Figure 31: Υ(1S) and Υ(2S) $R_{\rm AA}$ as a function of centrality (left) and $p_{\rm T}$ (right) in Ru+Ru and Zr+Zr collisions at $\sqrt{s_{\rm NN}}$ = 200 GeV.

uncertainties, the Υ $R_{\rm AA}$ integrated over 0-80% Isobar collisions are consistent with those for 0-60% Au+Au collisions. The right panel of Fig. 31 shows the Υ(1S) and Υ(2S) $R_{\rm AA}$ as a function of $p_{\rm T}$. No significant $p_{\rm T}$ dependence is seen for Υ(2S) $R_{\rm AA}$, while there seems a hint of rising trend for Υ(1S).

In addition to utilize jets for probing the hot medium effects, their substructures are also measured in p+p collisions to study the evolution of parton shower. Two such examples are shown in Fig. 32, which are produced with the first application of the MultiFold machine learning unfolding technique at RHIC [103]. It can correct multiple variables simultaneously and conserve the correlations among them on a jet-by-jet basis. The left panel shows the

distributions of collinear drop mass ($\Delta M = M - M_{\rm g}$) over jet mass (M) in different ranges of groomed jet radius ($R_{\rm g}$) for $R = 0.4$ jets with $20 < p_{\rm T,jet} < 30$ GeV/c in p+p collisions at $\sqrt{s}$ = 200 GeV. M and $M_{\rm g}$ are the jet masses before and after SoftDrop grooming [104,105], and $R_{\rm g}$ is the distance between the two subjets of the groomed jet in (η, φ) space. The SoftDrop grooming removes soft and large-angle radiations in the jet, which can be quantified with ΔM. With increasing $R_{\rm g}$, $\Delta M/M$ peaks at lower and lower values, *i.e.*, more early-time large-angle soft radiations correspond to smaller separations of later splittings. This is consistent with the angular ordering of parton showers. The right panel compares distributions

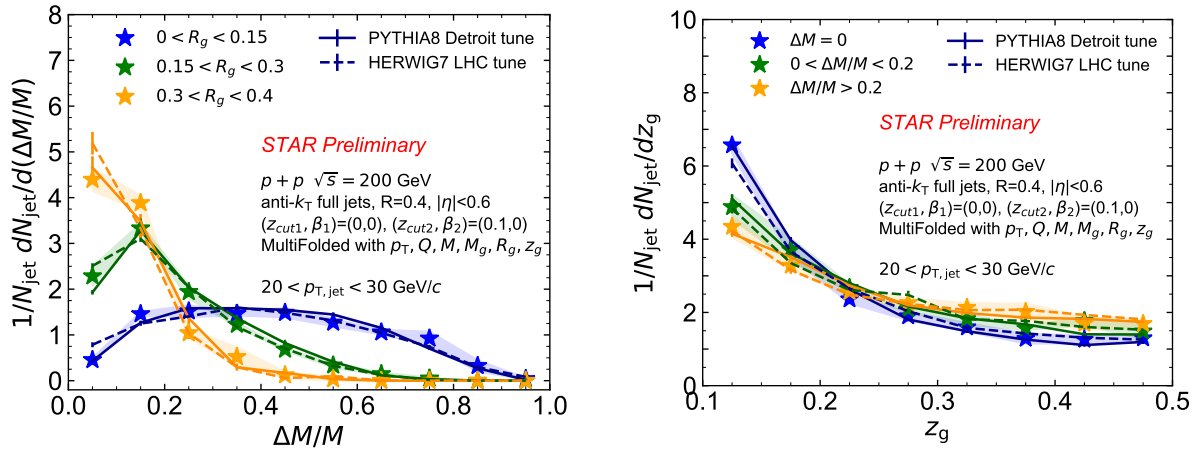

Figure 32: Left: distributions of collinear drop mass (ΔM) over ungroomed jet mass (M) in different ranges of groomed jet radius ($R_{\rm g}$) in p+p collisions at $\sqrt{s}$ = 200 GeV. Right: distributions of shared momentum fraction ($z_{\rm g}$) in different ranges of $\Delta M/M$. Solid and dashed lines correspond to predictions from PYTHIA 8 [106] and HERWIG 7 [107] event generators, respectively.

of shared momentum fraction ($z_{\rm g}$) among the two subjets, *i.e.*, $p_{\rm T}$ of the subleading jet to the $p_{\rm T}$ sum of the two subjets, after grooming for different $\Delta M/M$ selections. Here, more early-time radiations result in flatter $z_{\rm g}$ distributions or smaller momentum imbalance between the two subjets. Both results shown in Fig. 32 demonstrate the correlation between early-time soft radiation and late-time hard splitting. Calculations from PYTHIA 8 [106] and and HERWIG 7 [107] event generators can qualitatively describe data.

The process of parton shower and hadronization can be further studied using the energy-energy correlator (EEC), as shown in Fig. 33 for $R = 0.4$ jets with $15 < p_{\rm T,jet} < 20$ GeV/c (left) and $30 < p_{\rm T,jet} < 50$ GeV/c (right) in p+p collisions at $\sqrt{s} = 200$ GeV. EEC is defined as the angular separation (ΔR) of all combinations of two charged constituents in the jet in (η, φ) space, weighted by the product of the energies of the particle pair. As indicated by the vertical bands in the figure, three distinct regions are readily visible. The increasing trend in the small ΔR region corresponds to free hadrons, while the decreasing trend in the large ΔR region originates from correlations between quarks and gluons. The transition region in the middle scales with $1/p_{\rm T,jet}$, and is closely related to hadronization. pQCD calculations [108] are showed as colored bands, and can describe data in the parton region quite well.

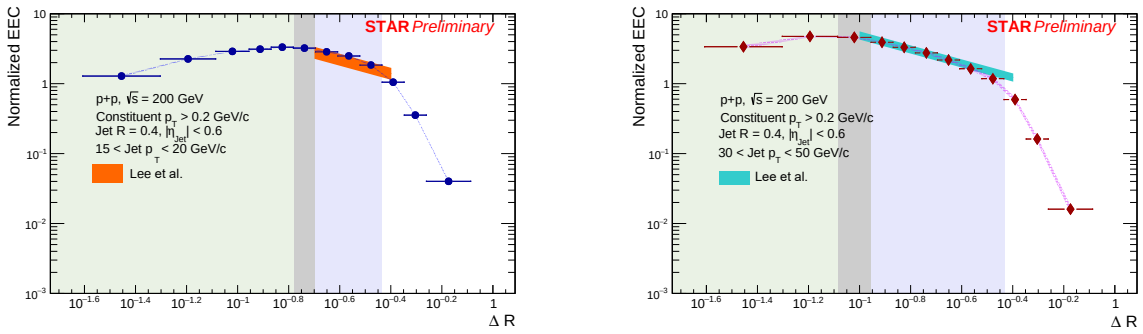

Figure 33: Energy-energy correlators as a function of charged-particle pair separation for $R = 0.4$ jets with $15 < p_{\mathrm{T}} < 20$ GeV/c (left) and $30 < p_{\mathrm{T}} < 50$ GeV/c (right) in p+p collisions at $\sqrt{s} = 200$ GeV. pQCD calculations [108] are compared to data in the partonic regions.

Going from p+p to heavy-ion collisions, first measurement of charged-particle jet v_2 at RHIC energies is shown in Fig. 34 for Ru+Ru and Zr+Zr collisions at $\sqrt{s_{\mathrm{NN}}} = 200$ GeV combined. Jet v_2 is considered a sensitive probe to study the path-length dependence of the parton energy loss in the QGP, as jets travelling along the event plane (shorter path length) are expected to lose less energy than those traveling perpendicular to the event plane (longer path length). A sizable jet v_2 is seen with weak dependence on jet p_{T} or R,

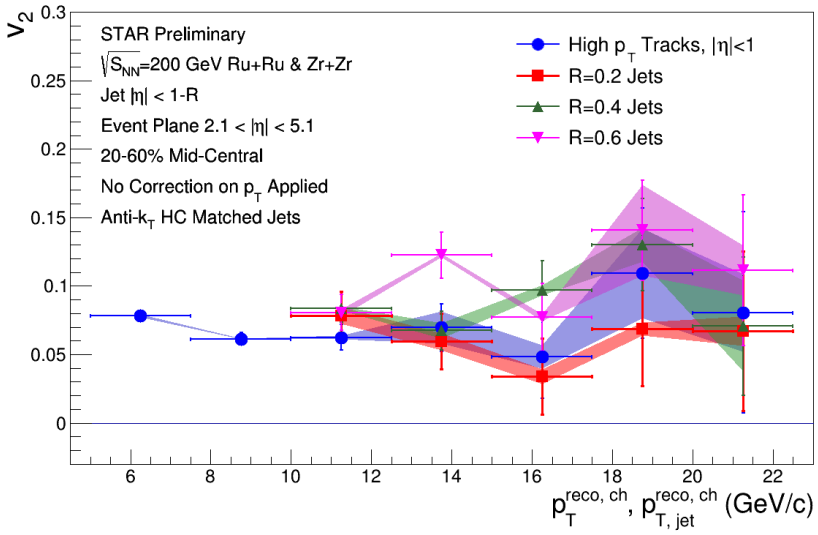

Figure 34: Charged-particle jet v_2 as a function of p_{T} for resolution parameters of $R = 0.2, 0.4, 0.6$ in Ru+Ru and Zr+Zr collisions at $\sqrt{s_{\mathrm{NN}}} = 200$ GeV. Similar measurement for high-p_{T} charged hadrons is also shown for comparison.

indicating significant parton energy loss and its path-length dependence. The jet v_2 is also compared to high-p_{T} charged hadron v_2, and they are seen to be compatible.

1.3 Run 23 Performance

1.3.1 DAQ Upgrade and Performance

As described in the 2023 BUR it was realized that it would be possible to improve the readout speed significantly of the TPC detector i.e. iTPC and the TPX for the outer sectors. It has been primarily a labor intensive upgrade of firmware and software.

It consists of the following components that are now completed:

- Rewrite the FPGA firmware for FEEs and RDOs. The FPGAs are different for the outer sectors (TPX) and inner sectors (iTPC). In particular the firmware for the TPX was challenging, as the FPGA and related software platform are from 2008, and had to be rewritten from scratch to fit together with the iTPC and online software.
- Rewrite the DAQ online software for iTPC and TPX in the new framework.
- Redo and evaluate the cluster finder in the common framework for iTPC and TPX. This was completed, and a comparison between new and old demonstrated that the differences are small and satisfactory.
- Improve network connectivity by rearranging topology with network switches.
- Add additional DAQ PCs and event builders to handle the increased data volume. This was accomplished by a combination of purchases and re-purposing of SDCC inventory.
- The original gating grid driver that had a limit of 2.2 kHz was replaced for Run-22 and can now easily handle more than 5 kHz. No issues were encountered during run 22.

The expectation is that the data rate can be approximately doubled with nominal dead time. What has been achieved so far is

- Minimum Bias data at low luminosity has been demonstrated to be able to record 3.9-4.1 kHz with 40-50% dead time, somewhat dependent on beam conditions as the primary limitation for the system is the total data volume read out. Note the dead time does not matter for the MB projections as the quoted rates are events to tape.
- High luminosity data for rare triggers should be able to be recorded at 2.5 kHz at 20% dead time. The beam conditions in Run 23 have yet to reach intensities of 100 kHz ZDC rate. But we demonstrated that for 70 kHz ZDC rate with the trigger-mix that is planned for the high luminosity running, the system handled 1.6 kHz trigger rate with just 15% dead time and 2.8 Gb/sec throughput.

The development started back in 2022, first for the iTPC, and then for the more challenging TPX development. During the initial part of Run 23 only a few sectors had the updated firmware, in order to identify issues. By end of June 2023 the system was fully implemented and has run very well since.

In order to achieve a balance between those physics observables that are acquired with a minimum bias trigger (and negatively impacted by excess tracks in the TPC) and the rare probes that require specialized triggers (Barrel High Tower (BHT), dimuon) and the highest luminosity that can be accommodated with the TPC, the collaboration will optimize the interaction rates at STAR by allocating high and low luminosity periods within fills. CAD can offset the beam to independently control the maximum luminosity in each IR. Clean minimum bias events will improve tracking efficiencies, which in turn are expected to benefit many of the proposed correlation analyses. Optimization of the available bandwidth for rare triggers would allow us to push for lower p_T thresholds, thus further reducing biases. The impact of such an optimization will lead to some reduction in the projected rates, while still enabling a significant improvement in the precision and kinematic reach of current STAR measurements, and making important measurements that are yet more differential possible.

1.3.2 Forward Detector Upgrade

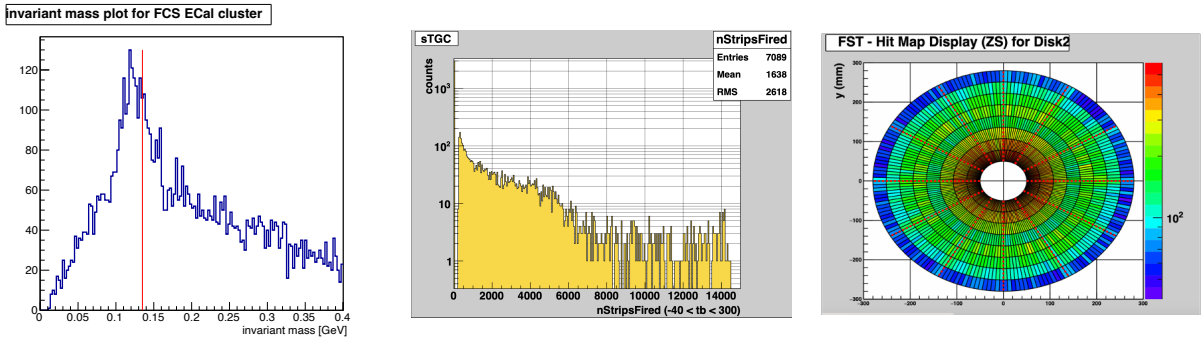

Figure 35: Left: The invariant mass distribution from FCS ECal clusters showing the π^0 peak. Middle: Multiplicity distribution for the sTGC detector showing an approximately negative binomial distribution as expected for the trigger mix. Right: FST hit map distribution from minimum bias Au+Au collisions.

The forward upgrade is comprised of four subsystems, an electromagnetic calorimeter (Ecal), a hadronic calorimeter (Hcal) and a tracking system, formed from a silicon detector (FST) and a small-strip Thin Gap Chambers (sTGC) tracking detector.

All subsystems have been installed since late December 2021 and final commissioning concluded during the early parts of Run 22. The array of forward tracking and calorimetry provide superior detection capabilities for neutral pions, photons, electrons, jets, and leading hadrons within the pseudorapidity range of $2.5 < \eta < 4$ A suite of 29 different triggers were used throughout stable $p + p$ collisions in Run 22. The loss of gain in each channel caused by radiation damage during Run 22 was within the expected range and was independently tracked by an LED system so that the operating conditions could adjusted on a weekly basis to ensure the trigger thresholds were not deviating from the desired range for the physics objectives. This procedure was especially critical for the rare triggers (e.g. Drell-Yan) which could potentially result in a reduction of good data of an order of magnitude or more. A

calibration procedure based on analysis of the π^0 has been developed utilizing the Run 22 data to accurately calibrate the gains for each channel in the detectors. Each period of fixed operating conditions, i.e. about one week each, is calibrated individually and time-dependent of gain factors are interpolated with the LED information providing well calibrated energy measurement for the entire detector across the entire time period.

During Run 23 with Au+Au collisions, the radiation load on the SiPMs is much less severe compared to the Run 22 conditions. The gain for each channel is tracked through the LED systems as well as pedestal shifts (noise) and dark current measurements. Relative changes are consistent between the different monitoring methods. Data from Run 23 showing with a visible π^0 peak in the invariant mass distribution from FCS ECal clusters is shown in Fig. 35 (left). In heavy-ion collisions, only a small subset of physics observables are based on triggers with the forward detectors. These are ultra-peripheral collisions, including UPC J/ψ and combinations of jet patch triggers from the forward and barrel detectors. The corresponding triggers have very low rates, and as such, they ideally run without prescales.

In Run 23 The forward tracking detectors have operated smoothly based on the successful past commissioning in Run 22. The hit maps of the forward silicon tracker (FST) disks (see Fig. 35 middle) match our expectations given known missing APVs and lower bias voltages on a few of the sensors. The FST operations have been smooth, with all trips being cleared with a simple power cycle of the FST. The forward small-strip thin gap chamber trackers (FTT) have operated smoothly in Run 23 setup with the same operating conditions as used in Run 22. The health of the gas system has been continuously monitored and the system has operated without issue during Run 23. Since this is the first time running in a high-multiplicity environment, special attention was given to check the efficiency of the FTT planes at various high-voltage set points to ensure consistency with past operational levels. The FTT hit multiplicity is shown in Fig. 35 (right) for a Run 23 dataset consisting of predominately minimum bias triggered events. The expected negative binomial multiplicity distribution is observed. The FTT multiplicity distribution shows some evidence of saturation at the highest-multiplicity Au+Au events.

Significant progress has been made on the reconstruction software for the forward rapidity upgrade. Figure 36 (left) shows the reconstructed charged track multiplicity ($N_{\mathrm{ch}}^{\mathrm{FWD}}$) from the forward tracking detectors. The data shows a healthy distribution consistent with expectations based on e.g. PYTHIA simulations including the forward detector response simulations. The FST and FTT had precise survey information collected upon installation. By utilizing the survey data, we find good alignment between each tracking detector and the forward calorimeter systems. Figure 36 shows correlations between projected track positions and HCAL cluster locations in the x (middle) and y (right) directions from Run 22 data. In both cases a strong peak is observed at zero, as expected for tracks that produced energy deposits in the calorimeters. Due to the different tracking detector technologies with different space-point resolution, the tracking software finds tracks utilizing points in either the FST or FTT before fitting to a track propagation model. After a track is fit it can be associated with compatible space points from the other tracking detector. An analysis was performed on Run 22 data to find MIPs in the ECAL. Figure 36 (bottom left) shows an event

display with ECAL hit positions along with track projection points (black points) and a 20 cm radius around each track projection (red circles) to show associated ECAL activity. From these matches a clear MIP peak can be observed. Figure 36 (bottom middle and bottom right) show the MIP peak for tracks fit with hits from only one detector (bottom middle) and from both detectors (bottom right). The distribution with hits from both detectors shows a clearer MIP peak, demonstrating that the combination of the two tracking detectors provide improved track finding and projection resolution. These results are based on the rough alignment provided by the survey data taken at the time of installation in STAR. A data driven alignment procedure that will achieve the designed space-point resolution has been developed utilizing the Run 22 datasets and will further improve the FST and FTT track agreement and improve the overall quality of the track projections to the forward calorimeters.

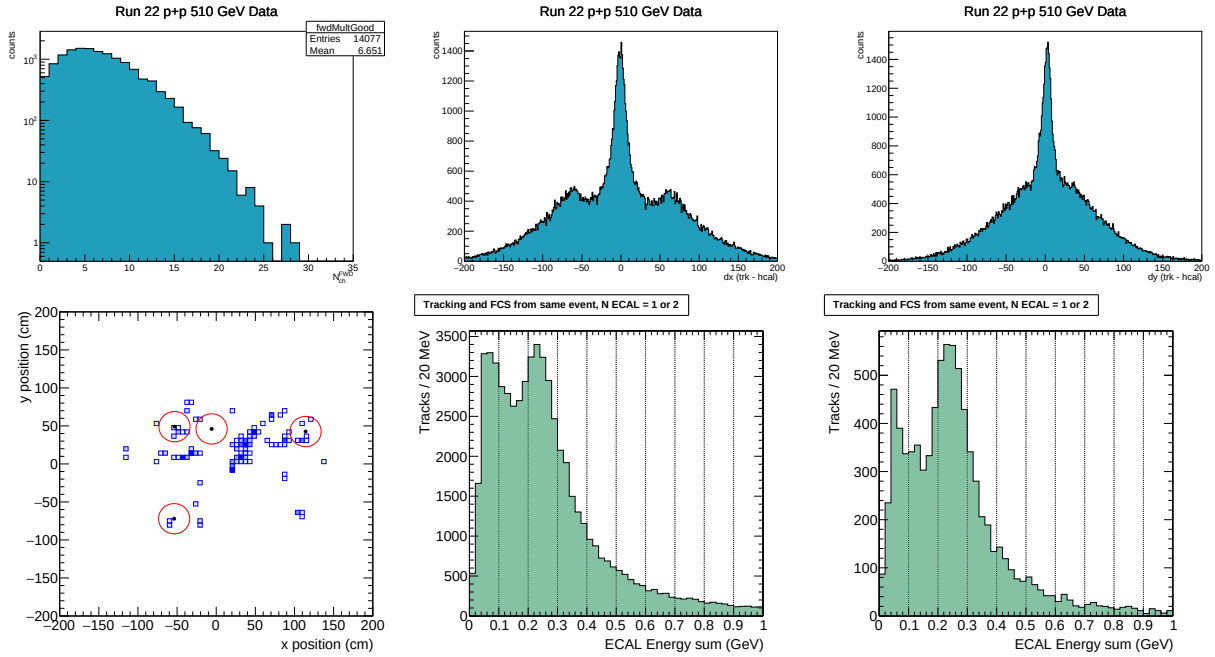

Figure 36: Top Left: Distribution of FWD charged tracks reconstructed per event from Run 22 p+p collisions at $\sqrt{s}$ = 510 GeV. Top Middle and Top Right: Demonstration of the matching between the forward tracks and forward calorimeter clusters. The x (y) difference between the projected track's position and the forward HCAL cluster position are shown in the top middle (top right) panels. Bottom Left: An event display showing the ECAL hit positions along with track projection points (black points) and a 20 cm radius around each track projection (red circles). Bottom Middle and Right: ECAL energy sum distribution for tracks with hits in only one tracking detector (bottom middle) vs. hits in both tracking detectors (bottom right).

2 Run-24 Request for Polarized p+p and p+Au Collisions at 200 GeV

The exploration of the fundamental structure of strongly interacting matter has always thrived on the complementarity of lepton scattering and purely hadronic probes. As the community eagerly anticipates the future Electron Ion Collider (EIC), an outstanding scientific opportunity remains to complete "must-do" measurements in p+p and p+Au physics during the final years of RHIC. These measurements will be essential if we are to fully realize the scientific promise of the EIC, by providing a comprehensive set of measurements in hadronic collisions that, when combined with future data from the EIC, will establish the validity and limits of factorization and universality. Much of the Run-24 physics program outlined here is, on the one hand, unique to proton-proton and proton-nucleus collisions and offers discovery potential on its own. On the other hand, these studies will lay the groundwork for the EIC, both scientifically and in terms of refining the experimental requirements of the physics program, and thus are the natural next steps on the path to the EIC. When combined with data from the EIC these STAR results will provide a broad foundation to a deeper understanding of fundamental QCD.

The separation between the intrinsic properties of hadrons and interaction-dependent dynamics, formalized by the concept of factorization, is a cornerstone of QCD and largely responsible for the predictive power of the theory in many contexts. While this concept and the associated notion of universality of the quantities that describe hadron structure have been successfully tested for unpolarized and, to a lesser extent, longitudinally polarized parton densities, its experimental validation remains an unfinished task for much of what the EIC is designed to study – the three-dimensional structure of the proton and the physics of dense partonic systems in heavy nuclei. To establish the validity and limits of factorization and universality, it is essential to have data from *both* lepton-ion and proton-ion collisions, with experimental accuracy that makes quantitative comparisons meaningful.

Run-24, with polarized p+p and p+Au collisions at $\sqrt{s_{\rm NN}} = 200$ GeV, will likely be the last RHIC spin/cold QCD run. This run will provide STAR with the unique opportunity to investigate these 200 GeV collision systems with the Forward Upgrade providing full tracking and calorimetry coverage over the region $2.5 < \eta < 4$ and the iTPC providing enhanced particle identification and expanded pseudorapidity coverage at mid-rapidity. These powerful detection capabilities, when combined with substantially increased sampled luminosity compared to Run-15, will enable critical measurements to probe universality and factorization in transverse spin phenomena and nuclear PDFs and fragmentation functions, as well as low-x non-linear gluon dynamics characteristic of the onset of saturation. This will provide unique insights into fundamental QCD questions in the near term, and essential baseline information for precision universality tests when combined with measurements from the EIC in the future.

We therefore request 12 weeks of polarized p+p data-taking at $\sqrt{s} = 200$ GeV and 10.5 weeks of polarized p+Au data-taking at $\sqrt{s_{\rm NN}} = 200$ GeV during Run-24. Effectively, we request approximately equal nucleon-nucleon luminosities for p+p and p+Au which is

essential to optimize several critical measurements that require comparisons of the same observable in (polarized or unpolarized) p+p and p+Au collisions described in the following sections.

All of the running will involve radially polarized protons. This will maximize the figure-of-merit for the measurements of the dijet Sivers effect and ultra-peripheral J/ψ production with the Forward Upgrade. It will also minimize important systematic uncertainties for the Collins asymmetry measurement using the Forward Upgrade. Based on recent CAD guidance, we expect to sample 142 pb^{-1} of p+p collisions and 0.69 pb^{-1} of p+Au collisions. These totals represent 2.7 times the luminosity that STAR sampled during transversely polarized p+p collisions in Run-15 and 1.5 times the luminosity that STAR sampled during transversely polarized p+Au collisions in Run-15.

The reduction in cyo-weeks from 28 to 24 is projected to have a significant impact on the sampled luminosity, reducing the statistics quoted above by about a factor of 1.3. The further reduction to 20 cyo-weeks will reduce the statistics by a factor of 1.7.

2.1 Spin Physics with Polarized p+p and p+Au Collisions at 200 GeV

Run-24 will enable STAR to probe the physics questions that can be assessed in the transversely polarized p+p and p+Au collisions, including those described in highlights section 1.1 and recent STAR publications [41, 42], but with a far more capable detector and much larger datasets than were available during Run-15. With the overlapping kinematic coverage for both p+p and p+Au data, this program is critical to set the stage for related future measurements at the EIC. Here we give brief descriptions of several of the opportunities presented by Run-24.

2.1.1 Forward Transverse-Spin Asymmetries

The experimental study of spin phenomena in nuclear and particle physics has a long history of producing important, and often surprising, results. Attempts to understand such data have pushed the field forward, forcing the development of both new theoretical frameworks and new experimental techniques. Recent detector upgrades at STAR, at mid- and forward-rapidity, coupled with the versatility of RHIC, will allow us to gain new insights into long-standing puzzles, and to probe more deeply the complexities of emergent behavior in QCD.

Results from PHENIX and STAR have shown that large transverse single-spin asymmetries (TSSA) for inclusive hadron production, first seen in p+p collisions at fixed-target energies and modest p_{T}, extend to the highest RHIC center-of-mass energies, $\sqrt{s} = 510$ GeV, and surprisingly large p_{T}. Figure 37 summarizes the world data for the inclusive neutral pion asymmetries A_N as a function of Feynman-x. The asymmetries are seen to be nearly independent of $\sqrt{s}$ over the very wide range of roughly 19 to 500 GeV.

To understand the observed TSSAs, one needs to go beyond the conventional leading-twist (twist-2) collinear parton picture for the hard-scattering processes. Two theoretical formalisms have been developed to try to explain these sizable asymmetries in the QCD

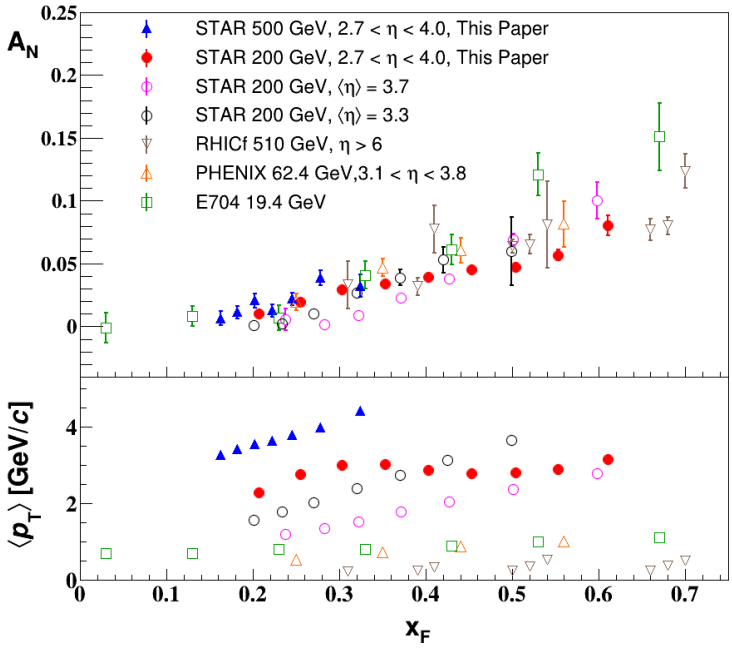

Figure 37: Transverse single-spin asymmetry A_N measurements for neutral pion in p+p collisions at different center-of-mass energies as a function of Feynman-x [109].

framework: transverse-momentum-dependent (TMD) parton distribution and fragmentation functions, such as the Sivers and Collins functions; and transverse-momentum-integrated (collinear) quark-gluon-quark correlations, which are twist-3 distributions in the initial state proton or in the fragmentation process. For many of the experimentally accessible spin asymmetries, several of these functions can contribute, and need to be disentangled in order to understand the experimental data in detail, in particular the observed p_T dependence. These functions manifest their spin dependence either in the initial state–for example, the Sivers distribution and its twist-3 analog, the Efremov-Teryaev-Qiu-Sterman (ETQS) function [110]–or in the final state via the fragmentation of polarized quarks, such as in the Collins function and related twist-3 function $\hat{H}_{FU}(z, z_z)$.

Incorporating the fragmentation term within the collinear twist-3 approach demonstrated the ability of this formalism to describe the large values of A_N for π^0 production observed at RHIC [111]. In this work, the relevant (non-pole) 3-parton collinear fragmentation function $\hat{H}_{FU}(z, z_z)$ was fit to the RHIC data. The so-called soft-gluon pole term, involving the ETQS function $T_{q,F}(x_1, x_2)$, was also included by fixing $T_{q,F}$ through its well-known relation to the TMD Sivers function $f_{1T}^{\perp}$. The authors obtained a very good description of the data due to the inclusion of the non-pole fragmentation function and based on this work they were able to make predictions for π^+ and π^- production asymmetries A_N at the forward rapidities covered by the STAR upgrades, $2.5 < \eta < 4$. The results are shown in Fig. 38 for $\sqrt{s}$= 200 and 500 GeV for two rapidity ranges, $2 < \eta < 3$ and $3 < \eta < 4$.

STAR recently published a pair of papers discussing forward transverse-spin asymmetries

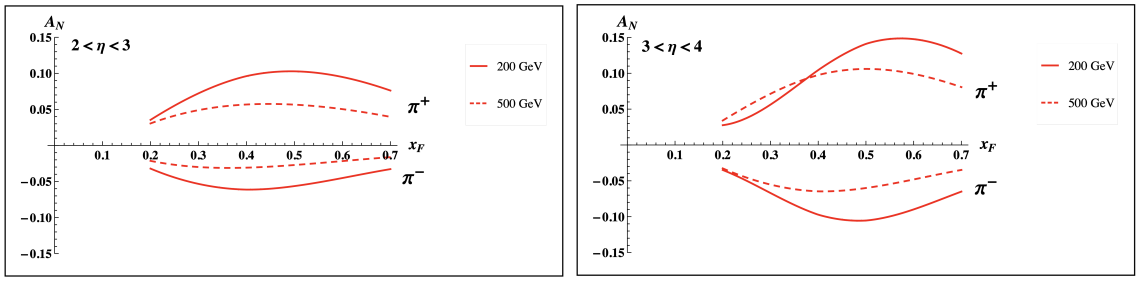

Figure 38: Predictions for A_N for π^+ and π^- production over the ranges $2 < \eta < 3$ (left) and $3 < \eta < 4$ (right) at $\sqrt{s} = 200$ GeV (solid lines) and 500 GeV (dashed lines).

in p+p, p+Al, and p+Au collisions measured with the Forward Meson Spectrometer (FMS). One paper focuses on the dynamics that underlie the large asymmetries that have been seen to date [109]. The data show that A_N for forward π^0 production in p+p collisions at 200 and 500 GeV is substantially larger when the π^0 is isolated than when it is accompanied by additional nearby photons. The same analysis also shows that A_N for inclusive electromagnetic jets (EM-jets) in 200 and 500 GeV collisions is substantially larger than that for EM-jets that contain three or more photons and that the Collins asymmetry for π^0 in EM-jets is very small. The other paper focuses on the nuclear dependence of A_N for π^0 in $\sqrt{s_{NN}} = 200$ GeV collisions [112]. It presents a detailed mapping of A_N as functions of x_F and p_T for all three collision systems. It is shown that the observed nuclear dependence is very weak. The same analysis shows that isolated *vs.* non-isolated π^0 behave similarly in p+Al and p+Au collisions as they do in p+p collisions.

These two papers provide a wealth of new data to inform the ongoing discussion regarding the origin of the large inclusive hadron transverse-spin asymmetries that have been seen in p+p collisions at forward rapidity over a very broad range of collision energies. Nonetheless, the STAR Forward Upgrade is a game changer for such investigations. It enables measurements of A_N for $h^{+/-}$, in addition to π^0. It enables isolation criteria to be applied to the $h^{+/-}$ and π^0 that account for nearby charged, as well as neutral, fragments. It enables full jet asymmetry and Collins effect measurements, again for $h^{+/-}$ in addition to π^0, rather than just EM-jet measurements. It will permit all of these measurements to be performed at both 510 GeV (measured during Run-22), and at 200 GeV (to be measured in Run-24).

In addition, all of these observables can be tagged by requiring rapidity gaps to identify the diffractive component of the observed transverse spin asymmetries, see results from Fig. 39. The measurement of A_N for singly and double diffractive events utilizes the STAR Roman Pot detectors to tag diffractive processes with scattered protons close to the beamline. Figure 39 shows the preliminary results for forward diffractive EM-jet A_N as a function of x_F at $\sqrt{s} = 200$ GeV [113]. The results favor a non-zero negative A_N with 3.3σ significance, so these diffractive processes are most probably not the source of the large positive A_N of π^0. The negative contribution from diffractive jets is not currently described by theory.

For p+p there will be considerable overlap between the kinematics at the two energies, but the 510 GeV measurements access higher p_T, while the 200 GeV measurements will access

higher x_F. Moreover, at 200 GeV we will also perform the full suite of measurements in p+Au to identify any nuclear effects. Furthermore, it is important to stress that the 200 GeV running with the Forward Upgrade will give the unique opportunity for jet reconstruction studies at the exact same rapidity that is critical for the future EIC. The data will provide an extraordinary possibility to exercise new reconstruction techniques incorporating AI/ML methods and train the next generation of scientists.

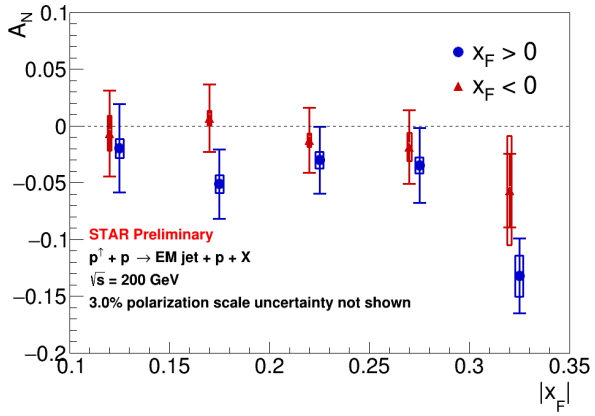

Figure 39: Transverse single-spin asymmetry for diffractive EM-jet as a function of x_F in transversely polarized proton-proton collisions at $\sqrt{s} = 200$ GeV [113]. The blue points are for $x_F > 0$. The red points are for $x_F < 0$ with a constant shift of -0.005 along x-axis for clarity. The rightmost points are for $0.3 < |x_F| < 0.45$.

2.1.2 Sivers and Efremov-Teryaev-Qiu-Sterman Functions

There is great theoretical interest in testing the relation between the ETQS correlation functions and the Sivers function. As discussed above, both the Sivers and the ETQS functions encapsulate partonic spin correlations within the proton, but they are formally defined in different frameworks. While the Sivers function is a TMD quantity that depends explicitly on spin-dependent transverse partonic motion k_T, the ETQS function is a twist-3 collinear distribution, in which SSAs are generated through soft collinear gluon radiation.

Measurements of forward jet production from the ANDY collaboration [114] indicated rather small asymmetries. This was argued to be consistent with the idea that the twist-3 parton correlation functions for up and down valence quarks should cancel, because their behavior reflects the Sivers functions extracted from fits to the SIDIS data that demonstrate opposite sign, but equal magnitude, up and down quark Sivers functions. STAR results on charge-tagged dijets at mid-rapidity [115] (see Fig. 43) support this interpretation, with the caveat that the measured observable (a spin-dependent $\langle k_T \rangle$) is defined in the TMD, and not the twist-3, framework. Moreover, recently published STAR results for forward inclusive electromagnetic jets [109] also show small TSSA as seen in Fig. 40. The results have been analyzed with the generalized parton model approach [116]. When incorporated in the reweighing procedure of the quark Sivers functions extracted from SIDIS data, they significantly improved its uncertainty at larger momentum fraction x (see Fig. 41).

To better test quantitatively the relation between the two regimes, one can measure spin asymmetries for jets which are *intentionally* biased towards up or down quark jets via detec-

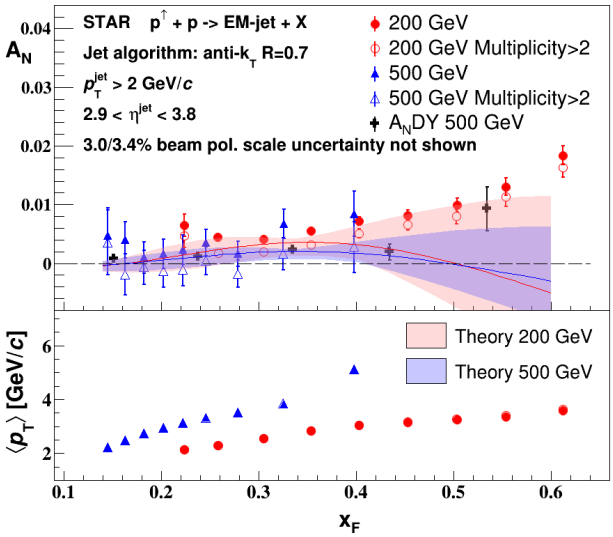

Figure 40: Recent STAR results on inclusive electromagnetic jets TSSA in pp collisions at both 200 and 500 GeV. [109] The results that require more than two photons observed inside a jet are shown as open symbols. Theory curves [117] for TSSA of full jets at rapidity $\langle y \rangle = 3.25$ for 200 GeV (red) and $\langle y \rangle = 3.57$ for 500 GeV (blue) are also shown. The average $p_{\rm T}$ of the jet for each $x_{\rm F}$ bin is shown in the lower panel.

tion of a high-z charged hadron within the jet. Higher-twist calculations of jet asymmetries based on the Sivers function predict sizeable effects for these flavor-enhanced jets. With the suite of new forward detectors installed at STAR, full jet reconstruction, along with identification of a high-z hadron of known charge sign is be possible at high pseudorapidity. Using realistic jet smearing in a forward calorimeter and tracking system, and requiring a charged hadron with $z > 0.5$, the asymmetries can be separated and compared to the predictions for the Sivers function based on current SIDIS data. The expected uncertainties, plotted at the predicted values, can be seen in Fig. 42. Dilutions by underlying event and beam remnants were taken into account. The simulations have assumed only an integrated luminosity of 100 pb^{-1} at $\sqrt{s} = 200$ GeV, which is less than what is currently expected for the Run-24 200 GeV polarized p+p run.

In a TMD framework, the Sivers effect manifests itself as a correlation (a triple product) between the transverse momentum of a parton ($\overrightarrow{k}_T$) with momentum fraction x, and the transverse spin ($\overrightarrow{S}$) of a polarized proton moving in the longitudinal ($\overrightarrow{p}$) direction. Thus, for transversely polarized protons, the Sivers effect probes whether the k_T of the constituent quarks is preferentially oriented in a direction perpendicular to both the proton momentum and its spin. Momentum conservation then implies that the two jets in the final state will not emerge back-to-back on average, but instead will 'tilt' in the direction of the summed k_T of the initial state partons. Moreover, the (average) tilt of interest will reverse direction under a 'flip' of the proton spin; a spin-dependent $\langle k_T \rangle$ can then be extracted by associating the azimuthal opening angle of the jet pair with this tilt.

Recently, the first observation of the Sivers effect in dijet production has been submitted to Phys. Rev. Lett., as presented in highlights Sect. 1.1 and also in Fig. 43. Compared to an earlier measurement of this transverse single-spin asymmetry using a dijet dataset with ∼1 pb^{-1} of integrated luminosity [118], several new techniques that were developed in the last 10 years are applied to improve the measurement. The jets were sorted according to their

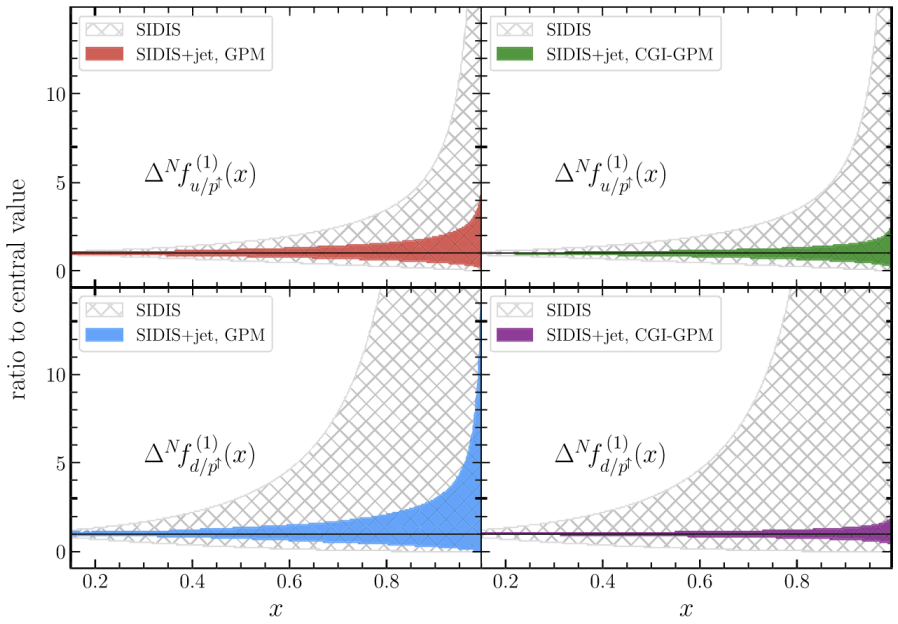

Figure 41: Comparison between the Sivers function first moments normalized to the corresponding central value from SIDIS data and their reweighted counterparts that incorporate new STAR results on electromagnetic jets [109] extracted in [116] in the generalized parton model (left panels) and color gauge invariant generalized parton model (right panels) framework. In both plots, results for u (upper panels) and d (lower panels) quarks are shown.

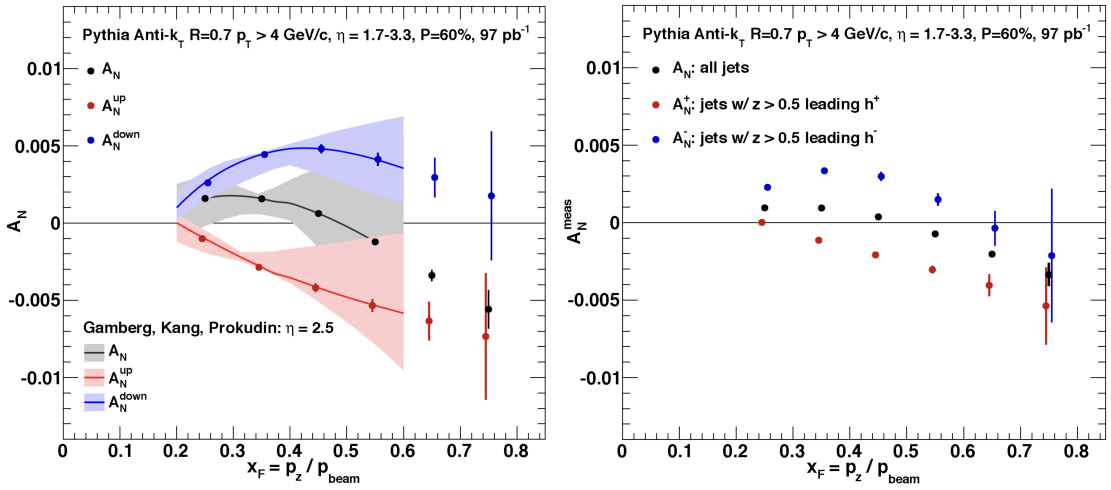

Figure 42: Left: up quark (red points), down quark (blue points) and all jet (black points) single spin asymmetries as a function of x_F as calculated by the ETQS based on the SIDIS Sivers functions. Right: Expected experimental sensitivities for jet asymmetries tagging in addition a positive hadron with z above 0.5 (red points), a negative hadron with z above 0.5 (blue points) or all jets (black) as a function of x_F. These figures are for 200 GeV center-of-mass energy proton collisions.

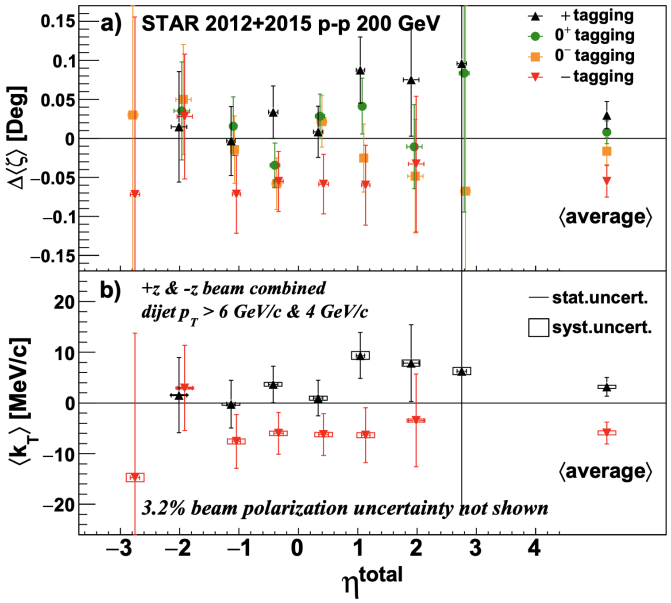

Figure 43: The $\Delta\zeta$ values and converted $\langle k_T \rangle$ plotted as a function of η^{total}. Rightmost points represent the average over the η^{total} bins. Individual 0^+ and 0^- points are suppressed in the lower panel to better view the η^{total} signal and systematic errors (dominated by fitting range contributions), indicated by the boxes. Plotted points are offset in η^{total} for clarity. Source [1].

net charge Q, calculated by summing the signed momentum of all particle tracks with $p > 0.8$ GeV, to minimize underlying event contributions, yielding jet samples with enhanced contributions from u quarks (positive Q) and d quarks (negative Q), with a large set near $Q = 0$ dominated by gluons. Simple kinematics allow for conversion from the spin-dependent 'tilt' of the dijet pair to a value of k_T on an event-by-event basis; these are then sorted by the Q of the jet and binned by the summed pseudorapidities of the outgoing jets, $\eta^{\text{total}} \equiv \eta_1 + \eta_2$. Because the contributions of different partons (u, d, all else) to $\langle k_T \rangle$ vary with both Q and also η^{total} in a way that can be estimated robustly using simulation, the data can be inverted to yield values of $\langle k_T \rangle$ for the individual partons, though with coarser binning in η^{total}.

Such measurements are crucial to explore questions regarding factorization of the Sivers function in dijet hadroproduction. [28–31] Those results were derived from 200 GeV transverse spin data that STAR recorded in Run-12 and Run-15 (total sampled luminosity ~ 75 pb^{-1} for the two years combined). Nonetheless, the uncertainties remain large, as can be seen in Fig. 43. Run-24 data will reduce the uncertainties for $|\eta_1 + \eta_2| < 1$ by nearly a factor of two. The increased acceptance from the iTPC will reduce the uncertainties at $|\eta_1 + \eta_2| \approx 2.5$ by a much larger factor, while the Forward Upgrade will enable the measurements to be extended to even larger values of $|\eta_1 + \eta_2|$. When combined with the 510 GeV data from Run-17 and Run-22, the results will provide a detailed mapping *vs.* x for comparison to results for Sivers functions extracted from SIDIS, Drell-Yan, and vector boson production i.e. as shown in Fig. 44.

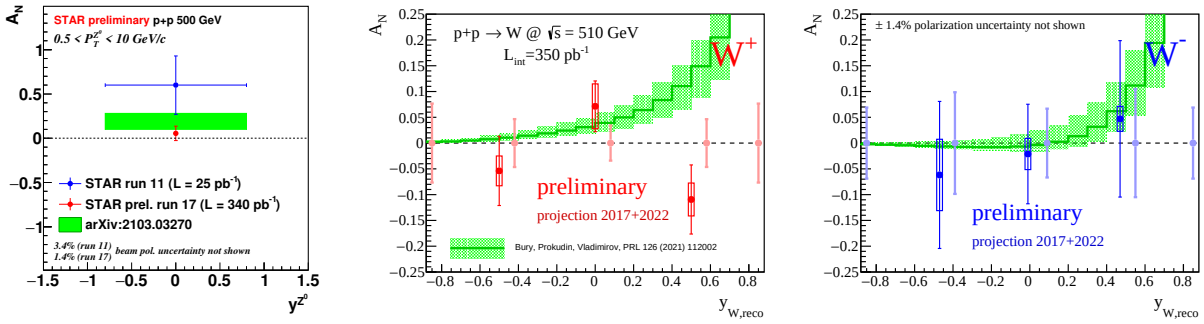

Figure 44: Left: Transverse single-spin asymmetry of Z^0 from STAR 2011 and 2017 data. The results are compared with the calculation from [119]. Middle and Right: Transverse single-spin asymmetry of $W^{\pm}$ from STAR 2017, and the projected statistical uncertainties from 2017 and 2022 data. The results are compared with calculation from [119] based on the next-to-next-to-next-to leading log (N^3LL) accuracy TMD evolution from [120].

2.1.3 Transversity, Collins Function and Interference Fragmentation Function

A complete picture of nucleon spin structure at leading twist must include contributions from the unpolarized and helicity distributions, as well as those involving transverse polarization, such as the transversity distribution [121–123]. The transversity distribution can be interpreted as the net transverse polarization of quarks within a transversely polarized proton. The difference between the helicity and transversity distributions for quarks and antiquarks provides a direct, x-dependent connection to nonzero orbital angular momentum components in the wave function of the proton [124]. Recently, the first lattice QCD calculation of the transversity distribution has been performed [125]. In addition, the measurement of transversity has received substantial interest as a means to access the tensor charge of the nucleon, defined as the integral over the valence quark transversity: $\delta q^a = \int_0^1 [\delta q^a(x) - \delta \bar{q}^a(x)]\, dx$ [122, 126]. Measuring the tensor charge is very important for several reasons. First, it is an essential and fundamental quantity to our understanding of the spin structure of the nucleon. Also, the tensor charge can be calculated on the lattice with comparatively high precision, due to the valence nature of transversity, and hence is one of the few quantities that allow us to compare experimental results on the spin structure of the nucleon directly to *ab initio* QCD calculations. Finally, the tensor charge describes the sensitivity of observables in low-energy hadronic reactions to beyond the standard model physics processes with tensor couplings to hadrons. Examples are experiments with ultra-cold neutrons and nuclei.

Transversity is difficult to access due to its chiral-odd nature, requiring the coupling of this distribution to another chiral-odd distribution. Semi-inclusive deep-inelastic scattering (SIDIS) experiments have successfully probed transversity through two channels: asymmetric distributions of single pions, convoluting the TMD transversity distribution with the TMD Collins fragmentation function, and azimuthally asymmetric distributions of dihadrons, coupling transversity to the so-called Interference Fragmentation Function (IFF) in the framework of collinear factorization. Yet in spite of a wealth of lepton-scattering

data, the kinematic reach of existing SIDIS experiments limits the precision with which the proton's transversity can be extracted, as the range of Bjorken-x values that can be accessed does not extend above $x_{\mathrm{Bj}} \sim 0.3$.

In hadronic collisions, the k_T integrated quark transversity distribution may be accessed mainly via two channels. The single-spin asymmetries of the azimuthal distribution of identified pions, kaons, and protons in high-energy jets measured at STAR probe the collinear quark transversity in the proton, coupled to the transverse momentum dependent Collins fragmentation function [127–129].

This makes the Collins asymmetry in p+p collisions a more direct probe of the Collins fragmentation function than SIDIS as the convolution with the TMD transversity distribution does not enter, and provides an ideal tool to explore the fundamental QCD questions of TMD factorization, universality, and evolution. The second channel is the single spin asymmetry of hadron pairs, where transversity couples to the collinear interference fragmentation function [130]. The choice of the hadron pair, such as $\pi\pi$, πK, and KK, provides an additional handle on the quark flavor. STAR mid-rapidity pion-pion IFF data [131] have been included in the first extraction of transversity from SIDIS and proton-proton IFF asymmetries [132].

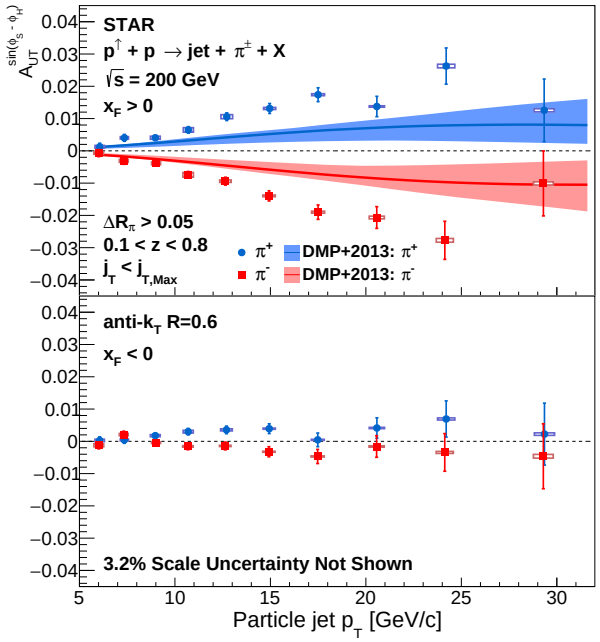

Figure 45: Collins asymmetry plotted for identified π^+ (blue) and π^- (red) particles as a function of jet p_{T} for jets that scatter forward relative to the polarized beam ($x_F > 0$) in the upper panel and those that scatter backward ($x_F < 0$) in the lower panel, extracted from data collected in 2012 and 2015 [42]. The full ranges of both z and j_{T} are integrated over. Theoretical evaluations from [129] with their uncertainties are presented for π^+ (blue) and π^- (red). Source: [42].

Figure 45 shows the recent results on combined 2012 and 2015 Collins asymmetries for charged pions within jets as a function of jet p_{T} [42]. By integrating over the hadron longitudinal and transverse momenta within the jets, Fig. 45 is sensitive primarily to the quark transversity. The measured asymmetries for jets that scatter forward relative to the polarized beam are larger than theoretical predictions [129], which are based on the transversity and Collins fragmentation function from SIDIS and e^+e^- processes within the TMD approach.

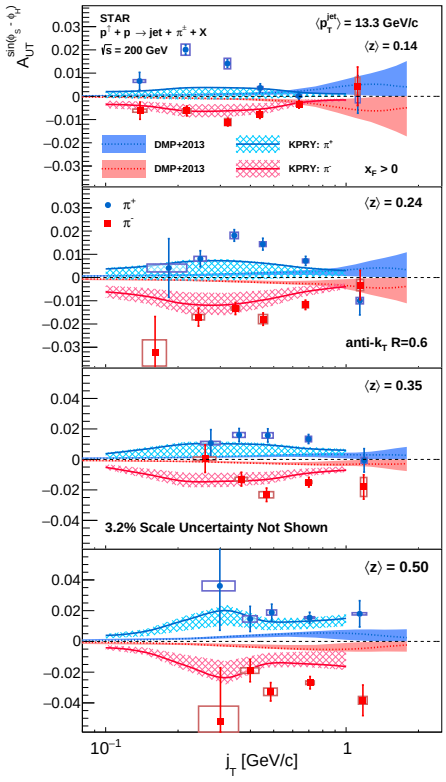

Figure 46: Collins asymmetry plotted for identified π^+ (blue) and π^- (red) particles as a function of j_T for four separate bins of hadron z, in jets with $p_T > 9.9$ GeV/c and $0 < \eta < 0.9$. Theoretical evaluations from [128] and [129] are also shown. Source: [42].

Alternatively, the asymmetries can be expressed as functions of the fraction z of jet momentum carried by the hadron, and the momentum j_T of the pion transverse to the jet axis, as shown in Fig. 46. This provides a direct measurement of the kinematic dependence of the Collins fragmentation function. The findings include the j_T dependence which appears to vary with z, contrary to the assumptions of most current phenomenological models [127–129].

STAR has also published Collins asymmetry measurements from a smaller 500 GeV data set collected in 2011 [133]. While statistics are limited, the results are consistent with those at 200 GeV for overlapping x_T, despite sampling Q^2 that is larger by a factor of 6. Analysis of the higher statistics 510 GeV data collected in 2017 is underway and will provide unique insight into the Q^2 evolution of the Collins TMD fragmentation function. Concurrent with the Collins effect measurements, STAR has also measured azimuthal modulations that are sensitive to the twist-3 analogs of the quark and gluon Sivers functions and to linear polarization of gluons in transversely polarized protons [42, 133]. Analysis is also underway to determine the unpolarized TMD fragmentation functions.

Figure 47 shows that 200 GeV p+p collisions interpolate between the kinematic coverage achieved with Run-22 data at high-x with the Forward Upgrade and at low-x with the STAR mid-rapidity detectors. They will also provide a coverage that spans in Q^2 by a factor of 6. This will provide valuable information about evolution effects, as well as cross-checks between measurements for various kinematic coverage. Furthermore, for most of the overlapping x region, 200 GeV p+p collisions will also provide the greatest statistical precision (see for example Fig. 48), thereby establishing the most precise benchmark for future comparisons to

ep data from the EIC. It is important to also recognize that the hadron-in-jet measurements with the STAR Forward Upgrade will provide valuable insight into jet detection close to beam rapidity that will guide the planning of future jet measurements in similar kinematics at the EIC.

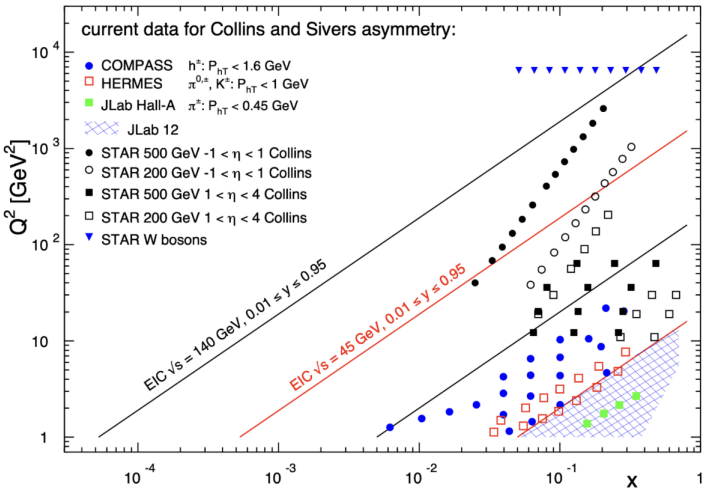

Figure 47: $x - Q^2$ coverage of RHIC measurements compared to existing Collins and Sivers effect measurements in SIDIS and the future coverage of the EIC.

The high statistical precision of the Run-24 data will enable detailed multi-dimensional binning for the Collins asymmetry results. This is particularly valuable because, as emphasized in [127, 128], hadron-in-jet measurements in p+p collisions provide a direct probe of the Collins fragmentation function that couples to the *collinear* transversity distribution. In general, the observed asymmetries are functions of jet (p_T, η), hadron (z, j_T), and Q^2. However, the physics interpretations associated with these variables differ; measurements of jet-p_T and η primarily probe the incident quark x and the polarization transfer in the hard

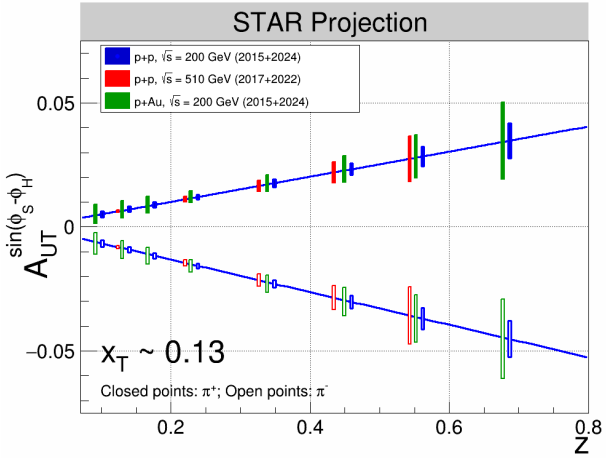

Figure 48: Projected statistical uncertainties for STAR Collins asymmetry measurements at $0 < \eta < 0.9$ in p+p at $\sqrt{s} = 200$ and 510 GeV and p–Au at $\sqrt{s_{\rm NN}} = 200$ GeV. The points have arbitrarily been drawn on the solid lines, which represent simple linear fits to the STAR preliminary 200 GeV p+p Collins asymmetry measurements from 2015. (Note that only one bin is shown spanning $0.1 < z < 0.2$ for 510 GeV p+p whereas three bins are shown covering the same z range for the 200 GeV measurements).

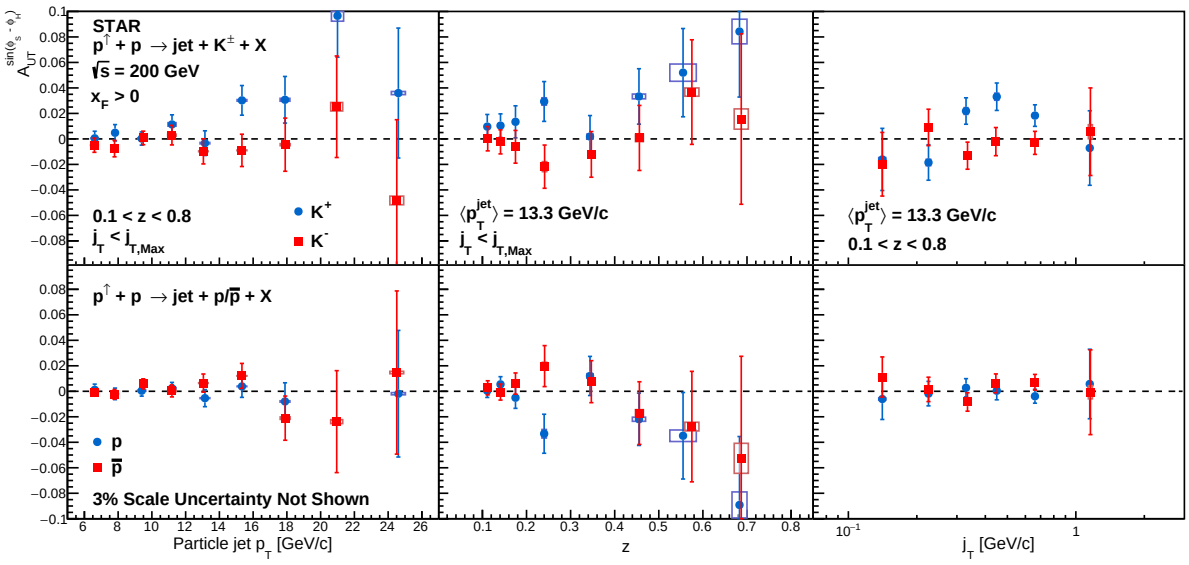

Figure 49: Collins asymmetries, $A_{UT}^{sin(\phi_S-\phi_H)}$, as a function of particle jet-p_T , hadron-z, and hadron-j_T for charged kaons (upper panels) and protons (lower panels) inside jets. In both cases, the $p_{\rm T}$ dependence is shown integrated over the full ranges of z and j_T, while the z and j_T dependencies are shown integrated over detector jet-$p_T > 9.9$ GeV/c. The bars show the statistical uncertainties, while the size of the boxes represent the systematic uncertainties.

scattering, while those of z and j_T characterize the fragmentation kinematics. Thus, A_{UT} *vs.* p_T provides information about the transversity distribution, while the (z, j_T) dependence provides a detailed look at the Collins fragmentation function. The published results based on Run-12 and Run-15 data sets (see Fig. 46) find the maximum value of A_{UT} shifting to higher values of j_T as p_T increases, which is not seen in the current theory evaluations [134]. Run 24 data set will greatly improve the precision of this measurement, reducing the statistical uncertainty by nearly a factor of 2.

The Run-15 Collins analysis has also, for the first time, measured the Collins effect for charged kaons and protons/anti-protons in p+p collisions, as shown in Fig. 49. The K^+ asymmetries, like π^+, have a contribution from favored fragmentation of u quarks, and thus are similar in magnitude to the π^+ asymmetries. On the other hand, those for K^- can only originate from unfavored fragmentation and are consistent with zero at 1-σ level. These trends are similar to those found in SIDIS by HERMES [135] and COMPASS [136], and provide additional insight into the Collins fragmentation function. Run 24 data set will reduce the statistical uncertainties by up to a factor of 3 from those in Fig. 49, owing to the increase in sampled luminosity and the improved dE/dx resolution provided by the iTPC. In addition, the iTPC will enable the measurements in Figs. 49 and 50 in an additional bin for higher values of η ($0.9 < \eta < 1.3$).

STAR has a unique opportunity to extend the Collins effect measurements to nuclei. This will provide an alternative look at the universality of the Collins effect in hadron-

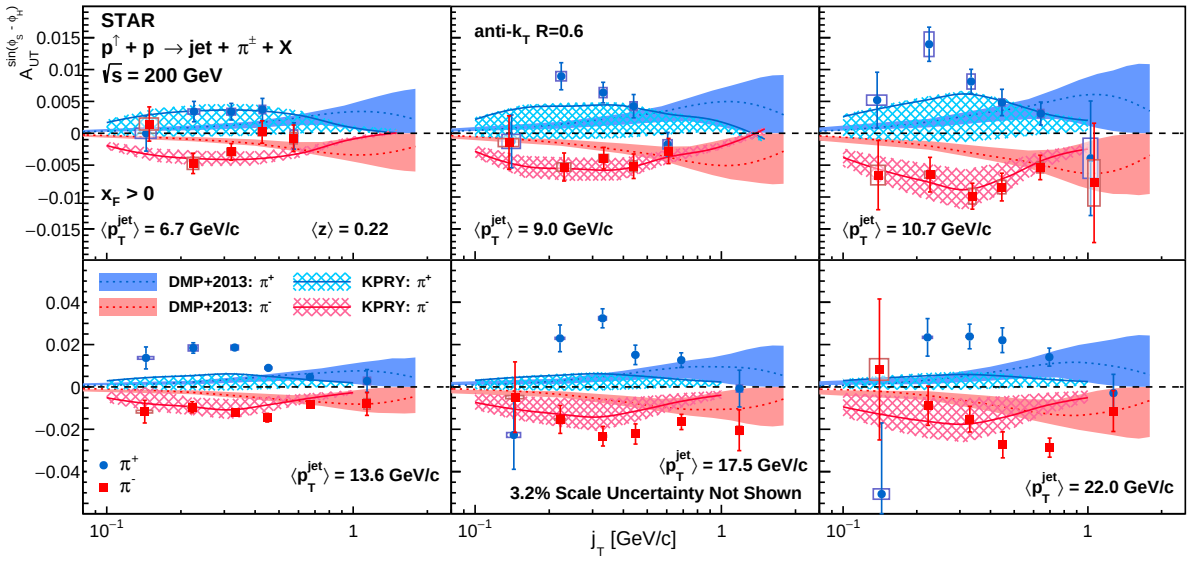

Figure 50: Collins asymmetries, $A_{\mathrm{UT}}^{\sin(\phi_{\mathrm{S}}-\phi_{\mathrm{H}})}$, as a function of the charged pion's momentum transverse to the jet axis, j_{T}, in different jet-p_{T} bins. The bars show the statistical uncertainties, while the size of the boxes represents the systematic uncertainties on $A_{\mathrm{UT}}^{\sin(\phi_{\mathrm{S}}-\phi_{\mathrm{H}})}$ (vertical) and hadron-j_{T} (horizontal). The asymmetries are shown in comparison to calculations with the DMP+2013 model from Ref. [134] and the KPRY model from Ref. [128].

production by dramatically increasing the color flow options. Breaking of factorization has been predicted for TMD PDFs similar to that for the Sivers effect [28, 29]. This will also explore the spin dependence of the hadronization process in cold nuclear matter. STAR collected a proof-of-principle data set during the 2015 p+Au run that is currently under analysis. Those data will provide a first estimate of medium-induced effects. However, the small nuclear effects seen by STAR for forward inclusive π^0 A_N [112] indicate that greater precision will likely be needed. Figure 48 shows the projected Run 15 and Run 24 statistical uncertainties for the p+Au Collins asymmetry measurement at $\sqrt{s_{\mathrm{NN}}} = 200$ GeV, compared to those for the p+p at the same energy.

In the dihadron channel, the transversity couples to the collinear IFF [130]. This gives rise to an asymmetric production of hadron pairs along the azimuthal direction in the mid-rapidity region, $|\eta| < 1$. The IFF is a collinear observable; therefore, these measurements provide a complementary probe of transversity to the Collins asymmetry measurements that obey different evolution equations. STAR has measured u- and d-quark transversity distributions via di-pion IFF in 200 [137] and 500 GeV p+p collisions [138]. The results from the first measurements of di-pion asymmetry at 200 GeV based on data recorded during 2006 [137] have been included together with IFF measurements from SIDIS in a global analysis [132], as shown in Fig. 51. The published STAR IFF measurements were found to provide significant constraints on the u- and d-quark transversities.

The dominant systematic uncertainties in the global analysis arose from the current lack

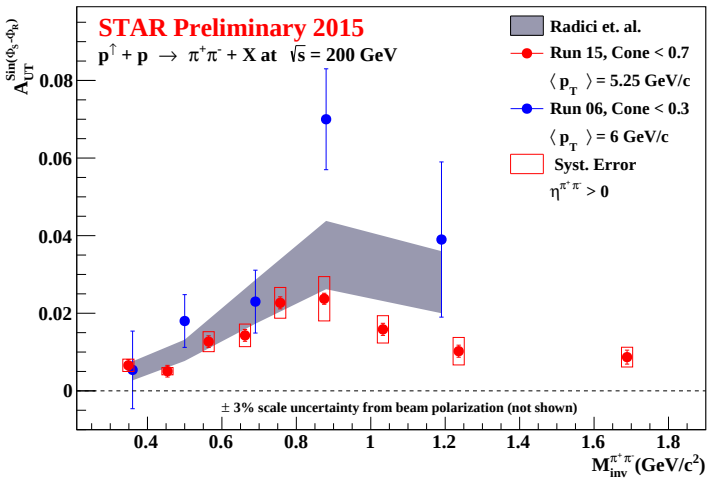

Figure 51: A comparison of STAR published [137, 138] and preliminary [139] IFF asymmetries vs. dipion invariant mass to predictions from the global analysis of [132], which only included the 200 GeV data from 2006 in the fit. Source: [139].

of knowledge regarding the unpolarized gluon dihadron fragmentation functions, $D_1^{hh/q}$. The $D_1^{hh/q}$ fragmentation functions can be extracted from measurements of the inclusive dihadron cross section in p+p collisions [140]. The preliminary results of di-pion cross section with Run 12, shown in Fig. 52, will help reduce these uncertainties. The analysis of IFF asymmetries with more recent STAR data taken in 2017 and 2022 at 510 GeV, together with the 200 GeV data taken in 2015 and those projected for 2024, will provide the most stringent constraints to date on u- and d-quark transversities when they are included in future global analyses.

Different types of hadron pairs can be chosen to investigate transversity distributions of other flavors of quarks. KK-pair production, for instance, provides sensitivity to transversity distribution of strange quarks, which is largely unconstrained at the moment. Investigations with KK pairs have not been considered due to the limited statistics available and the large systematic uncertainty arising from the quality of particle identification. However, the p+p collisions at $\sqrt{s} = 200$ GeV that are projected for 2024 period, along with improvements made in the recent analyses to precisely estimate the effect of imperfect particle identification, will enable measurements of KK-pair production. Figure 53 illustrates an estimate of the statistical uncertainty expected for KK-pair production with combined STAR Run 2015+2024 data set, as well as a projection for the production of $\pi\pi$ pairs. We expect that high-statistics sample with Run 24 will enable precision measurements of $\pi\pi$ production and the first measurement of KK production in hadron collisions near ϕ-meson mass region.

The universality of TMD PDFs and fragmentation functions in p+p collisions has been an open question. General arguments [28, 29] have shown that factorization can be violated in hadron-hadron collisions for TMD PDFs like the Sivers function, though very recent calculations indicate the violations might be quite small [30, 31]. In contrast, while there is no general proof that the Collins effect in p+p collisions is universal to all orders, explicit calculations [127, 128, 141, 142] have shown that diagrams like those that violate factorization of the Sivers function make no contribution to the Collins effect at the one- or two-gluon exchange level, thereby preserving its universality at least to that level.

Comparisons of the transversity distributions extracted from the Collins and IFF channels

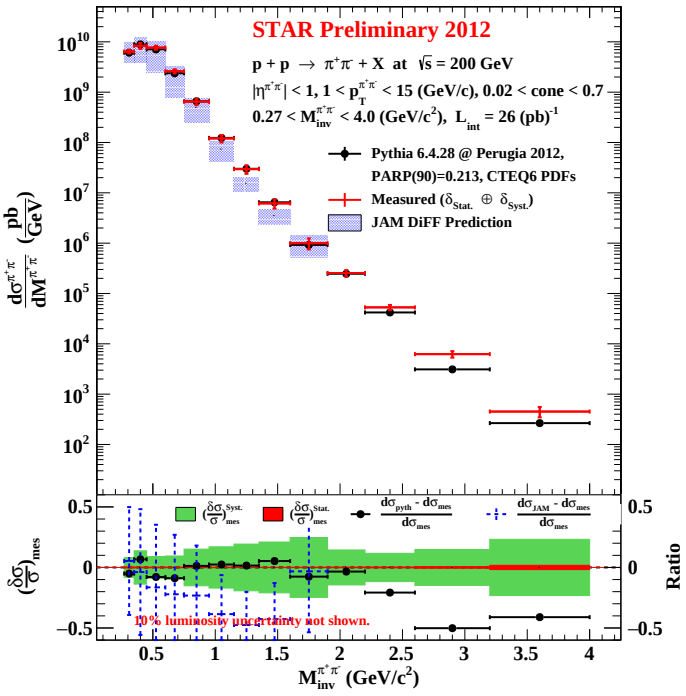

Figure 52: Top panel: the measured and PYTHIA cross-sections. Bottom panel: total relative systematic error (green band), statistical error (red band), shown on the left axis , and relative difference between the PYTHIA and measured cross-section (Ratio) is shown in the right axis.

will allow STAR to study the size and nature of any factorization breaking effects for TMD observables in hadronic collisions. Likewise, comparisons with the SIDIS measurements will shed light on universality and constrain evolution effects. The measurement of evolution effects in TMD distributions is particularly important because, unlike the collinear case, TMD evolution contains a non-perturbative component that cannot be calculated directly.

In addition, transverse spin transfer, D_{TT}, of Λ hyperons in p+p collisions is expected to provide sensitivity for the strange quark transversity through the polarized fragmentation functions. The strange quark transversity is not constrained at all currently. The first D_{TT} measurement of Λ and $\bar{\Lambda}$ hyperons at $\sqrt{s} = 200$ GeV has been performed with the Run-12 p+p dataset [143] and preliminary results based on Run-15 have been released [144]. Current results do not indicate a sizable spin transfer yet. The iTPC upgrade will help to reach near-forward pseudo-rapidity $\eta < 1.5$ for the spin transfer measurements.

2.1.4 Ultra-peripheral Collisions

The formalism of generalized parton distributions (GPDs) provides a theoretical framework which addresses some of the above questions [145–148]. Constraints on GPDs have mainly been provided by exclusive reactions in DIS, e.g. deeply virtual Compton scattering. RHIC, with its unique capability to collide transversely polarized protons at high energies, has the opportunity to measure A_N for exclusive J/Ψ production in ultra-peripheral collisions (UPCs) [149]. In such a UPC process, a photon emitted by the opposing beam particle (p

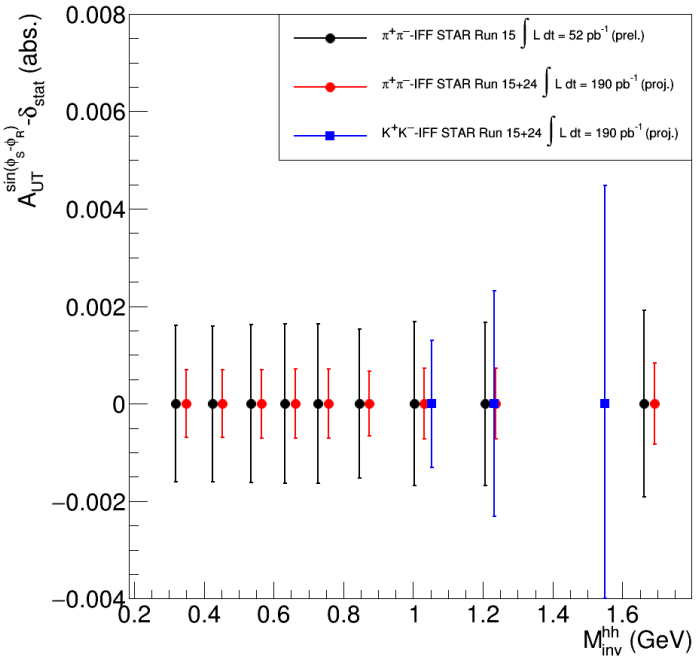

Figure 53: Projections of $\pi\pi$ and KK IFF measurements for STAR Run 2024. Black points represent the statistical uncertainty in the preliminary measurements of $\pi\pi$ production with Run 15 data set. A small offset was introduced in the black points along the horizontal direction for visual clarity. Red and blue points represent projections for Run 24 $\pi\pi$ and KK measurements, respectively. An integrated luminosity of ~ 140 pb^{-1} was assumed for Run 24.

or Au) collides with the polarized proton. The measurement is at a fixed $Q^2 \sim M_{J/\psi}^2 \approx 10$ GeV^2 and $10^{-4} < x < 10^{-1}$. A nonzero asymmetry would be the first signature of a nonzero GPD E_g for gluons, which is sensitive to spin-orbit correlations and is intimately connected with the orbital angular momentum carried by partons in the nucleon and thus with the proton spin puzzle.

The Run-15 $p^{\uparrow}$+Au data allowed a proof-of-principle of such a measurement. A trigger requiring back-to-back energy deposits in the Barrel Electromagnetic Calorimeter selected J/Ψ candidates. The e^+e^- mass distribution after selection cuts is shown in the left of Fig. 54, and the pair p_T distribution of the J/ψ mass peak is shown on the right of that figure. The data are well described by the STARlight model [150] (colored histograms in the figure), including the dominant γ+p$\uparrow\rightarrow J/\psi$ signal process and the γ+Au$\rightarrow J/\psi$ and $\gamma+\gamma\rightarrow e^+e^-$ background processes. The left of Fig. 55 shows the STAR preliminary measurement (solid circle marker) of the transverse asymmetry A_N^{γ} for the J/ψ signal, which have a mean photon-proton center-of-mass energy $W_{\gamma p} \approx 24$ GeV. The result is consistent with zero. Also shown is a prediction based on a parameterization of E_g [151]; the present data provide no discrimination of this prediction.

This measurement can be greatly improved with a high statistics transversely polarized p$^{\uparrow}$–Au Run-24. The integrated luminosity for the UPC trigger used for the Run-15 measurement was 140 nb^{-1}; Run-24 will provide about 5 times more sampled luminosity (scenario 0 in Fig. 62), allowing for a moderate reduction of statistical uncertainty in the same $W_{\gamma p}$ range, but not allowing accurate comparison with the GPD model in that $W_{\gamma p}$ bin. However, the Forward Upgrade and iTPC will also provide a significant extension of the $W_{\gamma p}$

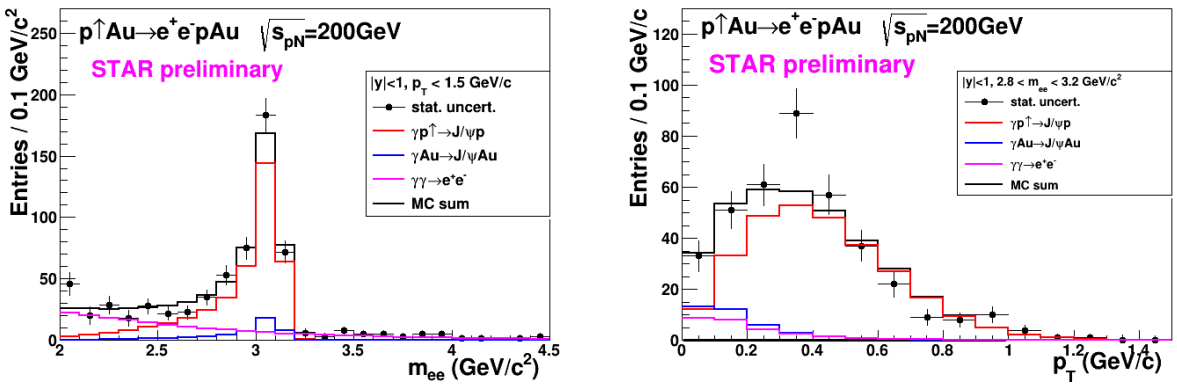

Figure 54: Mass distribution of selected e^+e^- pairs (left), and p_T distribution of the J/ψ mass peak (right). The colored histograms are the indicated processes modelled by STARlight and the sum fit to the data.

range of the measurement. The right panel of Fig. 55 shows the accepted cross section for γ+p$^\uparrow \rightarrow J/\psi$ for various detector pseudorapidity ranges. With the upgraded detector, the sensitive cross section is a factor of five times higher than the central barrel alone and the expected asymmetry is substantially larger. The projected statistical uncertainty on A_N^γ as shown in the left of Fig. 55 (blue square marker) offers a powerful test of a non-vanishing E_g. Also, the accepted region has a lower mean $W_{\gamma p} \approx 14$ GeV. Predictions based on E_g parameterizations such as shown in figure 55 have a larger asymmetry at lower $W_{\gamma p}$. Alternatively, the increased statistics will enable a differential measurement of A_N^γ as a function of $W_{\gamma p}$.

The UPC cross section scales with Z^2 of the the nucleus emitting the photon; for protons this is $1/79^2$ relative to Au nuclei, which makes analogous measurements in p+p collisions extremely luminosity-hungry. Therefore, the p+Au run is important for this measurement.

2.2 Physics Opportunities with Unpolarized p+Au Collisions

Our quest to understand QCD processes in Cold Nuclear Matter (CNM) centers on the following fundamental questions:

- Can we experimentally find evidence of a novel universal regime of non-linear QCD dynamics in nuclei?
- What is the role of saturated strong gluon fields, and what are the degrees of freedom in this high gluon density regime?
- What is the fundamental quark-gluon structure of light and heavy nuclei?
- Can a nucleus, serving as a color filter, provide novel insight into the propagation, attenuation and hadronization of colored quarks and gluons?

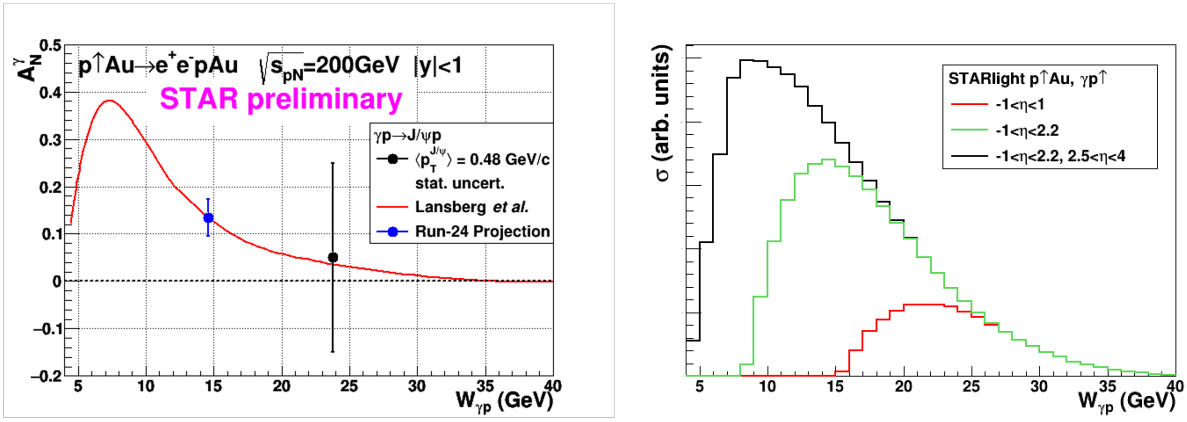

Figure 55: Left: The measured J/ψ transverse asymmetry A_N^γ and a prediction based on a parameterization of E_g. Right: The accepted cross section for γ+p↑→ J/ψ for various detector pseudorapidity η ranges; the black curve shows the result for the full STAR detector with the Forward Upgrade and the iTPC.

Various aspects of these questions have been addressed by numerous experiments and facilities around the world, most of them at significantly lower center-of-mass energies and kinematic reach than RHIC. Deep inelastic scattering on nuclei addresses some of these questions with results from, for instance, HERMES at DESY [152–154], CLAS at JLab [155], and in the future from the JLab 12 GeV. This program is complemented by hadron-nucleus reactions in fixed target p+A at Fermilab (E772, E886, and E906) [156] and at the CERN-SPS.

In the following we propose a measurement program unique to RHIC to constrain the initial state effects in strong interactions in the nuclear environment. We also highlight the complementarity to the LHC p+Pb program and stress why RHIC data are essential and unique in the quest to further our understanding of nuclei. The uniqueness of the RHIC program is based on the flexibility of the RHIC accelerator to run collisions of different particle species at very different center-of-mass energies. This in combination with the enhanced STAR detector capabilities in Run-24 allows to disentangle nuclear effects in the initial and final state as well as leading twist shadowing from saturation effects in a kinematic regime where all these effects are predicted to be large. Most of the discussed measurements critically rely on the Forward Upgrade.

2.2.1 The Initial State of Nuclear Collisions

Nuclear parton distribution functions: A main emphasis of the Run-15 and later p+A runs is to determine the initial conditions of the heavy ion nucleus before the collision to support the theoretical understanding of the A–A program both at RHIC and the LHC. In the following, the current status of nPDFs will be discussed, including where the unique contributions of RHIC lie, in comparison to the LHC and the future EIC.

Our current understanding of nuclear parton distribution functions (nPDFs) is still very

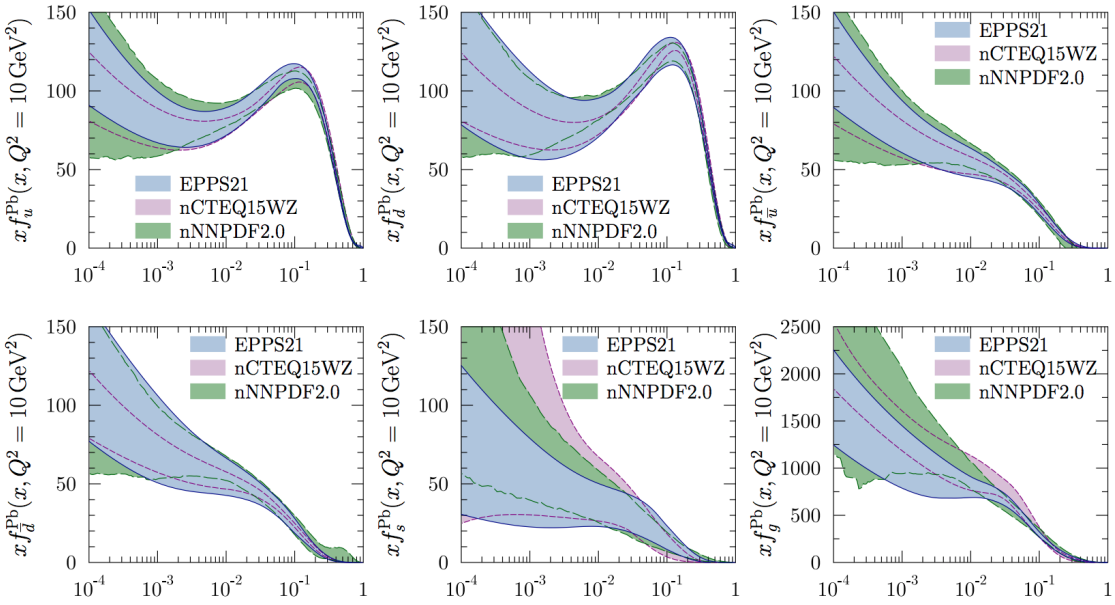

Figure 56: Summary of the most recent sets of nPDFs at 90% confidence-level. [157]

limited, in particular, when compared with the rather precise knowledge of PDFs for free protons collected over the past 30 years. Figure 56 shows an extraction of nPDFs from available data, along with estimates of uncertainties. All results are shown in terms of the nuclear modification ratios, i.e., scaled by the respective PDF of the free proton. The kinematic coverage of the data used in the EPPS21 fits [157] are shown in Fig. 57. Clearly, high precision data at small x and for various different values of Q^2 are needed to better constrain the magnitude of suppression in the x region where non-linear effects in the scale evolution are expected. In addition, such data are needed for several different nuclei, as the A-dependence of nPDFs cannot be predicted from first principles in pQCD and, again, currently relies on assumptions. The PHENIX midrapidity $\pi^0 R_{dAu}$ data [158], are the only data which can probe the gluon in the nucleus directly, but these data also suffer from unknown nuclear effects in the final state (see [159]). Therefore, it is critical to have high precision data only sensitive to nuclear modification in the initial state over a wide range in x and intermediate values of Q^2 (away from the saturation regime) to establish the nuclear modification of gluons in this kinematic range.

It is important to realize that the measurements from RHIC are compelling and essential even when compared to what can be achieved in p–Pb collisions at the LHC. Due to the higher center-of-mass system energy most of the LHC data have very high Q^2, where the nuclear effects are already reduced significantly by evolution and are therefore very difficult to constrain.

RHIC has the *unique* capability to provide data in a kinematic regime (moderate Q^2 and medium-to-low x) where the nuclear modification of the sea quark and the gluon is expected

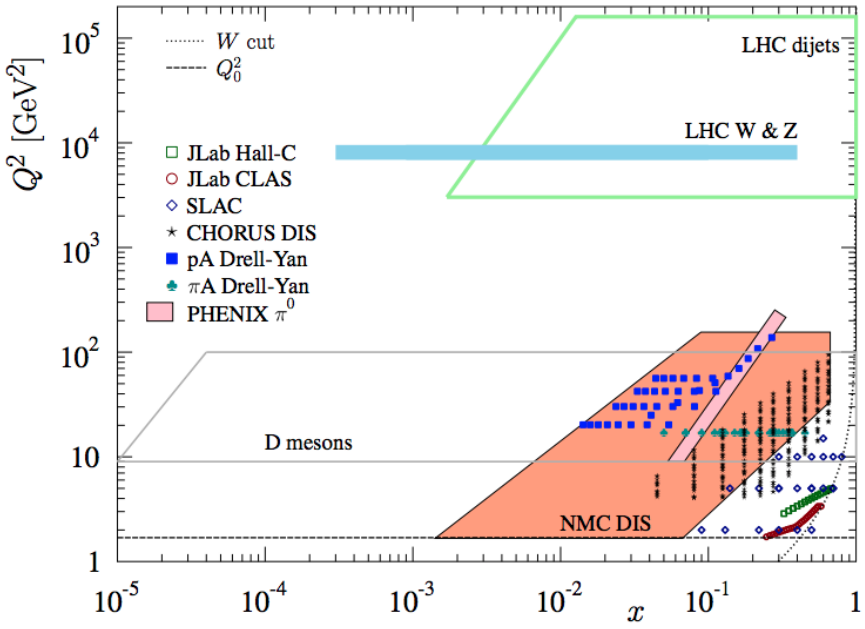

Figure 57: The kinematic x and Q^2 coverage of data used in the EPPS21 nPDF fits. [157]

to be sizable. In addition, and unlike the LHC, RHIC has the potential to vary the nucleus in p+A collisions and as such also constrain the A-dependence of nPDFs.

Extraction of this information is less ambiguous if one uses processes in which strong (QCD) final-state interactions can be neglected or reduced. Such golden channels would include a measurement of R_{pA} for Drell-Yan production at forward pseudo-rapidities with respect to the proton direction ($2.5 < \eta < 4$) to constrain the nuclear modifications of sea-quarks. Moreover, the R_{pA} for direct photon production in the same kinematic regime will help constrain the nuclear gluon distribution. Data for the first measurement of R_{pA} for direct photon production have already been taken during the p+Au and p+Al Run-15, with recorded luminosities by STAR of $L_{pAu} = 0.45$ pb^{-1} and $L_{pAl} = 1$ pb^{-1}, respectively. Like all other inclusive probes in p+p and p+A collisions, e.g., jets, no access to the exact parton kinematics can be provided event-by-event but global QCD analyses easily account for that. After the p+Au Run-24, the statistical precision of the prompt photon data will be sufficient to contribute to a stringent test of the universality of nuclear PDFs when combined with the expected data from the EIC (see Figure 2.22 and 2.23 in Ref [160]). The Forward Upgrade with its tracking at forward rapidities will also provide the possibility to measure R_{pA} for positive and negatively charged hadrons. Approximately equal nucleon-nucleon luminosities for p+p and p+Au are important for the optimization of R_{pA} measurements as they directly compare the same observable—yields—in both collision systems.

Figure 58 shows the kinematic coverage in x–Q^2 of past, present, and future experiments capable of constraining nuclear parton distribution functions. The shown experiments provide measurements that access the initial state parton kinematics on an event-by event basis

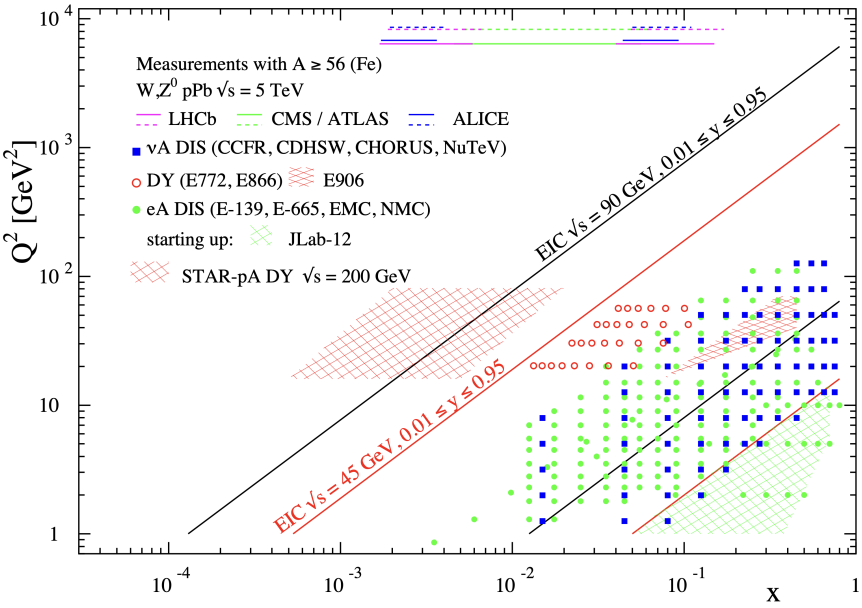

Figure 58: The kinematic coverage in $x - Q^2$ of past, present and future experiments constraining nPDFs with access to the exact parton kinematics event-by-event and no fragmentation in the final state.

(in a leading order approximation) while remaining insensitive to any nuclear effects in the final state. Some of the LHC experiments cover the same x-range as DY at forward pseudo-rapidities at RHIC but at a much higher scale Q^2, where nuclear modifications are already significantly reduced [161–163]. At intermediate Q^2, DY at STAR will extend the low-x reach by nearly one decade compared to EIC.

The biggest challenge of a DY measurement is to suppress the overwhelming hadronic background: the total DY cross-section is about 10^{-5} to 10^{-6} smaller than the corresponding hadron production cross-sections. Therefore, the probability of misidentifying a hadron track as a lepton has to be suppressed to the order of 0.1% while maintaining reasonable electron detection efficiencies. To that end, we have studied the combined electron/hadron discriminating power of the Forward Upgrade. It was found that by applying multivariate analysis techniques to the features of EM/hadronic shower development and momentum measurements we can achieve hadron rejection powers of 200 to 2000 for hadrons of 15 GeV to 50 GeV with 80% electron detection efficiency.

The potential impact of the DY R_{pA} data for the EPPS-19 sets of nPDFs was studied through a re-weighting procedure. [164] We expect a significant impact on the uncertainties of R_{pA} DY upon including the projected and properly randomized data. Clearly, the DY data from RHIC will be instrumental in reducing present uncertainties in nuclear modifications of sea quarks. Again, these data will prove to be essential in testing the fundamental universality property of nPDFs in the future when EIC data become available.

STAR's unique detector capabilities provide data on J/Ψ-production in ultra-peripheral collisions. This measurement can provide access to the spatial gluon distribution by measuring the t-dependence of $d\sigma/dt$. To study the gluon distribution in the gold nucleus, events need to be tagged where the photon is emitted from the proton (γ+Au$\rightarrow$ J/ψ). However, with the signal-to-background ratio in p+Au collisions (see the contribution from

the γ+Au$\rightarrow$ J/ψ process and the background processes in Fig. 54), we expect much better sensitivity to the gluon distributions in Au from the Au+Au program. In addition to J/ψ photoproduction in UPC for exclusive reactions, photoproduction of back-to-back jets is also sensitive the PDFs (nPDFs in Au+Au UPC). This measurement has never been performed at RHIC experiments, where the kinematic coverage can go to moderate to high-x. The anti-shadowing region in nuclei, for example, is of great interest by comparing to this measurement in the proton. Furthermore, we can possibly extend the measurement from inclusive photoproduction dijets to diffractive dijets in p+p and p+Au collisions, which will be sensitive to the QCD factorisation breaking [165]. For details, see Sec. 3.2 for discussion in UPCs.

Non-linear QCD effects: Our understanding of the proton structure and of the nuclear interactions at high energy would be advanced significantly with the definitive discovery of the saturation regime. [166–172] Saturation physics would provide an infrared cutoff for perturbative calculations, the saturation scale Q_s, which grows with the atomic number of the nucleus A and with decreasing value of x. If Q_s is large it makes the strong coupling constant small, $\alpha_s(Q_s^2) << 1$ allowing for perturbative QCD calculations to be under theoretical control.

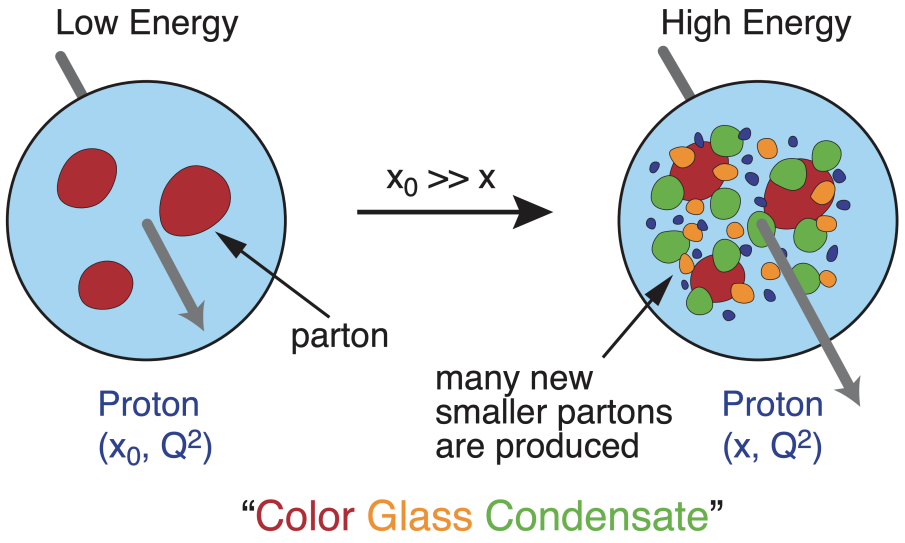

Figure 59: Proton wave function evolution towards small-x.

It is well known that PDFs grow at small-x. If one imagines how such a high number of small-x partons would fit in the (almost) unchanged proton radius, one arrives at the picture presented in Fig. 59: the gluons and quarks are packed very tightly in the transverse plane. The typical distance between the partons decreases as the number of partons increases, and can get small at low-x (or for a large nucleus instead of the proton). One can define the saturation scale as the inverse of this typical transverse inter-parton distance. Hence Q_s indeed grows with A and decreasing x.

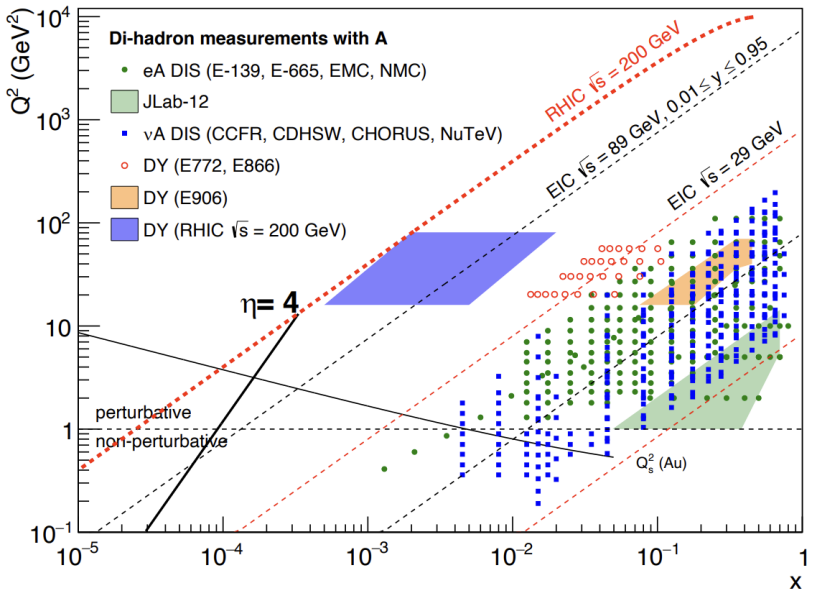

Figure 60: Kinematic coverage in the $x - Q^2$ plane for p+A collisions at RHIC, along with previous e+A measurements, the kinematic reach of an electron-ion collider, and estimates for the saturation scale Q_s in Au nucleus and the line illustrating the range in x and Q^2 covered with hadrons at rapidity $\eta = 4$.

The actual calculations in saturation physics start with the classical gluon fields (as gluons dominate quarks at small-x) [173–179], which are then evolved using the nonlinear small-x BK/JIMWLK evolution equations. [180, 181, 181–189] The saturation region can be well-approximated by the following formula: $Q_s^2 \sim (A/x)^{1/3}$. Note again that at small enough x the saturation scale provides an IR cutoff, justifying the use of perturbative calculations. This is important beyond saturation physics, and may help us better understand small-x evolution of the TMDs.

While the evidence in favor of non-linear QCD effects has been gleaned from the data collected at HERA, RHIC and the LHC, the case for saturation is not sealed and alternative explanations of these data exist. The EIC is slated to provide more definitive evidence for saturation physics. [190] To help the EIC complete the case for saturation, it is mandatory to generate higher-precision measurements in p+Au collisions at RHIC. These higher-precision measurements would significantly enhance the discovery potential of the EIC as they would enable a stringent test of universality of the CGC. We stress again that a lot of theoretical predictions and results in the earlier Sections of this document would greatly benefit from this physics: the small-x evolution of TMDs in a longitudinally or transversely polarized proton, or in an unpolarized proton, can all be derived in the saturation framework [191] in a theoretically better-controlled way due to the presence of Q_s. Hence non-linear QCD effects may help us understand both the quark and gluon helicity PDFs as well as the Sivers and Boer-Mulders functions.

The saturation momentum is predicted to grow approximately like a power of energy, $Q_s^2 \sim E^{\lambda/2}$ with $\lambda \sim 0.2 - 0.3$, as phase space for small-x (quantum) evolution opens up. The saturation scale is also expected to grow in proportion to the valence charge density at the onset of small-x quantum evolution. Hence, the saturation scale of a large nucleus should exceed that of a nucleon by a factor of $A^{1/3} \sim 5$ (on average over impact parameters). RHIC

is capable of running p+A collisions for different nuclei to check this dependence on the mass number. This avoids potential issues with dividing, e.g., p–Pb collisions in N_{part} classes . [192] Figure 60 shows the kinematic coverage in the $x - Q^2$ plane for p+A collisions at RHIC, along with previous e+A measurements and the kinematic reach of an EIC. The saturation scale for a Au nucleus is also shown. To access at RHIC a kinematic regime sensitive to non-linear QCD effects with $Q^2 > 1$ GeV^2 requires measurements at forward rapidities. For these kinematics the saturation scale is moderate, on the order of a few GeV^2, so measurements sensitive to non-linear QCD effects are by necessity limited to semi-hard processes.

Until today the golden channel at RHIC to observe strong hints of non-linear QCD effects has been the angular dependence of two-particle correlations, because it is an essential tool for testing the underlying QCD dynamics. [192] In forward-forward correlations facing the $p(d)$ beam direction one selects a large-x parton in the $p(d)$ interacting with a low-x parton in the nucleus. For $x < 0.01$ the low-x parton will be back-scattered in the direction of the large-x parton. Due to the abundance of gluons at small x, the backwards-scattered partons are dominantly gluons, while the large-x partons from the $p(d)$ are dominantly quarks. The measurements of di-hadron correlations by STAR and PHENIX [193, 194], have been compared with theoretical expectations using the CGC framework based on a fixed saturation scale Q_s and considering valence quarks in the deuteron scattering off low-x gluons in the nucleus with impact parameter $b = 0$. [195, 196] Alternative calculations [197] based on both initial and final state multiple scattering that determine the strength of this transverse momentum imbalance, in which the suppression of the cross-section in d+Au collisions arises from cold nuclear matter energy loss and coherent power corrections, have also been very successful to describe the data.

The p+A Run-15 at RHIC has provided unique opportunities to study this channel in more detail at STAR. The high delivered integrated luminosities allow one to vary the trigger and associated particle p_T from low to high values and thus crossing the saturation boundary as shown in Fig. 60 and reinstate the correlations for central p+A collisions for forward-forward π^0's. Studying di-hadron correlations in p+A collisions instead of d+A collisions has a further advantage. In reference [198], the authors point out that the contributions from double-parton interactions to the cross-sections for $dA \rightarrow \pi^0\pi^0 X$ are not negligible. They find that such contributions become important at large forward rapidities, and especially in the case of d+A scattering. Figure 61 left shows the relative area of back-to-back di-π^0 correlations in p+Al and p+Au collisions relative to p+p collisions. The results show suppression with increasing A, and an enhanced suppression that scales as $A^{1/3}$. This behavior is consistent with different calculations based on the CGC formalism and is a clear hint of non-linear effects. A comparison between p+p (Run-15), p+Au (Run-15), and d+Au (Run-16) collisions can help provide insight into the contributions from multiple parton scattering [198]. Figure 61 shows the invariant mass spectra for final p+p and p+Au results and the preliminary d+Au. It is clear from the comparison that there is significantly more background in the the d+Au data than the p+p and p+Au data. This combinatoric correlation dominates in d+Au collisions, which makes it very challenging to identify the signal correlation. The forward di-π^0 correlation measurement favors the cleaner p+A col-

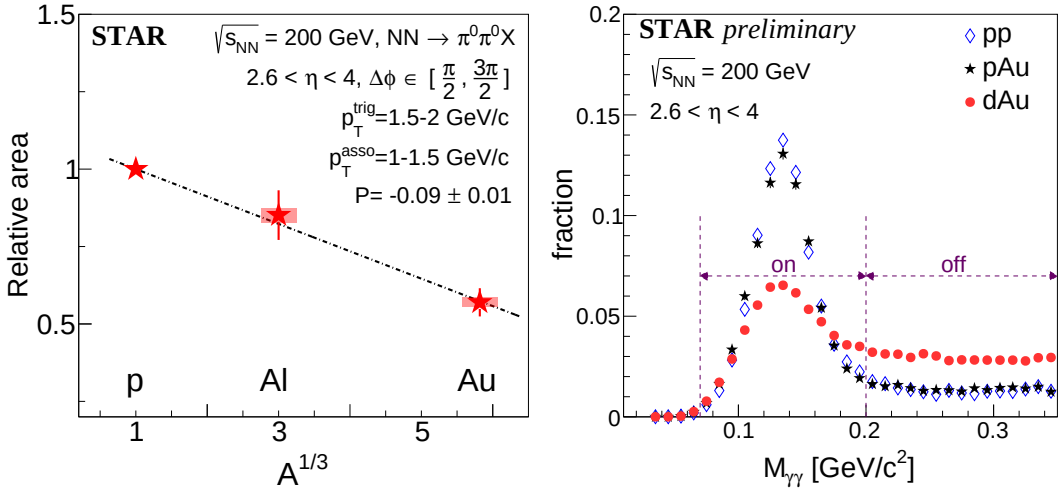

Figure 61: Left: Relative area of back-to-back di-π^0 correlations at forward pseudorapidities ($2.6 < \eta < 4.0$) in p+Au and p+Al relative to p+p collisions for $p_T^{\rm trig}$ = 1.5−2 GeV/c and $p_T^{\rm asso}$ = 1−1.5 GeV/c. The vertical bars for the Al and Au ratios indicate the statistical uncertainties and the vertical bands indicate the systematic uncertainties. The data points are fitted by a linear function, whose slope (P) is found to be -0.09 ± 0.01. Right: The invariant mass spectra for di-photon in p+p p+Au and d+Au. The on mass range is chosen as 0.07-0.2 GeV/c^2, the off mass range is 0.2-0.35 GeV/c^2.

lisions rather than d+A collisions. Run-24 will be able to measure di-hadron correlations taking advantage of the cleaner p+Au collisions and the extended pseudorapidity reach of the Forward Upgrade detectors.

The statistical projections of di-π^0 and di-$h^{\pm}$ measurements for Run-24 p+p and p+Au data are shown in Fig. 63 with various assumptions regarding Run-24. Five scenarios for Run-24 were considered, with the details shown in Tab. 5. Note that we assume set-up time of 5.5 weeks, based on the recent communication with CAD and the assumption that tuning the rotators for radial polarization will require 0.5 weeks. We considered three conditions for the total Cyro weeks as 28, 24, and 20. For 28 Cyro weeks we split p+p and p+Au data taking into three conditions – S0: 12 and 10.5 weeks for p+p and p+Au to provide equal nucleon-nucleon luminosities, S1: 11.3 and 11.2 weeks for p+p and p+Au with the same run times for the two collision systems, and S2: 17.5 and 5 weeks for p+p and p+Au as requested during the last PAC meeting. The other two scenarios include 2 conditions – S3: equal nucleon-nucleon luminosities for 24 Cryo weeks, and S4: equal nucleon-nucleon luminosities for 20 Cryo weeks.

For each scenario, the estimated luminosity for p+p and p+Au can be found in Fig. 62. The luminosity per week for Run-24 p+p and p+Au comes from the latest projection from CAD, which is the averaged number between maximum and minimum luminosity per week. According to CAD's luminosity guidance for Run-24, the maximum luminosity per week for p+p is 25 pb^{-1} and the minimum luminosity per week is 17 pb^{-1}; the maximum luminosity per week for p+Au is 0.14 pb^{-1} and the minimum luminosity per week is 0.1 pb^{-1}, which

Table 5: Five scenarios for the data taking during Run-24:

Scenarios	Cyro weeks [w]	Set-up [w]	p+p [w]	p+A [w]	Details
S0	28	5.5	12	10.5	equal nucleon-nucleon luminosity
S1	28	5.5	11.3	11.2	equal time
S2	28	5.5	17.5	5	request from the last PAC
S3	24	5.5	9.5	9	equal nucleon-nucleon luminosity
S4	20	5.5	7.5	7	equal nucleon-nucleon luminosity

	p+p			p+Au		
Year	2015	2024		2015	2024	
$\sqrt{s}$ [GeV]	200	200		200	200	
Lumi/week [$\frac{pb^{-1}}{week}$]	-	(25+17)/2 = 21		-	(0.14+0.1)/2 = 0.12	
Num of weeks Integrated Lumi. [pb^{-1}]	Num of weeks 10.9 Integrated Lumi. [pb^{-1}] 105	Num of weeks S0: 12 S1: 11.3 S2: 17.5 S3: 9.5 S4: 7.5	Integrated Lumi. [pb^{-1}] S0: 142 S1: 132 S2: 216 S3: 108 S4: 81	Num of weeks 5.1 Integrated Lumi. [pb^{-1}] 0.45	Num of weeks S0: 10.5 S1: 11.2 S2: 5 S3: 9 S4: 7	Integrated Lumi. [pb^{-1}] S0: 0.69 S1: 0.75 S2: 0.27 S3: 0.58 S4: 0.42

Figure 62: Estimated luminosity of p+p and p+A in Run-24.

indicates the performance is going to be worse than Run-15. Especially for S2, which was requested to be considered by the last PAC meeting, the integrated luminosity for p+Au is 0.27 pb^{-1} which is only 60% of the luminosity we collected in Run-15.

In Fig. 63, the back-to-back di-π^0 and di-$h^{\pm}$ yields in p+Au with respect to p+p collisions are presented as a function of the associated particle's p_T. The black open circles represent the data points published with Run-15 data with only statistical errors [41]. The rest are the projected statistical errors for Run-24, with the central value located on the fitting function from the Run-15 data. For the di-π^0 channel, S0 and S1 show similar performance in reducing the statistical uncertainty 13%-14% compared to Run-15 results. S2 with only 5 weeks of p+Au running indicates a 2% increase of the statistical error compared to Run-15, which leads no improvement for Run-24 data. The conclusion is worse for those analyses that only depend on p+Au data, without comparison to p+p such as the GPD and Collins asymmetry measurements. If the p+Au luminosity is reduced to 0.27 pb^{-1}, we cannot achieve our physics goals for these analyses. So, we strongly disfavor scenario S2 with only 5 weeks for p+Au running for Run-24.

Figure 63(right) presents the projected statistical errors for the di-$h^{\pm}$ channel, which is the golden channel to quantitatively probe gluon saturation. The forward tracking system enables us to detect charged hadrons in the forward region ($2.6 < \eta < 4.0$) at low p_T (down

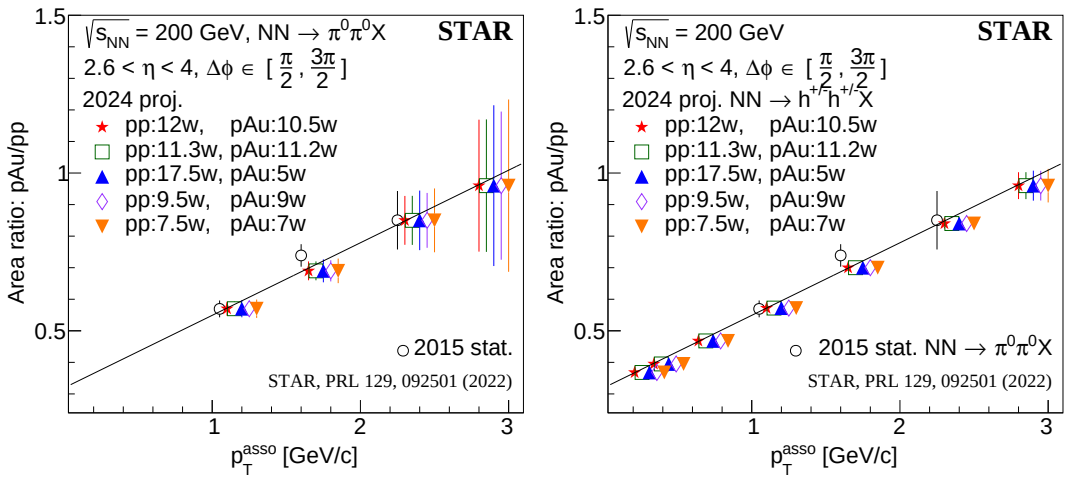

Figure 63: Relative area of back-to-back di-π^0 (Left) and di-$h^{\pm}$ (Right) correlations at forward pseudorapidities ($2.6 < \eta < 4.0$) in p+Au with respect to p+p collisions for Run-24 data, in comparison with the published Run-15 di-π^0 results. The black open circles represent the published Run-15 di-π^0 data points with statistical errors only. The rest of the data points come from the projected statistical errors under different data-taking assumptions (Tab. 5) for Run-24.

to 0.2 GeV/c). Lower p_T enables us to probe the lower x region in the phase space, where saturation is predicted to be stronger. So, with this channel, we are expecting to observe the largest suppression of the back-to-back di-$h^{\pm}$ correlations in p+Au with respect to p+p collisions at RHIC energy. With enough statistics for Run-24, STAR can further investigate the nonlinear QCD phenomena in the region closer to gluon saturation, where Run-15 data cannot access. In Fig. 63(right), the statistical errors are estimated through a different way compared to the di-π^0 channel, as for low p_T (< 1 GeV/c) we will use min-bias triggered data and for high p_T (> 1 GeV/c) we will use high-p_T data triggered by the forward calorimeters. Considering the prescale, we used the estimated number of events for Run-24 compared with the number of events recorded in Run-15 for both p+p and p+Au collisions, to calculate the statistical errors of Run-24. The number of events for Run-24 is

$$N_{evt} = \text{event rate} \times N_{week} \times N_{day} \times N_{min} \times N_{sec} \times t_{up} \times t_{live} \times eff_{trk} \quad (1)$$

where the recorded min-bias event rate is assumed to be 500 Hz, $t_{up} = 50\%$, $t_{live} = 70\%$, and the tracking efficiency is $eff_{trk} = 90\%$. Since the yield of di-$h^{\pm}$ pairs is much larger than di-π^0, overall we will obtain much smaller statistical errors for the Run-24 di-$h^{\pm}$ channel compared to di-π^0 results from Run-15.

It is important to note that for the measurements to date in $p(d)$+A collisions both initial and final states interact strongly, leading to severe complications in the theoretical treatment (see [200, 201], and references therein). As described in detail in the Section above, in p+Au collisions, these complications can be ameliorated by removing the strong interaction from the final state, by using photons and Drell-Yan electrons. The Run-15 p+Au run will for the first time provide data on R_{pA} for direct photons and therefore allow one to test CGC based

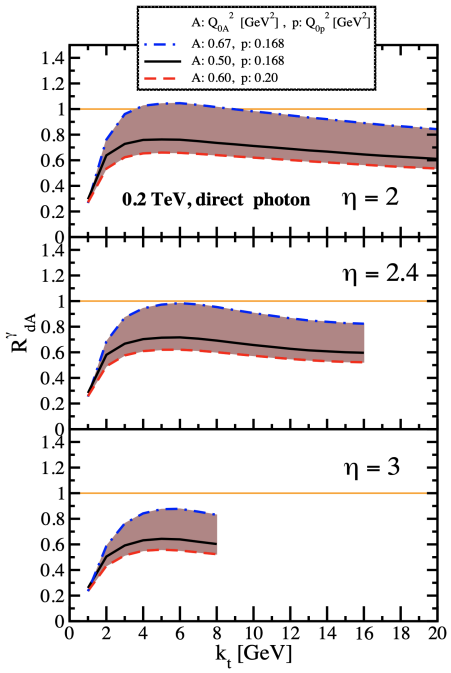

Figure 64: Nuclear modification factor for direct photon production in $p(d)$+A collisions at various rapidities at RHIC $\sqrt{s} = 200$ GeV. The curves are the results obtained from Eq. (12) in Ref. [199] and the solution to rcBK equation using different initial saturation scales for a proton Q_{op} and a nucleus Q_{oA}. The band shows our theoretical uncertainties arising from allowing a variation of the initial saturation scale of the nucleus in a range consistent with previous studies of DIS structure functions as well as particle production in minimum-bias p+p, p+A and A+A collisions in the CGC formalism, see Ref. [199] for details.

predictions on this observable as depicted in Fig. 64 (taken from Ref. [199]). The higher delivered integrated luminosity for the upcoming p+Au Run-24 together with the Forward Upgrade will enable one to study more luminosity hungry processes and/or complementary probes to the di-π^0 correlations, i.e. di-hadron correlations for charged hadrons, photon-jet, photon-hadron and di-jet correlations, which will allow a rigorous test of the calculation in the CGC formalism. It is important to stress that the comparison of these correlation probes in p+p and p+Au requires approximately equal nucleon-nucleon luminosities for these two collision systems for optimal measurements. It is noted that these results are crucial for the equivalent measurements at an EIC, which are planned at close to identical kinematics, because only if non-linear effects are seen with different complementary probes, i.e., $e + A$ and $p + A$, one can claim a discovery of saturation effects and their universality.

We use direct photon plus jet (direct γ+jet) events as an example channel to indicate what can be done in Run-24. These events are dominantly produced through the gluon Compton scattering process, $g + q \rightarrow \gamma + q$, and are sensitive to the gluon densities of the nucleon and nuclei in p+p and p+A collisions. Through measurements of the azimuthal correlations in p+A collisions for direct γ+jet production, one can study non-linear effects at small-x. Unlike di-jet production that is governed by both the Weizsäcker-Williams and dipole gluon densities, direct γ+jet production only accesses the dipole gluon density, which is better understood theoretically. [199, 202] On the other hand, direct γ+jet production is experimentally more challenging due to its small cross-section and large background contribution from di-jet events in which photons from fragmentation or hadron decay could be misidentified as direct photons. The feasibility to perform direct γ+jet measurements with the Forward Upgrade in unpolarized p+p and p+Au collisions at $\sqrt{s_{\rm NN}} = 200$ GeV has been

studied. PYTHIA-8.189 [203] was used to produce direct γ+jet and di-jet events. In order to suppress the di-jet background, the leading photon and jet are required to be balanced in transverse momentum, $|\phi^{\gamma} - \phi^{jet}| > 2\pi/3$ and $0.5 < p_T^{\gamma}/p_T^{jet} < 2$. Both the photon and jet have to be in the forward acceptance $1.3 < \eta < 4.0$ with $p_T > 3.2$ GeV/c in 200 GeV p+p collisions. The photon needs to be isolated from other particle activities by requiring the fraction of electromagnetic energy deposition in the cone of $\Delta R = 0.1$ around the photon is more than 95% of that in the cone of $\Delta R = 0.5$. Jets are reconstructed by an anti-k_T algorithm with $\Delta R = 0.5$. After applying these selection cuts, the signal-to-background ratio is around 3:1 [204]. The expected number of selected direct γ+jet events is around ~ 0.9M at $\sqrt{s_{\rm NN}} = 200$ GeV in p+Au collisions for the proposed Run-24. We conclude that a measurement of direct photon-jet correlation from p+Au collisions is feasible, which is sensitive to the gluon density in $0.001 < x < 0.005$ in the Au nucleus where parton saturation is expected.

There are other potential opportunities with the upcoming p+Au and p+p runs that can provide a clean baseline for studying the gluon saturation phenomena in Au+Au using ultra-peripheral collisions (UPC). For example, one of the most powerful measurements proposed at the EIC for discovery of gluon saturation is to look at the double ratio between a heavy nucleus and proton in terms of diffractive processes, see details in Sec. 3.2. With STAR Run-24, the p+Au UPC (also applies to p+p UPC) may provide two important measurements, e.g., exclusive and inclusive J/ψ production off the proton target, which will serve as a baseline for no saturation. The same measurement will be performed in Au+Au UPC with Run-20 and 25. The different system comparison with STAR data may provide strong evidence for gluon saturation.

2.2.2 The Final State-Fragmentation Functions

Fragmentation functions: In spite of the remarkable phenomenological successes of QCD, a quantitative understanding of the hadronization process is still one of the great challenges for the theory. Hadronization describes the transition of a quark or gluon into a final state hadron. It is a poorly understood process even in elementary collisions. RHIC's unique versatility will make it possible to study hadronization in vacuum and in the nuclear medium, and additionally with polarized beams (see Sect. 2.1 for the latter).

It has long been recognized that the hadron distributions within jets produced in p+p collisions are closely related to the fragmentation functions that have typically been measured in e^+e^- collisions and SIDIS. The key feature of this type of observable is the possibility to determine the relevant momentum fraction z experimentally as the ratio of the hadron to the jet transverse momentum. Recently [205] a quantitative relationship has been derived in a form that enables measurements of identified hadrons in jets in p+p collisions to be included in fragmentation function fits on an equal footing with e^+e^- and SIDIS data. Furthermore, hadrons in p+p jets provide unique access to the gluon fragmentation function, which is poorly determined in current fits [206], in part due to some tension found in the inclusive high p_T pion yields measured by the PHENIX and ALICE collaborations. Here, the proposed measurements can provide valuable new insight into the nature of this discrepancy.

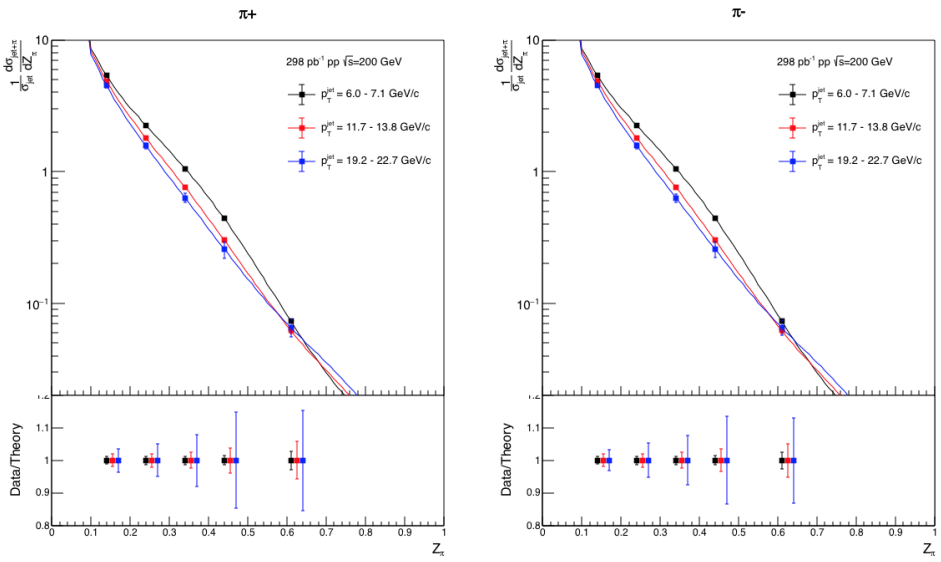

Figure 65: Anticipated precision for identified π^+(left) and π^-(right) within jets at $|\eta| < 0.4$ in 200 GeV p+p collisions for three representative jet p_T bins. The data points are plotted on theoretical predictions based on the DSSV14 pion fragmentation functions [205, 206]. Kaons and (anti)protons will also be measured, over the range from $z < 0.5$ at low jet p_T to $z < 0.2$ at high jet p_T, with uncertainties a factor of ∼3 larger than those for pions.

This development motivated STAR to initiate a program of identified particle fragmentation function measurements using p+p jet data at 200 and 500 GeV from Run-11, Run-12, and Run-15. Figure 65 shows the precision that is anticipated for identified π^+ and π^- in 200 GeV p+p collisions for three representative jet p_T bins after the existing data from Run-12 and Run-15 are combined with future 200 GeV p+p data from Run-24. Identified kaon and (anti)proton yields will also be obtained, with somewhat less precision, over a more limited range of hadron z. Once the Run-17 data are fully analyzed, the uncertainties for 510 GeV p+p collisions will be comparable to that shown in Fig. 65 at high jet p_T, and a factor of ∼ 2 larger than shown in Fig. 65 at low jet p_T. Identified hadron yields will also be measured multi-dimensionally vs. j_T, z, and jet p_T, which will provide important input for unpolarized TMD fits.

Data from the HERMES experiment [152, 154, 207] have shown that production rates of identified hadrons in semi-inclusive deep inelastic $e + A$ scattering differ from those in ep scattering. These differences cannot be explained by nuclear PDFs, as nuclear effects of strong interactions in the initial state should cancel in this observable. Only the inclusion of nuclear effects in the hadronization process allows theory to reproduce all of the dependencies (z, x, and Q^2) of R_{eA} seen in SIDIS, as shown in Fig. 66.

It is critical to see if these hadronization effects in cold nuclear matter persist at the higher $\sqrt{s}$ and Q^2 accessed at RHIC and EIC – both to probe the underlying mechanism, which is not understood currently, and to explore its possible universality. The combination of p+p jet data from RHIC and future SIDIS data from EIC will also provide a much

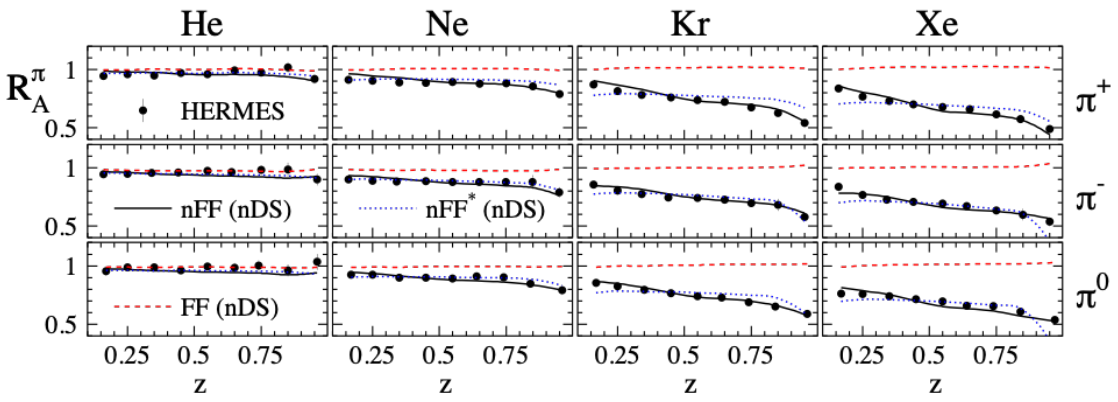

Figure 66: R_{eA} in SIDIS for different nuclei in bins of z as measured by HERMES [152, 154, 207]. The solid lines correspond to the results using effective nuclear FF [159] and the nDS medium modified parton densities [208]. The red dashed lines are estimates assuming the nDS medium modified PDFs but standard DSS vacuum FFs [209, 210] and indicate that nPDFs are insufficient to explain the data

clearer picture of modified gluon hadronization than will be possible with EIC data alone. Using the Run-15 200 GeV p+Au data, STAR will be able to make a first opportunistic measurement of these hadron-jet fragmentation functions in nuclei, but the precision will be limited. Additional p+p and p+Au data will be needed in Run-24 in order to provide a sensitive test for universality, as shown in Fig. 67.

2.2.3 QGP Droplet Substructure

Toroidal vorticity: In addition to cold QCD effects, a high-statistics measurement of p+Au collisions will be highly valuable to explore novel fluid configurations that have recently been predicted [211]. In particular, the data is needed to discover vortex rings or tubes at midrapidity, included by shear in the asymmetric initial state.

It has been suggested [212] that p+A collisions at RHIC form the "smallest QGP droplets." This claim is often based on anisotropic yields, which resemble those from A+A collisions that are attributed to hydrodynamic collective flow. Indeed, with well-chosen initial conditions and tuned parameters, three-dimensional viscous hydro calculations can reproduce the measured anisotropies from small, asymmetric collisions [213] at RHIC. However, a claim of QGP formation in such small systems would be much more compelling if it were based on more than one observable, especially since other, non-hydrodynamic mechanisms contribute to v_n in these systems, e.g. [214].

As Helmholtz observed more than 150 years ago [215], vortex rings are ubiquitous in hydrodynamic systems subject to initial conditions characterized by a "push down the middle," such as a smoker blowing a ring. Clear observation of this novel phenomenon would constitute important evidence that the smallest systems at RHIC truly do form a fluid system.

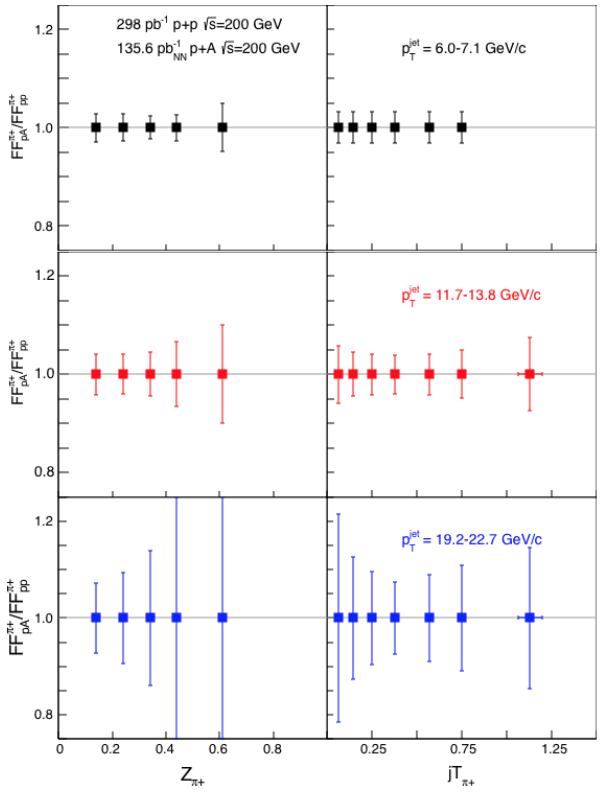

Figure 67: Anticipated precision for measurements of π^+ fragmentation functions in p+A,p+p at $|\eta| < 0.4$ vs. z and j_T in Run-24 for three representative jet $p_{\rm T}$ bins. Uncertainties for π^- will be similar to those shown here for π^+, while those for kaons and (anti)protons will be a factor of ~ 3 larger. Note that, to be species independent, the nucleon-nucleon equivalent luminosity is specified for p+Au.

This signature probes aspects of particular and fundamental importance to the RHIC program, as well. The vortex ring structure is sensitive to the degree and timescale of equilibration in these small systems, as well as the extreme shear fields in the initial state [216]. Fluctuations in the vortical fields probe hydrodynamic structures at the smallest possible scales, as they arise directly from rotational derivatives in the "surface" of the flux tube.

The experimental signature of toroidal vortex structure is the so-called "ring parameter" [211]:

$$\overline{\mathcal{R}}^z_\Lambda \equiv \left\langle \frac{\vec{S}'_\Lambda \cdot (\hat{z} \times \vec{p}'_\Lambda)}{|\hat{z} \times \vec{p}'_\Lambda|} \right\rangle, \tag{2}$$

where $+\hat{z}$ is the direction of the proton beam, and the average is taken over all particles and events. This is the average polarization relative to the hyperon production plane. Rings will be most clear for central collisions, but the detailed centrality dependence of the effect is currently under investigation [216]. We focus on 0-10% centrality.

Figure 68 shows $\overline{\mathcal{R}}^z_\Lambda$ calculated [211] for completely central Au+Au and p+Au collisions at $\sqrt{s_{NN}} = 200$ GeV. Calculations were done with MUSIC [217], a three-dimensional relativistic viscous hydrodynamics simulation that locally conserves baryon number, and calculation of the thermal vorticity along the freezeout hypersurface.

Initial condition (a) corresponds to the usual Bjorken "boost-invariant" flow profile used in most A+A simulations, whereas condition (b) features strong shear fields generated in

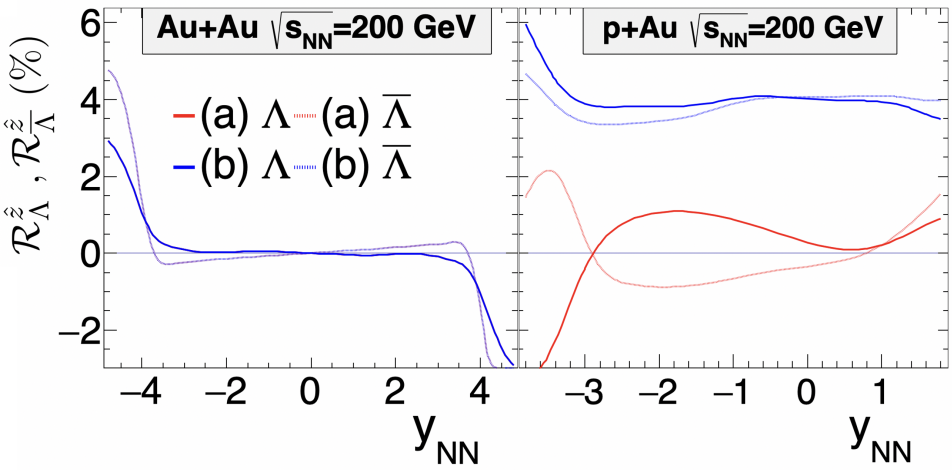

Figure 68: The "ring parameter" $\overline{\mathcal{R}}^{z}_{\Lambda}$ for $b = 0$ Au+Au and p+Au collisions at top RHIC energy. Blue (red) curves correspond to a scenario in which a toroidal vortex structure is (is not) generated by shear forces in the initial state. Solid (dashed) curves correspond to Λ ($\overline{\Lambda}$); note that baryon current is locally conserved in these collisions, so small differences between Λ and $\overline{\Lambda}$ are expected at finite baryon density. From [211].

the initial condition, leading to observable vortex toroids. Both initial conditions generate identical $dN/d\eta$ distributions, but the latter is argued [211] to be more natural.

The statistical requirement to discover these toroidal vortex structures may be estimated by STAR's previous hyperon polarization measurements. The uncertainty on global polarization measurements $\delta\overline{P}_{\Lambda} \propto N_{\Lambda}^{-1/2} \cdot R_{\rm EP}^{-1}$, where N_{Λ} is the total number of hyperons in the analysis, and $R_{\rm EP}$ is the event plane resolution [218]. Because there is no event plane involved in the production plane polarization, on the other hand, the uncertainty on the ring observable goes as $\delta\overline{\mathcal{R}}^{z}_{\Lambda} \propto N_{\Lambda}^{-1/2}$. For the same-magnitude signal, then, $\overline{\mathcal{R}}^{z}_{\Lambda}$ enjoys an effective $R_{\rm EP}^{-2}$ "statistical advantage" over $\overline{P}_{\Lambda}$. Since STAR measured [72] $\overline{P}_{\Lambda} \approx 1\%$ at $\sqrt{s_{NN}} = 11$ GeV with 3.5σ significance, with the same number of hyperons in the analysis, we should be able to measure $\overline{\mathcal{R}}^{z}_{\Lambda} \sim 1\%$ with 7σ significance. The 11-GeV analysis involved 6M Λs, and we estimate 0.02 Λs per central $(0-10\%)$ p+Au collision at $\sqrt{s_{NN}} = 200$ GeV. Therefore, the 7σ measurement will require $6M/0.02 = 300M$ central p+Au collisions.

Also crucial to this measurement is that data must be collected with both polarities of STAR's magnetic field. This is because of large and highly nontrivial decay-topology-dependent detector effects, which will give a "false" production plane polarization signal. The magnitude of the artifact is an order of magnitude larger than the physical signal of interest, and it is highly sensitive to momentum, PID, and topological cuts. We could not feel confident applying such large and complex "correction factors" based solely on detector simulations, if we claim a completely novel signature with far-reaching physical implications. Fortunately, the sign of this artifact flips with the magnetic field polarity.

Figure 69 illustrates these points. Au+Au collisions at $\sqrt{s_{NN}} = 27$ GeV were recorded by STAR using opposite polarities of the magnetic field. For Λs, the quantity $\hat{p}_{\rm p} \cdot (\hat{p}_{\Lambda} \times \hat{z})$,

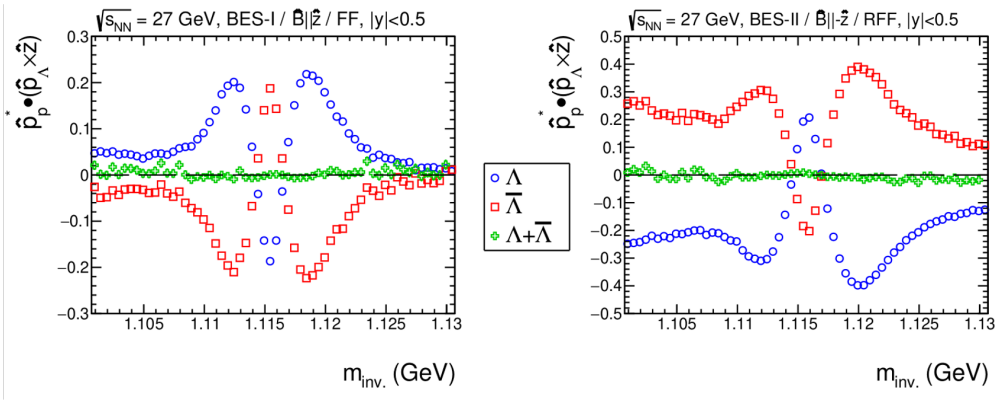

Figure 69: Production-plane polarization (modulo an overall scaling by $\frac{8\pi}{\alpha_\Lambda}$) for Λ (blue) and $\overline{\Lambda}$ (red) candidates, as a function of invariant mass. The data comes from STAR measurements of Au+Au collisions at $\sqrt{s_{NN}}$ in the BES-I (left) and BES-II (right) campaigns. STAR's solenoidal magnetic field was directed to the West and East, respectively, for these two datasets. For the BES-I data, hyperon candidates were identified with "standard" topological cuts, whereas the candidates shown in BES-II were identified using the new KFParticle package.

where $\hat{p}_{\rm p}$ is the daughter proton momentum, is proportional to $\overline{\mathcal{R}}^z_\Lambda$. For $\overline{\Lambda}$s, the quantity $\hat{p}_{\overline{\rm p}} \cdot (\hat{p}_{\overline{\Lambda}} \times \hat{z})$, where $\hat{p}_{\rm p}$ is the daughter proton momentum, is proportional to $-\overline{\mathcal{R}}^z_{\overline{\Lambda}}$.

A rapidity cut symmetric about midrapidity ($|y| < 0.5$) was used; for a symmetric system, the physical production plane polarization vanishes by symmetry– any nonvanishing value results purely from topologically-sensitive efficiency effects.

Consider first the Λ curve from BES-I, the blue points in the left panel. Clearly, the effect has a nontrivial dependence on invariant mass; note even the asymmetry about $m_{\rm inv} = m_\Lambda$. Equally clearly, it is large, corresponding to values $\overline{\mathcal{R}}^z_\Lambda = \frac{8}{\pi\alpha_\Lambda}\hat{p}_{\rm p} \cdot (\hat{p}_\Lambda \times \hat{z}) \approx 50\%$, an order of magnitude larger than the predicted value of physical effect of interest.

In terms of topologically-sensitive efficiency effects, substituting $\Lambda \to \overline{\Lambda}$ is equivalent to flipping the sign of the magnetic field. The red datapoints in the left panel are a perfect mirror image to the blue points in that panel, as indicated by the vanishing green points, which are the sum. Further note that naive interpretation of the data in the left panel would suggest that the vortical ring values for the hyperons and antihyperons ($\overline{\mathcal{R}}^z_\Lambda$ and $\overline{\mathcal{R}}^z_{\overline{\Lambda}}$) would be identical in magnitude and sign.

The right panel shows the same colliding system, but measured during the BES-II campaign with the opposite orientation of STAR's magnetic field. As expected from the above discussion, $\overline{\mathcal{R}}^z_\Lambda = -\overline{\mathcal{R}}^z_{\overline{\Lambda}}$. The shape and magnitude of the artifact is different from the BES-I case, however, because a different method has been used to identify hyperon candidates. This illustrates the cut-dependence of the artifact.

In short, for reliable extraction of the ring vorticity measure, STAR must measure p+Au collisions with both field orientations, in order to cancel the complex efficiency-driven artifacts. Finally, we point out that this sort of cancellation is not unique to this observable. Indeed, there is an analogous effect for the global polarization, which precludes extracting the *first*-order azimuthal dependence of $\overline{P}_\Lambda$; there, the artifact is of order 100%, compared

to the physical and measured value of $\sim 2\%$ [219].

For symmetric collisions (e.g. Au+Au), the quantity $\overline{\mathcal{R}}^z_\Lambda$ must be antisymmetric about midrapidity. However, at very forward/backward rapidities, circular vorticity has been reported in hydrodynamic [220–224] and transport [225–231] calculations. This effect, also visible in the left panel in figure 68, arises from strong temperature gradients and edge effects in three-dimensional space. It is of very different origin from the ring voriticity of interest here.

Finally, production plane polarization at large x_F has been observed (primarily) in p+p and (in some) p+A collisions [232–237] at energies up to $\sqrt{s_{NN}} = 41$ GeV. This effect, which is believed to be completely hadronic in origin but remains incompletely understood, is distinguishable from the hydrodynamically-driven ring vorticity discussed here by its rapidity dependence, which is strongly forward-focused, as well as the fact that $\overline{\Lambda}$s do not display production plane polarization at all. Thus, in addition to double-checking topologically-dependent efficiency artifacts (discussed above), it is important that STAR will measure the effect both for hyperons and antihyperons to distinguish hydrodynamic from hadronic phenomena.

3 Run-25 Requests for Au+Au Collisions at 200 GeV

3.1 Explore the Microstructure of the QGP

The completion of RHIC's scientific mission involves two central goals: (i) mapping out the QCD phase diagram, and (ii) understanding the inner workings of the QGP by resolving its properties at varying length scales [238]. The former goal is addressed by the BES-II/FXT program. For the latter goal, the complementarity of the RHIC and LHC facilities is scientifically as essential as having more than one experiment independently studying the microstructure of the QGP at RHIC. With several years of operating the iTPC upgrade and commissioning and operation of the forward detectors in Run-22, the STAR collaboration is in an excellent position to take advantage of its vastly improved detection capabilities. Combining this with the substantial increase in beam luminosities in Run-23 and Run-25, RHIC is uniquely positioned to fully engage in a detailed exploration of the QGP's microstructure.

Through careful discussions in its physics working groups, the STAR collaboration has identified a number of topics that together with the expected sPHENIX results in 2023-25 make up a comprehensive study of the QGP microstructure, and successfully complete RHIC's scientific mission. In this section, we present a selection of those topics that will take full advantage of both STAR and RHIC's unique capabilities and address the following important questions about the inner workings of the QGP. We enumerate questions below that follow the chronology of an event; from questions addressing the QCD vacuum and the initial conditions, to the formation, temperature, and properties of the QGP, to the quenching of jets in said QGP, to its phase transition back to hadronic matter, and finally to the interactions of those final state hadrons.

1. **What is the nature of the 3-dimensional initial state at RHIC energies?** How does a twist of the event shape break longitudinal boost invariance and decorrelate the direction of an event plane? Can the J/ψ v_1 tell us about the initial tilt angle of the source? Can the Wigner distributions of photon tell us about the magnetic field effects in the initial state?

2. **What is the precise temperature dependence of the shear (η/s) and bulk (ζ/s) viscosities?** Can combining precision flow results at different beam energies help determine the temperature dependence of the viscosity?

3. **What can we learn about confinement from charmonium measurements?** Can the elliptic flow of J/ψ tell us whether charmed quarks are deconfined?

4. **What is the temperature of the medium?** Do the Υ and ψ(2S) melt at RHIC energies, and if so can their suppression be used to determine the temperature of the QGP? The thermally produced dileptons are also sensitive to the medium temperature. Does their temperature agree with that found via quarkonium suppression?

5. **What are the electrical, magnetic, and chiral properties of the medium?** How is global vorticity transferred to the spin angular momentum of particles on such short time scales? And, how can the global polarization of hyperons be reconciled with the spin alignment of vector mesons? Can dilepton production in the low mass region tell us about the electrical conductivity of the plasma? Can clear observation of the ρ^0-a_1 mixing tell us about the degrees of freedom therefore the chirality of the plasma? Is there local parity violation and chiral magnetic effect?

6. **What are the underlying mechanisms of jet quenching at RHIC energies?** What do jets tell us about the microscopic structure of the QGP as a function of resolution scale?

7. **What is the precise nature of the transition near $\mu_B = 0$?** Where does the sign-change of the susceptibility ratio χ_6^B/χ_2^B take place?

8. **What can we learn about the strong interaction?** Can correlation functions between baryons emitted at the surface of the fireball tell us how they interact in free space.

The impetus for running STAR during Run-23 and Run-25 for Au+Au 200 GeV collisions comes from gains via: i) enhanced statistics, ii) extended acceptance, and iii) low material budget.

With the successful upgrade of the DAQ system, STAR is able to record minimum bias events at a rate about factor of 2 faster than before. The increased DAQ speed can also facilitate sampling a large luminosity for rare probes. The projected statistics for both minimum bias events and sampled luminosity are listed in Table 1. In order to achieve a balance between those physics observables which are acquired with a minimum bias trigger (and negatively impacted by excess tracks in the TPC) and the rare probes which require specialized triggers (Barrel High Tower (BHT), dimuon) and the highest luminosity which can be accommodated with the TPC, the collaboration will optimize the interaction rates at STAR by allocating high and low luminosity periods. CAD can offset the beam to independently control the maximum luminosity in each IR. Such separation will allow us to collect clean, low pile-up, minimum bias events, with improved tracking efficiency, which is expected to especially benefit many of the proposed correlation analyses. The dedicated high luminosity period will enable a significant improvement in the precision and kinematic reach of current STAR measurements, and making important measurements that are yet more differential possible.

The extended acceptance is important for analyses that probe the η dependencies and especially so for those that require correlations between particles (CME, $v_2(\eta)$, $r_n(\eta)$, and $P_H(\eta)$). With the BES-II upgrades and the recent forward upgrade, STAR's acceptance spans from mid-rapidity to beam rapidity. STAR's BES-II upgrade sub-systems comprised of the inner Time Projection Chamber (iTPC, $|\eta| < 1.5$), endcap Time Of Flight (eTOF, $1 < \eta < 1.5$) and Event Plane Detectors (EPDs, $2.1 < |\eta| < 5.1$), that are all fully operational since the beginning of 2019 [218, 239, 240]. In what follows, we will refer to the

combination of the existing TPC ($|\eta| < 1$) and the iTPC upgrade as iTPC ($|\eta| < 1.5$) for simplicity. The STAR Collaboration has also commissioned and operated a forward rapidity ($2.5 < \eta < 4$) upgrade that includes charged particle tracking and electromagnetic/hadronic calorimetry [241]. Charged particle tracking is achieved using a combination of silicon detectors and small strip thin gap chamber detectors. The combination of these two tracking detectors is referred to as the forward tracking system (FTS). The FTS is capable of discriminating the hadron charge sign. It can measure p_{T} of charged particles in the range of $0.2 < p_{\mathrm{T}} < 2$ GeV/c with $20 - 30\%$ momentum resolution.

In the previous 200 GeV Au+Au runs in 2014 and 2016, STAR included inner silicon detectors (the Heavy Flavor Tracker). This has since been removed and by comparison in Run-23–25 STAR will have a reduced material budget between the beam and the iTPC, which is essential for performing dielectron measurements. With these measurements, we propose to study the initial conditions (Wigner functions, photoproduction of J/ψ), the degree of freedom of the medium (excess yield), and its temperature (slope in the intermediate mass region).

A synopsis of the proposed analyses, which questions they address, whether they will be part of the minimum bias (low luminosity) or specialized trigger (high luminosity) program, which coverage is essential, and the required trigger is shown in Fig. 70. The following subsections will address the specific analyses which are proposed to answer the questions outlined above. The questions sequentially step through the chronology of an event.

Please note that all the following projection plots use assumed statistics of 20 B MB events and 34 nb^{-1} of sampled luminosity during high-luminosity running period for Run-23+25. Combined with the MB events, the total sampled luminosity is 37 nb^{-1}. As shown in Table 1 of the Executive Summary, the latest projected statistics is about 10% less than what's assumed in this section. Nevertheless, it is straightforward to scale the projected error bars to take into account such differences.

Observable	Question	PWG	MB/H$\mathcal{L}$	Coverage	Trigger
$v_2(\eta)$ Twist	1) Initial State	FCV	Min bias	iTPC, TOF, EPD, FTS	MB
$r_n(\eta_a,\eta_b)$	1) Initial State	FCV	Min Bias	iTPC, TOF, EPD, FTS	MB
J/ψ v_1	1) Initial State	HP	Luminosity	iTPC, TOF, EPD	MB+BHT
Photon WF	1) Initial State	LFSUPC	Min Bias	iTPC, TOF	MB
$v_2(\eta)$	2) Viscosity	FCV	Min bias	iTPC , TOF, EPD, FTS	MB
J/ψ v_2	3) Deconfinement	HP	Luminosity	iTPC, TOF, EPD	MB+BHT
Υ Suppression	4) Temperature	HP	Luminosity	iTPC, TOF	BHT+Dimuon
$\psi(2s)$ suppress.	4) Temperature	HP	Min Bias	iTPC, TOF	MB
Di-elec IMR	4) Temperature	LFSUPC	Min Bias	iTPC, TOF	MB
$P_H(\eta)$	5) Properties	FCV	Min Bias	iTPC, TOF, FTS, EPD	MB
P_H of J/ψ	5) Properties	FCV	Luminosity	iTPC, TOF, EPD	MB+BHT
ρ^0 a_1 mixing	5) Properties	LFSUPC	Min Bias	iTPC, TOF	MB
Di-elec LMR	5) Properties	LFSUPC	Min Bias	iTPC, TOF	MB
CME	5) Properties	FCV	Min Bias	iTPC, TOF, EPD	MB
γ_{Dir} + jet I_{AA}	6) Jet quenching	HP	Luminosity	BEMC, EEMC FCS	BHT
γ_{Dir} + jet acopl.	6) Jet quenching	HP	Luminosity	BEMC, EEMC, FCS	BHT
Jet substruct.	6) Jet quenching	HP	Luminosity	BEMC, EEMC, FCS	BHT
Net-p C_6	7) Phase Transition	CF	Min Bias	iTPC, TOF	MB
Baryon CF	8) Strong Interact.	CF	Min Bias	iTPC, TOF	MB
UPC ρ^0, ϕ, J/ψ	UPC – CNM	LFSUPC	Luminosity	iTPC, TOF, BEMC, EEMC	ZDCEW, UPC
v_2 in γ+Au (UPC)	UPC – CNM	FCV	Min Bias	iTPC, TOF, FTS	UPC
UPC di-jets	UPC – CNM	HP	Luminosity	iTPC, TOF, BEMC	UPC+BHT
UPC CP spectra	UPC – CNM	LFSUPC	Min Bias	iTPC, TOF	ZDCE(1n)+ZDCW

Figure 70: A tabulation of the proposed analyses. The columns indicate which of the eight questions a given analysis addresses, which physics working group will lead the analysis effort, whether the analysis will be part of the low or high luminosity program, which detector systems are essential, and the required trigger for that analysis.

3.1.1 What is the Nature of the 3D Initial State?

Pseudorapidity-dependent azimuthal correlations to constrain the longitudinal structure of the initial state ($v_n(\eta)$)

Initial-state longitudinal fluctuations and the fluid dynamical response of the medium formed in heavy-ion collisions can lead to de-correlations of the direction of the reaction planes Ψ_n (which determines the orientation of the harmonic anisotropies) with pseudorapidity (see Fig. 71). Such effects are often referred to as a torque or twist of the event shape [242–244] that eventually leads to a breaking of longitudinal/boost/rapidity invariance. The magnitude of the de-correlation is determined by the details of the dynamics of initial state, and the distribution of nucleons and partons inside the colliding nuclei.

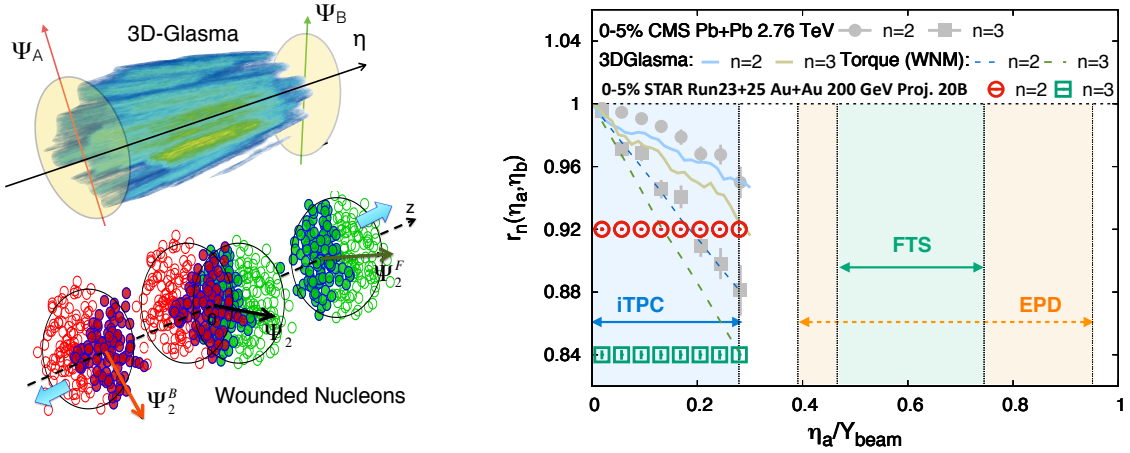

Figure 71: (Left) Cartoon to demonstrate the de-correlation of event planes in the longitudinal direction of a collision from a gluon saturation based 3D-Glasma model [245] and a wounded nucleon model (WNM). [242, 246] (Right) The longitudinal de-correlation of the elliptic anisotropy plane as a function of pseudorapidity in units of beam rapidity. CMS results are compared to predictions from two models, along with STAR projection for Run-23 (using preliminary Run-19 results) from a sample of anticipated 10 B min-bias events. The colored regions show that with iTPC+EPD+FTS one can extend such measurements with good precision by covering a large fraction of the beam rapidity at 200 GeV. This demonstrates the unique strength of STAR to study the physics of 3D initial state.

Several promising observables have been proposed to study this effect, Fig. 71 shows one which can be expressed as $r_n(\eta_a, \eta_b) = V_{n\Delta}(-\eta_a, \eta_b)/V_{n\Delta}(\eta_a, \eta_b)$, where $V_{n\Delta}$ is the Fourier coefficient calculated with pairs of particles taken from three different pseudorapidity regions $-\eta_a$, η_a and η_b. The observable $r_n(\eta_a, \eta_b)$ was originally introduced and measured by CMS collaboration in Ref. [247] and also been measured by the ATLAS collaboration in [248]. An observable using three-particle correlations that is sensitive to this effect is the relative pseudorapidity dependence of the three-particle correlator $C_{m,n,m+n}(\eta_a, \eta_b, \eta_c) = \langle \cos(m\phi_1(\eta_a) + n\phi_2(\eta_b) - (m+n)\phi_3(\eta_c)) \rangle$ [249]. Another variable, very similar to r_n in terms of design but involving four-particle correlations, is: $R_{n,n|n,n}(\eta_a, \eta_b)$ [250]. As shown in

Fig. 71, CMS measurements of r_n show strong de-correlation ($\sim$ 16% for n=3, $\sim$ 8% for n=2) in central events within the range of their acceptance. In the 3D-Glasma model of initial state, the breaking of boost invariance is determined by the QCD equations which predict the evolution of gluons in the saturation regime with Bjorken-x. At the LHC such models predict weaker de-correlations as compared to wounded nucleon models. The 3D-Glasma model underpredicts r_2 and overpredicts r_3 results from CMS [245].

One expects the nature of the initial state to change from LHC to RHIC, in particular the region of Bjorken-x probed is very different. It is therefore extremely important to utilize the enhanced acceptance of the STAR detector to study this effect in 200 GeV Au+Au collisions. In Fig. 71 STAR's projections using preliminary Run-19 results to estimate the uncertainties for 10 B events are shown for the measurement of r_n within the acceptance $|\eta| < 1.5$. The colored regions show that with iTPC+EPD+FTS one can extend such measurements using observables $r_n, C_{m,n,m+n}, R_{n,n|n,n}$ with good precision by covering either an equal (iTPC only) or larger (iTPC+FTS+EPDs) fraction of the beam rapidity at 200 GeV compared to the LHC measurements. This unique measurement capability will help pin down the nature of the 3-D initial state of heavy ion collisions. It will also help constrain different models of QCD that predict different rapidity (or Bjorken-x) dependence of valance quark and gluon distributions inside colliding nuclei as has been demonstrated by theoretical calculations in Ref. [245, 251].

$J\psi$ v_1 to study the initial tilt

Studies of the directed flow, v_1, as a function of rapidity provide crucial information to understand the initial tilt of the medium produced in heavy-ion collisions [252, 253]. Heavy quarks are produced in the early stage of a heavy-ion collision and thus are of particular interest for the medium initial asymmetry studies. STAR recently reported the first measurement of D-meson v_1 in Au+Au collisions at 200 GeV where the magnitude of the heavy-flavor meson v_1 is about 25 times larger than the v_1 for charged kaons.

With the Run-23 and Run-25 data, STAR would have a unique opportunity to study the v_1 of a bound $c\bar{c}$ state, the J/ψ mesons, for which even larger directed flow can be expected [254]. In addition to STAR's excellent capability to reconstruct low-$p_{\rm T}$ J/ψ, the iTPC will improve the momentum resolution and extend the pseudorapidity coverage. This will provide better precision for the slope extraction of v_1 vs. y, which quantifies the strength of the directed flow. The expected precision of a J/ψ v_1 measurement vs $p_{\rm T}$ at STAR in Runs-23 and 25, assuming 20 B MB events and 34 nb^{-1} of BHT trigger sampled luminosity, in 0-80% central Au+Au collisions at 200 GeV is shown in Fig. 72.

Studying the photon Wigner function and initial-state magnetic fields

The $p_{\rm T}$ broadening of the dilepton pairs from photon-photon interactions has been observed in hadronic heavy-ion collisions compared to that in UPCs [255, 256]. The unsuccessful description of STAR data by the STARLight model led to the attribution of the broadening to the possible residual magnetic field trapped in an electrically conducting QGP [255]; which is key information to the study of the chiral magnetic effect. Similarly, ATLAS quantified

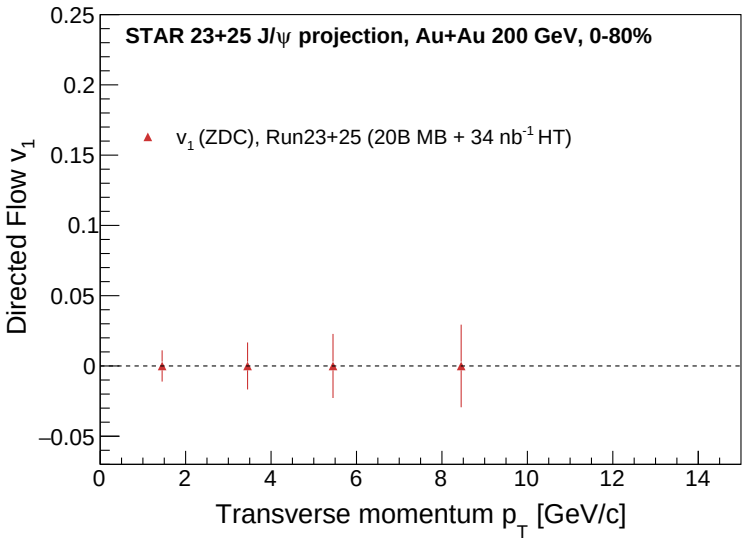

Figure 72: Precision projection for J/ψ ($J/\psi \to e^+e^-$) directed flow (v_1) vs J/ψ $p_{\rm T}$ in 0-80% Au+Au collisions at $\sqrt{s_{\rm NN}}$ = 200 GeV, assuming 20 B MB events and 34 nb^{-1} of BHT trigger sampled luminosity.

the effect via the acoplanarity of lepton pairs in contrast to the measurements in UPCs and explained the additional broadening by multiple electromagnetic scatterings in the hot and dense medium [256], which is analogous to the medium $P_\perp$-broadening effects for jet quenching. These descriptions of the broadening in hadronic collisions are based on the assumption that there is no impact parameter dependence of the p_T distribution for the electromagnetic production. Recent lowest-order QED calculations, in which the impact parameter dependence is recovered, could reasonably describe the broadening observed by STAR and ATLAS without any hot medium effect.

To further shed light on the underlying mechanism, we propose to precisely study the initial $p_{\rm T}$-broadening for the dilepton pair in ultra-peripheral and peripheral collisions. Different neutron emission tags serve as the centrality definition, which will allow us to explore the baseline broadening variation with impact parameter. Furthermore, the differential spectra as a function of pair $p_{\rm T}$, rapidity, and mass enable us to study the Wigner function of the initial electromagnetic field, which provides information to extract the momentum and space correlation of electromagnetic field.

As shown in Fig. 73, compared with the latest QED calculation, there still exists possible additional broadening in peripheral collisions, although the significance is only about 1σ, which leaves room for potential medium effects. In Run-23 and Run-25, as projected in the figure, we could judge the existence of additional broadening with much higher precision and further constrain the strength of final-state magnetic field in the QGP.

Precision measurement of the amplitude of the recently observed $\cos 4\Delta\phi$ modulation of the $\gamma\gamma \to e^+e^-$ process will allow mapping the photon Wigner function and provide additional constraints on possible final-state effects, thereby complementing the $p_{\rm T}$ broadening

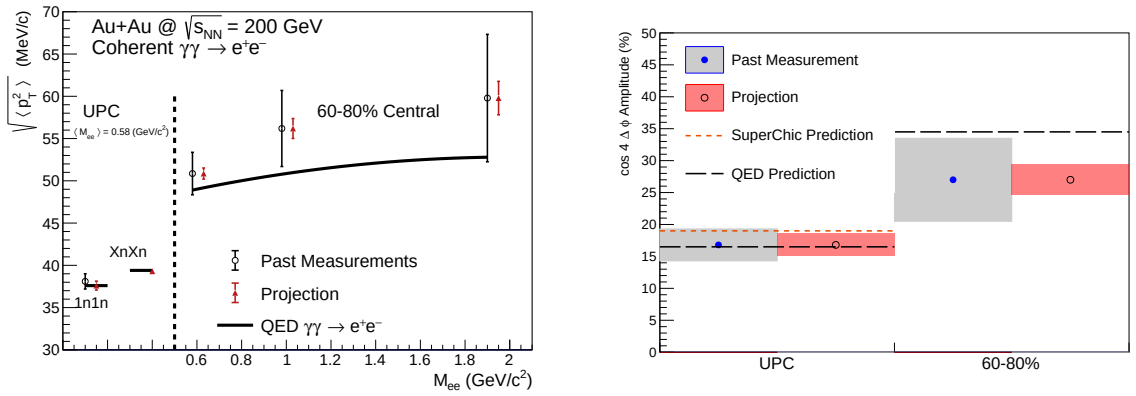

Figure 73: Projections for measurements of the $\gamma\gamma \to e^+e^-$ process in peripheral and ultra-peripheral collisions. Left: The $\sqrt{\langle p_T^2 \rangle}$ of dielectron pairs within the fiducial acceptance as a function of pair mass, M_{ee}, for 60–80% peripheral and ultra-peripheral Au+Au collisions at $\sqrt{s_{\rm NN}} = 200$ GeV. Right: The projection of the $\cos 4\Delta\phi$ measurement for both peripheral (60–80%) and ultra-peripheral collisions.

measurement. Figure 73 (right panel) shows the projected precision for a measurement of the $\cos 4\Delta\phi$ modulation in Run-23+25. The modulation is a direct result of the mismatch in initial and final spin configuration of the $\gamma\gamma \to e^+e^-$ process. Any final-state effect that modifies the $p_{\rm T}$ will necessarily reduce the amplitude of the modulation. Assuming the same central values as previously measured, evidence for suppression of the $\cos 4\Delta\phi$ modulation will be visible at the $> 3\sigma$ level (stat. & syst. uncertainty). Precision measurement of the $\cos 4\Delta\phi$ modulation in Run-23+25 may also allow a first direct experimental measurement of the impact parameter dependence of this new observable (by comparing UPC and 60–80%). Assuming the same central values as previously measured, the improved precision will provide evidence for impact parameter dependence at the $> 3\sigma$ level (stat. & syst. uncertainty). Assuming the central values predicted by QED would lead to a $> 5\sigma$ difference between the UPC case and the 60–80% case.

3.1.2 What is the Precise Temperature Dependence of Viscosity?

The idea of tightly constraining the temperature dependent viscosity of the QGP was envisioned in the 2015 Long Range Plan for Nuclear Science [238]. The QCD matter formed at RHIC shows nearly perfect fluidity characterized by the smallest viscosity to entropy ratio η/s known in nature. One major aim is to perform precision measurements to constrain the temperature dependence of the shear $\eta/s(T)$ and bulk $\zeta/s(T)$ viscosities. Recent state-of-the-art Bayesian analyses of flow and spectra data within sophisticated event-by-event hydrodynamic models has show strong evidence for temperature dependence of η/s and ζ/s [257–259], but the uncertainties are still quite large. On the other hand, hydrodynamic simulations have demonstrated that since the temperature of the produced fireball varies with rapidity, the measurement of the rapidity dependence of flow harmonics can pro-

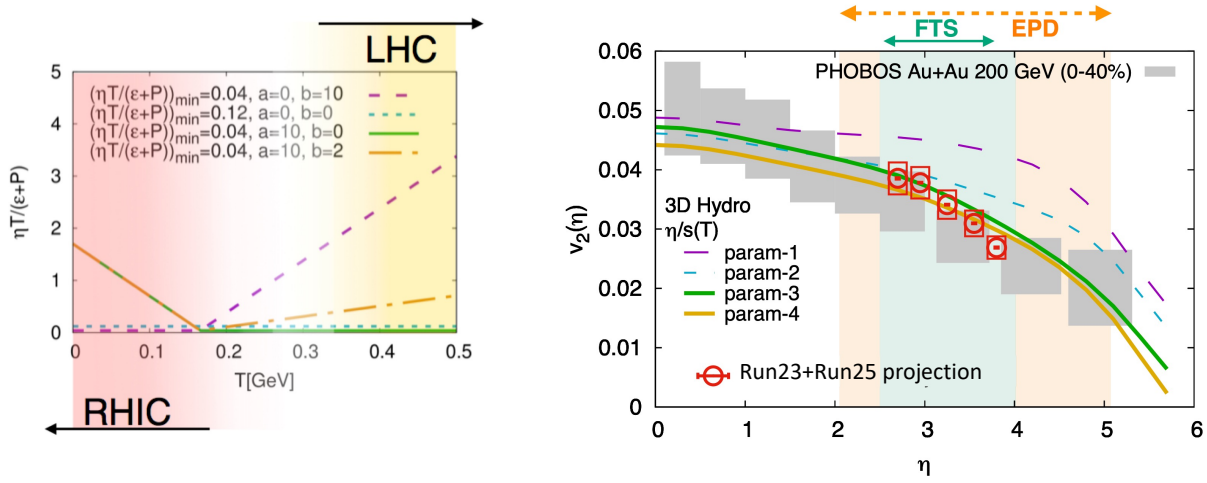

Figure 74: (Left) Different parameterizations of the temperature dependence of the shear viscosity to entropy ratio $\eta/s(T)$ (at $\mu_B = 0$) used in the hydrodynamic simulation of Ref. [260]. It has been demonstrated in Ref. [261] that the region of lowest η/s is the one that can be probed at RHIC. (Right) Effects on the elliptic flow co-efficient v_2 due to different parameterizations of the viscosity parameter, indicating better constraints on $\eta/s(T)$ can only be performed by measurements at forward rapidities at RHIC. The interpretation of the existing PHOBOS data is limited by the large uncertainties. Projections for STAR measurements are shown on the same plot.

vide additional constraints on the η/s(T) and $\zeta/s(T)$. [260] For this, RHIC measurements have an advantage over the LHC since the smaller beam rapidity at RHIC provides stronger variations of the temperature with rapidity. The beam energy scan at RHIC provides an additional handle on temperature to map $\eta/s(T)$, and $\zeta/s(T)$ over a wide range of temperatures. Indeed, the hydrodynamic simulation of Ref. [260] indicates that $\eta/s(T)$ at lower temperatures, near its possible minimum ($T = T_c$), can be better constrained by RHIC measurements. In this simulation, a number of QCD-motivated parameterizations of the temperature dependence of the shear viscosity were assumed, as shown in Fig. 74 (left).

Existing data from the PHOBOS collaboration suffer from large uncertainties, therefore only limited constraints on the temperature dependence of the transport parameters can be achieved. The BES-II upgrades and the FTS will provide precise estimations of different azimuthal correlation observables: $v_n(\eta)$ and other higher-order ($n > 2$) flow coefficients $v_n(\eta)$, its fluctuations $\sigma(v_n)/v_n$ that have never been measured at forward rapidity, which are essential in terms of constraining $\eta/s(T)$ near its possible minimum. These quantities previously measured at mid-rapidity are not enough for discriminating different parameterizations of $\eta/s(T)$ as shown in the hydrodynamic simulation of Ref. [260]. While $p_{\rm T}$ integrated quantities at forward rapidity can constrain the shear viscosity, measurement of the $p_{\rm T}$ of particles at forward rapidity (i.e. FTS) is essential to constrain the bulk ζ/s – in particular the information of $\langle p_T \rangle$ is needed to constrain $\zeta/s(T)$. With the FTS it will be possible to measure the $p_{\rm T}$ dependence of v_n in Au+Au collisions in Run-23+25.

3.1.3 What can Charmonium Tell Us About Deconfinement?

The strong collectivity of the QGP can be studied by measuring the azimuthal anisotropy of the produced particles in heavy-ion collisions. A positive elliptic flow coefficient (v_2) of the light flavor hadrons, and also D-mesons and electrons from heavy-flavor hadron decays are observed in Au+Au collisions at $\sqrt{s_{\rm NN}} = 54.4$ and 200 GeV at RHIC. This corroborates that, like light-flavor, the charm quarks could also be (partially) thermalized and show collectivity in the QGP.

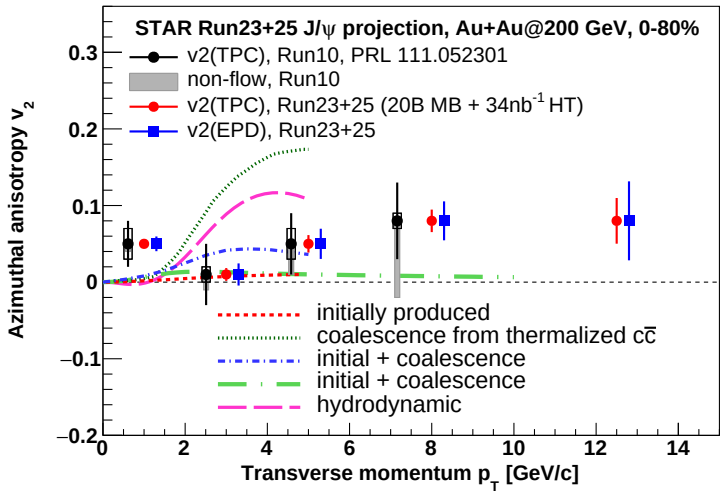

Figure 75: Precision projection for J/ψ ($J/\psi \to e^+e^-$) elliptic flow (v_2) vs J/ψ $p_{\rm T}$ in 0–80% Au+Au collisions at 200 GeV, assuming 20 B MB events and 34 nb^{-1} of BHT trigger sampled luminosity. Projections (red circles and blue squares) are compared with previously published results (black circles) [262] and various model calculations.

On the other hand, the v_2 of heavier J/ψ reported by STAR based on the 2010 Au+Au 200 GeV data sample [262], shown as black circles in Fig. 75, was found to be consistent with zero within large statistical uncertainties and systematic uncertainties due to non-flow effects. The precision of the measurement was not high enough to distinguish between theoretical model calculations that assume only primordial J/ψ production and ones that include additional J/ψ production via regeneration, illustrated as lines of different styles in Fig. 75. This calls for a larger sample of Au+Au collisions at 200 GeV, as will be provided by RHIC in Run-23 and Run-25, in order to observe a possible non-zero J/ψ v_2 at RHIC energies and provide additional insights to the J/ψ production mechanism especially regarding the regeneration contribution. Particularly important for these studies is STAR's ability to measure low $p_{\rm T}$ J/ψ with good precision, thanks to its low material budget and great particle identification capabilities.

The second order event plane will be reconstructed using the EPDs which will significantly decrease the contribution from the non-flow effects and consequently the measurement's systematic uncertainties. Also, an inverse of the event plane resolution enters directly the

J/ψ v_2 uncertainty calculation. Due to the use of the EPD, the resolution of the event plane at forward rapidity for the J/ψ v_2 measurement at STAR will improve. Figure 75 presents statistical projections for the J/ψ v_2 measurement in 0–80% Au+Au collisions assuming 20 B MB events and 34 nb^{-1} of BHT trigger sampled luminosity. Both cases of the second order event plane reconstruction, using the forward EPD and mid-rapidity TPC, are considered and shown. A significant improvement in the precision of the J/ψ v_2 can be seen across the experimentally accessible J/ψ p_{T} coverage, providing the potential to distinguish among different model calculations. In addition, the larger dataset would allow to extend the measured p_{T} range beyond 10 GeV/c.

3.1.4 What is the Temperature of the Medium?

Υ suppression

In the QGP, the confining potential of a heavy quark-antiquark pair is predicted to be screened by the surrounding partons leading to the quarkonium dissociation. Within this static picture, a quarkonium state dissociates if its size is larger than the Debye screening length of the medium that is inversely proportional to the medium temperature. Consequently, different quarkonium states, depending on their sizes, are expected to dissociate at different temperatures, which is usually referred to as the quarkonium sequential suppression. Quarkonia are therefore considered excellent probes of the medium thermodynamic properties. In particular, differences in the dissociation temperatures between Υ(1S), Υ(2S) and Υ(3S) states are larger compared to the charmonium states, providing a longer lever arm. In addition, the regeneration contribution for bottomonia is expected to be negligibly small at RHIC energies.

Figure 76 presents statistical projections for Υ(1S) and Υ(2S) R_{AA} as a function of p_{T} and N_{part} (centrality), compared to STAR's latest results from the 2011, 2014 and 2016 datasets [95]. One can see a clear improvement of the statistical precision for both Υ states. Due to the larger suppression of the Υ(3S) state, only an upper limit on the R_{AA}, 0.17 at 95% confidence level, was obtained so far [95]. With an integrated luminosity of 34 nb^{-1} plus 20 B MB events, we expect a precision of about 30% for Υ(3S) that may allow us to extract the Υ(3S) signal if the meson is not fully dissociated in the medium or at least significantly improve the precision of the upper limit. The requested luminosity is therefore crucial to obtain a full picture of the bottomonia suppression at the RHIC top energy.

ψ(2S) suppression

ψ(2S) is the most loosely bounded quarkonium state currently accessible by heavy-ion experiments. Its dissociation temperature is predicted to be around, or even below, the critical temperature, and is much smaller than that of J/ψ and Υ states. It is therefore more likely to be dissociated in the early stage and in the core of the fireball, and those ψ(2S) that are measured may have significant contributions from regeneration at a later stage in the evolution of the fireball. The relative suppression of ψ(2S) and J/ψ is sensitive to the temperature profile of the fireball produced in heavy-ion collisions and its space-time evolution. It is also argued that the charmonium formation process from a $c\bar{c}$ pair may be affected by both the

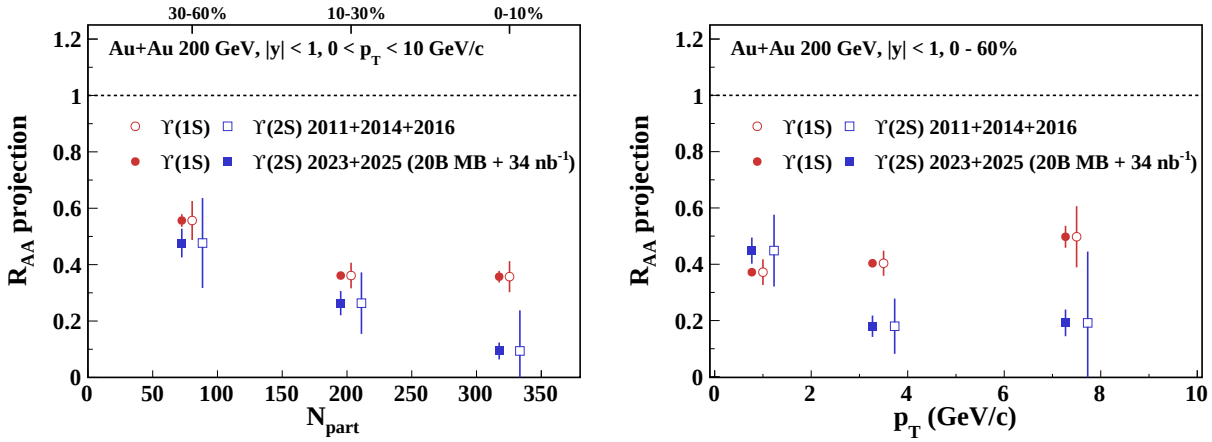

Figure 76: Statistical projections for the Υ(1S) and Υ(2S) $R_{\rm AA}$ as a function of $N_{\rm part}$ (left) and $p_{\rm T}$ (right) in 0–60% Au+Au collisions at $\sqrt{s_{\rm NN}}$ = 200 GeV, assuming 20 B MB events and 34 nb^{-1} of BHT trigger sampled luminosity. The projections (filled symbols) are compared to the STAR results from 2011, 2014 and 2016 datasets (open symbols) [95].

QGP and the initial strong magnetic field, altering the relative yields among different charmonium states. [263, 264] The measurement of ψ(2S) is much more difficult than that of J/ψ due to a much smaller production cross-section and dilepton decay branching ratio, resulting in a very low signal-to-background ratio. The ALICE Collaboration successfully measured the relative suppression of ψ(2S) and J/ψ in Pb+Pb collisions at forward rapidity [265], and the ATLAS and CMS Collaborations published the relative suppression in Pb+Pb collisions at mid-rapidity and high $p_{\rm T}$ [266, 267].

Attempts to measure ψ(2S) suppression in heavy-ion collisions at RHIC have not been successful to date. The low material budget and excellent particle identification capability of STAR together with the large data sample from Run-23+25 will provide a unique opportunity to measure the suppression of ψ(2S) at low $p_{\rm T}$ and mid-rapidity at RHIC. Figure 77 shows the projections of ψ(2S) signal and the yield ratio of ψ(2S) and J/ψ from 20 B MB events in 200 GeV Au+Au collisions. Here the ψ(2S)/J/ψ ratio is assumed to be 0.02, and the performance of detectors from existing data before STAR iTPC upgrade is used for the projection. As shown in the figure, the ψ(2S) signal significance will be around 3σ level in the 0-20% centrality bin. This significance could become even smaller depending on the level of further suppression for ψ(2S) compared to J/ψ. Despite the improvement of momentum and dE/dx resolution thanks to the STAR iTPC upgrade, it is crucial record a large data sample for a significant ψ(2S) measurement.

QGP temperature from dileptons in the IMR

The dilepton mass spectrum has many contributions, and a cocktail of known processes needs to be subtracted to find the excess radiation. To gain a deeper understanding of the microscopic origin of the excess radiation, we will

- separate early time radiation from later time radiation by measuring dilepton elliptic

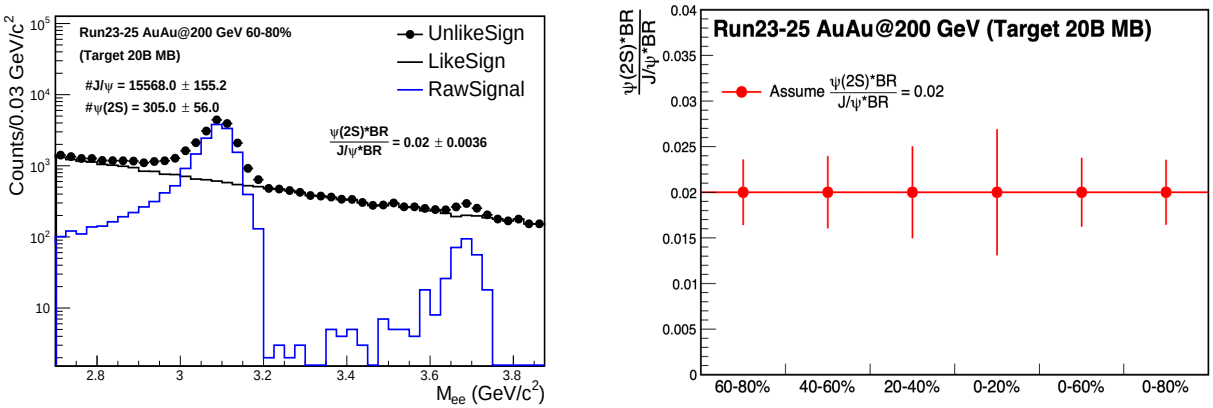

Figure 77: Projections for the J/ψ and ψ(2S) signals in 60–80% Au+Au collisions at $\sqrt{s_{\rm NN}} = 200$ GeV (left) and the ψ(2S) to J/ψ yield ratios in various centrality bins (right).

flow (v_2) as a function of dilepton mass;

- identify the source of dilepton radiation by studying dilepton polarization versus invariant mass (helicity angle);
- measure precisely the lifetime of the fireball. As an observable we will compare integrated low-mass yield to model calculations with various $\tau_{\rm fireball}$;
- extract the average radiating source temperature from the fit of a Boltzmann function to the invariant mass spectrum in the range of 1.1 - 2.5 GeV/c^2. The higher the invariant mass, the stronger the QGP contribution to the spectrum.

The dilepton intermediate mass region (IMR), between the peaks of ϕ and J/ψ, is dominated by thermal emission from the QGP. The slope of the spectrum in this region can be used as a blue-shift free measurement of the temperature at the time of dilepton emission. Extraction of the QGP temperature from the dilepton spectrum can be compared to the temperatures suggested by the Υ and ψ(2S) suppression.

Last but not least, concerning the direct photon emission, the existing difference, on the order of a factor of two, between the low momentum spectra from PHENIX and STAR in 200 GeV Au+Au collisions, needs to be resolved. In order to do so, we will carry out high-precision measurement of the direct virtual photon yield as well as its elliptic flow coefficient, which can also shed light on the so-called direct photon puzzle. In particular, we will focus on low $p_{\rm T}$ η meson measurement which might be instrumental in clarifying this long-standing question.

3.1.5 What are the Electrical, Magnetic, and Chiral Properties of the Medium?

The QGP medium which is created during the collision of two heavy ions has significant electric fields, magnetic fields, vorticity, and chirality.

Pseudorapidity dependence of global hyperon polarization ($P_H(\eta)$)
The global polarization of hyperons produced in Au+Au collisions has been observed by STAR [72]. The origin of such a phenomenon has yet to be understood. Several outstanding questions remain. How exactly is the global vorticity, and its associated strong magnetic fields, generated by the two incident heavy ions dynamically transferred to the fluid-like medium on the rapid time scales of a collision? How does the local thermal vorticity of the fluid gets transferred to the spin angular momentum (magnetic moment) of the produced particles during the process of hadronization and decay? In order to address these questions one may consider measurement of the polarization of different particles that are produced in different spatial parts of the system, or at different times. A concrete proposal is to: 1) measure the $\Lambda(\bar{\Lambda})$ polarization as a function of pseudorapidity and 2) measure it for different particles such as Ω and Ξ. Both are limited by the current acceptance and statistics available as recently published by STAR [268]. However, as shown in Fig. 78 with the addition of the iTPC and FTS as well as high statistics data from Run-23+25, it will be possible to perform such measurements with reasonable significance. iTPC has excellent PID capability

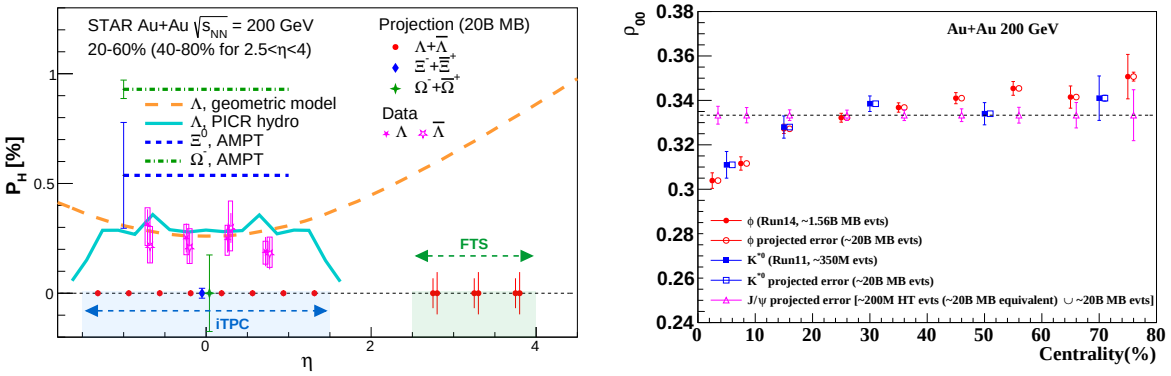

Figure 78: (Left) Projections (along with preliminary data) for differential measurements of $\Lambda(\bar{\Lambda})$ polarization over the extended range of pseudorapidity with the iTPC and FTS, which will help resolve tension between different theoretical model predictions (shown by curves) of polarization with η. In addition, projections for the measurements of spin-1/2 Ξ and spin-3/2 Ω particles are also shown. (Right) Spin alignment co-efficient ρ_{00} as a function of centrality, with projected errors. The enhanced statistics from Run-23+25, combined with the excellent dilepton capabilities of STAR, will enable us to measure J/ψ alignment and improve the significance of the ϕ and K^{*0} measurements.

to measure all these hyperons.

Although the FTS has no PID capability we can do combinatorial reconstruction of $\Lambda(\bar{\Lambda})$ candidates via displaced vertices. A similar analysis was performed and published by STAR using the FTPC [269] more than a decade ago. In order to make a projection, we assume similar momentum resolution of 10–20% for single charged tracks, similar overall tracking efficiency, charge state identification capability for the FTS and FTPC. We also assume that the FTS, with its novel tracking framework, will be able to measure a minimum separation

of 20 cm between a pair of one positive and one negative track (a possible decay vertex) from the collision vertex. This will give rise to about 5% efficiency of $\Lambda(\bar{\Lambda})$ reconstruction with about $15-20\%$ background contribution from $K^0_S \rightarrow \pi^+ + \pi^-$ [269]. With this we can make projections for a polarization measurement in 40–80% Au+Au collisions at $\sqrt{s_{\rm NN}} =$ 200 GeV within $2.5 < \eta < 4$, as shown in Fig. 78. The two different error bars correspond to lower and upper limits considering current uncertainties on the efficiency of charged track reconstruction.

Currently theoretical models predict contradictory trends for the pseudorapidity dependence of Λ polarization. If the initial local orbital angular momentum driven by collision geometry [270] plays a dominant role, it will lead to an increases of polarization with pseudorapidity. On the other hand, if the local thermal vorticity and hydrodynamic evolution [271] play a dominant role, it will predict decreasing trend or weak dependence with pseudorapidity. Such tensions can be easily resolved with the proposed measurement during Run-23 and Run-25.

Global spin alignment of J/ψ

Surprisingly large signals of global spin alignment of vector mesons such as $\phi(1020)$ and $K^{*0}(892)$ have been measured via the angular distribution of one of their decay products [272]. These experimental observations of vector meson spin alignment have yet to be interpreted satisfactorily by theory calculations. It has been realized that the mechanism driving the global polarization of hyperons can have its imprint on vector meson spin alignments albeit the observed strength of signals for the two measurements cannot be reconciled. In fact the large quantitative difference between the measurements of $\phi(1020)$ and $K^{*0}(892)$ spin alignment at low energies cannot be simultaneously explained by conventional mechanisms of spin-orbit coupling, driven by angular momentum, without invoking strong force fields [272]. It is argued that the strong force field makes a dominant contribution to the spin-alignment coefficient ρ_{00} of ϕ, while for K^{*0}, the contribution is diminished due to the mixing of quark flavors (averaging-out of different meson fields) [273, 274]. Therefore, the current experimental data from STAR [272] supports the role of strong force field as a key mechanism that leads to global spin alignment.

An extended test of such a prediction can be performed by measuring the spin alignment of J/ψ. This is because similar arguments apply for J/ψ, i.e. like s and $\bar{s}$, the strong field component also couples to c and $\bar{c}$ quarks leading to large ρ_{00} for J/ψ. ALICE recently reported $\rho_{00} \approx 0.37$ for J/ψ at forward rapidity ($2.5 < y < 4$) with a 3.9σ significance, seemingly supporting this argument. STAR can definitely contribute to this study by measuring J/ψ global spin alignment at midrapidity with the large dataset to be taken during Run-23+25.

In Fig. 78 we present the projected uncertainties for ρ_{00} of J/ψ estimated for various centralities assuming: 1) 20 B min-bias events for low $p_{\rm T}$ J/ψ measurements and, 2) 200 M BHT triggered events for the high $p_{\rm T}$ J/ψ. It is worth to mention that apart from J/ψ spin alignment, such a large statistics dataset will also allow addition differential study of global spin alignment of ϕ and K^{*0} and help to further elucidate the mechanism behind vector

meson spin alignment.

Probing electromagnetic effect via charge-dependent directed flow

One of the features in high energy heavy-ion collisions is the generation of an ultra-strong magnetic field, which is predicted to have the strength of 10^{18} Gauss [275–279]. The interplay between magnetic field and QGP may induce many interesting phenomena, such like the CME and CMW. Recent studies suggest that the charge dependent directed flow can be used to search for magnetic field related effects [92, 93], which predict a negative $\Delta dv_1/dy$ between positively and negatively charged particles due to the influence of electromagnetic field. Some experimental efforts have been made for searching this effect, such as the charge dependent v_1 measurements presented by LHC-ALICE collaboration [280], and the directed flow of D^0 and $\overline{D^0}$ from STAR experiment [281]. Results of light flavors in Pb+Pb collisions at $\sqrt{s_{\rm NN}} = 5.02$ TeV show large discrepancy to theoretical calculations, which gives an order of magnitude larger and positive Δv_1 slope. Similar results have been obtained in Au+Au collisions at several energies at RHIC, which measured positive Δv_1 slope between proton and anti-proton in semi-central collisions owning to the transported quark contributions.

Recent analyses in Au+Au and isobar collisions at $\sqrt{s_{\rm NN}} = 200$ GeV show striking centrality dependence of the Δv_1 slope. It was found that the $\Delta dv_1/dy$ between proton and anti-proton changes from positive to negative as centrality goes from central to peripheral. The negative value in peripheral collisions, with the significance of 5σ, qualitatively agrees with theoretical calculations. However, the $\Delta dv_1/dy$ between K^+ and K^-, π^+ and π^- are less significant because of the limitation of statistics. With 20 B events in Au+Au collisions at 200 GeV to be collected, the $\Delta dv_1/dy$ between K^+ and K^- can achieve a significance $> 5\sigma$, as illustrated in left panel of Fig. 79. Moreover, the EM-field prediction shows a non-trivial $p_{\rm T}$ dependence, but this measurement is currently limited by statistics. As illustrated in the right panel of Fig. 79, with the data accumulated from Run-23+25, we will be able to measure the $p_{\rm T}$ dependence of $\Delta dv_1/dy$ with higher precision.

The existing measurements of v_1 for Ξ and Ω in Au+Au collisions at $\sqrt{s_{\rm NN}} = 200$ GeV have large uncertainties. There is a hint of a large v_1 for Ω baryons from recent measurements, however, as shown in Fig. 80, the statistical uncertainties of the current STAR measurements are large. There are also measurements for electric charge and strangeness dependent splittings in Au+Au collisions at $\sqrt{s_{\rm NN}} = 200$ GeV. These measurements also suffer from insufficient statistics, as shown in Fig. 81. A large dataset from the upcoming Run-23 and 25 for Au+Au collisions at $\sqrt{s_{\rm NN}} = 200$ GeV will definitely help improve the precision of these measurements. The projected statistical precision, based on 20 B events to be collected Run-23+25, are shown in Figs. 80 and 81.

Chiral properties: ρ-a_1 mixing

In case the measured in-medium spectral function merges into the QGP description, it would indicate a transition from hadrons into a structure-less quark-antiquark continuum, thus providing the manifestation of chiral symmetry restoration. We will continue to search for a direct signature of chiral symmetry restoration via chiral ρ-a_1 mixing.

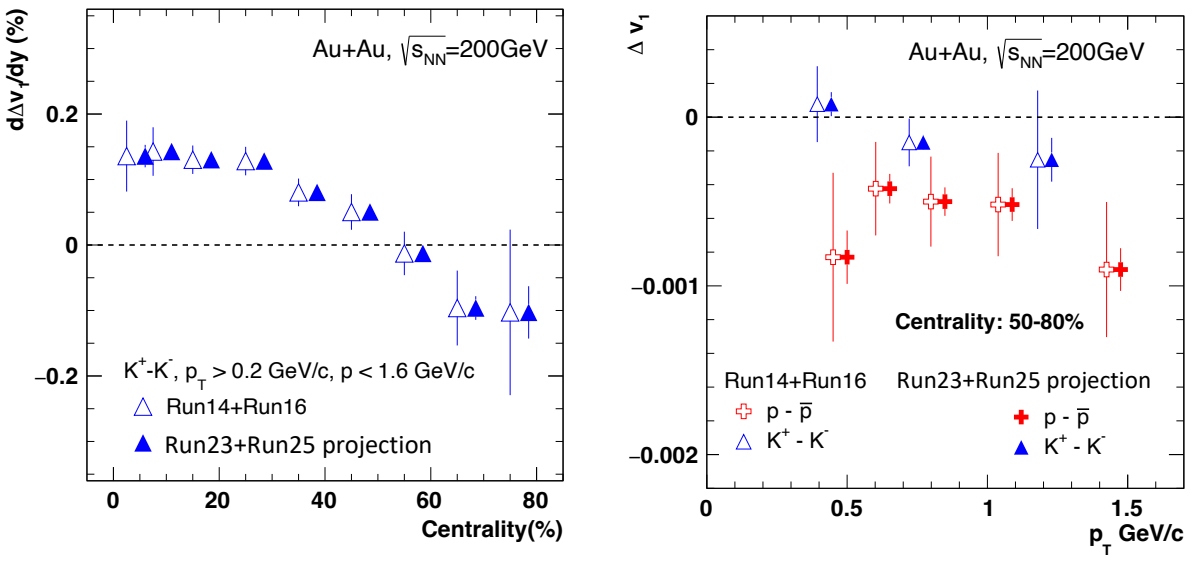

Figure 79: (Left) $\Delta dv_1/dy$ between K^+ and K^- as a function of centrality in Au+Au collisions at $\sqrt{s_{\rm NN}} = 200$ GeV. Open markers indicate the projected results. (Right) $\Delta dv_1/dy$ for proton and kaon as a function of $p_{\rm T}$ in 50–80% Au+Au collisions at 200 GeV.

The signal is predicted to be detectable in the dilepton intermediate mass range. Difficulties are related to the fact that correlated charm-anticharm decays and QGP emission saturate this invariant mass region of 1.1 — 1.3 GeV/c^2. Therefore an accurate measurement of the excess dilepton yield, i.e. dilepton yield after subtraction of the cocktail of contributions from final-state decays, Drell-Yan and those from correlated heavy-flavor decays, up to invariant mass of 2.5 GeV/c^2 is required. Deeper understanding of the origin of the thermal radiation in Au+Au collisions at $\sqrt{s_{\rm NN}} = 200$ GeV from ∼zero mass up to 2.5 GeV/c^2 will become possible with rigorous theoretical efforts and improved dielectron measurements. Figure 82 shows the expected statistical and systematic uncertainties of the dielectron excess mass spectrum with all the detector upgrades taken into account and for the anticipated statistics of 20 B events.

Electrical conductivity (dielectron LMR)

Another application of dielectron continuum is to measure transport coefficients. The electrical conductivity can be directly obtained as the low-energy limit of the EM spectral function. We aim to extract such information by studying excess dielectron yields at the low-energy regime of the dilepton spectra and the conductivity peak at small invariant masses, i.e. at low invariant mass and low $p_{\rm T}^{ee}$. Measurement of the Drell-Yan process in p+Au collisions at low $p_{\rm T}$ would provide an important reference to constrain the dilepton cocktail.

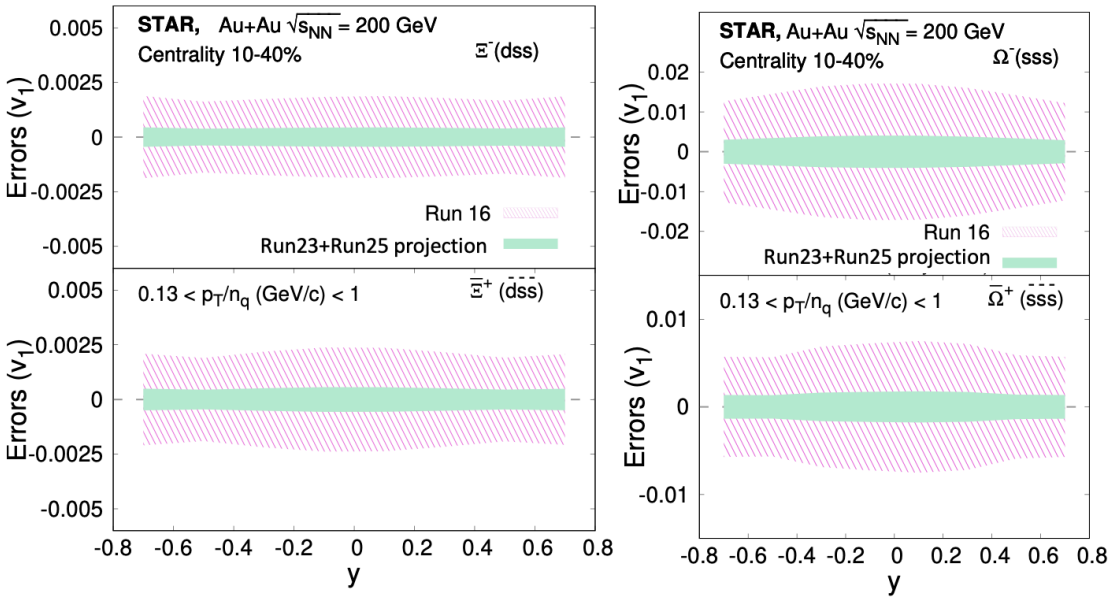

Figure 80: Projection of directed flow (v_1) error for Ξ^-, $\overline{\Xi}^+$, Ω^- and $\overline{\Omega}^+$ as a function of rapidity (y) in 10–40% central Au+Au collisions at $\sqrt{s_{\rm NN}}$ = 200 GeV. The projections are made by assuming 20 B MB events to be collected in Run-23+25.

Local parity violation and the chiral magnetic effect

A decisive experimental test of the Chiral Magnetic Effect (CME) has become one of the major scientific goals of the heavy-ion physics program at RHIC. The existence of CME would be a leap towards an understanding of the QCD vacuum, establishing a picture of the formation of a deconfined medium in which chiral symmetry is restored, and it would

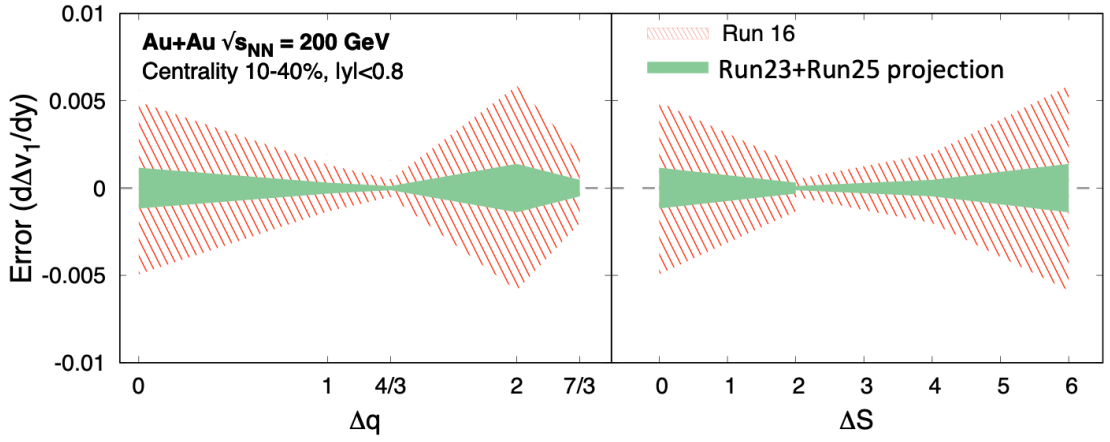

Figure 81: Δv_1 slope ($d\Delta v_1/dy$) error at mid-rapidity as a function of electric charge difference (Δq) and strangeness difference (ΔS) for 10-40% centrality in Au+Au collisions at $\sqrt{s_{\rm NN}}$ = 200 GeV. The projections are made assuming 20 B events to be collected in Run-23+25.

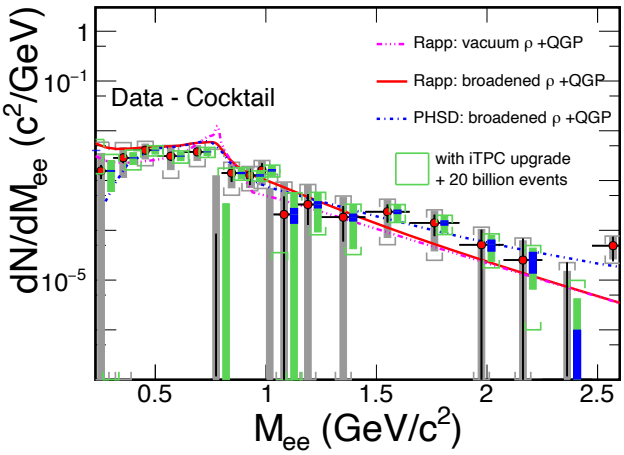

Figure 82: The expected statistical and systematic uncertainties on the dielectron excess mass spectrum with the iTPC upgrade compared to the current TPC case. Data are from current measurements in $\sqrt{s_{\rm NN}}$ = 200 GeV Au+Au collisions [282]. Model comparisons are also shown. The boxes represent systematic uncertainties from data and the brackets represent the total systematic uncertainties including those from cocktails. The grey ones are for the current case while the green ones are for the Run-23 and 25 case. The blue bands represent statistical uncertainties from 20 B min-bias events with the iTPC upgrade.

also provide unique evidence that the strongest known electromagnetic fields are created in relativistic heavy-ion collisions [283, 284]. The impact of such a discovery would go beyond the community of heavy-ion collisions and will possibly be a milestone in physics. The remaining few years of RHIC running and analyses of previously-collected data will likely provide the only chance for CME searches in heavy-ion collisions in the foreseeable future.

The isobar collisions provided an unique opportunity to search for the CME because of the $\sim$ 15% difference in B^2 and hence the CME correlation signals between Ru+Ru and Zr+Zr collisions. However, no clear CME signal has been observed in isobar data even with an improved understanding of the baseline. The signal-to-background ratio is expected on general ground to be smaller in isobar collisions than in Au+Au collisions by an approximately factor of 3 [285]. This is in line with the Au+Au results which indicate a positive CME signal of $\sim$ 8% with $\sim 2\sigma$ significance using the spectator/participant plane method [286]. The size of the current Au+Au data sample is about 2.4 B events from Run-11, Run-14 and Run-16 [286]. In order to achieve 5σ significance with the same analysis technique, one needs to have about 15 B events. Therefore, with the proposed 20 B events to be collected by STAR during Run-23 and 25, one can achieve more than 5σ significance provided the possible CME signal remains at 8%. A stringent upper limit will be possible on the CME if the size of the signal turns out to be smaller. This rough estimate does not account for two important facts that can lead to higher significance though. The first is that the iTPC upgrade enhances the charge particle multiplicity by 50% and therefore triplet($\sim dN/d\eta^3$) (pair $\sim dN/d\eta^2$) statistics by a factor of 3.4 (2.3). The second one is the addition of the EPD detector which will significantly reduce nonflow contaminations

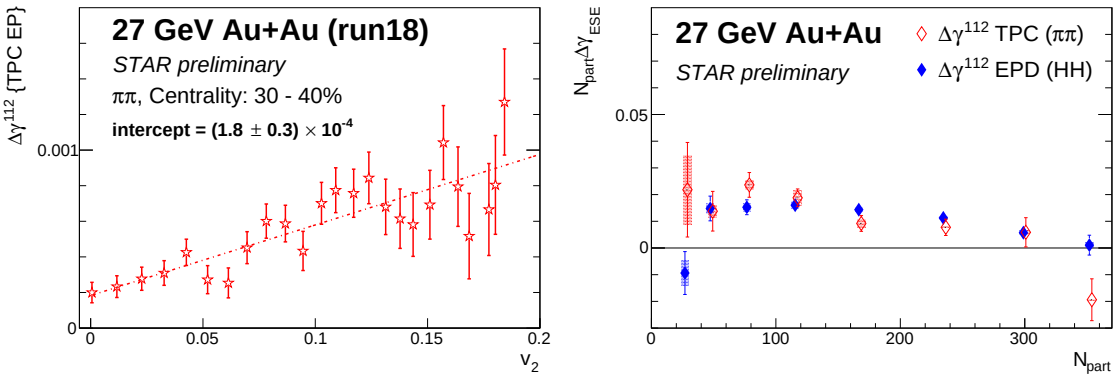

Figure 83: (Left) $\Delta\gamma_{112}$ for π-π vs v_2 measured with the TPC event plane in 30–40% Au+Au collisions at 27 GeV. (Right) $\Delta\gamma_{112,\mathrm{ESE}}$ scaled by N_{part} as a function of N_{part} for π-π using the TPC event plane, and for hadron-hadron using the EPD event plane in Au+Au collisions at 27 GeV.

in the measurements with respect to the participant plane. Our estimate assumes that the systematic uncertainty can be controlled to be smaller than the statistical uncertainty, i.e. below 1%.

Another technique used to search for the CME is based on the event-shape engineering (ESE). The dominant background in the CME-sensitive $\Delta\gamma_{112}$ correlator is caused by the coupling of elliptic flow with other mechanisms such as resonance decays and local charge conservation. The ESE method aims to project $\Delta\gamma_{112}$ to a class of events with minimal flow to suppress the v_2-related background. We adopt an ESE technique [287] that uses the flow vector ($q_{2,x} = \frac{1}{\sqrt{N}}\sum_i^N \cos(2\phi_i)$, $q_{2,y} = \frac{1}{\sqrt{N}}\sum_i^N \sin(2\phi_i)$) to select spherical sub-events with almost zero v_2. Observables like v_2 and γ_{112} are measured as a function of q_2^2 from the particles of interest (POIs), and then $\Delta\gamma_{112}$ is plotted against v_2 in the same q_2^2 interval to yield a reliable projection to the zero-flow mode. Figure 83 (left) demonstrates the application of the ESE approach to the STAR data of 30–40% Au+Au collisions at 27 GeV (run 2018). The decrease of $\Delta\gamma_{112}$ for π-π with decreasing v_2 illustrates how the v_2-related background is suppressed. Figure 83 (right) shows the centrality dependence of N_{part} $\Delta\gamma_{112\mathrm{ESE}}$ for π-π using the TPC event plane, and for hadron-hadron using the EPD event plane in Au+Au collisions at 27 GeV. The ESE method will be applied to the 200 GeV Au+Au data from Run-23 and Run-25. With the large dataset of anticipated 20 B events, we will be able to perform more differential measurements and involve identified particles such as kaons and protons.

Event-by-event correlations between CME charge separation and other parity-odd features of the event will also be studied. One such analysis is motivated by the idea that the local parity violation (characterized in each event by a net topological charge Q) that is expected to couple with the spectator-produced magnetic field to give rise to the CME should also cause a net helicity of $\Lambda(\bar{\Lambda})$ in the event. Importantly, even though both of these parity-odd signatures switch handedness event-by-event, in any given event they should have the same handedness and so can be compared. Specifically, a measured event-by-event cor-

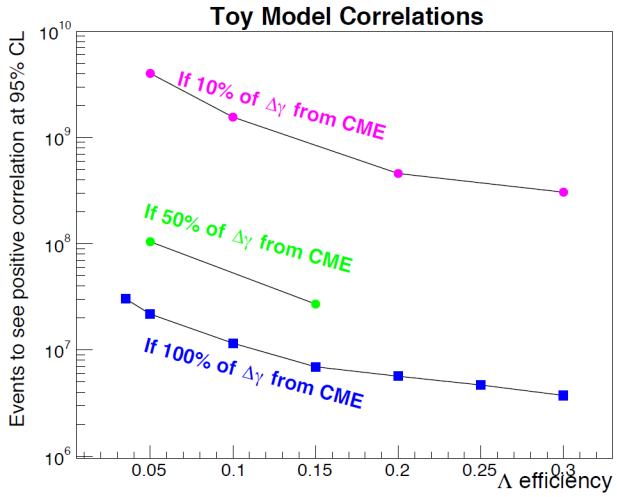

Figure 84: Estimation of the number of events required to see positive correlation between net Λ helicity and out-of-plane charge separation sensitive to local parity violation at the 95% confidence level, plotted against the efficiency of $\Lambda(\bar{\Lambda})$ reconstruction (see Ref. [289] for details).

relation between Δa_1 and ΔN would be strong evidence for the CME and underlying local parity violation. Note also that the flow-related backgrounds that plague charge-separation measurements are not expected to affect ΔN and so should not affect such correlation measurement. We use a similar toy model to estimate the number of events needed to see non-zero correlations between Δa_1 and ΔN with different CME signal fraction in the $\Delta\gamma$ measurement (see Fig. 84). The main unknown in this estimate is the extent to which strange quarks may be counted as light quarks and so will have a net handedness imparted by the parity-odd domain. Recent theoretical work [288] makes a direct connection between the net lambda helicity and the axial chemical potential developed from local parity violation. Figure 84 suggests that this will be a topic requiring the large datasets of Run-23+25. To better understand this correlation, we have analyzed the Run-18 Au+Au collision data at $\sqrt{s_{\rm NN}} = 27$ GeV [290]. The $\Lambda(\bar{\Lambda})$ baryons are reconstructed by their decay daughter tracks and identified by the `KFParticle` package. Each Λ handedness is estimated by decay kinematics. After a purity correction, $N_{\rm L}$ and $N_{\rm R}$ are calculated for both Λ and $\bar{\Lambda}$ in each event, and then Δn (normalized ΔN, $\Delta n = \frac{N_{\rm L}-N_{\rm R}}{\langle N_{\rm L}+N_{\rm R}\rangle}$) is calculated. The observable Δa_1 can be calculated from primordial particles' azimuthal angles w.r.t. the first-order EP measured by the EPD. The covariance between Δn and Δa_1 is then calculated for the event sample. In this exploratory measurement, the covariance is consistent with zero, and so no significant correlations have been observed (see Fig. 85). However, this event-by-event correlation method holds great potential with future high statistics data from Run-23+25 by a qualitatively new technique different from all existing analyses.

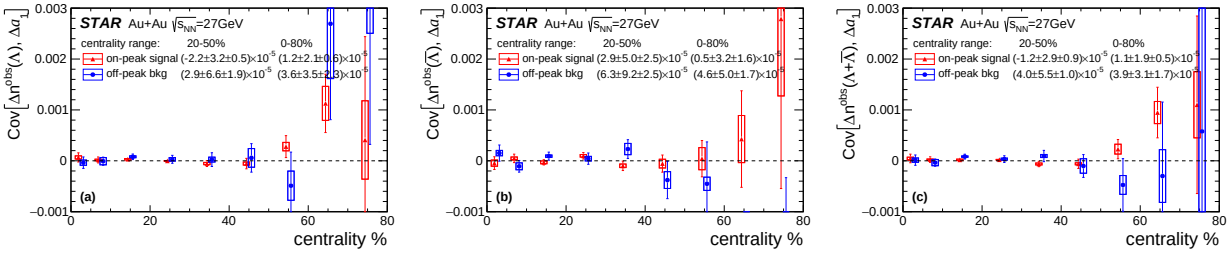

Figure 85: The covariance between Δa_1 and Δn for Λ (Left), $\bar{\Lambda}$ (Middle), and the sum of them (Right) as a function of centrality [290]. The red markers come from the $\Lambda(\bar{\Lambda})$ mass peak region with purity correction and blue markers come from the side bands for background.

3.1.6 What are the Underlying Mechanisms of Jet Quenching?

The dependence of jet energy loss on the jet p_{T} and/or resolution or angular scale tagged by jet substructure observables are key tools in discriminating various jet quenching mechanisms [97, 291–293]. In addition, the measurement of jet acoplanarity is a sensitive probe of p_{T} broadening and medium response [294], particularly for jets at low p_{T} which are accessible at STAR by selecting a given momentum transfer via a photon trigger. Such a measurement is also affected by background arising from vacuum Sudakov radiation at RHIC energies [295, 296].

STAR's unique geometry allows collection of events over a wide range of vertex positions along the beam direction (vz) for jet analyses, thereby efficiently sampling the provided RHIC luminosity. Optimization of the vz range used in the various analyses involves a balance between statistical precision and complexity of corrections, with the latter predominantly contributing to the systematic uncertainties of the measurement. Recent STAR jet measurements in Au+Au collisions have employed two classes of vz cuts: the inclusive charged-particle jet analysis [297] utilizes $|\mathrm{vz}| < 30$ cm, whereas the $\gamma_{\mathrm{dir}}+$jet analysis utilizes $|\mathrm{vz}| < 70$ cm. With the $\gamma_{\mathrm{dir}}+$jet measurement successfully utilizing the broad vz range with controlled systematic precision, we are exploring similar event selections maximizing the available statistics for future jet measurements, including the inclusive/differential jet analyses. In the following discussions, we assume an integrated luminosity of 34 nb^{-1} plus 20 B min-bias events, which is roughly a factor 3.7 increase in trigger statistics relative to the current analyses based on Run-14 data.

To quantify the effect of the marked increase in statistics, we utilize two mature jet measurements and discuss their expected improvements. These analyses are the semi-inclusive distribution of charged-particle jets recoiling from a high-E_{T} direct-photon trigger (γ_{dir}+jet); and the differential measurement of energy loss for jet populations selected by varying a substructure metric. Since these analyses are mature, their analysis methodologies and correction schemes are optimized, so that their projections based on increased statistics are meaningful.

Semi-inclusive $\gamma_{\rm dir}$ + jet measurements (I_{AA})

Figure 86 shows $I_{\rm AA}$ for fully-corrected semi-inclusive distributions of charged-particle jets (anti-$k_{\rm T}$, $R = 0.5$) recoiling from a direct-photon trigger with $15 < E_{\rm T} < 20$ GeV in 0–15% central Au+Au collisions at $\sqrt{s_{\rm NN}} = 200$ GeV, for the current analysis based on 10 nb^{-1} [298] within |vz| < 70 cm. The projected uncertainties, accounting for the Au+Au data from previous years and Run-23+25 as well as the projected p+p statistics from Run-24, are shown in green bands. Significant reduction in the uncertainty is seen resulting from the increase in integrated luminosity, together with a significant increase in kinematic reach as indicated by the extended green band along the x-axis.

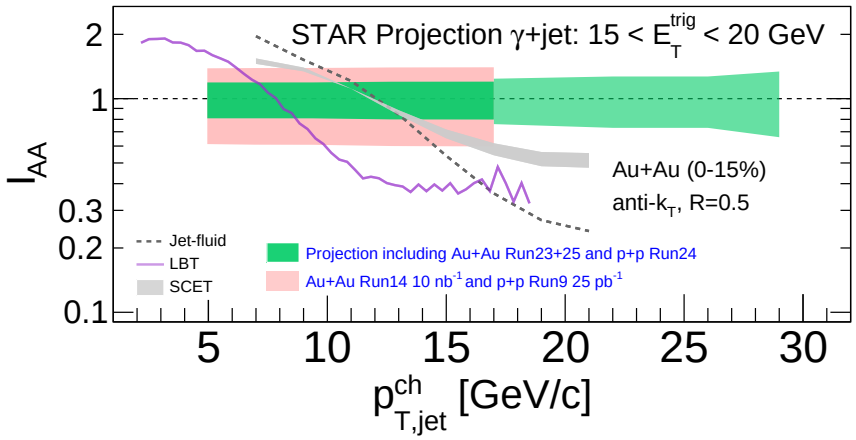

Figure 86: Projections of the $I_{\rm AA}$ for semi-inclusive anti-$k_{\rm T}$, $R = 0.5$ jets recoiling from a direct-photon trigger with $15 < E_{\rm T} < 20$ GeV for central (0-15%) Au+Au collisions at $\sqrt{s_{\rm NN}} = 200$ GeV. The colored bands show the cumulative uncertainties for the current analysis and projections for future analysis with the higher statistics datasets.

Jet acoplanarity

The $p_{\rm T}$ broadening due to medium effects not only modifies the shape but also introduces a decorrelation between the di-jet angular distributions. The vacuum QCD process (Sudakov radiation) makes such measurements challenging in heavy-ion collisions, but at RHIC the Sudakov effect is smaller than that at the LHC as it depends on the virtuality Q^2 [295,296]. A detailed study is needed to understand both effects (medium-induced and vacuum radiation) in a wide range of jet $p_{\rm T,jet}$ both at RHIC and the LHC energies.

In this direction, the STAR experiment has reported the first signature of medium-induced acoplanarity in central Au+Au collisions. However, due to limited available statistics, current preliminary result is limited to $\gamma_{\rm dir}$ and π^0 triggers of $11 < E_{\rm T} < 15$ GeV and charged-particle jets (anti-$k_{\rm T}$, $R = 0.2$ and 0.5) of $10 < p^{\rm ch}_{\rm T,jet} < 15$ GeV/c. To have a better understanding of the nature of this acoplanarity, we need to extend both $E^{\rm trig}_{\rm T}$ and recoil jet $p_{\rm T,jet}$ kinematic ranges which demands high statistics datasets. On the other hand, the STAR experiment also reported the same measurement in p+p collisions to study the effect of Sudakov radiation in vacuum and set the baseline for Au+Au collisions. Figure 87 shows

the semi-inclusive distributions of the azimuthal separation between a direct-photon trigger with $15 < E_{\mathrm{T}} < 20$ GeV and a charged-particle jet (anti-k_{T}, $R = 0.5$) with $10 < p_{\mathrm{T,jet}}^{\mathrm{ch}} < 15$ GeV/c in p+p (left) and 0–15% central Au+Au (right) collisions at $\sqrt{s_{\mathrm{NN}}} = 200$ GeV. The azimuthal smearing of this observable due to uncorrelated background is small, and such acoplanarity measurements are therefore strongly statistics limited [299, 300]. The grey vertical bars represent the statistical uncertainty with the current available statistics, whereas the red vertical bars correspond to statistics including Run-23, 24, and 25 datasets.

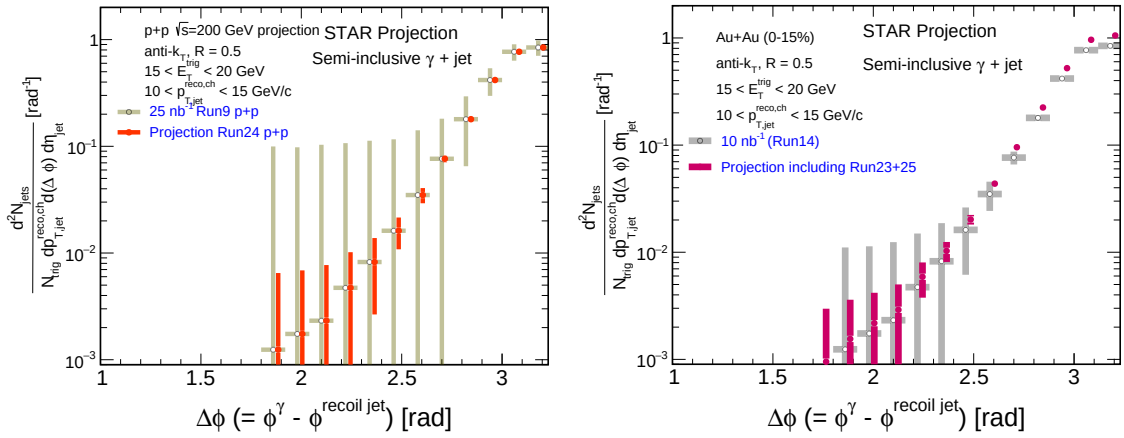

Figure 87: Projections of the acoplanarity for semi-inclusive anti-k_{T}, $R = 0.5$ jets of $10 < p_{\mathrm{T,jet}}^{\mathrm{ch}} < 15$ GeV/c recoiling from a direct-photon trigger with $15 < E_{\mathrm{T}} < 20$ GeV in p+p (left) and 0–15% central Au+Au (right) collisions at $\sqrt{s_{\mathrm{NN}}} = 200$ GeV. The vertical bands show the statistical uncertainties for the current analysis and projections for future analysis with the high statistics datasets.

It is worth noting that this measurement in p+p collisions could exploit forward triggering using forward calorimeter to explore a relatively small x region, compared to mid-rapidity measurement. This is important to study various pQCD effects like NLO corrections, ISR/FSR, and MPI effects, and upcoming Run-24 p+p collision data-taking is critical in this direction.

Differential measurement of energy loss tagged with a substructure metric

Systematic exploration of parton energy loss controlled for variations in the jet shower forms an integral part of the jet program at STAR. Since parton showers are inherently probabilistic, a jet population contains patterns of radiation varying in both angle and momentum scales which can be extracted via jet substructure measurements defined based on jet constituents' angle and/or momentum via algorithms or correlations. By selecting jets based on their substructure, STAR can differentially measure jet-medium interactions for various types of energy loss e.g. color coherence, dead cone, etc. In other words, part of the STAR jet program for Run-23+25 will focus on jet substructure as a jet-tagger.

Theory calculations show significant differences between energy loss signatures for jets

perceived by the medium as a single or multiple color charges [292]. The integrated luminosity from the Runs 23 and 25 datasets not only provide a substantial increase in statistics in the current measurements of jet substructure, they also increase the available phase space for rare processes such as wide angle emissions from high-p_{T} jets. This enables STAR to extend the current measurements of differential energy loss from a resolution of $\delta\theta = 0.1$ to finer resolution $\delta\theta \approx 0.025$ in the jet opening angle as shown in Fig. 88, and also extend to jets of higher momenta. By extending to high energy splittings within jets at varied opening angles, we can probe earlier formation times whereby vacuum-like emissions and medium induced radiations are expected to occur.

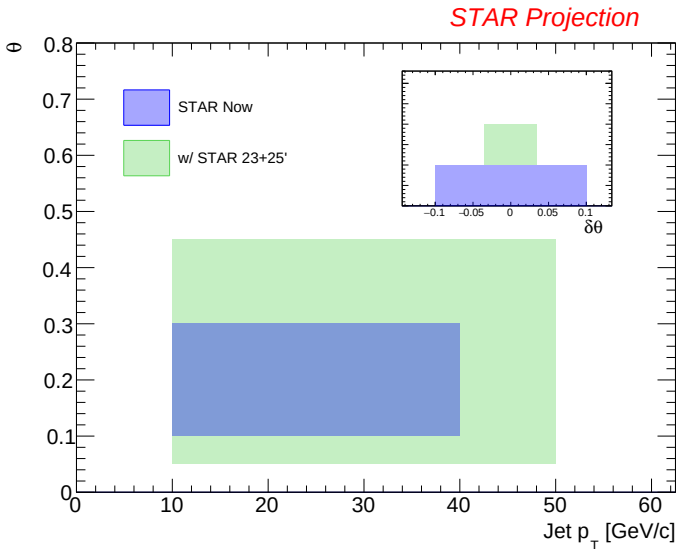

Figure 88: The subjet opening angle as a function of jet $p_{\mathrm{T,jet}}$ in 0-20% central Au+Au collisions. The inset is the corresponding resolution of θ. Blue and green represent current (10 nb^{-1}) and future (including Run-23 and 25) analyses, respectively.

Given the unique nature of jet-medium interactions at RHIC, with the jet and sub-jet scales sufficiently closer to the medium scale than the LHC, the aforementioned measurements bolster the importance of the STAR jet program with the goal of extracting the microscopic properties of the QGP.

3.1.7 What is the Nature of the Phase Transition Near $\mu_B = 0$?

Lattice-QCD calculations [301, 302] predict a sign change in the susceptibility ratio χ_6^B/χ_2^B with temperature (T) taking place in the range of 145-165 MeV at $\mu_B = 0$. The observation of this ratio going from positive to negative values is considered a signature of a crossover transition. Interestingly, values of net-proton C_6/C_2 are found to be systematically negative from peripheral to central 200 GeV Au+Au collisions within large statistical uncertainties [53]. The hint of negative C_6/C_2 is intriguing, but the current result has less than 2.3σ significance for 30-40% centrality in terms of statistical uncertainties. The systematic uncertainty

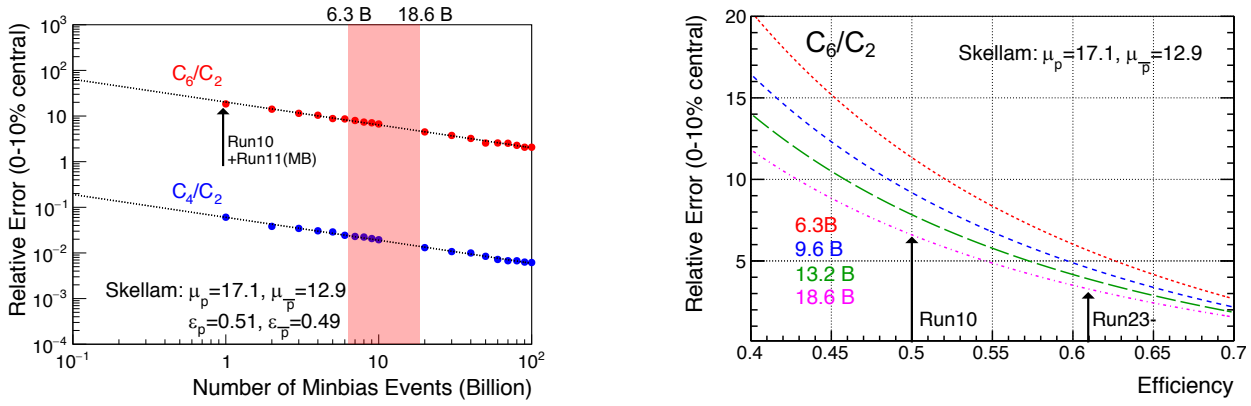

Figure 89: Projection for measurement of ratio of sixth order over second order cumulants of net-proton distribution.

is of similar magnitude as the statistical uncertainty. As shown in the projection plot of Fig. 89, it is possible to establish a definitive observation of negative C_6/C_2 at 200 GeV with 20 B minimum-bias events to be collected during Run-23 and 25 and taking into account an expected 15% increase in the reconstruction efficiency and enhanced acceptance thanks to the iTPC upgrade. A similar measurement can be performed at the LHC for vanishing baryon chemical potential, while only STAR measurements can explore the finite $\mu_{\rm B}$ region. Our measurement at $\sqrt{s_{\rm NN}} = 200$ GeV has the potential to establish the first experimental observation of QCD chiral crossover transition at $\mu_{\rm B} \approx 20$ MeV.

3.1.8 What Can We Learn About the Strong Interaction?

The strong interaction between baryons leads to a residual force; the most common example is the force between a nucleon and a hyperon (NY). The same force is responsible for binding n-p into d. So far, understanding the strong interaction has been limited to the effective theories related to nucleons and the scattering experiments, which are very challenging due to the short lifetime of those baryons (a few cm decay length). One of the current challenges is to evaluate the strong interaction between hyperons, as very little is known experimentally about NY and YY interactions. Hypernuclei (a hyperon bound inside an atomic nucleus) are proof of attractive interaction of NY. Measurements of NN and NY interactions have crucial implications for the possible formations of bound states. Studies of the strong interaction potential via two-particle correlations in momentum space measured in relativistic heavy-ion and elementary collisions have proven to be useful in gaining access to the interactions between exotic and rare particles. Possible combinations can be: $p\Lambda$, $p\Sigma$, $p\Omega$, $p\Xi$, $\Lambda\Lambda$, $\Xi\Xi$. In contrast to $p\Lambda$, the nature of $p\Sigma$, $p\Omega$, $\Lambda\Lambda$ still need experimental verification. Even if scattering experiments are available, they are not very conclusive.

Figure 90 shows the preliminary $p\Xi$ correlation function. All available statistics, 3 B events accumulated overall previous runs were used for the $p\Xi$ and $p\Omega$ cases. Combining datasets from different years leads to run-to-run variations, resulting in large systematic

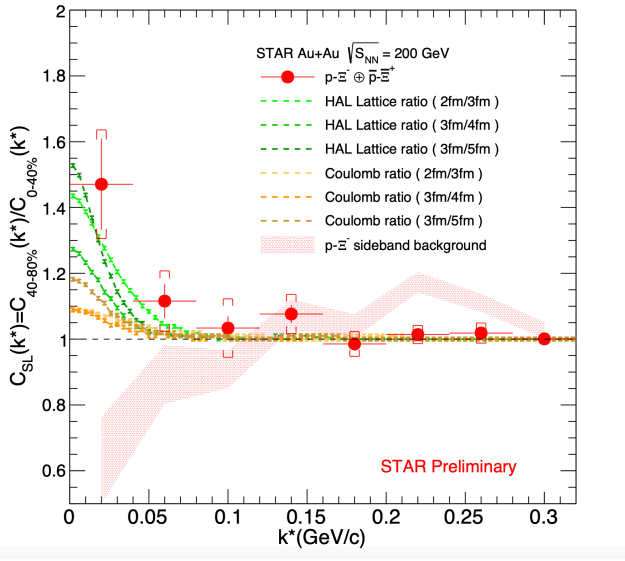

Figure 90: Solid circles represent the ratio (R) of the small system (40-80% collisions) to the large system (0-40% collisions) for proton–Ξ and $\bar{p}$–Ξ correlations. The bars correspond to the statistical uncertainties. The shaded area represents R for background candidates from the side band of the Ξ invariant mass distribution. Coulomb-induced R are shown in yellow and orange colors. HAL Lattice predictions of R are shown in green.

uncertainties in the detector responses. A long run with similar detector conditions during Run-23 and 25 will avoid such issues. Statistical uncertainties of the current measurements remain large, and the number of points used to build the correlation function is minimal. This means that the current results are not precise enough to study the strong interaction parameters in detail. The collection of 20 B events will make possible the construction of correlation functions of the $p\Xi$ case with double the number of points and smaller statistical uncertainties than the current measurement. The $p\Omega$ system is even more statistics-hungry. Previous STAR measurements of $p\Omega$ correlations show that the parameters of the strong interaction can be barely studied. More precise and detailed studies would require the large dataset to be collected in Run-25.

The description of the $\Lambda\Lambda$ interaction is still an open issue. Such a description is fundamental since it plays a decisive role in understanding the nature of hyperons that appear in neutron stars. If many hyperons appear close to each other and their fraction becomes significant, the YY interactions are expected to play an essential role in describing the equation of state of the dense system. Figure 91 shows preliminary $\Lambda\Lambda$ (left) and $\Xi\Xi$ (right) correlation functions. For current $\Lambda\Lambda$ and $\Xi\Xi$ measurements, data from all previous runs were combined, which also suffers from aforementioned run-to-run variations. The expected large sample of 20 B events is more critical for the $\Xi\Xi$ analysis, and it will enable the reduction of statistical uncertainties significantly and makes it possible to determine parameters of the strong interaction with high precision. Having this large dataset will also allow the hypothe-

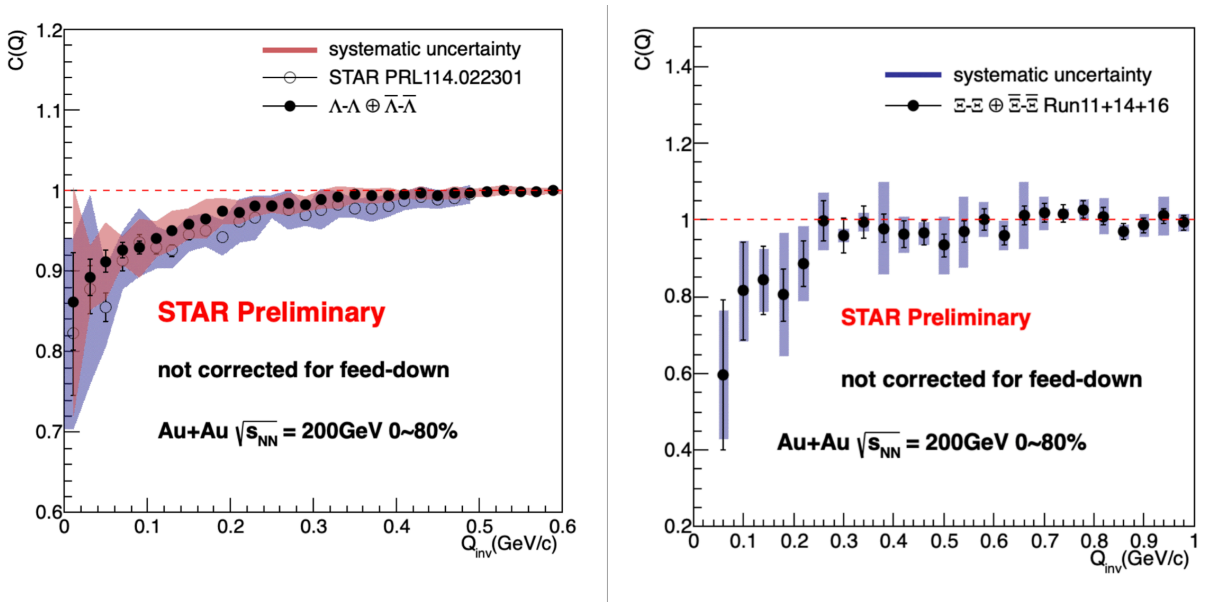

Figure 91: Left: combined ΛΛ and $\bar{\Lambda}\bar{\Lambda}$ preliminary correlation functions with systematic uncertainties compared with published results. Right: combined ΞΞ and $\bar{\Xi}\bar{\Xi}$ correlation functions with systematic uncertainties.

ses about possible bound states to be tested. Figure 92, left panel, shows error projections for the correlation functions of ΛΛ combined with $\bar{\Lambda}\bar{\Lambda}$ and ΞΞ with $\bar{\Xi}\bar{\Xi}$ assuming at least 2 correlated particles in the event. Compared to the results based on Run-11, Run-14, and Run-16 datasets, the relative statistical errors are expected to decrease by about a factor of 4 to 5 using Run-25 data. The reduction of the statistical uncertainties for the lowest relative pair momentum is shown in the right panel of Fig. 92.

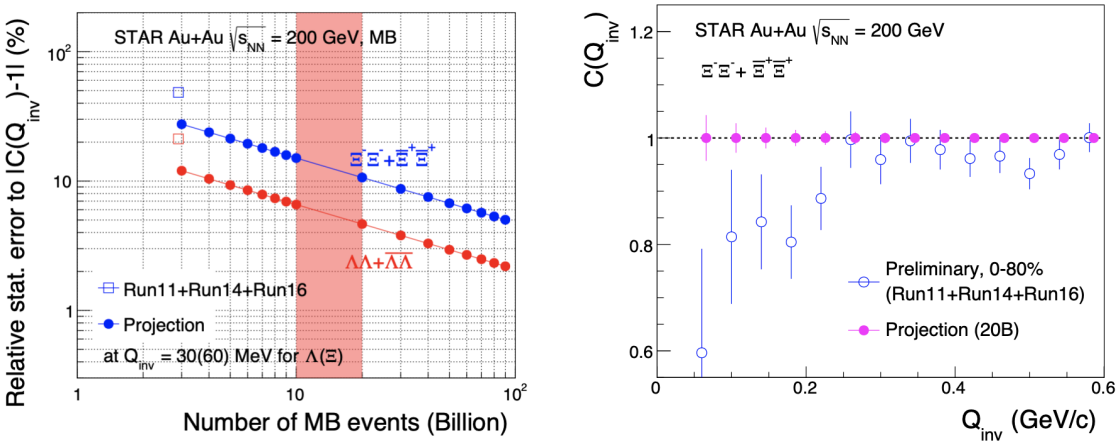

Figure 92: Left: error projections for ΛΛ together with $\bar{\Lambda}\bar{\Lambda}$ and ΞΞ together with $\bar{\Xi}\bar{\Xi}$ as a function of event statistics. Right: Error projections for ΞΞ together with $\bar{\Xi}\bar{\Xi}$ as a function of $Q_{\rm inv}$.

3.2 Ultra-Peripheral Collisions

One of the most important scientific goals in high-energy nuclear physics is to understand the nuclear structure under extreme conditions. Thanks to ultra-relativistic heavy-ion collider facilities, e.g., the Relativistic Heavy-Ion Collider, one direction is to create a system that has an extremely high temperature of partons, and study its deconfined properties of strongly interacting quarks and gluons. However, the other direction is to reveal the property of nucleons and nuclei before such violent collision happens, where the initial-state dynamics inside these particles may provide ultimate understanding of the Quantum Chromodynamics (QCD) in generating the visible matter. These two aspects are usually known as the heavy-ion hot Quark-Gluon-Plasma (QGP) physics and cold QCD physics, respectively. Both of them are indispensable building blocks of our fundamental understanding of nuclear physics. In this section, we will focus on the initial-state physics program via the ultra-peripheral collision in nucleus-nucleus (AA) interactions.

In relativistic heavy-ion collisions, a large fraction of the total cross section or interaction between the two colliding nucleus is provided by photon-induced reactions. Most of these events are removed by the requirement of inelastic collisions, because the hot quark-gluon-plasma (QGP) can be more likely, if not only, to be produced in such high parton density system. However, these events are difficult to understand if one wants to separate effects related to the initial state, e.g., nuclear parton distribution functions (nPDFs), from final-state interactions, such as fragmentation, medium-induced collective effects, etc. One way to overcome this difficulty is to "turn off" the QGP and use a simple and clean probe to examine the nuclear target - photon-nucleus collisions, which is also known as the "ultra-peripheral collisions" (UPC).

Typically, the UPC takes places when the impact parameter between the two colliding nucleus is greater than the sum of their radii. The interaction is initiated by one or multiple photons emitted from the moving charged ions, where the photon interacts with the other nucleus. Due to the large mass of the heavy nucleus, the emitted photons have very small virtualities or very small p_T. This process is regarded as *photoproduction*. For example, diffractive Vector Meson (VM) photoproduction has been extensively studied at the RHIC and at the LHC, where the gluon density distribution of the nucleon and nucleus target can be directly probed. In recent analyses carried out by the LHC collaborations [303–310], photoproduction of the J/ψ meson has been measured in UPCs of heavy ions. The resulting cross sections were found to be significantly suppressed with respect to that of a free proton. [303,304,308,309] Leading Twist Approximation (LTA) calculations strongly suggest that the suppression is caused by the gluon shadowing effect [311–313], while other models, e.g., the Color Dipole Model with gluon saturation and nucleon shape fluctuations [314], can also describe the UPC data qualitatively. The mechanism of gluon density modification in the nuclear environment remains unknown.

However, there are other processes of photoproduction that are sensitive to the nPDFs. For example, inclusive and diffractive back-to-back jets (dijets) in nuclei are sensitive to both quark and gluon distribution, and it is theoretically easier to be used in the global PDF analysis. Recent studies from Refs. [165, 315, 316] have shown the uncertainty of nPDFs

can be reduced by a factor of 2 by having these experimental measurements. In addition, the incoming low-virtuality photons can have properties of a point-like particle (direct process) or a hadron with partonic substructure (resolved process). The dijets photoproduction process can be extremely useful in constraining the photon structure, which still remains poorly known to-date. Finally, the diffractive dijets contribution is a sensitive experimental observable to understand the QCD factorisation breaking and the diffractive nPDFs.

Last but not least, inclusive particle photoproduction at high energy provides important insights to the *soft physics* of photon-nucleus interactions, where cold nuclear matter and Intra-Nuclear Cascade can be studied via fragmentation in both current and target fragmentation regions. One recent study led by Chang et al [317] has shown the difficulty of describing the charged particle production in nuclei of existing E665 experimental data. Although the experimental data of E665 is with higher photon virtualities, particle photoproduction in UPC at high energy can be complementary to the understanding of nuclear fragmentation in general. Furthermore, inclusive high-p_T charged particle or J/ψ photoproduction can be a baseline for comparison to the diffractive VM production, where different theoretical models have drastically different prediction, e.g., gluon saturation model [314] verse nuclear shadowing model. [311–313] The UPC data can provide important insights to the studies of non-linear gluon effects before the EIC. At the EIC, together with different VM productions and with different level arm of photon virtualities, this measurement will be extended much further and hopefully definitive.

Hereby, we propose to utilize the unique capability of the RHIC experimental program in the upcoming 2023-2025 runs with the STAR detector and its recent forward upgrades, to study photoproduction processes in details. The major advantage is that the top RHIC energy can access a kinematic regime that is hardly, if not at all, accessible by the LHC experiments, and provide a seamless transition to the physics at the EIC.

Photoproduction of Vector-Meson

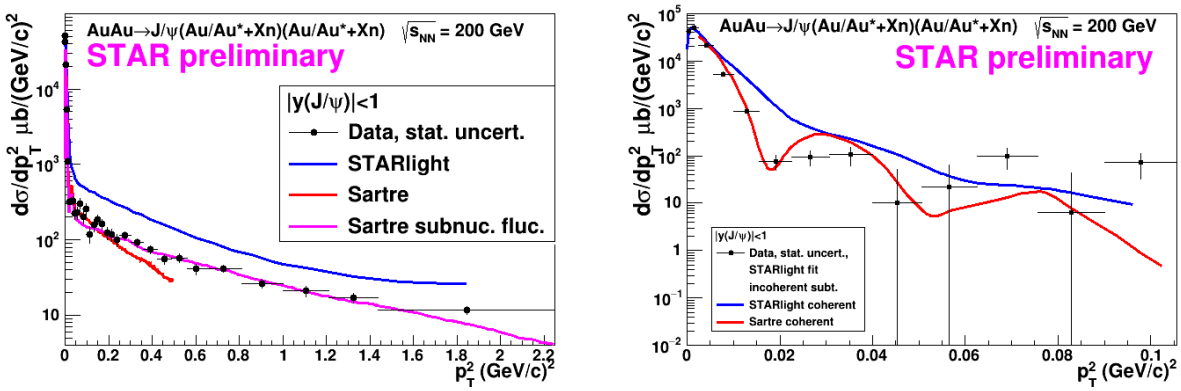

Figure 93: Left: differential cross section $d\sigma/dp_T^2$ of J/ψ photoproduction as a function of p_T^2 in Au+Au UPC at 200 GeV. Right: the same cross section but with incoherent contribution subtracted.

One of the most important and direct measurements of the gluon density in the initial-state of nuclei is the photoproduction of Vector-Meson, e.g., ρ^0, ϕ, and J/ψ. The process can be generally considered in a color dipole picture, where the quasi-real photon emitted from the heavy nucleus fluctuates into a quark and anti-quark pair (leading order). The quark and anti-quark pair scatters off the nucleus with a Pomeron exchange and becomes a Vector-Meson; the cross section of this process is directly sensitive to the gluon density and its spatial distribution.

In previous STAR publications, there has been studies on ρ^0 meson, e.g., the most recent analysis in Ref. [305] for coherent photoproduction. Although the measurement has provided important insights to the structure of the gold nucleus, e.g., the impact parameter distribution from a Fourier transform of the momentum transfer $-t$ distribution, the general theoretical concern is that the process lacks of a hard scale because the mass of ρ^0 is rather small. Therefore, perturbative calculations of QCD are difficult to be carried out. In addition, the scale dependence of the photoproduction process is also of great interest, which can be only achieved by varying the mass of the Vector-Meson in photoproduction. Therefore, heavier vector-mesons, e.g., J/ψ, are important to be measured.

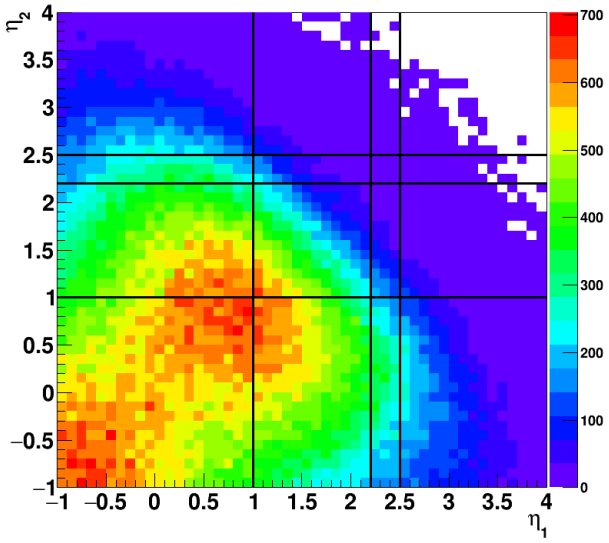

Figure 94: Pseudorapidity distribution of daughter electrons from the J/ψ decay using STARLight MC simulations. Lines are boundary acceptance of Barrel, Endcap, and Forward upgrade detectors.

In Fig. 93, the STAR preliminary results on J/ψ photoproduction are shown in Au+Au UPC at 200 GeV. The differential cross section of $d\sigma/dp_T^2$ as a function of p_T^2 is presented, with the total contribution (left) and coherent contribution only (right). The data has been compared with leading Monte Carlo models STARlight and Sartre, where a much better description by Sartre is found. This is the first differential measurement of J/ψ photoproduction off gold nucleus at the center-of-mass energy between photon and nucleon (proton or neutron), $W \sim 25$ GeV, which provides important constraints to the gluon density

and its spatial distribution at this kinematic region, $x_g \sim 0.01$. The observed suppression of the gluon density from this data, compared to the Impulse Approximation, is found to be 15-20%.

Since the data presented above was taken in 2016, the acceptance of J/ψ is limited to rapidity $y < 1$ due to the η acceptance of the daughter electrons. However, this can be significantly improved in Run-23+2025 Au+Au at 200 GeV with the endcap EMC, inner TPC, and forward upgrade detectors. The extension of acceptance in rapidity to $1 < y < 1.5$ can lead to a lower x down to 4×10^{-3}, which overlaps with the LHC kinematics, as well as going to higher x up to 0.05. With the forward upgrades, $y > 2.5$, the kinematic coverage will be even wider, where STAR can cover a regime that is complementary to the LHC, e.g., the anti-shadowing region $x_g \sim 0.1$.

In Fig. 94, it shows the pseudorapidity distribution of both daughter electrons from the J/ψ decay, simulated by the STARLight MC model. The lines are boundaries of the barrel, endcap, and forward detector acceptances. By extending to the endcap and forward, there is a significant improvement in the J/ψ acceptance. Based on the established UPC J/ψ trigger using both barrel and endcap, a high statistics event sample can be collected.

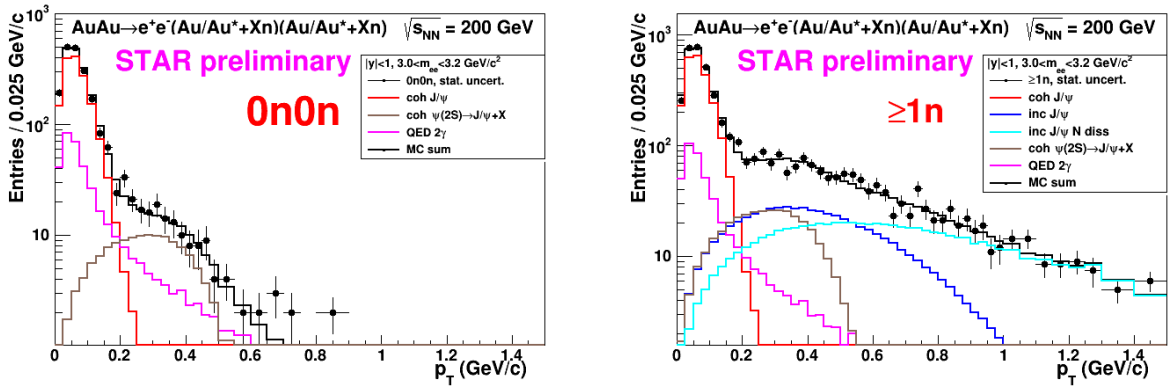

Figure 95: Uncorrected p_T of J/ψ mesons fitted with different contributions in Au+Au UPC at 200 GeV with no neutron on either side (left) and at least 1 neutron on either side (right).

When extending the acceptance of J/ψ to higher rapidity, there is a long standing issue of photon energy ambiguity. At a J/ψ rapidity that $y \neq 0$, the photon energy can be $(M_J/2)e^{\pm y}$, which corresponds to a higher and lower photon energy, respectively. However, thanks to the neutron tagging in the ZDCs, this ambiguity can be resolved by considering different neutron multiplicities and their theoretical expected photon fluxes. [318] The STAR analysis using this method has just begun. In order to qualitatively see the difference by introducing different neutron tagging classes, see Fig. 95. For details of this method, see Ref. [318].

Finally, for the STAR upcoming Run-23+25, there is an opportunity for measuring the photoproduction of ϕ meson for the first time. The experimental challenge of this measurement is that ϕ is usually reconstructed via the kaon channel. However, for photoproduction

process, the momentum of the kaon daughters are very soft, ~ 100 MeV/c, such that reconstructing the daughter tracks has been impossible with only the TPC. However, for the upcoming runs, the inner TPC could push the low momentum tracking down to ~ 100 MeV/c. There are two ways to achieve a statistical significant event sample of UPC ϕ meson.

The first one is to use ZDC coincidence trigger with no TOF requirement at the full magnetic field in STAR, while the second one is to use the standard TOF-base UPC Vector-Meson trigger at half-field. At full field, although the inner TPC can reconstruct tracks down to ~ 100 MeV/c, it would not reach TOF for triggers due to the small bending radius. Therefore, events can be collected without a dedicated UPC ϕ trigger. This requires a large integrated luminosity to reach a few thousand raw ϕ events, based on the recent study using 2019 Au+Au data. However, if STAR can be run at half field, the TOF-base trigger might be applicable. See Fig. 96 for illustration of the TOF-based trigger acceptance in kaon p_T. Half-field running is not currently being proposed, but detailed simulations are in progress to fully evaluate.

With all three Vector-Meson (ρ^0, ϕ, and J/ψ) measured at STAR in Au+Au UPC, they will provide an unprecedented understanding of the diffractive process off the gold nucleus in photoproduction, providing valuable experimental inputs to such physics at the EIC.

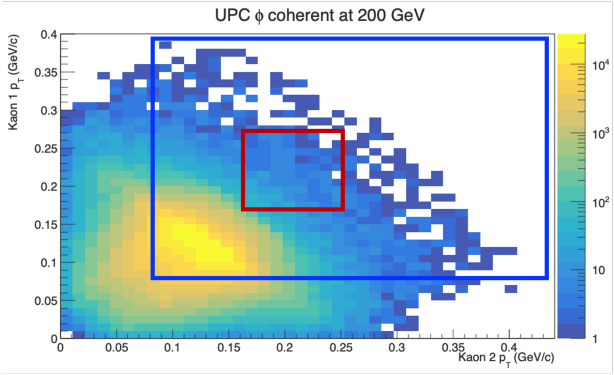

Figure 96: UPC ϕ meson decay p_{T} distributions of daughter 1 vs 2. The red box is the acceptance in p_{T} if requiring track to reach the location of TOF at STAR's full magnetic field; blue box is showing the same but with STAR at the half-field running.

Vetor-Meson decay: probing gluon distribution inside the nucleus

STAR recently observed a significant $\cos 2\Delta\phi$ azimuthal modulation in $\pi^+\pi^-$ pairs from photonuclear ρ^0 and continuum production. The structure of the observed modulation as a function of the $\pi^+\pi^-$ pair $P_\perp$, appears related to the diffractive pattern. Recent theoretical calculations [319], which implemented linearly polarized photons interacting with the saturated gluons inside a nucleus, have successfully described the qualitative features of the observed modulation (see Fig. 97), and indicate that the detailed structure of the $\cos 2\Delta\phi$ modulation vs. $P_\perp$ is sensitive to the nuclear geometry and gluon distribution. Data from

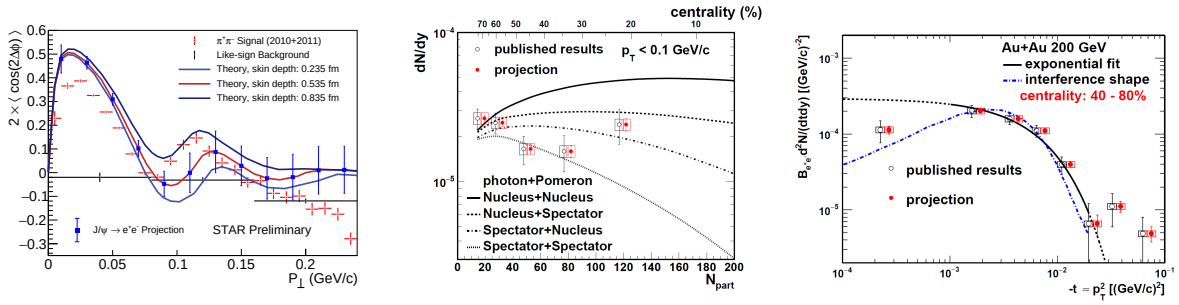

Figure 97: Left: Measurement of the $\cos 2\Delta\phi$ modulation of $\pi^+\pi^-$ pairs from photonuclear ρ^0 and continuum production compared to theoretical predictions [319]. Projections are shown for a similar measurement of the azimuthal modulation of e^+e^- pairs from photonuclear production of the J/ψ. Center: Projection of the dN/dy of photoproduced J/ψ in non-UPC events vs. the event centrality (N_{part}) compared to various theoretical production scenarios. Right: Projection of the t spectra of photoproduced J/ψ in $40-80\%$ central collisions.

Run-23 and Run-25 would allow the additional statistical reach needed to perform multi-differential analysis, providing stronger theoretical constraints. Specifically, multi-differential analysis of the $\cos 2\Delta\phi$ modulation with respect to pair rapidity and pair mass are needed. Multi-differential analysis with respect to pair mass is needed to separate the ρ^0 production from the continuum Drell-Soding production. Multi-differential analysis with respect to the pair rapidity is needed to quantitatively investigate how the double-slit interference mechanism effects the structure of the observed azimuthal modulation. Additional statistical precision is also needed for measurement of the higher harmonics. Similar measurements with $J/\Psi \to e^+e^-$ can be performed and such measurements at higher mass provide better comparison with more reliable QCD calculation.

Ultraperipheral AA collisions, where photons generated by the Lorentz-boosted electromagnetic field of one nucleus interact with the gluons inside the other nucleus, can provide certain 3D gluonic tomography measurements of heavy ions, even before the operation of the future EIC. STAR has performed experimental measurements of the photoproduction of J/ψ at low p_T in non-UPC heavy-ion collisions [320], accompanying the violent hadronic collisions. A detailed study with p_T distributions has shown that the $|t|$ distribution in peripheral collisions is more consistent with the coherent diffractive process than the incoherent process. Although models [321, 322] incorporating different partial coherent photon and nuclear interactions could explain the yields, it remains unclear how the coherent process happens and whether final-state effects play any role. [323] Resolving this puzzle with high statistical data and detailed $|t|$ distributions at different centralities at RHIC as projected for Run-23+25 in Fig. 97 may be important for understanding what defines the coherentness of the photoproduction, how vector mesons are formed in the process and how exclusive the similar process has to be in future EIC experiments with forward neutron veto/tagging.

Photoproduction of dijets

In addition to photoproduction of Vector-Meson, photoproduction of back-to-back jets has been increasingly interested in the context of nuclear PDF. The process is a two-to-two hard scattering between a direct or resolved photon from the projectile (photon from UPC) and the quarks or gluons from the nucleus target. The final-state is a pair of back-to-back jet, which is directly sensitive to the photon and nuclear structure in terms of parton distribution functions. At the LHC, this process corresponds to the kinematic region $x_A \sim 10^{-3}$, which is the gluon dominated regime. Here we propose to measure the photoproduction dijets at STAR, where kinematic regions, e.g., the anti-shadowing and the EMC region, can be reached. This measurement has never been done at RHIC and will provide a significant constraints to the nPDFs of heavy nucleus at this kinematics for photoproduction.

The pseudo-data from eA collisions used here is generated by BeAGLE (**B**enchmark **eA** **G**enerator for **LE**ptoproduction) [317], based on the lepton and gold beam energy of 18× 100 GeV, where the input PDF for the the exchanged photon is the CTEQ 5 from the LHAPDF library [324] and EPS09 for the nuclear PDF.

Jets are reconstructed by FastJet [325] with the anti-k_T algorithm, which is based on the energy distribution of final state particles in the angular space. All the stable and visible particles produced in the collisions with $p_T > 250$ MeV/c and $-1.5 < \eta < 1.5$ and $2.5 < \eta < 4.0$ in the laboratory system are taken as input. The jet cone radius parameter has been set to $R_{\rm jet} = 1$ in the jet finding algorithm. To obtain the events in Au+Au UPC collisions at $\sqrt{s_{\rm NN}} = 200$ GeV from simulations of eAu at 18×100 GeV, an event-by-event weight is applied according to the photon flux difference between eA and Au+Au UPC collisions.

After reweighing we obtain the dijet events with the pesudorapidity of jets ($\eta^{\rm jet}$) from -1.5 to 1.5 in middle rapidity region and $2.5 < \eta^{\rm jet} < 4.0$ in the forward region. In each event, the jet with the highest p_T is called the trigger jet, the jet with the second highest p_T is called the associate jet. Events are selected with the requirement that the trigger jet has $p_T^{\rm trig} > 5$ GeV/c and the associated one has $p_T^{\rm asso} > 4.5$ GeV/c. 100 M event are generated, after all cuts applied, we found ~ 5600 dijet events corresponding to the integrated luminosity $L = 9$ nb^{-1}. Therefore, with STAR Run-23+25 Au+Au collisions, an event sample of dijets of 50-60k is expected.

In 200 GeV Au+Au UPC collisions, the distributions of jets' pesudorapidity and p_T can be found in Fig. 98. Jets dominate at $\eta \sim 0.5$ with the maximum $p_T \sim 20$ GeV/c.

In BeAGLE, depending on the wave function components for the incoming virtual photon, the major hard processes are divided into three classes: the direct processes, the soft VMD processes and the resolved processes (hard VMD and anomalous). The direct photon interacts as a point-like particle with the partons of the nucleon, major subprocesses in direct category: LO DIS, Photon-Gluon Fusion (PGF) and QCD Compton (QCDC). While the VMD and anomalous components interact through their hadronic structure. Resolved photon processes play a significant part in the production of hard high-p_T processes at $Q^2 \approx 0$. The following hard subprocesses are grouped in the resolved processes category: $qq \to qq$, $q\bar{q} \to q\bar{q}$, $q\bar{q} \to gg$, $qg \to qg$, $gg \to q\bar{q}$, $gg \to gg$. The examples of Feynman diagrams of resolved and direct processes are shown in Fig. 99.

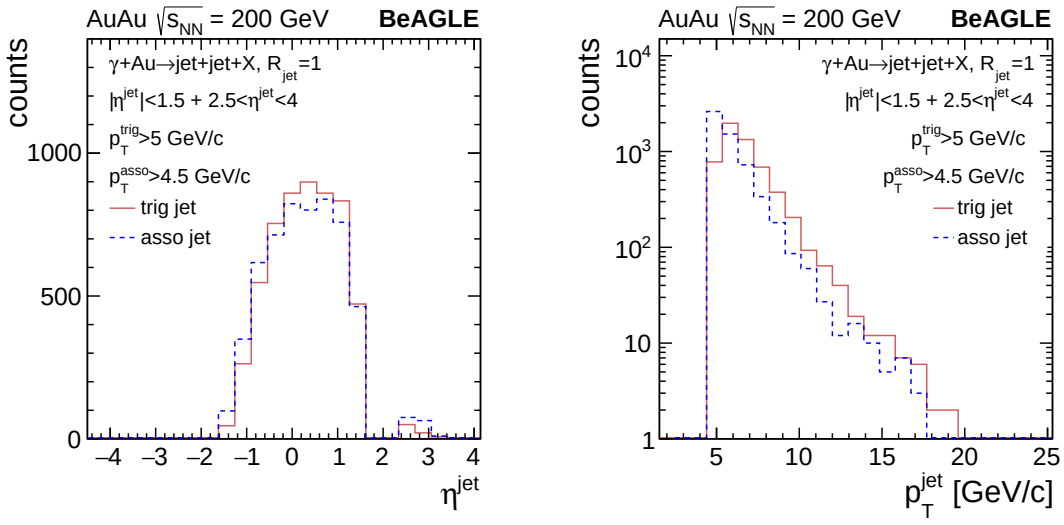

Figure 98: In Au+Au UPC collisions at $\sqrt{s_{\rm NN}}$ = 200 GeV, the dijet events are selected with $|\eta^{\rm jet}| < 1.5 + 2.5 < \eta^{\rm jet} < 4.0$. For the trigger jet: $p_T^{\rm trig} > 5$ GeV/c, associate jet: $p_T^{\rm asso} > 4.5$ GeV/c. Left: the pesudorapidity distributions of the trigger and associated jets; right: the p_T distributions of the trigger and associated jets.

The momentum fraction of the parton from the exchanged photon (x_γ) and the momentum fraction of the parton from the gold beam ($x_{\rm Au}$) can be reconstructed knowing the momentum and angles of dijets as

$$x_\gamma = \frac{1}{2E_\gamma}(p_T^{\rm tirg} e^{-\eta_{\rm trig}} + p_T^{\rm asso} e^{-\eta_{\rm asso}}) \tag{3}$$

$$x_{\rm Au} = \frac{1}{2E_{\rm Au}}(p_T^{\rm tirg} e^{\eta_{\rm trig}} + p_T^{\rm asso} e^{\eta_{\rm asso}}) \tag{4}$$

where E_γ is the photon energy which can be determined from the hadronic final-state, see later for details. Eq. 3 and Eq. 4 are valid in the lab frame in LO.

The reconstructed x_γ and $x_{\rm Au}$ in AuAu UPC dijet events can be seen from Fig. 100. The reconstructed x_γ covers a wide range from 0.2 to 0.9 in resolved process, and dominates at high x in direct process. The reconstructed $x_{\rm Au}$ distributions contain two peaks as there are two pseudorapidity regions. The forward pseudorapidity ($2.5 < \eta^{\rm jet} < 4.0$) leads to the peak at high $x_{\rm Au} \sim 0.5$, while middle rapidity jets ($|\eta^{\rm jet}| < 1.5$) contribute the peak at $x_{\rm Au} <\sim 0.2$. With the Run-23 and 25 data of Au+Au and Run-24 p$^\uparrow$+Au at STAR, this will become the first measurement at this kinematic region at RHIC with good statistical precision.

Taking one step further, the exclusive or diffractive dijets can also be measured in $p^\uparrow p^\uparrow$, p$^\uparrow$+Au, and Au+Au at $\sqrt{s_{\rm NN}} = 200$ GeV. The process is diffractive such that there are only two jets in the event, where the target nucleon or nucleus stay intact. Similar to exclusive Vector-Meson production discussed earlier, the exclusive dijets can provide a large impact in understanding the nucleon and nuclear structure over a wide range of kinematics. In

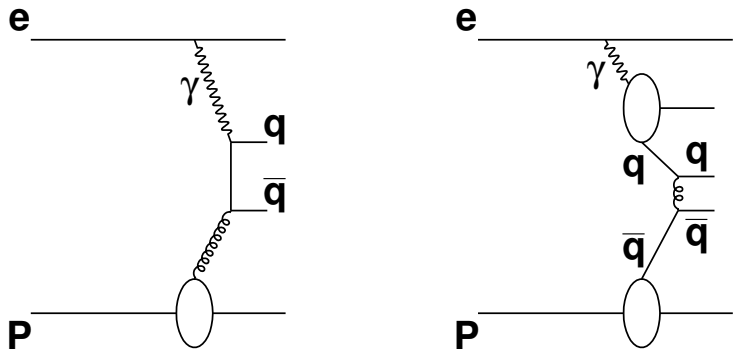

Figure 99: Examples of diagrams for direct (left) and resolved (right) processes in electron-proton scattering. In UPC, the photon emitter is replaced with the Au nucleus.

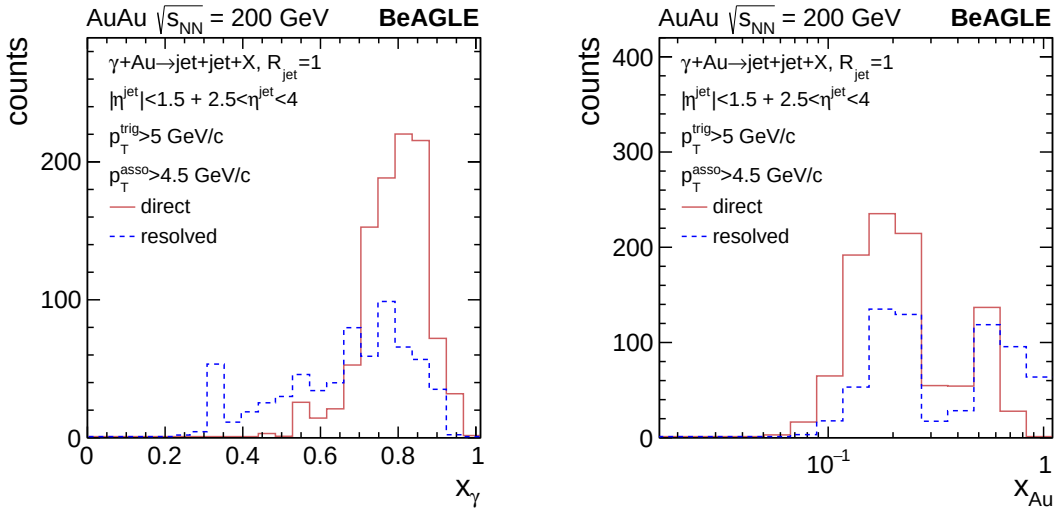

Figure 100: In AuAu UPC collisions at $\sqrt{s_{\rm NN}}$ = 200 GeV, the dijet events are selected with $|\eta^{\rm jet}| < 1.5 + 2.5 < \eta^{\rm jet} < 4.0$. For the trigger jet: $p_T^{\rm trig} > 5$ GeV/c, associate jet: $p_T^{\rm asso} > 4.5$ GeV/c. Left: the x_γ distributions in resolved and direct processes; right: he $x_{\rm Au}$ distributions in resolved and direct processes.

addition, with the unique target polarization at RHIC, the exclusive dijets could be sensitive to Generalized Parton Distributions and p_T Dependent PDFs. This process is expected to be complementary to the process discussed in Sec. 2.1. In Fig. 101, the diffractive dijets photoproduction in p+Au UPCs are shown, with the transverse energy ($E_{\rm T}$) on the left panel and the dijet η separation distribution on the right panel. For a first look, the STAR Upcoming run 2024 would have enough luminosity to achieve reasonable statistics of this measurement; the same measurement can be done in p+p and Au+Au collisions.

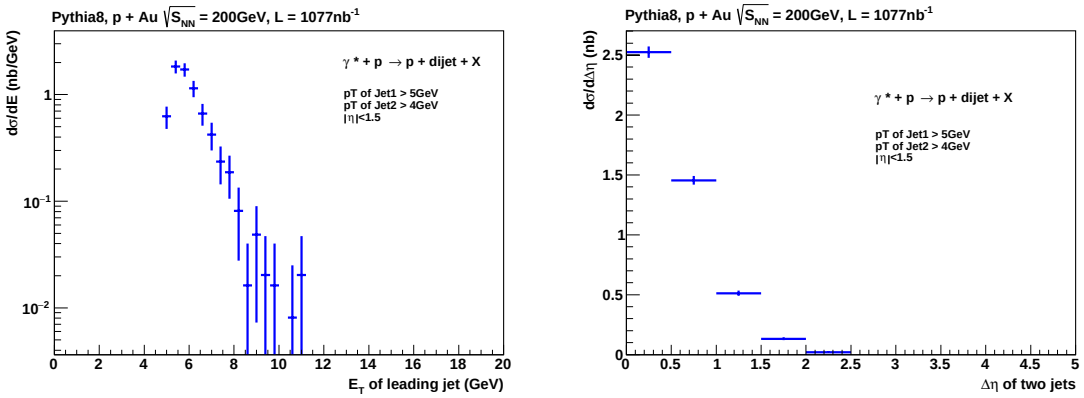

Figure 101: In p+Au UPC collisions at $\sqrt{s_{\rm NN}} = 200$ GeV, the diffractive dijet events are selected with the trigger jet: $p_T^{\rm trig} > 5$ GeV/c and associate jet: $p_T^{\rm asso} > 4.0$ GeV/c. The $E_{\rm T}$ distributions of the leading jet (left) and $\Delta\eta$ of the dijets distributions (right) are shown with ~ 1 μb^{-1} integrated luminosity.

Additional opportunities are available for STAR Run-23+25 based on UPC jets, e.g., measurement of diffractive dijets off polarized proton target, and azimuthal correlation of the dijets, which will be sensitive to nPDFs, diffractive nPDFs, QCD factorisation breaking, and spin structure of the proton. Here we do not elaborate them in details but defer the readers to Refs. [165, 316, 326–329] for both UPCs and at the EIC.

Photoproduction of inclusive charged particles and cross sections

Inclusive photoproduction processes in high-energy ep collisions have been extensively studied at HERA, e.g., charged particle productions, inclusive cross section, heavy-flavor production, etc. Recently, there have been efforts re-analyzing the HERA data in photoproduction and deep inelastic scattering to look for collectivity in terms of azimuthal correlations [330], inspired by the outstanding flow phenomena in heavy-ion collisions. At the LHC, experiments have just begun using the UPCs to look at collisions between photons and heavy nuclei in photoproduction, primarily to search for the collective phenomena. However, inclusive photoproduction processes in nuclei at high energy remains largely unexplored.

Inclusive photoproduction process is generally challenging for the UPC in heavy-ion experiments. At HERA, photoproduction in ep scattering can be unambiguously identified by the small angle electron taggers, where event kinematics can be reconstructed. However, in heavy-ion UPCs, the photon emitting nucleus is invisible to the experiment, leaving the kinematics, e.g., W, largely unconstrained. In a recent study using general-purpose eA MC model BeAGLE, it is found that the event kinematic reconstruction in UPC can be approached based on the hadronic final-state (HFS).

In Fig. 102 left, it shows the photon energy distribution based on MC simulation of BeAGLE of eAu 18 × 100 GeV. In addition, by using the photon flux generated by the

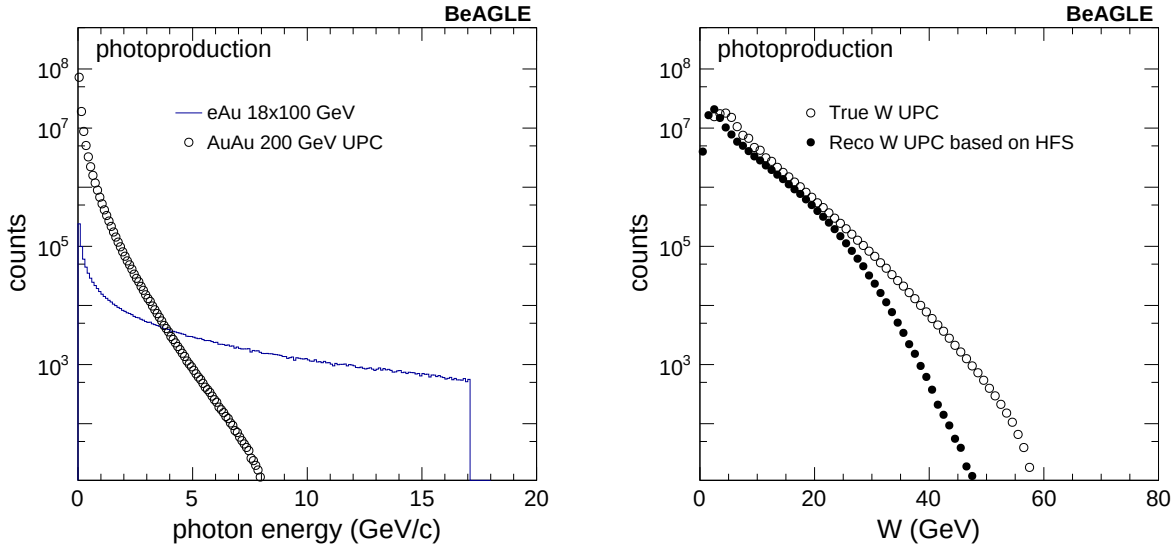

Figure 102: Left: photon energy distribution in eA and Au+Au UPC. Right: The truth level W in Au+Au UPC and the corresponding reconstructed level based on the HFS method.

UPC at 200 GeV Au+Au collisions, the photon energy spectra is reweighted and shown as the open circle. The low photon energy is greatly enhanced due to the large flux generated by the heavy nucleus, while the spectra is much steeper than in the eAu collisions. In Fig. 102 right, the HFS method has been adopted to reconstruct the kinematic variable W, based on the STAR acceptance including the forward upgrade detectors. The smearing from truth to reconstructed W is visible and stronger at large W. However, by selecting on the reconstructed W, the event kinematics can be better controlled than using the average only. Unfolding technique can be used here for correcting the bin migration in W as well. Note that there is no detector simulations shown here.

In the upcoming RHIC Run-23 and Run-25, the inclusive photoproduction is of great interest. The cross section of such events is generally large, while a different trigger is required comparing to the standard minimum-bias hadronic collision trigger. The baseline trigger has been developed during the Au+Au 200 GeV data taken in 2019, where only a ZDC coincidence was required. For Run-23 and 25, asymmetry BBC response could be added to more efficiently select the inclusive photoproduction process.

Search for collectivity and signatures of baryon junction in photo-nuclear (γ+Au) processes

Until the EIC is built, high-energy photoproduction processes (low virtuality limit of the deep inelastic scattering) can be studied using ultra-peripheral ion collisions (UPCs) that occur when two heavy ions interact at large impact parameters. Such collisions can be considered as γ+Au processes but unlike at the EIC, the photons involved in UPCs are

quasi-real. For UPCs at top RHIC energies one expects the energy of the quasi-real photon to be approximately $E_\gamma \approx 3$ GeV. The typical range of the center of mass energy of the photon-nucleon system will therefore be $W_{\gamma N} \approx 40$ GeV. Therefore, Au+Au collisions at $\sqrt{s_{NN}} = 200$ GeV will provide access to the γ+Au process at 40 GeV center of mass energy. Our specific interest is high activity inclusive γ+Au process to search for collectively and improve our understanding of the mechanism of baryon stopping.

A satisfactory microscopic explanation of how collectivity originates from the basic processes of QCD and evolves with collision system size is a topic of broad interest in the community of high energy nuclear physics. The formation of a quark-gluon plasma medium and its fluid-dynamic expansion explain the origin of collectivity in Au+Au collisions. Results from RHIC small system scan indicate fluid-dynamic expansion are essential to drive collectivity in ^{3}He/d/p+Au collisions. [331] A search for collectivity in γ+Au interactions at RHIC will be a natural continuation of the recent system size scan [331], extending it at the small end to complete the hierarchy: Au+Au > ^{3}He+Au > d+Au > p+Au > γ+Au. This will help better address how collectivity originates and evolves with system size. If collectivity is observed in γ+Au processes it can provide a way to explore the creation of a many-body system exhibiting fluid behavior in photon-induced processes. [332] A recent calculations in Ref [332] assumes γ+A processes are equivalent to collisions of vector meson with ions (ρ+A collisions) and describe first measurements of harmonic coefficients v_n in photonuclear processes measured by the ATLAS collaboration. [333] The hypothesis of γ+A process as ρ+A collisions and the formation of a fluid-dynamic medium can be tested at RHIC in a data-driven way. This can be done by comparing measurements in γ+Au processes at $W_{\gamma N} \approx$40 GeV and in d+Au collisions at $\sqrt{s_{\rm NN}}\bar{3}9$ GeV. The former will be possible if a high statistics data set is collected for Au+Au collisions at $\sqrt{s_{\rm NN}}\bar{2}00$ during the Run-23 and 25 and the latter can be performed with the existing RHIC data on tape. It is known from RHIC measurements, argument based on initial geometry and, fluid dynamic calculations that elliptic anisotropy coefficient follow a hierarchy of v_2(d+Au) > v_2(p+Au) at a fixed collision energy and multiplicity. [331, 334] Following a similar argument one expects v_2(d+Au) > v_2(ρ+Au). In the fluid dynamic picture of Ref [332] the elliptic anisotropy coefficient will show the following hierarchy: v_2(d+Au) > v_2(γ+Au). A similar test by comparing v_2(p+Pb) and v_2(γ+Pb) at the LHC is difficult since the center of mass energy differs by a factor of six between p+Pb and γ+Pb collisions.

Photonuclear processes can also be used to study the origin of baryon stopping and baryon structure in general. One proposed mechanism for explaining the baryon stopping is the baryon junction: a nonperturbative Y-shaped configuration gluons which is attached to all three valence quarks. In this picture it is the baryon junction that carries the baryon number rather than the valence quarks. The existence of baryon junctions and their interaction with the incoming target or projectile are theorized to be an effective mechanism for substantial baryon stopping in pp and AA [335], but this has yet to be confirmed experimentally. Photonuclear processes allow us to study baryon stopping in the simplest possible process. The vast majority of these collisions occur through what is called the resolved process where the quasi-real photon fluctuates into a quark-antiquark pair which then collides

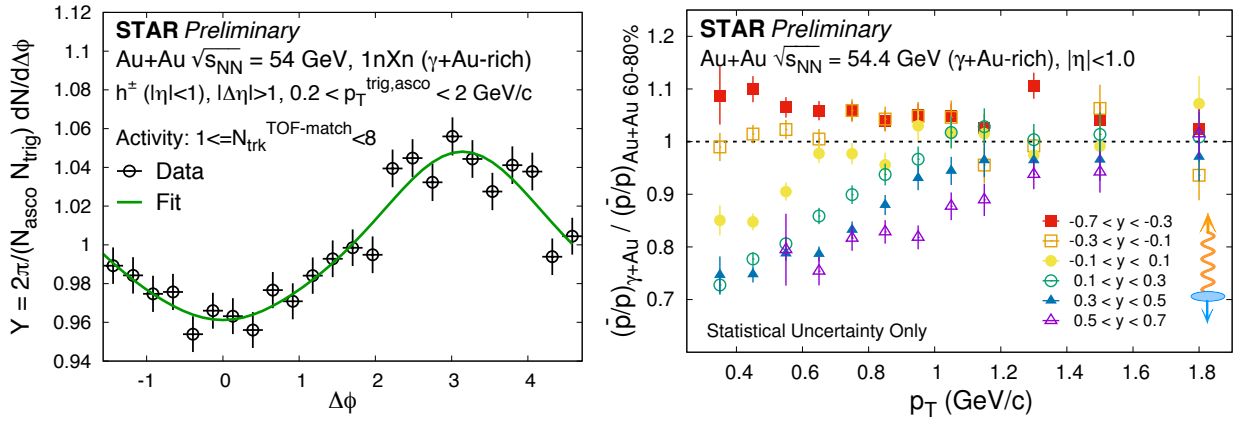

Figure 103: (Left) STAR preliminary data on normalized yield of long range di-hadron correlations in γ+Au-rich events with a relative pseudroapidity gap of $|\Delta\eta| > 1$ between two hadrons. The events are selected by applying asymmetric cuts on the energy deposition of neutrons in ZDCs (1nXn) and on TPC tracks matched with TOF $N_{\rm trk}^{\rm TOF-match}$ in the window of $1 <= N_{\rm trk}^{\rm TOF-match} < 8$. The green curve represents a fit to data using a function: $1 + 2\sum a_n \cos(n\Delta\phi)$. No signatures of collectivity associated with enhancement of correlation near relative azimuthal angle $\Delta\phi \sim 0$ is observed. (Right) The double ratio of antiprotons to protons in γ+Au-rich events compared to peripheral Au+Au events, indicating significant enhancement of protons at low p_T and at mid-rapidity. The enhancement shows a strong rapidity dependence while going from the photon to ion direction.

with the other ion. [336] If the baryon number were carried by the three valence quarks, then this quark-antiquark pair would not be able to stop the baryons, but it is possible for the quark-antiquark pair to interact with the junction and produce a midrapidity baryon. An added benefit is that photonuclear processes are highly asymmetric and baryons only enter from one side of the collision. The baryon-junction stopping mechanism is predicted to cause an exponential damping of the cross section with rapidity $\sim \exp\left(-\alpha_0^J(y - Y_{\rm beam})\right)$, where $\alpha_0^J \simeq 1/2$ is the Regge intercept of the baryon junction. [335] In a symmetric hadronic collision, baryons are traveling from either direction so the stopping of both the target ($\sim \exp\left(-\alpha_0^J(y - Y_{\rm beam})\right)$) and the projectile ($\sim \exp\left(\alpha_0^J(y - Y_{\rm beam})\right)$) will likely compensate for each other, leading to a nearly symmetric distribution. But in an asymmetric system like a photonuclear collision, this exponential shape should be visible.

A handful of data sets exist on the disk with the appropriate event trigger selection for studying photonuclear processes at RHIC. In Fig. 103 we present preliminary results on γ+Au-rich interactions using Au+Au 54 GeV data from STAR shown at the Quark Matter 2022 conference. By identifying the single neutron peak for individual ZDCs, we require the cuts equivalent to 1nXn. We apply an asymmetric cut on east and west BBCs to improve the purity. We also make sure the position of the primary vertex along collision direction V_z from TPC and VPD detectors differs by about 10 cm. After applying such cuts on Au+Au 54 GeV data we perform measurements in γ+Au-rich events.

Figure 103 (left) shows the normalized yield, differential in relative azimuthal angle of the trigger and associated particles $Y(\Delta\phi) = 2\pi/N_{\rm trig}/N_{\rm asco}dN^{\rm pair}/d\Delta\phi$ integrated over a

relative pseudorapidity window of $|\Delta\eta| > 1$. For this analysis, the p_T of trigger and associated particles is chosen to be within $0.2 < p_T^{\rm trig,asco} < 2$ GeV/c. The distribution $Y(\Delta\phi)$ is shown for two different bins of activity characterized by the number of TPC tracks matched with the TOF $1 <= N_{\rm trk}^{\rm TOF} < 8$ (low activity). The distribution is fitted using a Fourier function of the form $(1 + 2\sum a_n \cos(n\Delta\phi))$ (green curve). No ridge-like component associated with a significant enhancement of $Y(\Delta\phi)$ near $\Delta\phi = 0$ that is related to the signature of collectivity is seen.

Figure 103 (right) shows the measurement of the yield of anti-protons-to-protons ($\bar{p}/p$) with $p_{\rm T}$. The quantity plotted is a double ratio of $\bar{p}/p$ for the measurements in γ+Au-rich events over the same in 60–80% peripheral Au+Au events. We see a suppression of the $\bar{p}/p$ yield in γ+Au events at low $p_T < 0.6$ GeV/c and for the symmetric window of $-0.1 < y < 0.1$ around mid-rapidity. The suppression of $\bar{p}/p$ yield gets stronger while going from the photon to the ion direction, with the double ratio dropping by a factor 0.75 at low p_T. We have checked that this trend is not seen for π^-/π^+, K^-/K^+ and not explained by PYTHIA 6 model. This important observation provides the necessary impetus for further exploration using various available data sets. In particular, we would like to test if this strong rapidity dependence of the $\bar{p}/p$ yield is consistent with the picture of baryon junction that predicts an exponential dependence of stopping with rapidity of form $\exp(-\alpha(y - Y_{\rm beam}))$ with α =0.5.

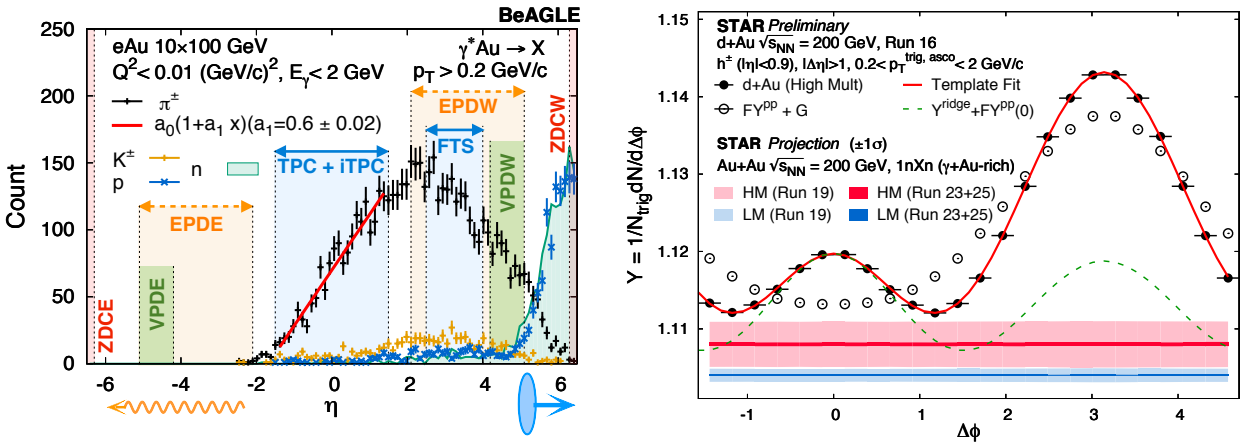

Figure 104: (Left) Pseudorapidity distribution of different particles using the state-of-the-art BeAGLE [317, 337] event generator for the EIC in e+Au events. By restricting the virtuality and energy of the photon (γ^*) we try to mimic the kinematics of a $\gamma + Au$ (Au+Au UPC) event. The purpose of this plot is to demonstrate how different STAR detectors will be used to identify such UPC processes. (Right) STAR preliminary data on per-trigger yield estimated using di-hadron correlations in d+Au (hadronic) 200 GeV collisions. The correlation function in p+p collisions (open circle) is used as a template to fit the same in relatively high multiplicity d+Au collisions (solid circle) and to extract the long-range ridge-like component. The red and blue band show projections for $\gamma + Au$ enriched events for two different multiplicity bins. The aim is to use the correlation function from the low multiplicity $\gamma + Au$ to perform template fit in the high multiplicity bin.

Our aim will be extend these measurements with high statistics γ+Au-rich event samples

using Run-23 and 25 data on Au+Au collisions at $\sqrt{s_{\rm NN}}$ = 200 GeV. Fig. 104(left) shows the pseudorapidity (η) distribution of identified particles with $p_T > 0.2$ GeV/c in inclusive e+Au photoproduction (γ^*+Au, where γ^* refers to a virtual photon) processes simulated using the EIC Monte Carlo BeAGLE event generator [317, 337] with electron and ion beam energy of 10 and 100 GeV, respectively. The virtuality of the exchanged photon is restricted to be $Q^2 < 0.01$ GeV/c^2 and photon energy is restricted to be $E_\gamma < 2$ GeV to mimic γ+Au interactions in Au+Au UPCs at $\sqrt{s_{NN}}$=200 GeV. This figure demonstrates how the combination of the inner Time Projection Chamber (iTPC), the new highly granular Event-Plane Detectors (EPD) and forward tracking system (FTS) and the Zero-Degree Calorimeters (ZDC) can be used to isolate γ+Au events from peripheral Au+Au events (symmetric in η with no gaps). In terms of triggering the γ+Au interactions, the most stringent selection criterion is that the ZDCE detector should be restricted to have a single neutron hit (1n), while no restriction (Xn) should be placed on the ZDCW to trigger on γ+Au candidates with east-going photons, and vice versa. We perform a feasibility study using Run=19 data on min-bias Au+Au collisions using about 130 M events. Figure 104 shows STAR preliminary data on the per-trigger yield in di-hadron correlations in d+Au events where a clear ridge can be seen after template fitting. On the same plot we show projections of uncertainties for the di-hadron correlations in possible γ+Au-rich events using Au+Au 200 GeV data from Run 19 (130 M events) and using Au+Au 200 GeV data from anticipated Run=23+25 (20 B events). Projections are shown for high activity (HM) and low activity (LM) event classes determined by the uncorrected track multiplicity in TPC matched with TOF of 15 <= $N_{\rm trk}^{\rm TOF} < 25$ and 1 <= $N_{\rm trk}^{\rm TOF} < 8$, respectively. Even without any dedicated trigger, 20 B minbias Au+Au events can already give us enough $\gamma + Au$ candidates to significantly reduce the uncertainties shown by the red and blue projection bands in Fig. 104. This will enable us to perform differential measurements of di-hadron correlations with different combinations of triggers and associated p_T and perform a search for collectivity and in addition to testing the baryon-junction conjecture.

Other inclusive photoproduction measurements

Besides the search for collectivity in photon-nucleus collisions, there are many other inclusive photoproduction processes are of great interest. In the upcoming Run-23 and Run-25, inclusive photoproduction processes only require a large sample of "minimum-bias" photo-nucleus collision events, instead of special triggered events.

For example, one measurement that will have a large impact is the inclusive J/ψ photoproduction. Note that STAR has results on exclusive J/ψ photoproduction, the complementary inclusive measurement (together with exclusive measurements) can be sensitive to the saturation or non-linear gluon dynamics. The observable is as follows,

$$\frac{\sigma_{\rm J/\psi}^{\rm exclusive}/\sigma_{\rm J/\psi}^{\rm inclusive}|_{\rm Au}}{\sigma_{\rm J/\psi}^{\rm exclusive}/\sigma_{\rm J/\psi}^{\rm inclusive}|_{\rm p}}. \quad (5)$$

The J/ψ inclusive and exclusive photoproduction both provide a hard scale that theo-

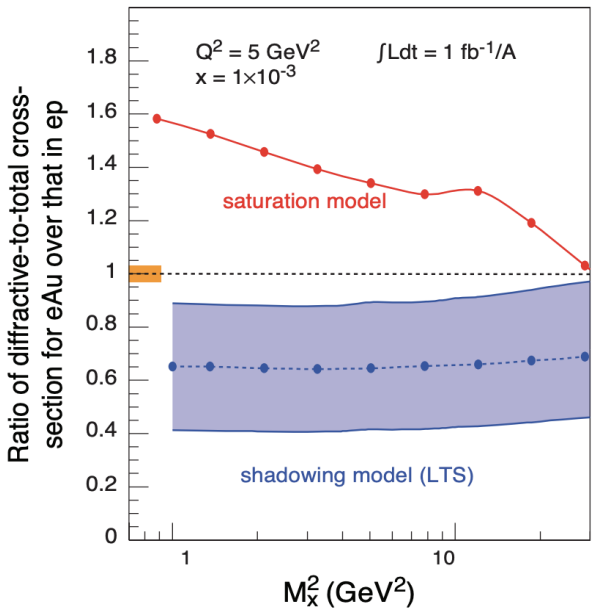

Figure 105: Figure from the EIC White Paper - Fig 1.6 [190]. The ratio of diffractive over total cross-section for DIS on gold normalized to DIS on proton plotted for different values of M_x^2, the mass squared of hadrons produced in the collisions for models assuming saturation and non-saturation. The statistical error bars are too small to depict and the projected systematic uncertainty for the measurements is shown by the orange bar. The theoretical uncertainty for the predictions of the LTS model is shown by the grey band.

retical calculations can be performed. Qualitatively, the nuclear shadowing model (Leading Twist Approximation [311–313]) predicts this double ratio to be below unity, while saturation models predict above unity. [190] This is one of the very few observables that qualitatively separates these two long standing models. In the upcoming STAR runs of Au+Au and p+Au collisions, this measurement will play an important role in understanding the saturation phenomena before the EIC. For the similar EIC measurement, see Fig. 105 for details. The reason we can do this similar measurement in UPCs is because we can replace the DIS measurement (finite Q^2) with photoproduction of J/ψ (both exclusive and inclusive), where the charm quark mass provides the hard scale. Even though the UPC measurement cannot provide a wide range of diffractive mass state (M_x^2), this can provide important insights to the underlying physics mechanism, e.g., gluon saturation and nuclear shadowing effect.

4 Computing Resources

In 2019, STAR submitted the computing resource request for years 2021–2025. Recently, we have completed the upgrade on the STAR DAQ system that allows STAR to take data at 5kHz, which is running successfully during run-2023 and will approximately doubles the bandwidth in the 2023-2025 runs as compared to the 2022 rates. The increased DAQ bandwidth will improve the statistical precision for various observables aimed towards the detail investigation of microscopic structure of QGP. These include the net-proton high order cumulant ratios C_6/C_2, thermal dilepton spectra and low p_T J/ψ v_1, v_2 etc which are unique at STAR compared to sPHENIX at the top RHIC energy. Furthermore, STAR will be able to accommodate the triggers reading out forward and mid-rapidity tracking/calorimeter detectors together which offers a unique chance to characterize the QGP over a wide pseudorapidity coverage.

An updated request on the additional resources due to this upgrade was submitted to SDCC in November 2021. The request was discussed with NPP management at the mini-retreat on "Nuclear Physics Computing from RHIC to EIC" in January 2022. We would like to emphasize that the requested resources are essential for completing the scientific mission of the STAR experiment, by producing and finishing the analyses from the requested datasets taken in 2023–2025 in a timely fashion.

Table 6 and Table 7 list the updated requests on the network capacity needs and the storage/CPU resource needs, respectively.

Network and HPSS capability	2022 capacity	2023-2025 needs
DAQ to SDCC network upload	40 Gbps	40 Gbps
SDCC to DAQ local network	28×1 Gbps	48×1 Gbps
Tape Drive Capacity	20 Gbps	40 Gbps

Table 6: Updated request on network capacity needs.

Year	Species	Additional HPSS Space Needed (RAW+DST) (PB)	Total Storage Space Needed (Xrootd) (PB)	Total Storage Space Needed (NFS/Central) (PB)	Required CPU Total [kHS06]
2021	BES-II	0.43	3.06	3.504	203
2022	500 GeV p+p	11.07	3.63	3.854	295
2023	200 GeV Au+Au	55.4	7.0	4.75	626
2024	200 GeV p+p/p+Au	35.5	9.1	4.75	626
2025	200 GeV Au+Au	73.8	13.5	4.75	626

Table 7: Updated request on storage and CPU resources.

5 Future Opportunities

Experience from the BES-II has shown us that the excellent performance from RHIC may allow us to take short opportunistic datasets that enable unique physics programs with minimal extra running time. Below we outline two such opportunistic programs, both are of great interest to STAR and the larger nuclear physics community.

5.1 Imaging Shape and Radial Profile of Atomic Nuclei

The success of the hydrodynamic framework of heavy-ion collisions permits us today to perform quantitative extractions of the transport properties of the QGP via the state-of-the-art multi-system Bayesian analysis approaches. [257–259] Such extractions rely largely on a correct description of the initial condition of the QGP prior to the hydrodynamic expansion. Recent experimental data in ^{96}Ru+^{96}Ru and ^{96}Zr+^{96}Zr isobar collisions [65], ^{238}U+^{238}U [77] and ^{129}Xe+^{129}Xe [338–342] collisions, as well as dedicated theoretical studies [78, 81, 84, 85, 343–348], have indicated the importance of nuclear deformation and the nuclear radial profile, i.e. radial distribution of proton and neutrons in the nucleus, on the measured anisotropic flow. However, the impact of these collective nuclear structure effects are not yet considered in these Bayesian approaches. For a reliable extraction of transport properties and initial-state from the collective flow data, we need to ensure that the uncertainty associated with the structure of the colliding ions is under control in the hydrodynamic models, especially since all species at RHIC and the LHC are expected to present some deformations and some uncertainties in the nuclear skin and radius (as indicated in Table 8 for nuclear deformation). These uncertainties can be gauged precisely using pairs of isobar collisions, as demonstrated by the ^{96}Ru+^{96}Ru and ^{96}Zr+^{96}Zr collisions at RHIC, where the ratio of flow observables can be determined with $< 0.4\%$ precision. [65] Note that these ratios are made at the same $N_{\rm ch}$ in each isobar, and therefore are essentially insensitive to final state effects and are precision probes of the initial conditions as we shall discuss below.

	β_2	β_3	β_4
^{238}U	0.286 [349]	0.078 [350]	0.09 [351]
^{208}Pb	0.05 [349]	0.04 [352]	?
^{197}Au	-(0.13-0.16) [351, 353]	?	-0.03 [351]
^{129}Xe	0.16 [351]	?	?
^{96}Ru	0.05-0.16 [349, 351]	?	?
^{96}Zr	0.08 [349]	?	0.06 [351]

Table 8: Some estimates of the deformation values β_2, β_3, and β_4 for the large nuclei collided at RHIC and the LHC with references given, mostly on global analysis of $B(En)$ transition data over a broad range of nuclei. There are also uncertainties in their values for surface diffuseness a_0 and half radius R_0 which are not listed.

It is straightforward to see why the geometry of heavy-ion collisions is sensitive to nuclear deformation and radial profile. We refer to the cartoon in Fig. 106. A nucleus can be modeled

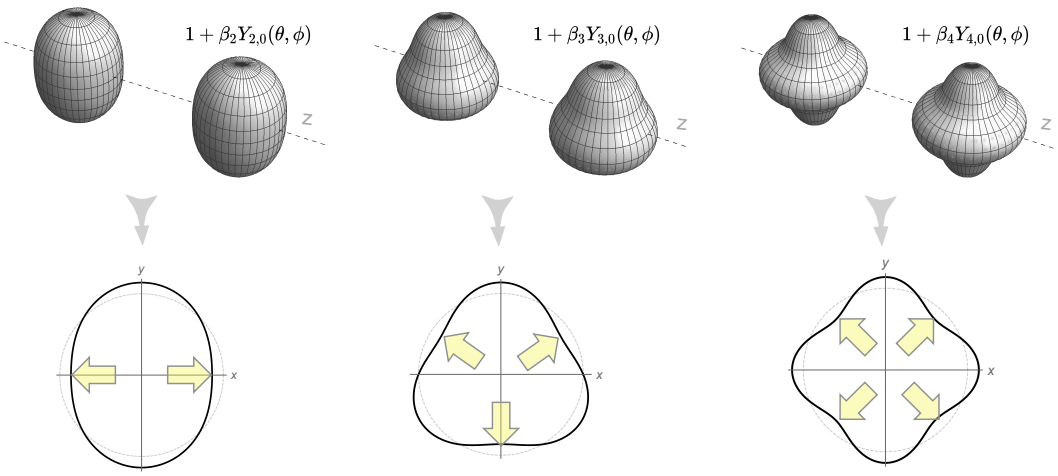

Figure 106: A cartoon of a collision of nuclei with quadruple (left), octupole (middle) and hexadecapole (right) deformations including only the $Y_{n,0}$ mode and with $\beta_n = 0.25$ (we ignore the large Lorentz contraction in the z-direction). The bottom row shows how the initial condition of the medium formed after the collision looks in the transverse plane. The yellow arrows indicate the direction of maximum pressure gradients along which the medium expands with the largest velocity, leading to final state harmonic flow v_n with n-fold symmetry.

through a nucleon density of Woods-Saxon form:

$$\rho(r,\theta,\phi) = \frac{\rho_0}{1+e^{[r-R(\theta,\phi)]/a_0}},\ R(\theta,\phi) = R_0\left(1+\beta_2[\cos\gamma Y_{2,0}+\sin\gamma Y_{2,2}]+\beta_3 Y_{3,0}+\beta_4 Y_{4,0}\right), \tag{6}$$

where the nuclear surface $R(\theta,\phi)$ includes only the most relevant deformation components from nuclear structure physics, quadrupole $n=2$, octupole $n=3$ and hexadecapole $n=4$. The angle $0 \le \gamma \le \pi/3$ controls the triaxiality of the quadruple deformation or the three radii R_a, R_b, R_c of the ellipsoid, with $\gamma = 0$ corresponds to prolate ($R_a = R_b < R_c$), and $\gamma = \pi/3$ corresponds to oblate ($R_a < R_b = R_c$). The nuclear radial profile is controlled by the surface diffuseness or nuclear skin a_0 and half radius R_0. In heavy-ion collisions, the shape of the deformed ions strongly affects the geometry of overlap. The entire mass distribution is probed simultaneously, and one can use multi-particle correlation observables to infer information of all these parameters. This way of probing nuclear densities is different from the standard techniques of low-energy physics, where β_n, a_0 and R_0 are inferred from the orientation-averaged form factor data from e+A and hadron+A scatterings and multipole transition probabilities, $B(En)$, between low-lying rotational states. Furthermore, the time scales involved in high-energy heavy-ion collisions are much shorter ($< 10^{-24}$s), than the typical timescale of the EM transition involved in the rotational bands (typically on the order of 10^{-20} s [354]). As we shall also argue below, a remarkable question is whether the manifestation of nuclear deformation and nuclear skin– collective features of the nuclear many-body system – is the same across energy scales.

The presence of multipoles, β_n, in the colliding ions modifies non-trivially the corresponding spatial anisotropy, ε_n, of the produced QGP, and consequently the final-state flow harmonic, v_n. Similarly, different values of a_0 and R_0 modify the effective size of the overlap region and therefore the "radial" flow or the event-by-event mean transverse momentum [$p_{\rm T}$]. [85] Recent studies show that nuclear skin a_0 also impacts the v_2, and simple event activity observables such as multiplicity distributions $p(N_{\rm ch})$ and participants $p(N_{\rm part})$. [84,348] Predictions for many other observables and their sensitivities to nuclear deformation and nuclear skin have been made, such as $p_{\rm T}$ fluctuations [80], spectator neutron production [355], mixed-flow harmonics [356], and v_n–$p_{\rm T}$ correlations. [342,345,357]

Earlier studies of nuclear deformation are mainly focused on the elliptic flow, v_2 in central collisions. They have established a simple relation between quadrupole deformation and ϵ_2 and v_2 [357,358],

$$\left\langle \epsilon_2^2 \right\rangle = a' + b'\beta_2^2, \qquad \left\langle v_2^2 \right\rangle = a + b\beta_2^2, \tag{7}$$

where the a' and a are mean-squared eccentricity and elliptic flow without deformation, while the b' and b describe the parametric dependence of the deformation-enhanced component of eccentricity and elliptic flow, respectively. The strict quadratic dependence of Eq. 7 leads to a very robust equation relating the β_2 between any pair of collision systems. Applied to RHIC data, it allows one to derive a constraint on the $\beta_{2,\rm U}$ and $\beta_{2,\rm Au}$, as shown in the right panel of Fig. 107. This highlights how, at present, the low-energy nuclear structure model calculation and the flow data from high-energy nuclear collisions are fairly inconsistent. Relations similar to Eq. 7 can also be written down for v_3 and v_4, which can be used to potentially constrain octupole and hexadecapole deformations. [79]

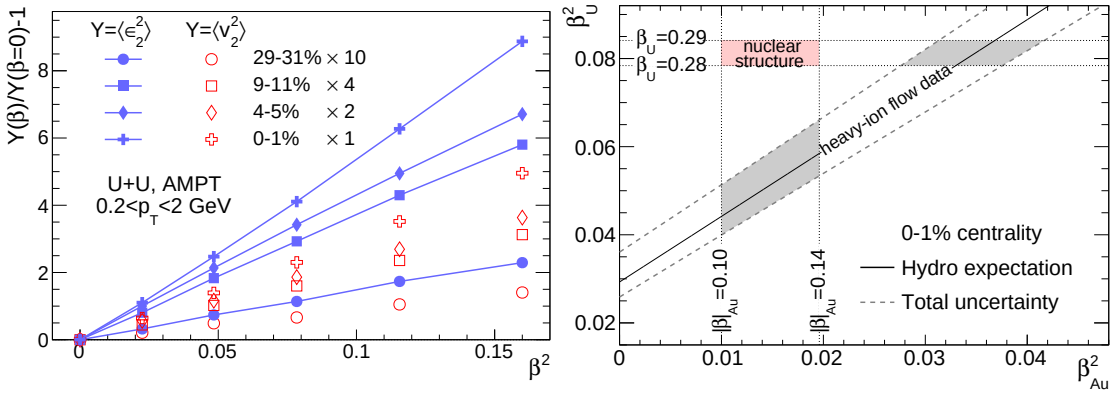

Figure 107: Left panel: $\left\langle v_2^2(\beta)\right\rangle / \left\langle v_2^2(0)\right\rangle - 1 = b/a\ \beta_2^2$ (empty symbols) and $\left\langle \epsilon_2^2(\beta_2)\right\rangle / \left\langle \epsilon_2^2(0)\right\rangle - 1 = b'/a'\ \beta_2^2$ (full symbols) as a function of β_2^2 in U+U collisions from the AMPT model. Different symbols correspond to different centrality classes. Right panel: $\beta_{2,\rm U}^2$ as a function of $\beta_{2,\rm Au}^2$. The region between the dashed lines is consistent with the hydrodynamic expectation based on Eq. (7) and STAR v_2 data in 0–1% centrality. Figures taken from Ref. [347].

The most precise tool for structure imaging, however, is provided by collision of isobaric systems, as demonstrated by recent measurements in ^{96}Ru+^{96}Ru and ^{96}Zr+^{96}Zr collisions. [65] The crucial point is that since isobar nuclei have the same mass number, deviations

from unity of the ratio of any observable must originate from differences in their structures, which impact the initial state of QGP and its final state observables. Ratios of many observables between ^{96}Ru+^{96}Ru and ^{96}Zr+^{96}Zr, both published and new preliminary results shown in QM2022 [65, 359], show deviations from unity in an observable- and centrality-dependent manner, which must originate from differences in their structures. Model studies show that the isobar ratio for a given observable $\mathcal{O}$ probes only the nuclear structure parameter differences, i.e. $\Delta\beta_n^2 = \beta_{n\mathrm{Ru}}^2 - \beta_{n\mathrm{Zr}}^2$,$\Delta a_0 = a_{0\mathrm{Ru}} - a_{0\mathrm{Zr}}$ and $\Delta R_0 = R_{0\mathrm{Ru}} - R_{0\mathrm{Zr}}$ [82]:

$$R_{\mathcal{O}} \equiv \frac{\mathcal{O}_{\mathrm{Ru}}}{\mathcal{O}_{\mathrm{Zr}}} \approx 1 + c_1\Delta\beta_2^2 + c_2\Delta\beta_3^2 + c_3\Delta a_0 + c_4\Delta R_0 \ , \tag{8}$$

where the coefficients c_1–c_4 describe how the heavy-ion initial state is controlled by the nuclear structure and are weak functions of system size. Figure 108 highlights some recent

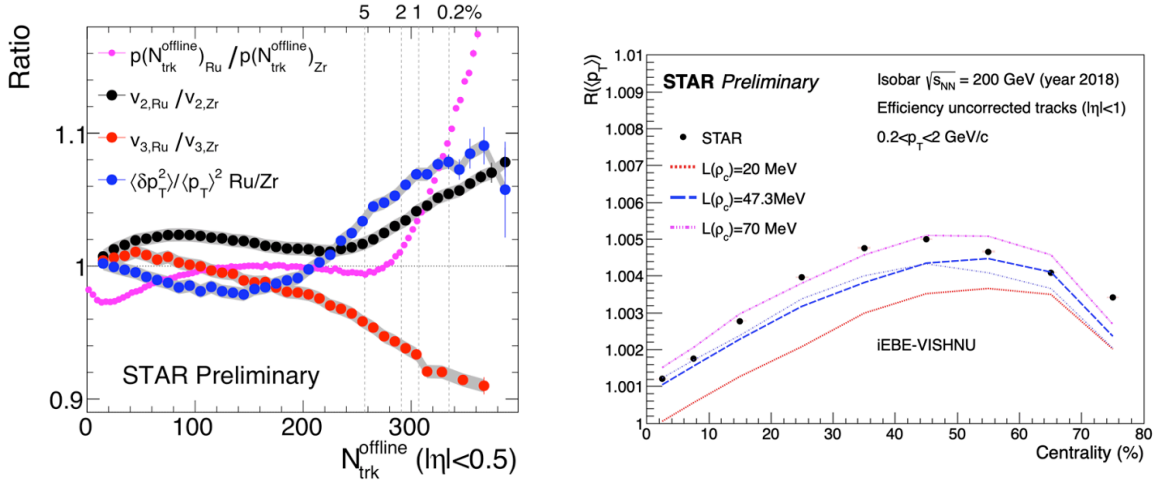

Figure 108: Left panel: STAR preliminary results of isobar ratio of $p(N_{\mathrm{ch}})$, v_2, v_3, and variances $\langle\delta p_{\mathrm{T}}^2\rangle/\langle p_T\rangle^2$ as a function of N_{ch}. Right panel: The centrality dependence of the Ru+Ru/Zr+Zr ratio of $\langle p_T\rangle$, compared with hydrodynamic model calculations [85].

measurements: ratios of multiplicity distribution $p(N_{\mathrm{ch}})$, v_2, v_3, variance of p_{T} fluctuations $\langle\delta p_T^2\rangle/\langle p_T\rangle^2$, and $\langle p_{\mathrm{T}}\rangle$ between the isobar systems. All of them show non-monotonic centrality dependence similar in shape to the theoretical predictions that include effects of nuclear skin as well as nuclear deformations. [81, 82, 356, 360] In particular, the data imply a larger quadrupole deformation β_2 in ^{96}Ru, a larger octupole deformation β_3 in ^{96}Zr, and a larger a_0 value consistent with a larger neutron skin in ^{96}Zr, Δr_{np}, defined as the rms radius difference between the neutron and proton distributions: $\langle r_n^2\rangle^{1/2} \equiv \langle r_n^2\rangle^{1/2} - \langle r_p^2\rangle^{1/2}$. These detailed measurements over-constrain the WS parameters and can be used to test the initial conditions used in hydrodynamic models. Note that the neutron skin thickness Δr_{np} is directly related to the slope parameter L for the density dependence of the symmetry energy, which is particularly important in astrophysics concerning neutron stars. [361] The preliminary extraction of L from the measured $\langle p_{\mathrm{T}}\rangle$ ratio in the isobar data seems to prefers a value of 47–70 MeV as shown in Fig. 108, quite consistent with low-energy nuclear reaction measurements [362] but systematically lower than the PREXII results [363].

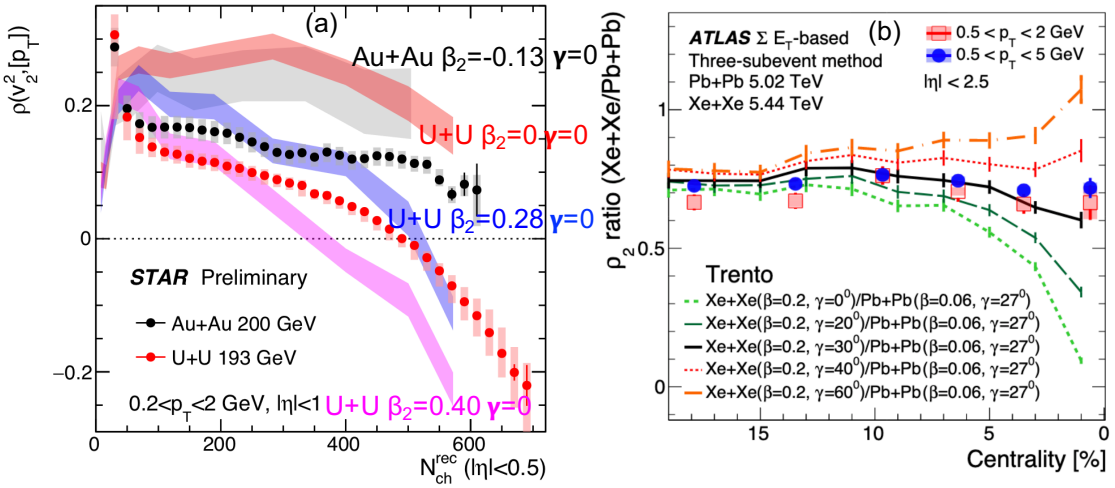

Figure 109: Left panel: STAR preliminary results of Pearson correlation coefficient $\rho(v_2^2, [p_T])$ in U+U and Au+Au collisions, showing a sign-change due to large prolate deformation of ^{238}U. Right panel: ATLAS results of the ratio of $\rho(v_2^2, [p_T])$ between Xe+Xe and Pb+Pb collisions, showing a strong preference for ^{129}Xe being a highly-deformed triaxial ellipsoid.

An additional observable showing large sensitivity to the nuclear quadrupole deformation is the Pearson correlation coefficient, $\rho(v_2^2, [p_T])$, between v_2 and the mean transverse momentum, $[p_T]$. This observable probes in particular the full quadrupole structure of the colliding ions, i.e., both β_2 and its triaxiality γ in Eq. 6 [80, 357],

$$\rho(v_2^2, [p_T]) \approx a - b\cos(3\gamma)\beta^3, \; a, b > 0. \tag{9}$$

Therefore prolate deformation in the colliding nuclei is expected to reduce $\rho(v_2^2, [p_T])$, while oblate deformation is expected to increase it. This observable has been measured by the STAR collaboration in U+U and Au+Au collisions, which established unambiguously the large and dominating influence of the nuclear quadruple deformation, see Fig. 109(a). The large prolate deformation of ^{238}U yields a strong negative contribution to the $v_2 - [p_T]$ correlation, enough to make it change sign. A large impact of β_{2U} has further been observed in the fluctuations of $[p_T]$. The same measurement is also performed by the ATLAS and ALICE collaborations in ^{129}Xe+^{129}Xe and ^{208}Pb+^{208}Pb collisions [341, 364], see Fig. 109(b). A comparison with a Trento model calculation based on input from nuclear structure theory [342] provide strong evidence that ^{129}Xe is a highly-deformed triaxial ellipsoid with an overall quadrupole deformation of $\beta_{2Xe} \sim 0.2$ and triaxiality of $\gamma_{Xe} \sim \pi/6$. Hydrodynamic models based on state-of-the-art initial conditions with deformation values from Table 8 struggle to describe quantitatively all these experimental measurements. [365–367] The reason could be that the radial flow response of the system to fluctuations induced by the deformation of the colliding ions is not fully captured by the existing models. Collisions of well-deformed ions, and their comparisons with the collisions of more spherical species, provide us with a new way to test the hydrodynamic description.

To summarize, flow measurements in heavy-ion collisions have large potential to provide detailed information on the shape and radial profile of colliding nuclei. By connecting the

highest and lowest energy scales, they allow us to answer important questions in heavy ion physics and have broader impact to the larger nuclear physics community. Here are a few of them:

- How distributions of protons and neutrons in atomic nuclei give rise to the complex initial condition of heavy ion collisions? Can we use nuclear shapes and nuclear radial profiles as additional handles to understand particle production and generation of eccentricities, e.g. by comparing flow observables at the same final state multiplicity in isobar systems with different nuclear structures?

- Can we gauge uncertainties in the extraction of the transport properties of the QGP due to uncertainties in the initial condition arising from nuclear structure?

- Are the nuclear shape and radial profile inferred from hydrodynamic response the same as those measured in nuclear structure experiments? Can isobar collisions serve as a precision tool for the extraction of the neutron skin, competitive to the existing measurements? and what are the energy and longitudinal dependence of nuclear structures?

To address these and other related questions, several workshops exploring the intersection between nuclear structure and heavy-ion collisions have been planned, including a month-long INT program in early 2023. Rapid progress is expected in the next two years.

Thus we propose to collide more species to extract their value of deformation parameters β_2, γ, β_3 and β_4, and a_0 and associated neutron skin from flow measurements, with a twofold purpose: 1) provide a new handle on the initial state and hydrodynamic response of the QGP, 2) perform studies of nuclear structure physics at high energy to complement the information coming from lower energies, and so assess the consistency of nuclear phenomena across energy scales. The ground state of almost all stable nuclei is deformed (see for example the interactive chart in Ref. [368]). RHIC, with its flexibility to collide almost any nuclei from p+p to U+U is a unique facility to perform such studies in the foreseeable future. The best example to showcase this capability is the run of isobars performed in 2018, where the two systems, Zr+Zr and Ru+Ru, were alternated on a fill-by-fill basis, leading to extremely small systematic uncertainties on the final observables. [65] This allows one to detect minute differences in the physics observables such as multiplicity, $[p_{\mathrm{T}}]$ and v_n in the comparison of the two systems. Consequently, even small differences in the values of β_n and a_0 of the colliding systems can be precisely mapped. [78] For each species, we need roughly 100 million minimum bias and 50 million 0–5% central events. Assuming the standard 50% RHIC+STAR up time and 1.5 KHz DAQ rate, same as Au+Au running, we will be able to collect 130M minbias events and 64M central events in three days of physics running. This is slightly less than the existing U+U dataset taken in 2011, but with comparable statistical precision due to the increased acceptance from the iTPC. Adding two days of setup time, this leads to about five days of total time for each species.

The system scan we propose can be divided into two steps. Given the tight schedule for the next few years, instead of making an explicit proposal on how much running time are

needed to fully explore these topics, we discuss what can be achieved if we are given certain number of days.

- **≈10 days:** In the first step, we would like to scan two nuclei in the vicinity of the most studied species at RHIC, ^{197}Au, to improve the modeling of Au+Au collisions, information which is crucial for the future precision interpretation of high-statistics data expected from Run-23+25. To achieve this, ideal candidates are ^{208}Pb and ^{196}Hg (^{198}Hg could be a substitute). Having ^{208}Pb at $\sqrt{s_{\rm NN}}$ = 200 GeV provides a crucial bridge with the ^{208}Pb at LHC energies: comparison between ^{208}Pb measurements at RHIC and the LHC will constrain any possible energy dependence of the initial state effects and pre-equilibrium dynamics. Additionally, ^{208}Pb is nearly spherical, so that Pb+Pb collisions at the same energy will allow us to better understand the impact of the moderate deformation of ^{197}Au in Au+Au collisions, as well as the impact of the difference of a_0 parameter and neutron skin between ^{197}Au and ^{208}Pb. The Hg+Hg collisions would then permit us to understand more deeply the nature of the deformation of ^{197}Au, which, being an odd-mass nucleus, hasn't been determined in low-energy experiments. ^{196}Hg is an oblate nucleus with $|\beta_2| \approx 0.1$, and the observable $\rho(v_2^2, [p_{\rm T}])$ can be used quantify whether ^{197}Au is more or less oblate than ^{196}Hg, an information which will gauge more tightly the initial geometry of Au+Au collisions. Adding Hg+Hg collisions will also provide an independent cross-check on the initial state, for example one can setup three relations like Eq. 7 from Pb+Pb, Hg+Hg and Au+Au to triangulate the consistency of the three deformation values. [79]

- **Additional time:** In the second step, our proposal is to use hydrodynamics and flow measurements to perform precision cross-checks of low-energy nuclear physics by constraining the evolution of the quadrupole deformation and neutron skin along the chain of stable samarium isotopes. It would be useful in particular to collide three isotopes: ^{144}Sm ($\beta_2 = 0.08$, as spherical as ^{208}Pb), ^{148}Sm ($\beta_2 = 0.14$, triaxial much as ^{129}Xe and ^{197}Au), and ^{154}Sm ($\beta_2 = 0.34$ well-deformed like ^{238}U). The evolution of the quadrupole deformation can be mapped precisely at RHIC, thus offering a valuable test of nuclear structure knowledge. If data on ^{154}Sm+^{154}Sm collisions is available, it would be desirable to also have ^{154}Gd+^{154}Gd ($\beta_2 = 0.31$) collisions. The comparison between the two well-deformed isobaric systems could potentially yield the most precise information about the relative deformation and relative neutron skin between two ground state nuclei. Theoretical studies further suggest that ground states in the region $Z \sim 56/N \sim 88$ [369] (including the samarium isotopes) may display enhanced octupole correlations, i.e., β_3 values. These would manifest in high-energy collisions as enhanced v_3, as well as in the correlators $\rho(v_3^2, [p_{\rm T}])$. Such enhancements are already observed in ^{96}Zr+^{96}Zr relative to ^{96}Ru+^{96}Ru collisions (Fig. 108 and Ref. [359]), however nuclear structure modeling for these medium mass nuclei are quite challenging and it is unclear yet whether the observed enhancements are due to octupole correlation or static octupole deformation. The heavier species mentioned above would be a more sensitive choice for identifying static octupole deformation. The study of octupole deformation is also fundamentally interesting because nuclei with large β_3 provides a

stringent test of the electric-dipole moment (EDM) [370]. The exact choice of species is still under refinement, presently we have a preference for ^{154}Sm and ^{148}Sm, followed by ^{154}Gd and ^{144}Sm.

Finally, one should note that the STAR DAQ rate for these moderate-sized systems could be significantly larger, possibly reaching 2KHz. This enhanced DAQ rate will compensate partially the smaller number of charged particles expected in these systems compared to larger systems.

5.2 Nuclear Data for Space Radiation Protection

This section presents the background and rationale for measurements of differential cross sections measurements of light nuclei relevant for space radiation. This is not part of the STAR physics program in the final RHIC phase but represents an opportunity for RHIC to contribute with some important nuclear data should the resources and time for these brief measurements be available. STAR has made a commitment to execute this should the opportunity materialize.

The 2015 Long Range Plan for Nuclear Science identified four key science questions for the field. The fourth of those questions was “How can the knowledge and technical progress provided by nuclear physics best be used to benefit society?" This question addresses the broader impact of the data and the knowledge generated by field of research. Recently it has come to the attention of the STAR collaboration that fixed-target collisions using light beam and target combinations could benefit the Space Radiation Protection community.

Space radiation is a serious concern to astronauts, electronics, and spacecraft. The term “space radiation" refers to the flux of energetic charges particles in the solar system. NASA has been aware of the dangers of space radiation for several decades. The energy spectrum and species composition have been studied using instruments on balloons, satellites (such as the Advanced Composition Explorer), deep space probes (such as Voyager 1), and the Space Station (Alpha Magnetic Spectrometer). The sun is responsible much of the space radiation (see fig. 110). The solar wind is comprised of protons from 0.5 to 10 keV. Solar flare events produce energetic particles (protons and some light nuclei) with energies up to a few hundred MeV/n. The highest energy portion of the space radiation field in comprised of galactic cosmic rays. 90% of the galactic cosmic ray flux is comprised of energetic protons and another 9% is Helium nuclei, the remaining 1%, is made up of nuclei from Li to Fe. The peak of the energy spectrum of the galactic cosmic rays is about 1 GeV/n, although measurable yield extends for several orders of magnitude. Solar wind particles are stopped in a few microns of material. Additionally, particles from the solar wind are deflected at the bow shock of the Earth's magnetic field, therefore they are not a concern for equipment or personnel in low earth orbit. Energetic particles from solar flares can be anticipated and can be stopped with a few tens of centimeters of shielding. Galactic rays can not effectively be shielded, therefore their affect must be studied or simulated. Although ion make up a small percentage of the GCR flux, their importance is not negligible both because the energy loss is proportional to Z^2 and because additional damage is done by the energetic light nuclei

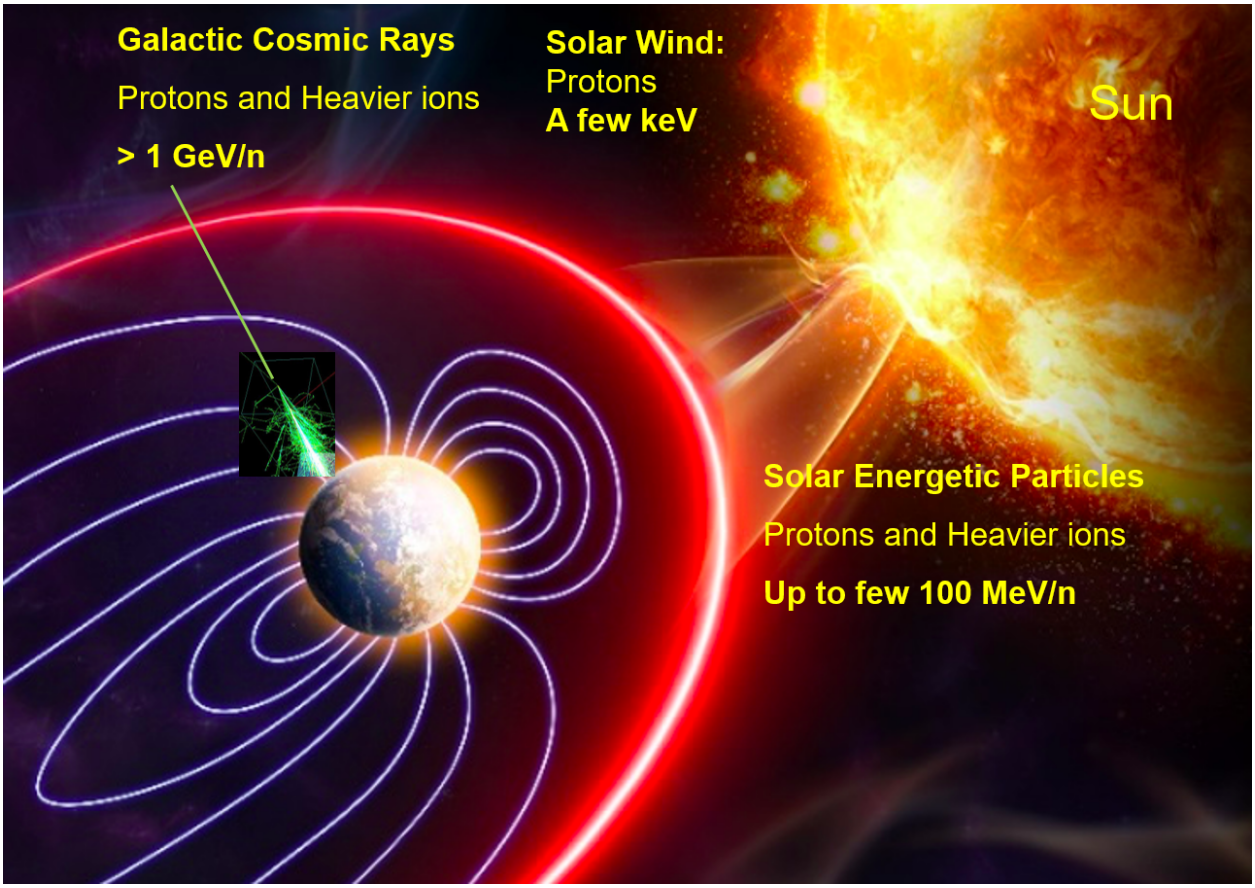

Figure 110: An illustration of the major sources and components of the space radiation flux.

(p, d, t, ^3He, and ^4He) produced through the fragmentation of the target and projectile nuclei. The damage done by the light nuclei becomes increasingly important for higher energy cosmic rays. Light ion cross section measurements represent the largest uncertainty in space radiation estimates.

Space radiation can affect electronics through single event upsets or can induce noise in detectors or scientific equipment. The impact on astronauts is estimated by considering the total ionizing does.

Currently all components going into space are tested for radiation hardness at facilities such as the Michigan State Linac stage 1, the UC Davis cycloton, the Texas A&M K50 and K500, the LLBNL 88 inch cyclotron and several other lower energy university facilities. Extensive measurements up to 1 GeV/n have been made at BNL at the dedicated NSRL facility which uses the booster when RHIC is not injecting beams. In addition to testing equipment, nuclear cross section data have been compiled for various beams with energies up to roughly 1 GeV/n to allow for detailed simulations of the damage incurred from both the primary particles and the secondaries created as the projectile breaks up. The Space Radiation Community has recently identified higher energy systems, using beams from 3 to 50 GeV/n on C, Al, and Fe targets as one of the next areas of need. [371] This energy range

is dominated by Galactic Cosmic Rays (GCR). The requirements would be to measure the cross section for light nucleus (p, d, t, ^3He, and ^4He) production through fragmentation of the target and projectile. These data are needed now as NASA is commencing an ambitious program of long duration manned exploration beyond low earth orbit. The Artemis 1 mission launched on November 16th, 2022 for a twenty-five day unmanned transit to the moon and back. The Artemis II mission will take four astronauts to circle moon and return in late 2024, while Artemis III, in 2025, will land astronauts on the lunar surface. NASA's ambitious program sees the establishment of a lunar base and then a mission to Mars. Can the Hot QCD community provide the data needed by NASA to maximize the safety of these missions?

The RHIC/STAR FXT program has demonstrated that RHIC can efficiently develop and deliver the beams (C, Al, Fe) and energies (3-50 GeV) of interest, that STAR has excellent particle identification for light nuclei (p, d, t, ^3He, and ^4He) using both dE/dx and time-of-flight (capabilities specifically identified as essential in the NASA report [371], and that there is an efficient conduct of operations. We do note that the acceptance using the TPC and the barrel TOF is only in the target-side of the rapidity distribution. For symmetric systems this is not a problem; the results will be reflected about midrapidity. For asymmetric systems, both the light-on-heavy and heavy-on-light combinations will be run to ensure that both sides of the rapidity distribution will be studied. In addition, the collaboration has decided to install targets on the blue beam side of the detector to allow use of the STAR forward upgrades to make measurements of projectile fragmentation (see Fig. 111). STAR has reached out to the NASA space radiation community on several occasions determine if the STAR detector has sufficient acceptance in p_T and y to meet the needs of the Space Radiation Protection community. An overview of the RHIC/STAR capabilities was presented at the Workshop for Applied Nuclear Data Activities (WANDA2022) conference in February of 2022, at the Nuclear Data Conference (ND2022), and at a special session at DNP2022. The opportunity to make these measurements at RHIC is a unique and time-limited option to obtain critical high-energy data.

NASA had been considering constructing detector systems to make these measurements at the FAIR facility at GSI in Darmstadt, Germany. STAR is an existing detector with the required capabilities and analysis teams that have proven expertise to measure the light nuclei cross sections in fixed-target experiments. The RHIC facility has demonstrated capability to efficiently deliver the required beams. In addition, there is significant uncertainty about when the SIS-100 accelerator will be available as the construction timeline has been disrupted by the war in Ukraine and the cessation of cooperation between Germany and Russia.

It has been determined that the measurements that could be made at RHIC using the STAR detector will meet the needs of the Space Radiation Protection community. These can be achieved by brief energy scans using C, Al, and Fe beams on light targets (C, Al, and Ni). Because there was a window of opportunity in December of 2022 when there was very little activity in the STAR experimental hall, we took the opportunity to open the vacuum pipe and install the three targets (see fig. 112). The carbon and nickel targets are 1 mm thick; the aluminum target is 1.5 mm thick. All target are approximately 1.8 m to the East of the center of the STAR TPC.

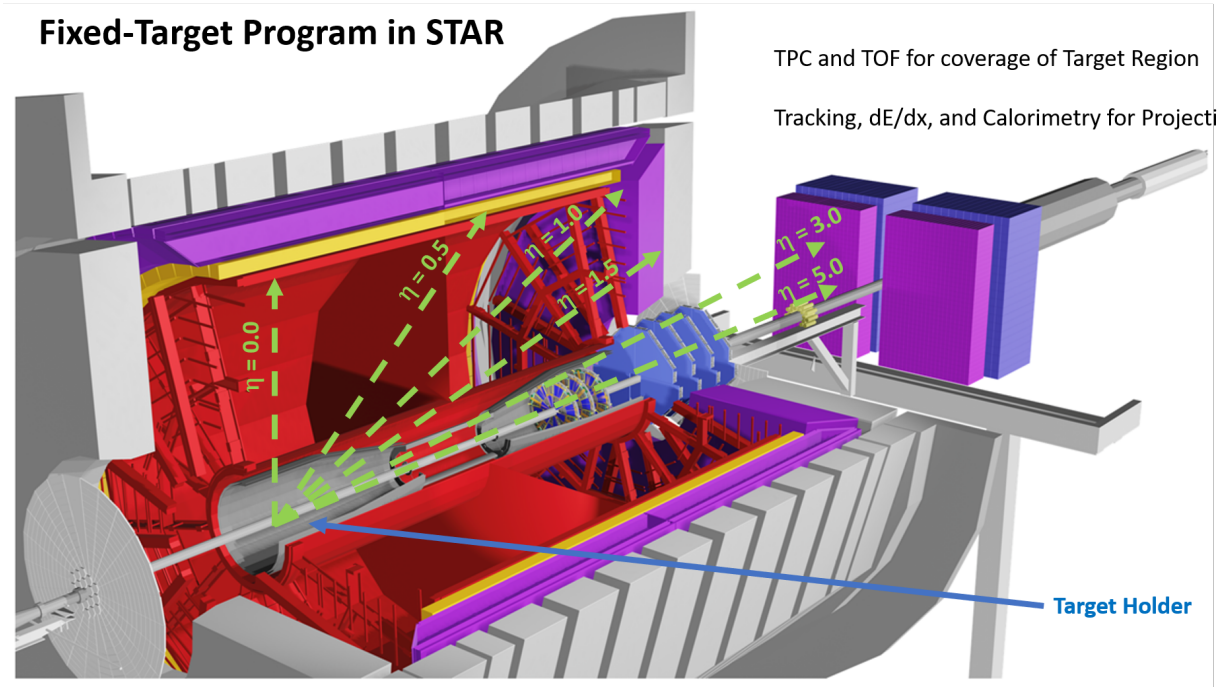

Figure 111: A schematic view of the STAR detector showing the location of the targets and the detector systems which would be needed for the measurements.

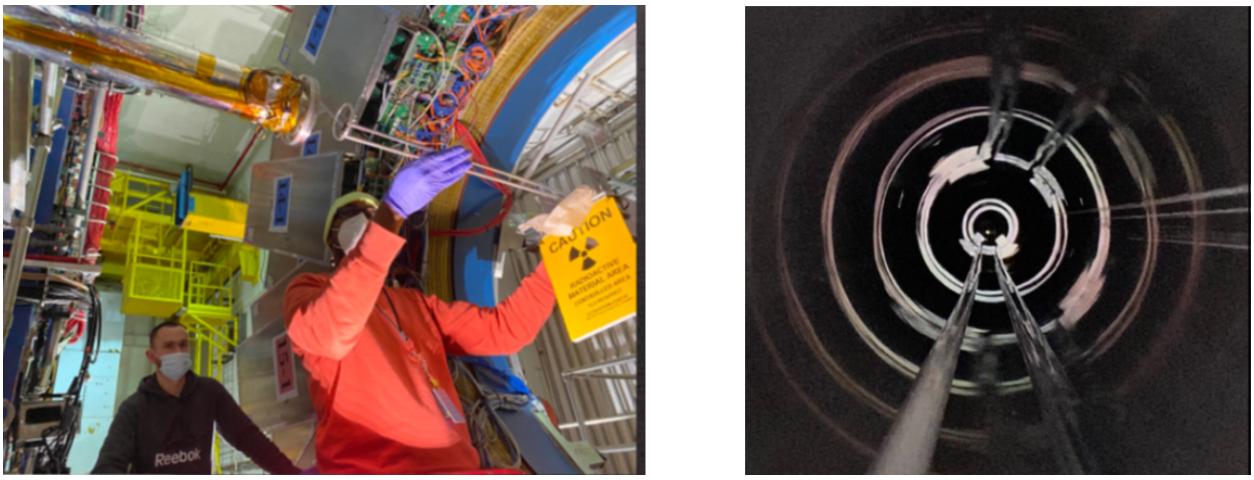

Figure 112: Left panel: Installation of the targets and holder on the East side of the STAR detector. Right Panel: A view down the beam pipe showing the three targets (C, Al, and Ni) installed at STAR.

The suggested three energies for each beam are (E_{Tot} = 6, 21, and 51 GeV, E_{Kin} = 5, 20, and 50, or $\sqrt{s_{\rm NN}}$ = 3.6, 6.4, and 9.8 GeV respectively). For each beam species (C, Al, and Fe), the collider would need to develop the beam extraction at both E_{Tot} = 6 GeV and at the nominal injection for RHIC (12.18 GeV for Carbon, 11.729 GeV for Aluminum, and 11.31 GeV for Iron). The work needed to develop extraction could be done behind stores as the ion sources, booster, and AGS are available while beams are circulating in RHIC for the core physics program. Additional beam development time would be needed for each beam species at each energy. The experience with the FXT program suggests that the E_{Tot} = 6 GeV would need 16 hours for beam development in RHIC. The E_{Tot} = 21 GeV add the need to accelerate the beams in RHIC and therefore it is expected that these each would take 20 hours of beam development. The E_{Tot} = 51 GeV beams, would need to be accelerated more in RHIC, but due to the similarities with the E_{Tot} = 21 GeV it is expected to only need 4 hours to develop these beams. In order to get enough statistics on each of the three targets, 6 hours would be needed for each beam-energy combination. Although the grand total for this request would be 11.75 days, due to the large number of beams and the importance of scheduling beam development time, two weeks would be a more appropriate time estimate.

High energy ion-on data are needed by the Space Radiation Protection community. The RHIC and STAR has developed techniques, facilities, and a knowledge base that allows us make the measurements that would benefit society by addressing a key identified need of the Space Radiation Protection community. Timely acquisition of relevant data sets would reduce the risk to astronauts, spacecraft, and equipment.

Beam	Energy	Targets	Time
Develop beam	5 GeV		16 hours
Carbon	5 GeV	C, Al, Ni	6 hours each (18 hours)
Develop beam	20 GeV		20 hours
Carbon	20 GeV	C, Al, Ni	6 Hours each (18 hours)
Develop beam	50 GeV		4 hours
Carbon	50 GeV	C, Al, Ni	6 hours each (18 hours)
Total			94 hours
Develop beam	5 GeV		16 hours
Aluminum	5 GeV	C, Al, Ni	6 hours each (18 hours)
Develop beam	20 GeV		20 hours
Aluminum	20 GeV	C, Al, Ni	6 Hours each (18 hours)
Develop beam	50 GeV		4 hours
Aluminum	50 GeV	C, Al, Ni	6 hours each (18 hours)
Total			94 hours
Develop beam	5 GeV		16 hours
Iron	5 GeV	C, Al, Ni	6 hours each (18 hours)
Develop beam	20 GeV		20 hours
Iron	20 GeV	C, Al, Ni	6 Hours each (18 hours)
Develop beam	50 GeV		4 hours
Iron	50 GeV	C, Al, Ni	6 hours each (18 hours)
Total			94 hours
Grand Total			11.75 days (i.e. two weeks)

Table 9: Summary of the FXT beam/target scan request. Assumptions are 16 hours of beam development for each beam at 5 GeV, 20 hours of beam development for each beam at 20 GeV, and 4 hours of beam development for each beam at 50 GeV. There would then be 18 hours of physics running (6 hours for each of the three targets) of data taking for each beam. Additionally one day would be needed to configure RHIC for low energy running.

BNL Nuclear Physics PAC 2023 Charge

[updates highlighted in red]

Dear Dave, Frank, Gunther and Lijuan:

I am writing to provide you the charge for your submission of the Beam Use Request for the PAC to consider at the upcoming September 2023 PAC meeting.

sPHENIX: Beam Use Requests for Runs 24-25
STAR: Beam Use Requests for Runs 24-25
The Beam Use Requests should be submitted in written form to PAC by August 11, 2023 by emailing Fran and copy me and John the BUR directly or provide a link to access the BUR before the due date.

The BURs should be based on the following number of cryo-weeks. For Run 2024, we ask that you consider three scenarios for 20, 24 and 28 cryo-weeks each, given the uncertain budgetary situation. Additionally, due to the recent Blue Ring valve box event, we ended Run 2023 in August. Six Au+Au weeks from Run 2023 will be carried forward into Run 2024

For Run 2025, the first number is the proposed RHIC run duration for scenario 1 and the second number corresponds to optimal duration (scenario 2) presented to the DOE-ONP in BNL's FY25 Lab Managers' Budget Briefing:

2024: 20/24/28 + six cryo-weeks of Au+Au collisions
2025: 24 (28)

Note the eventual running cryo-weeks for each run will depend on the final budget guidance for that year. Please let me know if you have any questions. Thank you.

Best, Haiyan

References

[1] STAR Collaboration, (2023), 2305.10359.

[2] RHIC SPIN, E.-C. Aschenauer *et al.*, (2023), 2302.00605.

[3] STAR Collaboration, B. I. Abelev *et al.*, Phys. Rev. Lett. **97**, 252001 (2006).

[4] STAR Collaboration, B. I. Abelev *et al.*, Phys. Rev. Lett. **100**, 232003 (2008).

[5] STAR Collaboration, L. Adamczyk *et al.*, Phys. Rev. D **86**, 032006 (2012).

[6] STAR Collaboration, L. Adamczyk *et al.*, Phys. Rev. Lett. **115**, 092002 (2015).

[7] STAR Collaboration, J. Adam *et al.*, Phys. Rev. D **100**, 052005 (2019).

[8] STAR Collaboration, M. S. Abdallah *et al.*, Phys. Rev. D **103**, L091103 (2021), 2103.05571.

[9] STAR Collaboration, M. S. Abdallah *et al.*, Phys. Rev. D **105**, 092011 (2022), 2110.11020.

[10] STAR Collaboration, L. Adamczyk *et al.*, Phys. Rev. D **95**, 071103 (2017).

[11] STAR Collaboration, J. Adam *et al.*, Phys. Rev. D **98**, 032011 (2018).

[12] PHENIX Collaboration, A. Adare *et al.*, Phys. Rev. D **76**, 051106 (2007).

[13] PHENIX Collaboration, A. Adare *et al.*, Phys. Rev. Lett. **103**, 012003 (2009).

[14] PHENIX Collaboration, A. Adare *et al.*, Phys. Rev. D **79**, 012003 (2009).

[15] STAR Collaboration, B. Abelev *et al.*, Phys. Rev. D **80**, 111108 (2009).

[16] STAR Collaboration, L. Adamczyk *et al.*, Phys. Rev. D **89**, 012001 (2014).

[17] PHENIX Collaboration, A. Adare *et al.*, Phys. Rev. D **90**, 012007 (2014).

[18] PHENIX Collaboration, A. Adare *et al.*, Phys. Rev. D **93**, 011501 (2016).

[19] STAR Collaboration, J. Adam *et al.*, Phys. Rev. D **98**, 032013 (2018).

[20] PHENIX Collaboration, U. A. Acharya *et al.*, Phys. Rev. D **102**, 032001 (2020), 2004.02681.

[21] PHENIX, U. Acharya *et al.*, Phys. Rev. Lett. **130**, 251901 (2023), 2202.08158.

[22] STAR Collaboration, N. Lukow, Constraining the Polarized Gluon Distribution Function of the Proton with Recent STAR Measurements, in *24th International Spin Symposium*, 2021.

[23] PHENIX Collaboration, A. Adare *et al.*, Phys. Rev. D **93**, 051103 (2016), 1504.07451.

[24] STAR Collaboration, J. Adam *et al.*, Phys. Rev. D **99**, 051102 (2019), 1812.04817.

[25] DSSV Preliminary.

[26] D. de Florian, R. Sassot, M. Stratmann, and W. Vogelsang, Phys. Rev. Lett. **113**, 012001 (2014).

[27] Jefferson Lab Angular Momentum (JAM), Y. Zhou, N. Sato, and W. Melnitchouk, Phys. Rev. D **105**, 074022 (2022), 2201.02075.

[28] J. Collins and J.-W. Qiu, Phys. Rev. D **75**, 114014 (2007).

[29] T. C. Rogers and P. J. Mulders, Phys. Rev. D **81**, 094006 (2010).

[30] X. Liu, F. Ringer, W. Vogelsang, and F. Yuan, Factorization and its breaking in dijet single transverse spin asymmetries in *pp* collisions, 2020, 2008.03666.

[31] Z.-B. Kang, K. Lee, D. Y. Shao, and J. Terry, The sivers asymmetry in hadronic dijet production, 2020, 2008.05470.

[32] V. Bertone, I. Scimemi, and A. Vladimirov, JHEP **06**, 028 (2019), 1902.08474.

[33] A. Bacchetta, F. Delcarro, C. Pisano, M. Radici, and A. Signori, JHEP **06**, 081 (2017), 1703.10157, [Erratum: JHEP 06, 051 (2019)].

[34] ATLAS, G. Aad *et al.*, JHEP **12**, 060 (2010), 1010.2130.

[35] ATLAS, G. Aad *et al.*, Phys. Lett. B **759**, 601 (2016), 1603.09222.

[36] CMS, V. Khachatryan *et al.*, JHEP **01**, 080 (2011), 1012.2466.

[37] D. de Florian, M. Stratmann, and W. Vogelsang, Phys. Rev. Lett. **81**, 530 (1998), hep-ph/9802432.

[38] X. Liu and B.-Q. Ma, Eur. Phys. J. C **79**, 409 (2019), 1905.02360.

[39] W. V. (priviate communication).

[40] Q.-h. Xu, Z.-t. Liang, and E. Sichtermann, Phys. Rev. D **73**, 077503 (2006), hep-ph/0511061.

[41] STAR Collaboration, M. S. Abdallah *et al.*, Phys. Rev. Lett. **129**, 092501 (2022), 2111.10396.

[42] STAR Collaboration, M. Abdallah *et al.*, Phys. Rev. D **106**, 072010 (2022), 2205.11800.

[43] M. A. *et al.* [STAR], Phys. Lett. B **827** (2022).

[44] STAR, M. S. Abdallah *et al.*, Phys. Lett. B **831**, 137152 (2022), 2108.00924.

[45] STAR, M. S. Abdallah *et al.*, Phys. Rev. Lett. **128**, 202303 (2022), 2112.00240.

[46] STAR, M. S. Abdallah *et al.*, Phys. Lett. B **827**, 137003 (2022), 2108.00908.

[47] STAR, M. Abdallah *et al.*, Phys. Rev. Lett. **128**, 202301 (2022), 2110.09513.

[48] STAR, M. S. Abdallah *et al.*, Phys. Rev. C **104**, L061901 (2021), 2108.00044.

[49] STAR, B. Aboona *et al.*, Phys. Rev. Lett. **130**, 212301 (2023), 2211.16981.

[50] STAR, M. Abdallah *et al.*, Phys. Rev. C **107**, 024908 (2023), 2209.11940.

[51] STAR, B. Aboona *et al.*, Phys. Rev. Lett. **130**, 082301 (2023), 2207.09837.

[52] STAR, M. Abdallah *et al.*, Phys. Lett. B **834**, 137449 (2022), 2207.00778.

[53] STAR, M. Abdallah *et al.*, Phys. Rev. Lett. **127**, 262301 (2021), 2105.14698.

[54] STAR, M. I. Abdulhamid *et al.*, Phys. Rev. C **108**, 014909 (2023).

[55] STAR, M. I. Abdulhamid *et al.*, Phys. Rev. C **107**, L061901 (2023).

[56] STAR, (2023), 2305.08705.

[57] STAR, (2023), 2304.03430.

[58] STAR, (2023), 2304.02831.

[59] STAR, (2023), 2303.03546.

[60] STAR, B. Aboona *et al.*, Phys. Lett. B **839**, 137779 (2023), 2209.03467.

[61] STAR, J. Adam *et al.*, (2018), 1810.10159.

[62] STAR, M. Abdallah *et al.*, Phys. Rev. C **107**, 034907 (2023), 2210.02909.

[63] STAR, M. Abdulhamid *et al.*, Phys. Rev. Lett. **130**, 202301 (2023), 2209.08058.

[64] STAR, M. S. Abdallah *et al.*, Phys. Rev. C **107**, 024901 (2023), 2208.00653.

[65] STAR, M. Abdallah *et al.*, Phys. Rev. C **105**, 014901 (2022), 2109.00131.

[66] STAR, Y. Feng, EPJ Web Conf. **276**, 06013 (2023), 2209.13078.

[67] STAR, M. I. Abdulhamid *et al.*, Phys. Rev. C **108**, 014908 (2023), 2210.14027.

[68] R. Belmont and J. L. Nagle, Phys. Rev. C **96**, 024901 (2017).

[69] STAR Collaboration, M. I. Abdulhamid *et al.*, Phys. Rev. C **108**, 014909 (2023).

[70] Z.-T. Liang and X.-N. Wang, Phys. Rev. Lett. **94**, 102301 (2005), nucl-th/0410079, [Erratum: Phys.Rev.Lett. 96, 039901 (2006)].

[71] S. A. Voloshin, (2004), nucl-th/0410089.

[72] STAR, L. Adamczyk *et al.*, Nature **548**, 62 (2017), 1701.06657.

[73] I. Karpenko and F. Becattini, Eur. Phys. J. C **77**, 213 (2017), 1610.04717.

[74] S. Alzhrani, S. Ryu, and C. Shen, Phys. Rev. C **106**, 014905 (2022), 2203.15718.

[75] STAR, X. Gou, EPJ Web Conf. **276**, 04007 (2023).

[76] STAR Collaboration, M. I. Abdulhamid *et al.*, Phys. Rev. C **108**, 014910 (2023).

[77] STAR, L. Adamczyk *et al.*, Phys. Rev. Lett. **115**, 222301 (2015), 1505.07812.

[78] G. Giacalone, J. Jia, and V. Somà, (2021), 2102.08158.

[79] J. Jia, Phys. Rev. C **105**, 014905 (2022), 2106.08768.

[80] J. Jia, Phys. Rev. C **105**, 044905 (2022), 2109.00604.

[81] C. Zhang and J. Jia, Phys. Rev. Lett. **128**, 022301 (2022), 2109.01631.

[82] J. Jia and C.-J. Zhang, (2021), 2111.15559.

[83] H.-J. Xu *et al.*, Phys. Rev. Lett. **121**, 022301 (2018), 1710.03086.

[84] H. Li *et al.*, Phys. Rev. Lett. **125**, 222301 (2020), 1910.06170.

[85] H.-j. Xu *et al.*, (2021), 2111.14812.

[86] A. Bilandzic, C. H. Christensen, K. Gulbrandsen, A. Hansen, and Y. Zhou, Phys. Rev. C **89**, 064904 (2014), 1312.3572.

[87] J. Jia, M. Zhou, and A. Trzupek, Phys. Rev. C **96**, 034906 (2017), 1701.03830.

[88] N. Borghini, P. M. Dinh, and J.-Y. Ollitrault, Phys. Rev. C **63**, 054906 (2001), nucl-th/0007063.

[89] STAR, M. Abdallah *et al.*, Phys. Rev. Lett. **129**, 252301 (2022), 2201.10365.

[90] ALICE, J. Adam *et al.*, Phys. Rev. Lett. **117**, 182301 (2016), 1604.07663.

[91] STAR, B. Aboona *et al.*, Phys. Lett. B **839**, 137755 (2023), 2211.11637.

[92] U. Gursoy, D. Kharzeev, and K. Rajagopal, Phys. Rev. C **89**, 054905 (2014), 1401.3805.

[93] U. Gürsoy, D. Kharzeev, E. Marcus, K. Rajagopal, and C. Shen, Phys. Rev. C **98**, 055201 (2018), 1806.05288.

[94] STAR, M. S. Abdallah *et al.*, Phys. Rev. Lett. **130**, 082301 (2023), 2207.09837.

[95] STAR, B. Aboona *et al.*, Phys. Rev. Lett. **130**, 112301 (2023), 2207.06568.

[96] STAR, M. I. Abdulhamid *et al.*, JHEP **06**, 176 (2023), 2303.06590.

[97] S. Cao, G.-Y. Qin, and S. A. Bass, Phys. Rev. C **92**, 024907 (2015), 1505.01413.

[98] T. Song *et al.*, Phys. Rev. C **92**, 014910 (2015), 1503.03039.

[99] T. Song *et al.*, Phys. Rev. C **96**, 014905 (2017), 1605.07887.

[100] STAR, M. S. Abdallah *et al.*, Eur. Phys. J. C **82**, 1150 (2022), 2111.14615, [Erratum: Eur.Phys.J.C 83, 455 (2023)].

[101] STAR, M. Abdallah *et al.*, Phys. Rev. C **106**, 044906 (2022), 2204.11661.

[102] STAR, (2023), 2307.13891.

[103] A. Andreassen, P. T. Komiske, E. M. Metodiev, B. Nachman, and J. Thaler, Phys. Rev. Lett. **124**, 182001 (2020), 1911.09107.

[104] M. Dasgupta, A. Fregoso, S. Marzani, and G. P. Salam, JHEP **09**, 029 (2013), 1307.0007.

[105] A. J. Larkoski, S. Marzani, G. Soyez, and J. Thaler, JHEP **05**, 146 (2014), 1402.2657.

[106] M. R. Aguilar *et al.*, Phys. Rev. D **105**, 016011 (2022), 2110.09447.

[107] M. H. Seymour and A. Siodmok, JHEP **10**, 113 (2013), 1307.5015.

[108] K. Lee, B. Meçaj, and I. Moult, (2022), 2205.03414.

[109] STAR Collaboration, J. Adam *et al.*, Phys. Rev. D **103**, 092009 (2021).

[110] J.-w. Qiu and G. F. Sterman, Phys. Rev. D **59**, 014004 (1999), hep-ph/9806356.

[111] K. Kanazawa, Y. Koike, A. Metz, and D. Pitonyak, Phys. Rev. D **89**, 111501 (2014).

[112] STAR Collaboration, J. Adam *et al.*, Phys. Rev. D **103**, 072005 (2021).

[113] STAR, *Transverse Single Spin Asymmetry for Inclusive and Diffractive Electromagnetic Jets at Forward Rapidities in $p^{\uparrow}p$ Collisions at $\sqrt{s}$ = 200 GeV and 510 GeV at STAR*, Zenodo, 2022.

[114] L. Bland *et al.*, Physics Letters B **750**, 660 (2015).

[115] STAR, H. Liu, Measurement of transverse single-spin asymmetries for dijet production in polarized pp collisions at $\sqrt{s} = 200$ GeV at STAR, in *Nuclear Physics Seminar, Brookhaven National Laboratory*, 2020, https://indico.bnl.gov/event/8633/.

[116] M. Boglione *et al.*, Phys. Lett. B **815**, 136135 (2021), 2101.03955.

[117] L. Gamberg, Z.-B. Kang, and A. Prokudin, Phys. Rev. Lett. **110**, 232301 (2013).

[118] STAR, B. Abelev *et al.*, Phys. Rev. Lett. **99**, 142003 (2007), 0705.4629.

[119] M. Bury, A. Prokudin, and A. Vladimirov, JHEP **05**, 151 (2021), 2103.03270.

[120] M. Bury, A. Prokudin, and A. Vladimirov, Phys. Rev. Lett. **126**, 112002 (2021), 2012.05135.

[121] J. P. Ralston and D. E. Soper, Nuclear Physics B **152**, 109 (1979).

[122] R. Jaffe and X.-D. Ji, Nucl. Phys. B **375**, 527 (1992).

[123] P. Mulders and R. Tangerman, Nucl. Phys. B **461**, 197 (1996), hep-ph/9510301, [Erratum: Nucl.Phys.B 484, 538–540 (1997)].

[124] D. Sivers, Nuovo Cim. C **035N2**, 171 (2012), 1109.2521.

[125] C. Alexandrou *et al.*, Phys. Rev. D **98**, 091503 (2018).

[126] R. Jaffe and X.-D. Ji, Phys. Rev. Lett. **67**, 552 (1991).

[127] Z.-B. Kang, X. Liu, F. Ringer, and H. Xing, JHEP **11**, 068 (2017), 1705.08443.

[128] Z.-B. Kang, A. Prokudin, F. Ringer, and F. Yuan, Phys. Lett. B **774**, 635 (2017), 1707.00913.

[129] U. D'Alesio, F. Murgia, and C. Pisano, Phys. Rev. D **83**, 034021 (2011), 1011.2692.

[130] J. C. Collins, S. F. Heppelmann, and G. A. Ladinsky, Nucl. Phys. B **420**, 565 (1994), hep-ph/9305309.

[131] L. Adamczyk *et al.*, Phys. Lett. B **780**, 332–339 (2018).

[132] M. Radici and A. Bacchetta, Phys. Rev. Lett. **120**, 192001 (2018), 1802.05212.

[133] STAR, L. Adamczyk *et al.*, Phys. Rev. D **97**, 032004 (2018), 1708.07080.

[134] U. D'Alesio, F. Murgia, and C. Pisano, Phys. Lett. B **773**, 300 (2017), 1707.00914.

[135] A. Airapetian *et al.*, Phys. Lett. B **693**, 11–16 (2010).

[136] C. Adolph *et al.*, Phys. Lett. B **744**, 250–259 (2015).

[137] STAR, L. Adamczyk *et al.*, Phys. Rev. Lett. **115**, 242501 (2015), 1504.00415.

[138] STAR, L. Adamczyk *et al.*, Phys. Lett. B **780**, 332 (2018), 1710.10215.

[139] B. Pokhrel, JPS Conf. Proc. **37**, 020121 (2022).

[140] A. Metz and A. Vossen, Prog. Part. Nucl. Phys. **91**, 136 (2016), 1607.02521.

[141] F. Yuan, Phys. Rev. Lett. **100**, 032003 (2008).

[142] F. Yuan, Phys. Rev. D **77**, 074019 (2008).

[143] STAR, J. Adam *et al.*, Phys. Rev. D **98**, 091103(R) (2018), 1808.08000.

[144] STAR, Y. Xu, Longitudinal and Transverse Spin Transfer of Λ and $\overline{\Lambda}$ Hyperons in Polarized p+p Collisions at $\sqrt{s} = 200$ GeV at RHIC-STAR, in *XXVIII International Workshop on Deep-Inelastic Scattering and Related Subjects, Stony Brook University*, 2021, https://indico.bnl.gov/event/9726/contributions/46261/.

[145] D. Müller, D. Robaschik, B. Geyer, F.-M. Dittes, and J. Hořejši, Fortsch. Phys. **42**, 101 (1994), hep-ph/9812448.

[146] X.-D. Ji, Phys. Rev. Lett. **78**, 610 (1997), hep-ph/9603249.

[147] A. Radyushkin, Phys. Lett. B **380**, 417 (1996), hep-ph/9604317.

[148] M. Burkardt, Phys. Rev. D **62**, 071503 (2000), hep-ph/0005108, [Erratum: Phys.Rev.D 66, 119903 (2002)].

[149] S. Klein and J. Nystrand, Photoproduction of J / psi and Upsilon in pp and anti-p p collisions, in *5th Workshop on Small x and Diffractive Physics*, 2003, hep-ph/0310223.

[150] S. R. Klein, J. Nystrand, J. Seger, Y. Gorbunov, and J. Butterworth, Comput. Phys. Commun. **212**, 258 (2017), 1607.03838.

[151] J. Lansberg, L. Massacrier, L. Szymanowski, and J. Wagner, Phys. Lett. B **793**, 33 (2019), 1812.04553.

[152] HERMES, A. Airapetian *et al.*, Phys. Lett. B **577**, 37 (2003), hep-ex/0307023.

[153] HERMES, A. Airapetian *et al.*, Nucl. Phys. B **780**, 1 (2007), 0704.3270.

[154] HERMES, A. Airapetian *et al.*, Phys. Lett. B **684**, 114 (2010), 0906.2478.

[155] W. Brooks and H. Hakobyan, Nucl. Phys. A **830**, 361C (2009), 0907.4606.

[156] NuSea, M. Vasilev *et al.*, Phys. Rev. Lett. **83**, 2304 (1999), hep-ex/9906010.

[157] K. J. Eskola, P. Paakkinen, H. Paukkunen, and C. A. Salgado, Epps21: A global qcd analysis of nuclear pdfs, 2021.

[158] PHENIX, S. Adler *et al.*, Phys. Rev. Lett. **98**, 172302 (2007), nucl-ex/0610036.

[159] R. Sassot, M. Stratmann, and P. Zurita, Phys. Rev. D **81**, 054001 (2010), 0912.1311.

[160] E. Aschenauer *et al.*, (2014), 1409.1633.

[161] N. Armesto, H. Paukkunen, J. M. Penín, C. A. Salgado, and P. Zurita, Eur. Phys. J. C **76**, 218 (2016), 1512.01528.

[162] H. Paukkunen, K. J. Eskola, and C. Salgado, Nucl. Phys. A **931**, 331 (2014), 1408.4563.

[163] K. J. Eskola, H. Paukkunen, and C. A. Salgado, JHEP **10**, 213 (2013), 1308.6733.

[164] H. Paukkunen and P. Zurita, JHEP **12**, 100 (2014), 1402.6623.

[165] V. Guzey and M. Klasen, Phys. Rev. D **104**, 114013 (2021), 2012.13277.

[166] L. Gribov, E. Levin, and M. Ryskin, Phys. Rept. **100**, 1 (1983).

[167] E. Iancu and R. Venugopalan, The Color glass condensate and high-energy scattering in QCD, in *In *Hwa, R.C. (ed.) et al.: Quark gluon plasma* 249-3363*, 2003, hep-ph/0303204.

[168] H. Weigert, Prog. Part. Nucl. Phys. **55**, 461 (2005), hep-ph/0501087.

[169] J. Jalilian-Marian and Y. V. Kovchegov, Prog. Part. Nucl. Phys. **56**, 104 (2006), hep-ph/0505052.

[170] F. Gelis, E. Iancu, J. Jalilian-Marian, and R. Venugopalan, Ann. Rev. Nucl. Part. Sci. **60**, 463 (2010), 1002.0333.

[171] G. Giuliani, H. Zheng, and A. Bonasera, Prog. Part. Nucl. Phys. **76**, 116 (2014), 1311.1811.

[172] Y. V. Kovchegov and E. Levin, *Quantum Chromodynamics at High Energy*Cambridge Monographs on Particle Physics, Nuclear Physics and Cosmology (Cambridge University Press, 2012).

[173] A. H. Mueller and J.-w. Qiu, Nucl. Phys. B **268**, 427 (1986).

[174] L. McLerran and R. Venugopalan, Phys. Rev. D **49**, 2233 (1994).

[175] L. McLerran and R. Venugopalan, Phys. Rev. D **49**, 3352 (1994).

[176] L. McLerran and R. Venugopalan, Phys. Rev. D **50**, 2225 (1994).

[177] Y. V. Kovchegov, Phys. Rev. D **54**, 5463 (1996).

[178] Y. V. Kovchegov, Phys. Rev. D **55**, 5445 (1997).

[179] J. Jalilian-Marian, A. Kovner, L. McLerran, and H. Weigert, Phys. Rev. D **55**, 5414 (1997).

[180] A. H. Mueller, Nucl. Phys. **B415**, 373 (1994).

[181] A. H. Mueller and B. Patel, Nucl. Phys. B **425**, 471 (1994), hep-ph/9403256.

[182] I. Balitsky, Nucl. Phys. **B463**, 99 (1996), hep-ph/9509348.

[183] I. Balitsky, Phys. Rev. D **60**, 014020 (1999), hep-ph/9812311.

[184] Y. V. Kovchegov, Phys. Rev. **D60**, 034008 (1999), hep-ph/9901281.

[185] Y. V. Kovchegov, Phys. Rev. D **61**, 074018 (2000), hep-ph/9905214.

[186] J. Jalilian-Marian, A. Kovner, and H. Weigert, Phys. Rev. D **59**, 014015 (1998), hep-ph/9709432.

[187] J. Jalilian-Marian, A. Kovner, A. Leonidov, and H. Weigert, Phys. Rev. D **59**, 014014 (1998), hep-ph/9706377.

[188] E. Iancu, A. Leonidov, and L. D. McLerran, Phys. Lett. B **510**, 133 (2001), hep-ph/0102009.

[189] E. Iancu, A. Leonidov, and L. D. McLerran, Nucl. Phys. **A692**, 583 (2001), hep-ph/0011241.

[190] A. Accardi *et al.*, Eur. Phys. J. A **52**, 268 (2016), 1212.1701.

[191] Y. V. Kovchegov and M. D. Sievert, Nucl. Phys. B **903**, 164 (2016), 1505.01176.

[192] CMS, S. Chatrchyan *et al.*, Eur. Phys. J. C **74**, 2951 (2014), 1401.4433.

[193] STAR, E. Braidot, Nucl. Phys. A **854**, 168 (2011), 1008.3989.

[194] PHENIX, A. Adare *et al.*, Phys. Rev. Lett. **107**, 172301 (2011), 1105.5112.

[195] C. Marquet, Nucl. Phys. A **796**, 41 (2007), 0708.0231.

[196] J. L. Albacete and C. Marquet, Phys. Rev. Lett. **105**, 162301 (2010), 1005.4065.

[197] Z.-B. Kang, I. Vitev, and H. Xing, Phys. Rev. D **85**, 054024 (2012), 1112.6021.

[198] M. Strikman and W. Vogelsang, Phys. Rev. D **83**, 034029 (2011), 1009.6123.

[199] J. Jalilian-Marian and A. H. Rezaeian, Phys. Rev. D **86**, 034016 (2012), 1204.1319.

[200] J. L. Albacete and C. Marquet, Nucl. Phys. A **854**, 154 (2011), 1009.3215.

[201] K. J. Eskola, H. Paukkunen, and C. A. Salgado, JHEP **07**, 102 (2008), 0802.0139.

[202] A. H. Rezaeian, Phys. Rev. D **86**, 094016 (2012), 1209.0478.

[203] T. Sjostrand, S. Mrenna, and P. Z. Skands, Comput. Phys. Commun. **178**, 852 (2008), 0710.3820.

[204] Di-jet production from pythia8.189 is scaled down due to its overestimation of inclusive π_0 yields compared to those reported by BRAHMS in phys. rev. lett. 98 (2007) 252001 and STAR in phys. rev. lett. 97 (2006) 152302.

[205] T. Kaufmann, A. Mukherjee, and W. Vogelsang, Phys. Rev. D **92**, 054015 (2015), 1506.01415, [Erratum: Phys.Rev.D 101, 079901 (2020)].

[206] D. de Florian, R. Sassot, M. Epele, R. J. Hernández-Pinto, and M. Stratmann, Phys. Rev. D **91**, 014035 (2015), 1410.6027.

[207] A. Khouaja *et al.*, Nucl. Phys. A **780**, 1 (2006).

[208] D. de Florian and R. Sassot, Phys. Rev. D **69**, 074028 (2004), hep-ph/0311227.

[209] D. de Florian, R. Sassot, and M. Stratmann, Phys. Rev. D **75**, 114010 (2007), hep-ph/0703242.

[210] D. de Florian, R. Sassot, and M. Stratmann, Phys. Rev. D **76**, 074033 (2007), 0707.1506.

[211] M. A. Lisa *et al.*, (2021), 2101.10872.

[212] J. L. Nagle and W. A. Zajc, Ann. Rev. Nucl. Part. Sci. **68**, 211 (2018), 1801.03477.

[213] PHENIX, C. Aidala *et al.*, Phys. Rev. C **95**, 034910 (2017), 1609.02894.

[214] G. Giacalone, B. Schenke, and C. Shen, Phys. Rev. Lett. **125**, 192301 (2020), 2006.15721.

[215] H. Helmholtz, The London, Edinburgh, and Dublin Philosophical Magazine and Journal of Science **33**, 485 (1867), https://doi.org/10.1080/14786446708639824.

[216] C. Shen *et al.*, In preparation.

[217] B. Schenke, S. Jeon, and C. Gale, Phys. Rev. **C82**, 014903 (2010), 1004.1408.

[218] J. Adams *et al.*, Nucl. Instrum. Meth. A **968**, 163970 (2020), 1912.05243.

[219] I. Upsal, *Global Polarization of the $\Lambda/\overline{\Lambda}$ system in the STAR BES*, Ph.D. thesis, The Ohio State University, 2018.

[220] Y. B. Ivanov and A. Soldatov, Phys. Rev. C **95**, 054915 (2017), 1701.01319.

[221] Y. B. Ivanov and A. Soldatov, Phys. Rev. C **97**, 044915 (2018), 1803.01525.

[222] Y. B. Ivanov, V. Toneev, and A. Soldatov, Phys. Atom. Nucl. **83**, 179 (2020), 1910.01332.

[223] Y. B. Ivanov, V. Toneev, and A. Soldatov, J. Phys. Conf. Ser. **1435**, 012012 (2020).

[224] B. Fu, K. Xu, X.-G. Huang, and H. Song, (2020), 2011.03740.

[225] M. Baznat, K. Gudima, A. Sorin, and O. Teryaev, Phys. Rev. C **88**, 061901 (2013), 1301.7003.

[226] O. Teryaev and R. Usubov, Phys. Rev. C **92**, 014906 (2015).

[227] M. I. Baznat, K. K. Gudima, A. S. Sorin, and O. Teryaev, Phys. Rev. C **93**, 031902 (2016), 1507.04652.

[228] W.-T. Deng and X.-G. Huang, Phys. Rev. C **93**, 064907 (2016), 1603.06117.

[229] D.-X. Wei, W.-T. Deng, and X.-G. Huang, Phys. Rev. C **99**, 014905 (2019), 1810.00151.

[230] X.-L. Xia, H. Li, Z.-B. Tang, and Q. Wang, Phys. Rev. C **98**, 024905 (2018), 1803.00867.

[231] A. Zinchenko, A. Sorin, O. Teryaev, and M. Baznat, J. Phys. Conf. Ser. **1435**, 012030 (2020).

[232] G. Bunce *et al.*, Phys. Rev. Lett. **36**, 1113 (1976).

[233] COSY-TOF, F. Hauenstein *et al.*, Eur. Phys. J. A **52**, 337 (2016), 1607.06305.

[234] F. Abe *et al.*, Phys. Rev. D **34**, 1950 (1986).

[235] B. Lundberg *et al.*, Phys. Rev. D **40**, 3557 (1989).

[236] HERA-B, I. Abt *et al.*, Phys. Lett. B **638**, 415 (2006), hep-ex/0603047.

[237] HADES, G. Agakishiev *et al.*, Eur. Phys. J. A **50**, 81 (2014), 1404.3014.

[238] A. Aprahamian *et al.*, (2015).

[239] F. Shen *et al.*, Nucl. Instrum. Meth. A **896**, 90 (2018), 1805.03938.

[240] STAR, CBM eTOF Group, The CBM Collaboration eTOF Group, (2016), 1609.05102.

[241] STAR, Y. Yang, Nucl. Phys. A **1005**, 121758 (2021).

[242] P. Bozek, W. Broniowski, and J. Moreira, Phys. Rev. **C83**, 034911 (2011), 1011.3354.

[243] J. Jia and P. Huo, Phys. Rev. **C90**, 034915 (2014), 1403.6077.

[244] L.-G. Pang, H. Petersen, G.-Y. Qin, V. Roy, and X.-N. Wang, Eur. Phys. J. **A52**, 97 (2016), 1511.04131.

[245] B. Schenke and S. Schlichting, Phys. Rev. **C94**, 044907 (2016), 1605.07158.

[246] W. Li, Nucl. Phys. A **967**, 59 (2017), 1704.03576.

[247] CMS, V. Khachatryan *et al.*, Phys. Rev. C **92**, 034911 (2015), 1503.01692.

[248] ATLAS, M. Aaboud *et al.*, Eur. Phys. J. C **78**, 142 (2018), 1709.02301.

[249] STAR, L. Adamczyk *et al.*, Phys. Rev. C **98**, 034918 (2018), 1701.06496.

[250] A. Behera, M. Nie, and J. Jia, Phys. Rev. Res. **2**, 023362 (2020), 2003.04340.

[251] C. Shen and B. Schenke, Phys. Rev. **C97**, 024907 (2018), 1710.00881.

[252] S. K. Das *et al.*, Phys. Lett. B **768**, 260 (2017), 1608.02231.

[253] S. Chatterjee and P. Bożek, Phys. Rev. Lett. **120**, 192301 (2018), 1712.01189.

[254] B. Chen, M. Hu, H. Zhang, and J. Zhao, Phys. Lett. B **802**, 135271 (2020), 1910.08275.

[255] STAR, J. Adam *et al.*, Phys. Rev. Lett. **121**, 132301 (2018), 1806.02295.

[256] ATLAS, M. Aaboud *et al.*, Phys. Rev. Lett. **121**, 212301 (2018), 1806.08708.

[257] J. E. Bernhard, J. S. Moreland, S. A. Bass, J. Liu, and U. Heinz, Phys. Rev. C **94**, 024907 (2016), 1605.03954.

[258] JETSCAPE, D. Everett *et al.*, Phys. Rev. C **103**, 054904 (2021), 2011.01430.

[259] G. Nijs, W. van der Schee, U. Gürsoy, and R. Snellings, Phys. Rev. Lett. **126**, 202301 (2021), 2010.15130.

[260] G. Denicol, A. Monnai, and B. Schenke, Phys. Rev. Lett. **116**, 212301 (2016), 1512.01538.

[261] H. Niemi, G. S. Denicol, P. Huovinen, E. Molnar, and D. H. Rischke, Phys. Rev. C **86**, 014909 (2012), 1203.2452.

[262] STAR, L. Adamczyk *et al.*, Phys. Rev. Lett. **111**, 052301 (2013), 1212.3304.

[263] X. Guo, S. Shi, N. Xu, Z. Xu, and P. Zhuang, Phys. Lett. B **751**, 215 (2015), 1502.04407.

[264] B. Chen, X. Du, and R. Rapp, Nucl. Part. Phys. Proc. **289-290**, 475 (2017), 1612.02089.

[265] ALICE, J. Adam *et al.*, JHEP **05**, 179 (2016), 1506.08804.

[266] ATLAS, M. Aaboud *et al.*, Eur. Phys. J. C **78**, 762 (2018), 1805.04077.

[267] CMS, A. M. Sirunyan *et al.*, Phys. Rev. Lett. **118**, 162301 (2017), 1611.01438.

[268] STAR, J. Adam *et al.*, Phys. Rev. Lett. **126**, 162301 (2021), 2012.13601.

[269] STAR, B. Abelev *et al.*, Phys. Rev. C **76**, 064904 (2007), 0706.0472.

[270] Z.-T. Liang, J. Song, I. Upsal, Q. Wang, and Z.-B. Xu, Chin. Phys. C **45**, 014102 (2021), 1912.10223.

[271] Y. Xie, D. Wang, and L. P. Csernai, Eur. Phys. J. C **80**, 39 (2020), 1907.00773.

[272] STAR, M. S. Abdallah *et al.*, Nature **614**, 244 (2023), 2204.02302.

[273] X.-L. Sheng, L. Oliva, and Q. Wang, Phys. Rev. D **101**, 096005 (2020), 1910.13684.

[274] X.-L. Sheng, Q. Wang, and X.-N. Wang, Phys. Rev. D **102**, 056013 (2020), 2007.05106.

[275] V. Voronyuk *et al.*, Phys. Rev. C **83**, 054911 (2011), 1103.4239.

[276] W.-T. Deng and X.-G. Huang, Phys.Rev. **C85**, 044907 (2012), 1201.5108.

[277] X.-L. Zhao, G.-L. Ma, and Y.-G. Ma, Phys. Rev. C **99**, 034903 (2019), 1901.04151.

[278] X.-L. Zhao, Y.-G. Ma, and G.-L. Ma, Phys. Rev. C **97**, 024910 (2018), 1709.05962.

[279] D. E. Kharzeev, L. D. McLerran, and H. J. Warringa, Nucl. Phys. A **803**, 227 (2008), 0711.0950.

[280] ALICE, S. Acharya *et al.*, Phys. Rev. Lett. **125**, 022301 (2020), 1910.14406.

[281] STAR, J. Adam *et al.*, Phys. Rev. Lett. **123**, 162301 (2019), 1905.02052.

[282] STAR, L. Adamczyk *et al.*, Phys. Rev. Lett. **113**, 022301 (2014), 1312.7397, [Addendum: Phys.Rev.Lett. 113, 049903 (2014)].

[283] D. Kharzeev and R. D. Pisarski, Phys.Rev. **D61**, 111901 (2000), hep-ph/9906401.

[284] D. Kharzeev, Phys. Lett. B **633**, 260 (2006), hep-ph/0406125.

[285] Y. Feng, Y. Lin, J. Zhao, and F. Wang, Phys. Lett. B **820**, 136549 (2021), 2103.10378.

[286] STAR, M. Abdallah *et al.*, Phys. Rev. Lett. **128**, 092301 (2022), 2106.09243.

[287] R. Milton *et al.*, Phys. Rev. C **104**, 064906 (2021), 2110.01435.

[288] F. Becattini, M. Buzzegoli, A. Palermo, and G. Prokhorov, Phys. Lett. B **822**, 136706 (2021), 2009.13449.

[289] L. Finch and S. Murray, Phys. Rev. C **96**, 044911 (2017), 1801.06476.

[290] STAR, (2023), 2304.10037.

[291] JETSCAPE, A. Kumar *et al.*, Nucl. Phys. A **1005**, 122009 (2021), 2002.07124.

[292] Y. Mehtar-Tani and K. Tywoniuk, Phys. Rev. D **98**, 051501 (2018), 1707.07361.

[293] Y. Mehtar-Tani and K. Tywoniuk, Nucl. Phys. A **979**, 165 (2018), 1706.06047.

[294] B. G. Zakharov, Eur. Phys. J. C **81**, 57 (2021), 2003.10182.

[295] L. Chen, G.-Y. Qin, S.-Y. Wei, B.-W. Xiao, and H.-Z. Zhang, Phys. Lett. B **773**, 672 (2017), 1607.01932.

[296] A. H. Mueller, B. Wu, B.-W. Xiao, and F. Yuan, Phys. Lett. B **763**, 208 (2016), 1604.04250.

[297] STAR, J. Adam *et al.*, Phys. Rev. C **102**, 054913 (2020), 2006.00582.

[298] STAR, N. R. Sahoo, PoS **HardProbes2020**, 132 (2021), 2008.08789.

[299] ALICE, J. Adam *et al.*, JHEP **09**, 170 (2015), 1506.03984.

[300] STAR, L. Adamczyk *et al.*, Phys. Rev. C **96**, 024905 (2017), 1702.01108.

[301] A. Bazavov *et al.*, Phys. Rev. D **95**, 054504 (2017), 1701.04325.

[302] S. Borsanyi *et al.*, JHEP **10**, 205 (2018), 1805.04445.

[303] CMS, V. Khachatryan *et al.*, Phys. Lett. B **772**, 489 (2017), 1605.06966.

[304] ALICE, B. Abelev *et al.*, Phys. Lett. B **718**, 1273 (2013), 1209.3715.

[305] STAR, L. Adamczyk *et al.*, Phys. Rev. C **96**, 054904 (2017), 1702.07705.

[306] ALICE, S. Acharya *et al.*, JHEP **06**, 035 (2020), 2002.10897.

[307] ALICE, S. Acharya *et al.*, (2021), 2101.02581.

[308] ALICE, S. Acharya *et al.*, (2021), 2101.04623.

[309] ALICE, S. Acharya *et al.*, (2021), 2101.04577.

[310] LHCb, R. Aaij *et al.*, Phys. Rev. C **105**, L032201 (2022), 2108.02681.

[311] M. Alvioli, L. Frankfurt, V. Guzey, M. Strikman, and M. Zhalov, CERN Proc. **1**, 151 (2018).

[312] V. Guzey and M. Zhalov, JHEP **10**, 207 (2013), 1307.4526.

[313] V. Guzey, M. Strikman, and M. Zhalov, Phys. Rev. C **99**, 015201 (2019), 1808.00740.

[314] B. Sambasivam, T. Toll, and T. Ullrich, Phys. Lett. B **803**, 135277 (2020), 1910.02899.

[315] V. Guzey, Phys. Part. Nucl. Lett. **16**, 498 (2019).

[316] V. Guzey and M. Klasen, Inclusive and diffractive dijet photoproduction in ultraperipheral heavy ion collisions at the LHC, in *28th International Workshop on Deep Inelastic Scattering and Related Subjects*, 2021, 2106.16084.

[317] W. Chang *et al.*, Phys. Rev. D **106**, 012007 (2022), 2204.11998.

[318] V. Guzey, M. Strikman, and M. Zhalov, Eur. Phys. J. C **74**, 2942 (2014), 1312.6486.

[319] H. Xing, C. Zhang, J. Zhou, and Y.-J. Zhou, JHEP **10**, 064 (2020), 2006.06206.

[320] STAR, J. the STAR Collaboration, Adam *et al.*, Phys. Rev. Lett. **123**, 132302 (2019), 1904.11658.

[321] W. Zha *et al.*, Phys. Rev. C **97**, 044910 (2018), 1705.01460.

[322] M. B. Gay Ducati and S. Martins, Phys. Rev. D **97**, 116013 (2018), 1804.09836.

[323] W. Shi, W. Zha, and B. Chen, Phys. Lett. B **777**, 399 (2018), 1710.00332.

[324] M. R. Whalley, D. Bourilkov, and R. C. Group, The Les Houches accord PDFs (LHAPDF) and LHAGLUE, in *HERA and the LHC: A Workshop on the Implications of HERA and LHC Physics (Startup Meeting, CERN, 26-27 March 2004; Midterm Meeting, CERN, 11-13 October 2004)*, pp. 575–581, 2005, hep-ph/0508110.

[325] M. Cacciari and G. P. Salam, Phys. Lett. B **641**, 57 (2006), hep-ph/0512210.

[326] X. Ji, F. Yuan, and Y. Zhao, Phys. Rev. Lett. **118**, 192004 (2017), 1612.02438.

[327] Y. Hatta, Y. Nakagawa, F. Yuan, Y. Zhao, and B. Xiao, Phys. Rev. D **95**, 114032 (2017), 1612.02445.

[328] S. Bhattacharya, R. Boussarie, and Y. Hatta, Phys. Rev. Lett. **128**, 182002 (2022), 2201.08709.

[329] Y. Hatta, B.-W. Xiao, and F. Yuan, Phys. Rev. Lett. **116**, 202301 (2016), 1601.01585.

[330] ZEUS, I. Abt *et al.*, JHEP **12**, 102 (2021), 2106.12377.

[331] PHENIX, C. Aidala *et al.*, Nature Phys. **15**, 214 (2019), 1805.02973.

[332] W. Zhao, C. Shen, and B. Schenke, Phys. Rev. Lett. **129**, 252302 (2022), 2203.06094.

[333] ATLAS, G. Aad *et al.*, Phys. Rev. C **104**, 014903 (2021), 2101.10771.

[334] STAR, R. A. Lacey, Nucl. Phys. A **1005**, 122041 (2021), 2002.11889.

[335] D. Kharzeev, Phys. Lett. B **378**, 238 (1996), nucl-th/9602027.

[336] C. A. Bertulani, S. R. Klein, and J. Nystrand, Ann. Rev. Nucl. Part. Sci. **55**, 271 (2005), nucl-ex/0502005.

[337] Z. Tu *et al.*, Phys. Lett. B **811**, 135877 (2020), 2005.14706.

[338] ALICE Collaboration, Phys. Lett. B **784**, 82 (2018), 1805.01832.

[339] CMS, A. M. Sirunyan *et al.*, Phys. Rev. C **100**, 044902 (2019), 1901.07997.

[340] ATLAS Collaboration, (2019), 1911.04812.

[341] ATLAS, G. Aad *et al.*, Phys. Rev. C **107**, 054910 (2023), 2205.00039.

[342] B. Bally, M. Bender, G. Giacalone, and V. Somà, Phys. Rev. Lett. **128**, 082301 (2022), 2108.09578.

[343] U. W. Heinz and A. Kuhlman, Phys.Rev.Lett. **94**, 132301 (2005), nucl-th/0411054.

[344] Q. Y. Shou *et al.*, Phys. Lett. B **749**, 215 (2015), 1409.8375.

[345] G. Giacalone, Phys. Rev. Lett. **124**, 202301 (2020), 1910.04673.

[346] G. Giacalone, *A matter of shape: seeing the deformation of atomic nuclei at high-energy colliders*, PhD thesis, U. Paris-Saclay, 2020, 2101.00168.

[347] G. Giacalone, J. Jia, and C. Zhang, (2021), 2105.01638.

[348] H.-j. Xu, H. Li, X. Wang, C. Shen, and F. Wang, Phys. Lett. B **819**, 136453 (2021), 2103.05595.

[349] S. Raman, C. W. G. Nestor, Jr, and P. Tikkanen, Atom. Data Nucl. Data Tabl. **78**, 1 (2001).

[350] S. E. Agbemava, A. V. Afanasjev, and P. Ring, Phys. Rev. C **93**, 044304 (2016), 1603.03414.

[351] P. Möller, A. J. Sierk, T. Ichikawa, and H. Sagawa, Atom. Data Nucl. Data Tabl. **109-110**, 1 (2016), 1508.06294.

[352] L. M. Robledo and G. F. Bertsch, Phys. Rev. C **84**, 054302 (2011), 1107.3581.

[353] S. Hilaire and M. Girod, Eur. Phys. J. A **33**, 237 (2007).

[354] T. Nakatsukasa, K. Matsuyanagi, M. Matsuo, and K. Yabana, Rev. Mod. Phys. **88**, 045004 (2016), 1606.04717.

[355] L.-M. Liu *et al.*, (2022), 2203.09924.

[356] S. Zhao, H.-j. Xu, Y.-X. Liu, and H. Song, (2022), 2204.02387.

[357] J. Jia, S. Huang, and C. Zhang, (2021), 2105.05713.

[358] G. Giacalone, Phys. Rev. C **99**, 024910 (2019), 1811.03959.

[359] STAR, H. Xu, Acta Phys. Polon. Supp. **16**, 30 (2023), 2208.06149.

[360] G. Nijs and W. van der Schee, (2021), 2112.13771.

[361] J. M. Lattimer and M. Prakash, Phys. Rept. **442**, 109 (2007), astro-ph/0612440.

[362] B.-A. Li, B.-J. Cai, W.-J. Xie, and N.-B. Zhang, Universe **7**, 182 (2021), 2105.04629.

[363] PREX, D. Adhikari *et al.*, Phys. Rev. Lett. **126**, 172502 (2021), 2102.10767.

[364] ALICE, S. Acharya *et al.*, (2021), 2111.06106.

[365] B. Schenke, C. Shen, and D. Teaney, Phys. Rev. C **102**, 034905 (2020), 2004.00690.

[366] G. Giacalone, Phys. Rev. C **102**, 024901 (2020), 2004.14463.

[367] G. Giacalone, F. G. Gardim, J. Noronha-Hostler, and J.-Y. Ollitrault, Phys. Rev. C **103**, 024910 (2021), 2004.09799.

[368] N. N. D. Center, Chart of nuclear quadrupole deformations.

[369] P. A. Butler, J. Phys. G **43**, 073002 (2016).

[370] C. J. Lister and J. Butterworth, Nature **497**, 190 (2013).

[371] J. W. Norbury *et al.*, Frontiers in Physics **8** (2020).